The Pennsylvania State University
The Graduate School
Eberly College of Science

# INTERPRETING THE SPECTRAL SIGNATURES OF SURFACE-ENHANCED RAMAN SCATTERING

A Dissertation in
Chemistry
by
Dhabih V. Chulhai



Submitted in Partial Fulfillment
of the Requirements
for the Degree of

Doctor of Philosophy

August 2016

The dissertation of Dhabih V. Chulhai was reviewed and approved* by the following:

Lasse Jensen
Associate Professor of Chemistry
Dissertation Advisor, Chair of Committee

Miriam A. Freedman
Assistant Professor of Chemistry

William G. Noid
Associate Professor of Chemistry

Adrianus C. Van Duin
Kenneth Kuan-Yun Kuo Early Career Professor
Professor of Mechanical, Nuclear and Chemical Engineering

Kenneth S. Feldman
Professor of Chemistry
Graduate Program Chair

*Signatures are on file in the Graduate School.

# Abstract

Molecules may be uniquely identified through the inelastic light scattering process known as Raman scattering. The Raman scattered intensities are often weak, but may be enhanced by several orders of magnitude—through the process known as surface-enhanced Raman scattering (SERS)—by placing the molecules near the surface of metallic nanoparticles. Through SERS, we can detect the scattering from a single molecule, which means that the technique is useful for the ultra-sensitive detection of chemical and biological agents. However, the SERS signals are often very different from the signals of normal Raman scattering, as they now reflect the various interactions of the molecule(s) with the nanoparticle. Understanding these spectral changes are, therefore, vital in both identifying the probed molecule, and in understanding and extracting information of the molecule's interaction with the surface. To understand these changes, we have developed the dressed-tensors formalism that takes into account the interaction of the molecule with the inhomogeneous local electric fields from the nanoparticle. With this method, we show that the field gradient contribution to the spectral changes often reflect the relative orientation of the molecule with respect to the surface. This result, coupled with the dynamics of the probed molecule, suggests that the translational and rotational motions of a single molecule may be tracked through its SERS spectral changes. We have also extended this method to describe other types of surface-enhanced spectroscopies, namely Raman optical activity (ROA), which is sensitive to chiral structures and used to probe the behavior of biomolecules in solution, and circular dichroism (CD), which is often used to investigate the secondary structure of proteins. For surface-enhanced ROA (SEROA), we find that spectral changes are highly sensitive to the local electric field gradient, the orientation of the molecule, and the surface plasmon frequency width, giving insight into why mirror-image SEROA is yet to be observed for enantiomers. We also find that the spectral signatures of plasmonic CD are similarly complicated. However, this electromagnetic fields description of the enhancement is insufficient at describing the spectral changes for certain chemical systems. We find that, at low temperatures and for single or few molecules, the observed shift of particular normal modes may be reflective of the specific binding interactions of the molecule with the surface. In the case of resonant single molecule SERS of rhodamine-6G, we show that the relative intensity fluctuations are independent of the orientation of the molecule, but may rather describe picometer changes in its excited state geometry. These results indicate that we need a rigorous method to account for the quantum mechanical interactions between the molecule and the surface. To this end, we have developed an exact subsystem density functional theory (DFT) method that can exactly reproduce the supermolecular energies and densities of a wide range of systems, including covalently bonded subsystems. We have also extended this method to the time-dependent DFT regime, and show that we can accurately reproduce supermolecular excitation energies of strongly coupled subsystems. The spectral changes observed in SERS contain a lot of information of the molecule-nanoparticle interactions, and the methods developed here have allowed—and will continue to allow—us to interpret these changes.

# Table of Contents

**List of Figures** x

**List of Tables** xiii

**List of Symbols** xv

**Acknowledgments** xvii

**I Introductory Material** 1

**Chapter 1**
**Introduction** 2
Overview of Dissertation . . . 3

**Chapter 2**
**Overview of the Electromagnetic Theory of Surface-Enhanced Raman Scattering** 8
2.1 Raman Scattering . . . 8
2.2 Surface-Enhanced Raman Scattering . . . 12
2.3 Theoretical Models of the Electromagnetic Mechanism . . . 14
2.3.1 Silberstein's equations . . . 14
2.3.2 Gersten-Nitzan model . . . 15
2.3.3 Image field effect . . . 16
2.3.4 The discrete interaction model/quantum mechanical method . . . 17

**Chapter 3**
**Overview of Other Theoretical Methods Used** 19
3.1 Kohn-Sham Density Functional Theory . . . 19
3.2 Subsystem Density Functional Theory . . . 21
3.2.1 Frozen density embedding . . . 21
3.2.2 Kinetic energy density functionals and external orthogonality . . . 24
3.3 Subsystem Response Theory . . . 26
3.3.1 Time-dependent density functional theory . . . 26
3.3.2 Subsystem time-dependent density functional theory . . . 29

**II The Dressed-Tensors Formalism** **31**

**Chapter 4**
**Determining Molecular Orientation With Surface-Enhanced Raman Scattering Using Inhomogeneous Electric Fields** **32**
4.1 Introduction . . . 33
4.2 Theory . . . 34
4.2.1 SERS in an inhomogeneous electric field . . . 34
4.3 Computational Details . . . 36
4.4 Results and Discussion . . . 38
4.4.1 Enhancement factors in an inhomogeneous electric field . . . 38
4.4.2 SERS of benzene . . . 39
4.4.3 SERS of pyridine . . . 42
4.4.4 Field-gradient effects in atomistic models . . . 46
4.5 Conclusion . . . 47

**Chapter 5**
**Simulating Ensemble-Averaged Surface-Enhanced Raman Scattering** **49**
5.1 Introduction . . . 50
5.2 Computational Details . . . 51
5.2.1 Molecular dynamics simulations . . . 51
5.2.2 The dressed-tensors formalism . . . 51
5.2.3 Quantum mechanical calculations . . . 52
5.3 Results and Discussion . . . 53
5.3.1 Advantages and limitations . . . 53
5.3.2 Analyzing hot-spots . . . 53
5.3.3 Distribution and spectral dependence on theoretical models . . . 57
5.3.3.1 The impact of the electrodynamics method on the SERS distribution 57
5.3.3.2 The effect of sampling methods on the SERS distribution . . . 58
5.3.3.3 The SERS spectral signatures with field gradients . . . 59
5.3.4 Tracking single molecules . . . 60
5.4 Conclusion . . . 62

**Chapter 6**
**Simulating Surface-Enhanced Raman Optical Activity Using Atomistic Electrodynamics-Quantum Mechanical Models** **63**
6.1 Introduction . . . 64
6.2 Theory . . . 65
6.2.1 General ROA theory . . . 65
6.2.2 DIM/QM in the modified velocity gauge . . . 66
6.2.3 Dressed-tensors formalism . . . 69
6.3 Computational Details . . . 71
6.4 Results and Discussion . . . 71
6.4.1 SEROA with DIM/QM . . . 71
6.4.2 SEROA using dressed tensors . . . 73
6.4.3 SEROA dependence on plasmon width . . . 75
6.4.4 SEROA of bromohexahelicene . . . 78
6.5 Conclusion . . . 80

**Chapter 7**
**Plasmonic Circular Dichroism of 310- and alpha-Helix Using a Discrete Interaction Model / Quantum Mechanics Method** **82**
7.1 Introduction . . . 83
7.2 Theory . . . 84
7.3 Computational Details . . . 85
7.4 Results and Discussion . . . 86
7.5 Conclusion . . . 92

**III An Exact Subsystem Density Functional Theory** **93**

**Chapter 8**
**Frozen Density Embedding with External Orthogonality** **94**
8.1 Introduction . . . 95
8.2 Theory . . . 96
8.3 Computational Details . . . 98
8.4 Results and Discussion . . . 98
8.4.1 Exact KS-DFT results . . . 98
8.4.2 Effects of basis set truncation . . . 101
8.5 Conclusion . . . 107

**Chapter 9**
**External Orthogonality in Subsystem Time-dependent Density Functional Theory** **109**
9.1 Introduction . . . 110
9.2 Theory . . . 111
9.2.1 Subsystem TDDFT . . . 111
9.2.2 The FDE-EO method . . . 113
9.2.3 The EO coupling matrix . . . 113
9.3 Computational Details . . . 114
9.4 Results and Discussion . . . 114
9.4.1 Dependence on $\mu$-parameter . . . 114
9.4.2 LiH . . . 116
9.4.3 He-dimer . . . 117
9.4.4 2-aminopyridine–methanol . . . 119
9.4.5 Benzaldehyde-dimer . . . 120
9.5 Conclusion . . . 122

**IV Using Theory to Elucidate Experimental Observations** **124**

**Chapter 10**
**The Tip-enhanced Raman Scattering of H2TBPP Monolayer** **125**
10.1 Introduction . . . 126
10.2 Computational Details . . . 126
10.3 Correctly Describing the Tip-enhanced Raman Scattering of H2TBPP . . . 127
10.4 Conclusion . . . 129

**Chapter 11**
**The Origin of Relative Intensity Fluctuations in Single-Molecule Tip-Enhanced Raman Spectroscopy** **132**
11.1 Introduction . . . 133
11.2 Computational Details . . . 134
11.3 Results and Discussion . . . 135
11.4 Conclusion . . . 136

**Chapter 12**
**Binding Orientation of Rhodamine-6G From Tip-Enhanced Raman Spectroscopy** **141**
12.1 Introduction . . . 142
12.2 Computational Details . . . 143
12.3 Spectral Shifts in LT-TERS . . . 143
12.4 Conclusion . . . 147

**V Summary and Outlook** **148**

**Chapter 13**
**Summary and Outlook** **149**
13.1 Dissertation Summary . . . 149
13.2 Future Directions for the Dressed-Tensors Formalism . . . 150
13.2.1 Field gradient effects in non-linear spectroscopies . . . 150
13.2.2 Octopole response in surface-enhanced Raman scattering . . . 152
13.2.3 Tip-enhanced Raman imaging of molecular vibrations . . . 153
13.2.4 Molecule-molecule interactions in ensemble surface-enhanced Raman scattering . . . 153
13.3 Future Directions for the Exact Subsystem Density Functional Theory . . . 154
13.3.1 Applications to few-states resonant Raman scattering . . . 155
13.3.2 Calculation of general response properties . . . 155

**Appendices** **156**

**Appendix A**
**Fixed-frame and Orientationally-averaged Raman Scattering** **157**
A.1 Electric and Magnetic Multipole Radiation Fields . . . 157
A.2 Stokes Parameters . . . 159
A.3 Beyond the $a_{\alpha\beta} \approx \alpha_{\alpha\beta}$ Approximation . . . 163
A.4 Isotropically-Averaged Raman Scattering . . . 166
A.5 Isotropic Averaging About the $z$-Axis . . . 167
A.6 Polarized Incident Light . . . 168

**Appendix B**
**Summary of the Dressed-tensors Formalism** **170**
B.1 Derivation of the Formalism . . . 170
B.2 Local Field Gradients . . . 172
B.3 Point-Dipole / Point-Quadrupole Molecule . . . 172
B.4 Other Dressed Polarizability Tensors . . . 174

B.4.1 Surface-enhanced Raman optical activity . . . . . 174
B.4.2 Nonlinear tensors . . . . . 175

**Appendix C**
**Origin-dependence of Multipole Moments and Higher Order Polarizabilities 176**
C.1 Multipole Moments . . . . . 176
C.1.1 Electric dipole and quadrupole . . . . . 176
C.1.2 Magnetic dipole . . . . . 177
C.2 Polarizabilities . . . . . 177
C.2.1 Electric dipole-dipole polarizability . . . . . 177
C.2.2 Electric dipole-quadrupole polarizability . . . . . 178
C.2.3 Electric quadrupole-quadrupole polarizability . . . . . 178
C.2.4 Electric dipole-magnetic dipole polarizability . . . . . 179
C.2.5 Electric quadrupole-magnetic dipole polarizability . . . . . 180

**Appendix D**
**Supporting Information for: Determining Molecular Orientation With Surface-Enhanced Raman Scattering Using Inhomogeneous Electric Fields 181**
D.1 Origin-Dependence of Terms . . . . . 181
D.1.1 Origin-dependence of the induced dipole . . . . . 181
D.1.2 Origin-dependence of the effective dipole . . . . . 183
D.1.3 Proof of origin-invariance . . . . . 184

**Appendix E**
**Supporting Information for: Simulating Ensemble-Averaged Surface-Enhanced Raman Scattering 187**
E.1 Ag-Pyridine Force Field Details . . . . . 187
E.2 Enhancement Distributions . . . . . 189

**Appendix F**
**Supporting Information for: Simulating Surface-Enhanced Raman Optical Activity Using Atomistic Electrodynamics-Quantum Mechanical Models 191**
F.1 ROA of 2BrHH . . . . . 191
F.2 Origin-Dependence of $A$, $G'$, $C$ and $D$ Response Tensors . . . . . 191
F.3 Damping in the Modified Velocity Gauge . . . . . 193
F.3.1 The modified velocity gauge . . . . . 193
F.3.2 Finite lifetime effects in MVG . . . . . 194

**Appendix G**
**Supporting Information for: Frozen Density Embedding with External Orthogonality 196**
G.1 System Geometries . . . . . 196
G.2 Energy, Density, and Dipole Differences . . . . . 203
G.3 Extended Monomer Truncation . . . . . 205
G.4 DZP-Truncated Basis Data . . . . . 206

**Appendix H**
**Supporting Information for: External Orthogonality in Subsystem Time-dependent Density Functional Theory** **207**
H.1 EO Operator in MO Basis . . . . . 207
H.2 Long-Range Correction to the NAKP . . . . . 208
H.3 Significance of the EO Kernel . . . . . 208

**Appendix I**
**Potential Energy Distributions for all Normal Modes of Rhodamine-6G** **210**

**Bibliography** **214**

# List of Figures


1.1 Experimental NRS and SERS of pyridine . . . . . 3

2.1 Schematic of Rayleigh and Raman scattering . . . . . 9
2.2 Schematic of a plasmon interacting with an electric field . . . . . 12
2.3 Illustration of the mechanisms of SERS . . . . . 14

3.1 Illustration of KS-DFT, subsystem DFT, and FDE . . . . . 22

4.1 SERS spectrum of benzene on silver colloids excited at 488 nm . . . . . 40
4.2 SERS of benzene flat on a surface with field gradient . . . . . 40
4.3 SERS of benzene perpendicular to a surface with field gradient . . . . . 41
4.4 Simulated SERS of benzene titled at 10° with respect to the surface . . . . . 42
4.5 SERS of pyridine perpendicular and parallel to the surface . . . . . 43
4.6 The major contributors to the FG SERS spectrum of pyridine . . . . . 44
4.7 Comparison of experimental and simulated SERS spectrum of pyridine . . . . . 45
4.8 SERS spectrum of benzene showing field and gradient effects in DIM/QM . . . . 46

5.1 Field enhancement along a cut plane for different substrates . . . . . 54
5.2 Individual molecules colored by their enhancement factors . . . . . 55
5.3 TPD analyses of the different substrates . . . . . 56
5.4 Ensemble SERS spectra using DIM and DDA methods . . . . . 59
5.5 Tracking translational motion of a single molecule . . . . . 61
5.6 Tracking rotational motion of a single molecule . . . . . 62

6.1 Orientation of DMO on a $Ag_{2057}$ icosahedron . . . . . 71
6.2 SEROA of DMO on a $Ag_{2057}$ cluster . . . . . 72
6.3 ROA and SEROA of DMO on $Ag_{2057}$ . . . . . 73
6.4 Dressed-tensor and DIM/QM SEROA spectra of DMO on a $Ag_{2057}$ cluster . . . 74
6.5 SERS enhancement for DMO on $Ag_{2057}$ as a function of distance . . . . . 75
6.6 SEROA enhancement for DMO on $Ag_{2057}$ as a function of distance . . . . . 76
6.7 SERS and SEROA of DMO with different NP polarizability at $\omega_I$ and $\omega_S$ . . . . 77
6.8 Orientation of (+)2Brhh and (-)2Brhh on $Ag_{21k}$ . . . . . 78
6.9 DIM/QM and dressed-tensors comparison of the SEROA of (+/-)2Brhh . . . . . 79
6.10 SEROA of 2Brhh enantiomers with and without mirror symmetry . . . . . 80

7.1 Absorption spectra of $3_{10}$- and $\alpha$-helix $Ala_{20}$, and of $Ag_{104k}$ . . . . . 86
7.2 CD spectra of $\alpha$- and $3_{10}$-helices . . . . . 87
7.3 Orientations of $3_{10}$- and $\alpha$-helices with respect to $Ag_{104k}$ . . . . . 88

7.4 Absorption spectra of perpendicular and parallel $3_{10}$- and $\alpha$-helices on $Ag_{104k}$ . . 88
7.5 CD spectra of perpendicular and parallel $\alpha$-helix on $Ag_{104k}$ . . . . . 89
7.6 CD spectra of perpendicular and parallel $3_{10}$-helix on $Ag_{104k}$ . . . . . 90
7.7 CD spectra of achiral pyridine on $Ag_{147}$ with image and local fields . . . . . 91

8.1 Density difference for benzene using FDE-TF FDE-EO . . . . . 100
8.2 $|\Delta E|$ of FDE-EO for alkanes and alkenes . . . . . 102
8.3 $\Delta^{\text{abs}}$ of FDE-EO for alkanes and alkenes . . . . . 103
8.4 Example of basis set truncation in $C_{16}H_{20}$ . . . . . 104
8.5 $|\Delta E|$-dependence on $\mu$ for $C_{10}H_{20}$ and $C_{10}H_{12}$ . . . . . 105
8.6 $E^{\text{ovrlp}}$ with freeze-and-thaw for $C_{14}H_{28}$ and $C_{18}H_{20}$ . . . . . 106
8.7 Basis set truncation results . . . . . 107

9.1 Stability of $|\Delta E|$ and excitation energies with respect to $\mu$ . . . . . 115
9.2 Excitation energies of LiH with respect to inter-atomic separation . . . . . 117
9.3 Excitation energies of a He-dimer as a function of atomic separation . . . . . 118
9.4 Isosurface plots of the $\pi$ and $\pi^*$ orbitals of 2-aminopyridine–methanol . . . . . 119
9.5 Excitation energy of the $\pi \to \pi^*$ transition in 2-aminopyridine–methanol . . . . . 119
9.6 Isosurface plots of the $\pi$ and $\pi^*$ orbitals of benzaldehyde . . . . . 120
9.7 Excitation energies of the $\pi \to \pi^*$ excitation of benzaldehyde-dimer . . . . . 121
9.8 Absorption of benzaldehyde using TDDFT, FDEc-TF, and FDEc-EO . . . . . 122

10.1 Absorption, UHV-TERS, and normal modes of H2TBPP . . . . . 128
10.2 SERRS excitation profile of the $Q_y$ band of H2TBPP . . . . . 130
10.3 SERRS excitation profile of the $Q_x$ band of H2TBPP . . . . . 131

11.1 SMTERS waterfall plot of R6G . . . . . 138
11.2 Four most intense normal modes in R6G TERS . . . . . 139
11.3 Experimental and theoretical TERS fluctuations . . . . . 139
11.4 Ensemble SERS and TERS compared to summed SMTERS . . . . . 140

12.1 Spectral comparisons for R6G on silver surfaces . . . . . 144
12.2 Eigenvectors of R6G normal modes . . . . . 146

13.1 The inhomogeneity of the local field in a symmetric junction . . . . . 152
13.2 Sub-nanometer TERS imaging of water . . . . . 154

B.1 SERS surface selection for benzene . . . . . 173

D.1 Origin-dependence of the SERS of benzene . . . . . 181
D.2 Origin-independent SERS expression with a local field and gradient . . . . . 183
D.3 SERS of benzene using the common-origin expression . . . . . 186

E.1 Interaction energy as a function of Ag–N distance . . . . . 188
E.2 TPD analysis with field and gradient . . . . . 189
E.3 TPD analysis for MD and random sampling . . . . . 190

F.1 ROA of 2Brhh enantiomers using the BP86-TZ2P level of theory . . . . . 191
F.2 ROA of the 1600 and 1064 $cm^{-1}$ modes of 2Brhh with the DIM/QM force field . 192

G.1 $|\Delta\mu|$ of FDE-EO for alkanes and alkenes . . . . . 205
G.2 Number of fragment basis functions in the conjugated alkenes . . . . . 206
G.3 Computation time for KS-DFT and FDE-EO . . . . . 206

H.1 Excitation energies of LiH with long-range correction to the NAKP . . . . . 208
H.2 EO kernel contribution to excitation energies of He-dimer . . . . . 209

# List of Tables


4.1 SERS terms and their relevant enhancement factors . . . . . 39

5.1 TPD enhancement distribution results from the different nanoparticle systems . . 56
5.2 TPD enhancement distribution results from the different models . . . . . 57

8.1 Energy errors with FDE-TF and FDE-EO . . . . . 98
8.2 $\Delta^{\text{abs}}$ for FDE-TF and FDE-EO . . . . . 99

10.1 Calculated excited states properties of H2TBPP . . . . . 128

11.1 Parameters used to reproduce experimental spectra . . . . . 136

12.1 Calculated PEDs for R6G LT-TERS . . . . . 145

B.1 EM enhancement factor contributions to the SERS intensity. . . . . 174

E.1 Morse potential parameters in EAM potential . . . . . 187
E.2 Signal contribution from the different nanoparticle systems . . . . . 189
E.3 Signal contribution from the different models . . . . . 190

G.1 Water dimer geometry . . . . . 196
G.2 $FHF^-$ geometry . . . . . 196
G.3 $BH_3NH_3$ geometry . . . . . 196
G.4 $C_2H_6$ geometry . . . . . 197
G.5 $C_6H_{12}$ geometry . . . . . 197
G.6 $C_8H_{16}$ geometry . . . . . 197
G.7 $C_{10}H_{20}$ geometry . . . . . 198
G.8 $C_{12}H_{24}$ geometry . . . . . 198
G.9 $C_{14}H_{28}$ geometry . . . . . 199
G.10 $C_6H_8$ geometry . . . . . 199
G.11 $C_8H_{12}$ geometry . . . . . 199
G.12 $C_{10}H_{12}$ geometry . . . . . 200
G.13 $C_{12}H_{16}$ geometry . . . . . 200
G.14 $C_{14}H_{16}$ geometry . . . . . 201
G.15 $C_{16}H_{20}$ geometry . . . . . 201
G.16 $C_{18}H_{20}$ geometry . . . . . 202
G.17 $C_{20}H_{24}$ geometry . . . . . 202
G.18 $\Delta E$ for FDE-EO with basis set truncation . . . . . 203

G.19 $\Delta^{\text{abs}}$ for FDE-EO with basis set truncation . . . . . 203
G.20 $|\Delta\mu|$ for FDE-EO with basis set truncation . . . . . 204

I.1 Theoretical PEDs for all normal modes of R6G . . . . . 213

# List of Symbols

Below are a list of the most common sub- and super-scripts:

| | |
|---|---|
| $i, j$ | Occupied orbitals |
| $a, b$ | Virtual or unoccupied orbitals |
| $p, q$ | General orbitals |
| $\alpha, \beta, \gamma$ | Cartesian coordinates or atomic orbital index, depending on context |

Symbols will be defined as they are introduced, but the most common symbols are:

| | |
|---|---|
| $\omega$ | Angular frequency |
| $E_\alpha$ | Electric field |
| $B_\alpha$ | Magnetic field |
| $\mu_\alpha$ | Electric dipole |
| $\theta_{\alpha\beta}$ | Traceless electric quadrupole |
| $m_\alpha$ | Magnetic dipole |
| $\alpha_{\alpha\beta}$ | Electric dipole-dipole polarizability |
| $A_{\alpha,\beta\gamma}$ | Electric dipole-quadrupole polarizability |
| $\mathscr{A}_{\alpha\beta,\gamma}$ | Electric quadrupole-dipole polarizability |
| $C_{\alpha\beta,\gamma\delta}$ | Electric quadrupole-quadrupole polarizability |
| $G'_{\alpha\beta}$ | Magnetic dipole-electric dipole polarizability |
| $\mathscr{G}_{\alpha\beta}$ | Electric dipole-magnetic dipole polarizability |
| $D_{\alpha\beta,\gamma}$ | Electric quadrupole-magnetic dipole polarizability |
| $\mathscr{D}_{\alpha,\beta\gamma}$ | Magnetic dipole-electric quadrupole polarizability |
| $\chi^{(n)}$ | General $n$th order response tensor |
| $\delta_{\alpha\beta}$ | Kronecker delta |

| | |
|---|---|
| $\epsilon_{\alpha\beta\gamma}$ | Levi-Civita (anti-symmetric) tensor |
| $Q_k$ | $k$th normal mode coordinates |
| $T^{(n)}$ | $n$th order interaction tensor |
| $T_s$ | Non-interacting kinetic energy |
| $\nu_T$ | Non-additive kinetic potential |
| $\rho$ | Electron density |
| $\phi$ | Kohn-Sham orbital |
| $\chi$ | Atomic orbital |
| $\mathbf{I}$ | Identity matrix |
| $\mathbf{S}$ | Overlap matrix |
| $\mathbf{K}$ | Response kernel / coupling matrix |

# Acknowledgments

Acknowledging everyone who has had an impact on my graduate studies, by name, is an impossible task. There are countless names without whose support this phase of my academic career would not be possible. Among these names, I would like to first thank Prof. Lasse Jensen for all his help and guidance throughout my Ph.D. research. I came to Penn State wanting to do theoretical research, but without any knowledge of what that entails. It was under these conditions, and without any rotations, that Dr. J. accepted me into his research group. Over the past five years, his advice, guidance, kindness, and keen insight were instrumental in shaping my graduate career, and have made the whole experience a rewarding and enjoyable one.

I would also like to thank the members of the Jensen research group, who have all striven to establish an atmosphere of learning, friendliness and humility within which to work. I would like to thank Dr. Seth Morton, Dr. Dan Silverstein and Dr. John Payton for their guidance in my earlier years. I would like to thank Dr. Justin Moore, Phil Weiss, and later Jeff Becca and Pengchong Liu for the many fruitful discussions on topics such as science, movies, television shows, video games, and much more. I would also like to thank Dr. Xing Chen for her knowledge and hard work that has resulted in a collaborative publication. Finally, from the Jensen group I would like to thank Zhongwei Hu for his many questions in group meetings and his careful reading of many of my pre-publication manuscripts as well as this dissertation.

I would like to thank the Penn State Graduate school for awarding me the Eugene and Jane Apple Science Graduate Fellowship, and the Center for Chemistry at the Space-Time Limit for funding. The annual CaSTL retreats were both fun and educational, and provided lots of networking and collaborative opportunities, as well as helped further my understanding of experimental techniques. Many of the work in this dissertation stemmed from discussions with members from the Van Duyne group at Northwestern University and the Apkarian group at University of California at Irvine during these retreats. In particular, I want to thank Dr. Matt Sonntag and Naihao Chiang of the Van Duyne group for the opportunity to include my theoretical insights with their collected data.

I could not have done a lot of this research without support from, and would therefore like to also acknowledge, Research Computing and Cyberinfrastructure at the High Performance Computing Center (now Institute for CyberScience Advanced CyberInfrastructure) at Penn State.

My life outside of the office here in State College has been a most pleasant one. For this, I would like to acknowledge all the members of the Baha'í community of State College and surrounding areas, and in particular the Rath family, who have all made me feel at home. You guys have become my second family, and I will surely miss you.

Finally I would like to thank my parents, Jasmatie and Dindyal Chulhai, for their love, hard work and sacrifice throughout every stage of my academic career. You have sacrificed more than most, and have always taught me that education is a most precious gift. Now my formal education is complete, and it is all because of you. Thank you.

# Dedication

*To my parents*

# Part I

# Introductory Material

# Chapter 1
# Introduction

The interaction of electromagnetic radiation with a molecule may yield spectroscopic signatures that can characterize the the molecule and its surrounding environment. One such spectroscopic technique is Raman scattering,[1] which is the inelastic light scattering process that occurs when a molecule absorbs a photon with frequency $\omega_L$ and scatters a photon with frequency $\omega_s = \omega_L \pm \omega_\nu$, where $\omega_\nu$ is the frequency of a vibrational normal mode. This difference in the incident and scattered frequencies allows Raman scattering to uniquely characterize molecules based on their vibrational signatures.[2]

In the 1970s, it was discovered that the Raman intensities of molecules on the surface of roughened electrodes may be enhanced by many orders of magnitude, and the technique was subsequently named surface-enhanced Raman scattering (SERS).[3–5] The mechanisms responsible for SERS are often grouped into two categories, the chemical mechanism (CM) and the electromagnetic mechanism (EMM). The large enhancement seen in SERS is primarily due to the EMM, which describes the effects of the large local electric fields generated near the surface of plasmonic nano-structures.[6–9] These local fields are generated when light shines on metallic nano-structures and causes the loose conduction electrons to oscillate collectively, thus creating a plasmon.[10,11] The CM also contributes to the enhancement, and it describes all other effects due to the interactions between the molecule and the nanoparticle. Since the discovery of SERS, the study of the interactions between light and molecules near plasmonic nano-structures have opened an entire sub-field of surface-enhanced spectroscopies.[12,13]

Of these spectroscopies, SERS has remained the most popular, showing near exponential growth over the past two decades.[14] This is due to the fact that SERS has now become a reliable technique,[15–17] with enhancements that are strong enough to detect single molecules.[18,19] Because of this, the technique has seen use in real-time glucose sensing for diabetes testing,[20,21] real-time detection of drugs and chemical and biological warfare agents,[22,23] ultra-sensitive DNA detection,[24–26] and non-destructive art analysis.[27–29] The chemical sensitivity of SERS has also been coupled with the spatial resolution of scanning tunneling microscopes and atomic force microscopes, fitted with plasmonically active noble metal tips,[30,31] in a technique known as tip-enhanced Raman scattering (TERS).[32,33] This technique has even shown the ability to observe the vibrations of a single molecule.[34]

However, the spectral signatures observed in SERS are often very different from the spectral signatures in normal Raman scattering for the same molecule.[35] An example of this is shown in

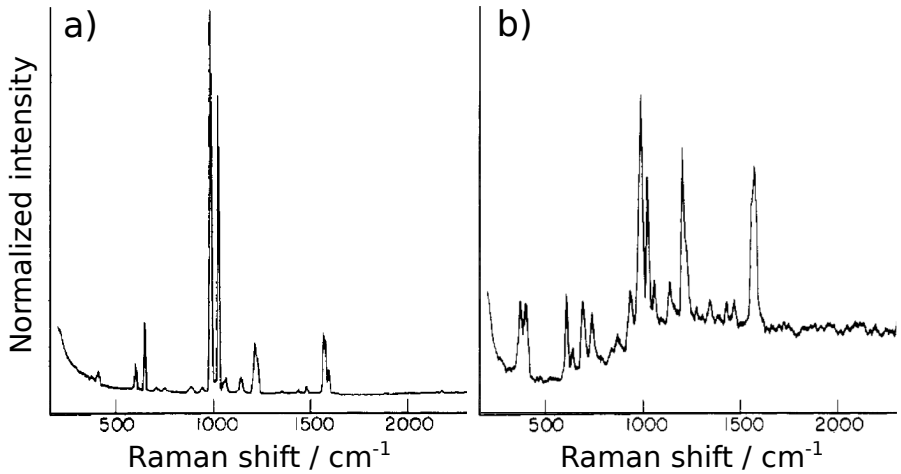


**Figure 1.1.** Comparison between (a) normal Raman scattering and (b) SERS on rough silver under vacuum for pyridine. Taken from Ref. 35.

Figure 1.1, where observed spectral differences include large changes in the relative intensities of vibrational modes, as well as the observation of Raman inactive modes.[35–38] The changes in the spectral signatures of SERS reflect the interactions of the molecule(s) with the plasmonic nanoparticle, and are due to both the CM and EMM.[12,39–42] Therefore, understanding these spectral changes is important for identifying the probed molecular specie(s), and can be a powerful tool in elucidating the nature of the interactions of molecules with metal surfaces. Yet, there is a lack of efficient theoretical tools that can account for these observed spectral changes.

In this dissertation, theoretical methods based on both the CM and EMM of SERS are developed in order to help us understand these spectral changes. In particular, we have developed a rigorous and efficient method to account for the inhomogeneity of the local electric field responsible for the EMM, and the results show how the SERS spectral changes contain information of the molecule's orientation with respect to the nanoparticle's surface. With this method, it is also possible to show that the translational and rotational motions of a single molecule can be obtained from its SERS spectrum. We have also extended this method to describe other forms of surface-enhanced spectroscopies, including surface-enhanced Raman optical activity and plasmonic circular dichroism. In order to account for the CM of SERS, we have begun development of an exact subsystem method that accounts for the quantum mechanical interactions between different subsystems. We show that this method can correctly reproduce supermolecular results for both ground and excited states properties. Finally, we show that spectral changes observed from experimental collaborations reflect changes in the molecular properties that are due to the molecule interacting with the plasmonic surface.

## Overview of Dissertation

In the following, a brief outline of each chapter will be presented. Chapters 2, and 4 through 12 are all adapted from published work. Chapters 10, 11 and 12 contain only the theoretical analyses

of experimental collaborations; full experimental details for these chapters may be found in Refs. 43–45.

**Chapter 2: Overview of the Electromagnetic Theory of Surface-Enhanced Raman Scattering**

The theoretical principles of Raman and surface-enhanced Raman scattering are introduced. The mechanisms of surface-enhanced Raman scattering are discussed, including three detailed models of the electromagnetic mechanism: Silberstein's equations; the Gersten-Nitzan model; and the image field effect. These models serve as precursors to the dressed-tensors formalism in Part II.

**Chapter 3: Overview of Other Theoretical Methods Used**

An in-depth review of the theoretical methods used in this dissertation is presented. This review includes the topics of density functional theory and time-dependent density functional theory for isolated systems, as well as their subsystem counterparts. These topics are presented as they give background and context to the theories presented in Part II, as well show the state-of-the-art of the methods developed in Part III.

**Chapter 4: Determining Molecular Orientation With Surface-Enhanced Raman Scattering Using Inhomogeneous Electric Fields**

An origin-independent formalism describing the effects of the local electric-field gradient in surface-enhanced Raman scattering is presented—this formalism is henceforth referred to as the dressed-tensors formalism. The formalism predicts that the inhomogeneous electric field near the metal surface of plasmonic nanoparticles leads to observation of Raman-inactive modes, and allows molecular orientation to be determined from surface-enhanced Raman scattering.

**Chapter 5: Simulating Ensemble-Averaged Surface-Enhanced Raman Scattering**

Molecular dynamics simulations are combined with the dressed-tensors formalism in order to simulate some 18 million SERS spectra. It is found that the preferential binding location and orientation of the molecules, the choice of electrodynamics method, and the inclusion of field gradient effects influence both the enhancement distribution and the spectral signatures. It is also found that both the translational and rotational motions of a pyridine molecule near a nanoparticle junction may be effectively tracked through its surface-enhanced Raman spectrum.

**Chapter 6: Simulating Surface-Enhanced Raman Optical Activity Using Atomistic Electrodynamics-Quantum Mechanical Models**

The dressed-tensors formalism, and the extension of the discrete interaction model/quantum mechanical method with velocity gauge local fields, are presented for surface-enhanced Raman optical activity. It is shown that the observed mode intensities and signs of surface-enhanced Raman optical activity are highly sensitive

to the nature of the local electric field and gradient, the orientation of the molecule, and the surface plasmon frequency width.

**Chapter 7: Plasmonic Circular Dichroism of 310- and alpha-Helix Using a Discrete Interaction Model / Quantum Mechanics Method**

The discrete interaction model/quantum mechanical method is used to simulate the plasmonic circular dichroism of the 310- and $\alpha$-helix conformations of a short alanine peptide. The results show that the specific interactions of the molecule with the nanoparticle can lead to large changes to the circular dichroism spectrum in both the molecular and plasmonic regions, which complicates the interpretation of the results.

**Chapter 8: Frozen Density Embedding with External Orthogonality**

An implementation of external orthogonality into the frozen density embedding framework using the level-shift projection operator method is presented. It is shown that the exact ground state energies and densities may be reproduced through iterative freeze-and-thaw cycles for a number of systems, including a charge delocalized benzene molecule starting from atomic subsystems.

**Chapter 9: External Orthogonality in Subsystem Time-dependent Density Functional Theory**

A method that extends a subsystem density functional theory method with external orthogonality into the time-dependent density functional theory regime is presented. The method therefore removes the need for approximations to the kinetic energy potential and kernel, and it is shown that it can accurately reproduce the supermolecular results for weakly and strongly coupled subsystems, and for systems with strongly overlapping densities.

**Chapter 10: The Tip-enhanced Raman Scattering of H2TBPP Monolayer**

The chemical information that is contained in the spectral signatures of *meso*-tetrakis-(3,5-ditertiarybutylphenyl)-porphyrin tip-enhanced Raman scattering obtained from different Q-band excitations is analyzed. Results indicate that these spectral signatures reflect excitations of specific vibronic transitions of the molecule lying flat on a Ag(111) surface.

**Chapter 11: The Origin of Relative Intensity Fluctuations in Single-Molecule Tip-Enhanced Raman Spectroscopy**

An explanation of the relative intensity fluctuations observed in single-molecule Raman experiments is described utilizing both single-molecule tip-enhanced Raman spectroscopy and time-dependent density functional theory calculations. Theoretical calculations provide convincing evidence that the fluctuations are not the result of diffusion, orientation, or local electromagnetic field gradients but rather from subtle variations of the excited-state lifetime, energy, and geometry of the molecule.

**Chapter 12: Binding Orientation of Rhodamine-6G From Tip-Enhanced Raman Spectroscopy**

Low-temperature tip-enhanced Raman spectral signatures are shown to be different from room-temperature tip-enhanced, and low and room-temperature surface-enhanced Raman scattering. These differences include narrowed and shifted vibrational lines, revealing additional chemical information about adsorbate-substrate interactions. In the case of rhodamine 6G on Ag(111) surfaces, it is found that these spectral differences are reflective of the binding orientation of the molecule on the surface.

**Chapter 13: Summary and Outlook**

The findings of this dissertation are summarized, and several potential future projects using the methods described within are proposed.

In addition to these chapters, there are nine appendices.

**Appendix A: Fixed-frame and Orientationally-averaged Raman Scattering**

The theory of Raman scattering introduced in Chapter 2 is expanded upon, including the details of orientational averaging and light polarization.

**Appendix B: Summary of the Dressed-tensors Formalism**

The dressed-tensors formalism of Part II, including detailed derivations of the field gradient terms, is summarized.

**Appendix C: Origin-dependence of Multipole Moments and Higher Order Polarizabilities**

The origin dependence of the various multipole moments and polarizabilities used in the dressed-tensors formalism is presented.

**Appendix D: Supporting Information for: Determining Molecular Orientation With Surface-Enhanced Raman Scattering Using Inhomogeneous Electric Fields**

Supporting information for Chapter 4 is given.

**Appendix E: Supporting Information for: Simulating Ensemble-Averaged Surface-Enhanced Raman Scattering**

Supporting information for Chapter 5 is given.

**Appendix F: Supporting Information for: Simulating Surface-Enhanced Raman Optical Activity Using Atomistic Electrodynamics-Quantum Mechanical Models**

Supporting information for Chapter 6 is given.

**Appendix G: Supporting Information for: Frozen Density Embedding with External Orthogonality**

Supporting information for Chapter 8 is given.

**Appendix H: Supporting Information for: External Orthogonality in Subsystem Time-dependent Density Functional Theory**

Supporting information for Chapter 9 is given.

**Appendix I: Potential Energy Distributions for all Normal Modes of Rhodamine-6G**

The potential energy distributions for all the normal modes of the rhodamine 6G molecule analyzed in Chapter 12 is given.

# Chapter 2
# Overview of the Electromagnetic Theory of Surface-Enhanced Raman Scattering

Chulhai, D. V.; Hu, Z.; Moore, J.E.; Chen, X.; Jensen, L. "*Theory of Linear and Nonlinear Surface-Enhanced Vibrational Spectroscopy*" *Annu. Rev. Phys. Chem.* **2016**, *67*, 541–564. (excerpts within)

## 2.1 Raman Scattering

The inelastic scattering of light—that is to say the scattering of light with a change in frequency—by molecules is called Raman scattering, named for its discoverer Sir Chandrasekhara V. Raman.[1] This scattered light carries with it the vibrational signatures of the molecule, and occurs both at frequencies less than that of the incident light for Stokes scattering, and at frequencies greater than the incident light for anti-Stokes scattering.

The Raman effect may be understood using several theoretical treatments.[2] The simplest of these is purely classical; the incident light is treated as an oscillating electric field, and the molecule consists of a single classical vibrator. The scattering of light by this molecule will be described by an induced oscillating dipole $\mu$, defined as

$$\mu = \alpha \cdot \mathbf{E} \tag{2.1}$$

where $\mathbf{E}$ is the incident electric field and $\alpha$ is the polarizability of the molecule. The frequency by which $\mu$ oscillates will depend on on the oscillations in both $\alpha$ and $\mathbf{E}$. We will define the time-dependence of $\mathbf{E}$ as

$$\mathbf{E} = \mathbf{E}_0 \cos(\omega_I t) \tag{2.2}$$

where $\mathbf{E}_0$ is the amplitude of our incident electric field oscillating at frequency $\omega_I$. The time-dependence of $\alpha$ will be defined as

$$\alpha = \alpha_0 + \alpha_p \cos(\omega_p t) \tag{2.3}$$

where $\alpha_0$ is the time-independent part of the molecule's polarizability, and $\alpha_p$ is the amplitude of the change of the polarizability of the molecule with vibrational frequency $\omega_p$. As we will see, this $\alpha_p$ term has to be non-zero in order to observe Raman scattering. If we solve for the

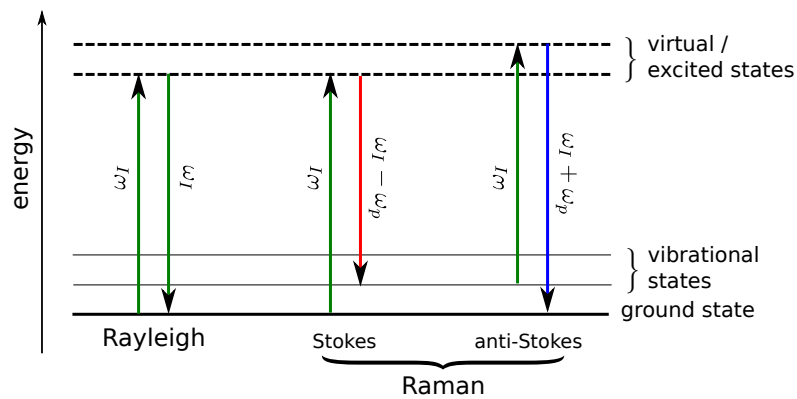


**Figure 2.1.** Schematic of the quantum phenomenon of Rayleigh, and Raman Stokes and anti-Stokes scattering

time-dependence of the induced dipole, we get

$$\mu = \alpha_0 \cdot \mathbf{E}_0 \cos(\omega_I t) + \frac{1}{2}\alpha_p \cdot \mathbf{E} \cos\left[(\omega_I - \omega_p)t\right] + \frac{1}{2}\alpha_p \cdot \mathbf{E} \cos\left[(\omega_I + \omega_p)t\right] \tag{2.4}$$

The first term on the right-hand-side of Equation 2.4 is responsible for Rayleigh scattering, which is the scattering of light without change in frequency that causes the blue color of the sky.[46] The second and third terms are responsible for Raman Stokes and anti-Stokes scattering, respectively. We see that each of these terms carries some information about the vibration of the molecule through $\alpha_p$ and $\omega_p$.

This classical theory of Raman scattering, however, does not provide any information on how $\alpha_p$ is related to the properties of the molecule or to the frequency of the incident light. In the quantum mechanical theory of Rayleigh and Raman scattering, a simplified illustration of which is given in Figure 2.1, these processes may be described as the absorption followed by emission of a photon by the molecule. As such, this emitted photon contains information of the ground and excited electronic (and vibrational) states of the molecule and, in the case of Raman scattering, can reveal much about the character and identity of the molecule.

In the quantum theory of Raman scattering, $\alpha_p$ is obtained from the transition polarizability—also referred to as the polarizability derivative or the Raman polarizability in different parts of this dissertation—of the molecule. This general transition polarizability $(\alpha_{\alpha\beta})_{fi}$ may be defined as[2,47,48]

$$(\alpha_{\alpha\beta})_{fi} = \sum_{r \neq i,f} \left[ \frac{\langle f|\hat{\mu}_\alpha|r\rangle\langle r|\hat{\mu}_\beta|i\rangle}{\omega_{ri} - \omega_I - i\Gamma_r} + \frac{\langle f|\hat{\mu}_\alpha|r\rangle\langle r|\hat{\mu}_\beta|i\rangle}{\omega_{rf} + \omega_I + i\Gamma_r} \right] \tag{2.5}$$

where the Greek subscripts are Cartesian directions, $i$ and $f$ are the initial and final (vibronic) states, and $r$ is some general state with an inverse lifetime of $\Gamma_r$ and with energy differences of $\omega_{ri}$ and $\omega_{rf}$ between the initial and final states, respectively. In all cases considered in this dissertation, we will assume that both $i$ and $f$ belong to the same electronic state, that is the ground electronic state, but to different vibrational states; we will therefore use $(\alpha_{\alpha\beta})_{fi} = (\alpha_{\alpha\beta})_p$

interchangeably, where $p$ describes the vibrational transition. This transition polarizability is a rather difficult property to calculate exactly, and often we approximate $(\alpha_{\alpha\beta})_p$ depending on the frequency of the incident light. If the frequency is far from any molecular excitations, the Raman scattering is described as far-from-resonance or non-resonant. In such cases, the non-resonant Raman scattering (NRS) transition polarizability may be obtained, using Placzek's theory of polarizability, from the derivatives of the frequency-dependent electronic polarizability with respect to normal mode coordinates, as[49–51]

$$(\alpha_{\alpha\beta})_p = \frac{1}{\sqrt{2\omega_p}} \left( \frac{\partial \alpha_{\alpha\beta}}{\partial Q_p} \right)_0 \tag{2.6}$$

where $\alpha_{\alpha\beta}$ is the electronic polarizability, and $p$ is the vibrational transition with normal mode coordinates $Q_p$ and frequency $\omega_p$. Obtaining the electronic polarizabilities from time-dependent density functional theory (TDDFT) is reviewed in Chapter 3.

The calculation of the transition polarizability is less straightforward when $\omega_I$ is on or near resonance with electronic (or vibronic) transitions, termed resonance Raman scattering (RRS).[52–61] RRS is often two to six orders of magnitude larger in intensity than NRS,[62,63] and the spectrum now reflects vibrations that strongly couple to the resonant excited state—this often makes the spectral signatures from RRS very different from what is observed in NRS for the same molecule. There are two general approaches used to calculated the RRS transition polarizabilities used in this dissertation. The first such theory uses a Placzek-like approximation to obtain the transition polarizabilities from the derivatives of the electronic polarizability on resonance, similar to Equation 2.6.[50] This theory relies on a the inclusion of a general lifetime-broadening parameter $\Gamma$ for all electronic excited states, and is valid if only short-time dynamics are relevant. This Placzek-like approximation is particularly useful since it is valid for both NRS and RRS, and implicitly includes all excited states in the calculation of the electronic polarizability. We use this method for calculating the transition polarizabilities in Chapters 4, 5, and 6.

The second method for calculating the RRS transition polarizabilities is based on the expressions derived by Albrecht and co-workers.[52–54,64] In this method, we invoke the Born-Oppenheimer approximation to separate the vibronic states ($i$, $r$ and $f$ in Equation 2.5) into products of electronic and vibrational states. The electronic transition dipole moments are then expanded in a Taylor series, resulting in the Franck-Condon (or A-term), the first Herzberg-Teller (or B-term), and other higher expansion contributions to the transition polarizability $(\alpha_{\alpha\beta})_{FI} = A_{\alpha\beta} + B_{\alpha\beta} + \cdots$. These terms are defined as

$$A_{\alpha\beta} = \sum_{R,r} (\mu_\alpha^{0r})^{eq} (\mu_\beta^{r0})^{eq} \frac{\langle F_0 | R_r \rangle \langle R_r | I_0 \rangle}{(\epsilon_{R_r} - \epsilon_{I_0}) - \omega_I - i\Gamma_r} \tag{2.7}$$

and

$$
\begin{aligned}
B_{\alpha\beta} = & \sum_{R,r} (\mu_\alpha^{0r})^{eq} \sum_a \left( \frac{\partial \mu_\beta^{r0}}{\partial Q_a} \right) \frac{\langle F_0 | R_r \rangle \langle R_r | Q_a | I_0 \rangle}{(\epsilon_{R_r} - \epsilon_{I_0}) - \omega_I - i\Gamma_r} \\
& + \sum_{R,r} \sum_b \left( \frac{\partial \mu_\alpha^{0r}}{\partial Q_b} \right) (\mu_\beta^{r0})^{eq} \frac{\langle F_0 | Q_b | R_r \rangle \langle R_r | I_0 \rangle}{(\epsilon_{R_r} - \epsilon_{I_0}) - \omega_I - i\Gamma_r}
\end{aligned} \tag{2.8}
$$

where $a$ and $b$ are normal modes with coordinates $Q_a$ and $Q_b$, uppercase letters are vibrational states and lowercase letters are electronic states, $\mu^{0r}$ is the electronic transition between the ground state and electronic state $r$, and $\epsilon$ is the energy of a state. $I$ and $F$ are the initial and final vibrational states. In this theory, we usually only consider one or a few electronic states $r$ that are thought to be important for the RRS at a given frequency. The vibrational overlaps in Equations 2.7 and 2.8 may be calculated by assuming that the excited state vibrational Hamiltonian are accurately described by displacing the ground state harmonic oscillator vibrational Hamiltonian along each normal mode coordinate, called the independent mode displaced harmonic oscillator (IMDHO) model.[65] This method for calculating the transition polarizabilities is particularly useful when there are modes that strongly couple to the excited state(s) that is being examined (that is, vibronic effects), or when only a few states contribute to the RRS; we use this method in Chapters 10, 11, and 12.

Finally, the intensity of the Raman scattered light may be calculated from the transition polarizabilities using

$$
\langle I_p \rangle = \frac{K_p}{45} \left( 45\alpha_p^2 + 7\gamma_p^2 + 5\delta_p^2 \right) \tag{2.9}
$$

where $\alpha_p^2$, $\gamma_p^2$ and $\delta_p^2$ are invariants of the transition polarizabilities for vibrational mode $p$. This equation assumes linearly polarized light and a scattering angle of 90°; the invariants for other polarizations and scattering angles may be found in Ref. 2. The transition polarizabilities need not be symmetric and therefore the tensor invariants are given by[2,66,67]

$$
\alpha_p^2 = \frac{1}{9} (\alpha_{\alpha\alpha})_p (\alpha_{\beta\beta}^*)_p \tag{2.10}
$$

$$
\gamma_p^2 = \frac{3}{4} \left[ (\alpha_{\alpha\beta})_p (\alpha_{\alpha\beta}^*)_p + (\alpha_{\alpha\beta})_p (\alpha_{\beta\alpha}^*)_p \right] - \frac{1}{2} (\alpha_{\alpha\alpha})_p (\alpha_{\beta\beta}^*)_p \tag{2.11}
$$

$$
\delta_p^2 = \frac{3}{4} \left[ (\alpha_{\alpha\beta})_p (\alpha_{\alpha\beta}^*)_p - (\alpha_{\alpha\beta})_p (\alpha_{\beta\alpha}^*)_p \right] \tag{2.12}
$$

The Einstein summation convention is assumed for repeated Greek indices. For Stokes scattering with an experimental set-up as described above, the parameter $K_p$ is given by[68]

$$
K_p = \frac{\pi^2}{\epsilon_0^2} \left( \tilde{\nu_0} - \tilde{\nu_p} \right)^4 \frac{1}{8\pi^2 c \tilde{\nu_p}} \frac{1}{1 - \exp[-hc\tilde{\nu_p}/k_B T]} \tag{2.13}
$$

where $\tilde{\nu_0}$ and $\tilde{\nu_p}$ are the frequencies (in wave numbers) of the incident light and of vibrational mode $p$, respectively. A more thorough presentation of the orientationally averaged Raman expression is given in Appendix A.

## 2.2 Surface-Enhanced Raman Scattering

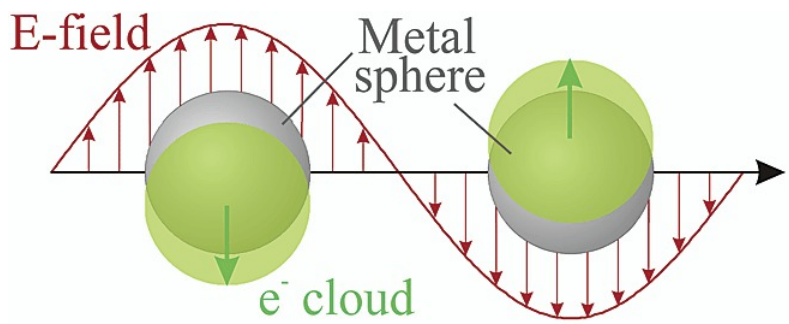


**Figure 2.2.** Schematic of a plasmon interacting with an electric field. Taken from Ref. 10.

When small metallic nano-structures are irradiated by light, the oscillating electric field may cause the "loose" conduction electrons to oscillate coherently. A schematic of this is illustrated in Figure 2.2 for a small metallic sphere. This collective oscillation is called a plasmon resonance, and depends on the material(s) of the nanoparticle (NP), its shape and size, and the frequency of the incident radiation.[10] These oscillations also generate strong oscillating electric fields at the surface of the NPs, often in very small spatially localized regions called "hot-spots". This ability of plasmonic metal NPs to localize light well below the diffraction limit offers unique opportunities for enhancing the spectroscopy of molecules situated at or near these hot-spots.[69] By taking advantage of carefully designed nanostructures, it becomes possible to enhance and localize the near-field with resolutions that are starting to reach the length-scale of molecules.[34]

The enhancement of a large variety of linear spectroscopies, such as surface-enhanced infrared absorption (SEIRA), surface-enhanced Raman scattering (SERS), tip-enhanced-Raman scattering (TERS), and surface-enhanced Raman optical activity (SEROA), as well as nonlinear spectroscopies, such as surface-enhanced hyper-Raman scattering (SEHRS), surface-enhanced coherent anti-Stokes Raman spectroscopy (SECARS), surface-enhanced femto-second stimulated Raman scattering (SE-FRSR), and surface-enhanced sum-frequency generation (SESFG), have been demonstrated.[69–72] In particular, the strong near-field provided by these nano-antennas supplies sufficient enhancement that vibrational spectroscopy at the single-molecule level is possible. Using the bi-analyte method,[18,19] where two molecules or isotopologues with distinct vibrational signatures are used, single-molecule sensitivity has been demonstrated for SERS,[18,19] TERS,[30] SEHRS,[73] and SECARS.[74]

Of these surface-enhanced spectroscopies, SERS is currently the most widely used.[13,24,75–80] It was first discovered in 1974 by Fleischmann, Hendra and McQuillan,[3] and later correctly, and independently, identified in 1977 by Jeanmaire and Van Duyne[4], and Albrecht and Creighton.[5] This spectroscopic technique, owing to the large enhancements afforded by the near field of plasmonic NPs, is one of a few that can, currently, simultaneously detect and provide the chemical fingerprint of single molecules.[18,19,81–84] This makes SERS an important tool in the areas of biological,[24–26,85–92] and chemical sensing.[22,23,93–97] The popularization of SERS is also due, in no small part, to the advances in nanofabrication[15–17,98–100] and an increased understanding of

the properties of plasmonic NPs,[10,101–103] which has increased our understanding of chemistry at—and even beyond—the limit of single molecules.[34,44,45,104–106]

After nearly 40 years, the enhancement of SERS is now (almost) universally accepted to arise from two main mechanisms.[12,41] The first is the electromagnetic mechanism (EMM) caused by the enhanced near-field generated by exciting the plasmon. The second mechanism is loosely called the chemical mechanism (CM) and lumps together all other changes to the molecule's geometric and electronic structure that arises from binding to the metal surface. Although there has been a great deal of controversy over their relative importance, it is by now well established that the EMM is responsible for the bulk of the enhancement, while the CM only contributes a little to the total enhancements. As our understanding of the enhancement mechanisms are being refined, it remains a significant challenge to explain in detail the specific spectral changes that occur in surface-enhanced spectroscopies.[12,41,107] The reason for this is that although the EMM dominates the enhancement, the CM often dominates the spectral changes. A prime example of this is the SERS of p-aminothiophenol (ATP) adsorbed on silver, where certain strong bands not present in the normal Raman spectrum of the molecule are observed.[108] This was initially ascribed to a resonance Raman mechanism involving a metal-molecule charge-transfer (CT) state,[108] however, it was later proposed using theoretical simulations[109] and demonstrated experimentally[110] that the band arose from a new chemical species formed during the SERS experiments. It therefore remains a significant theoretical challenge to correctly describe the spectral changes that occur in surface-enhanced vibrational spectroscopies through these mechanisms.

In order to understand the differences between the EMM and the CM, we will re-write Equation 2.9 as

$$I_p^{\text{Raman}} \propto \left| \frac{\partial \alpha^M}{\partial Q_p} \cdot \mathbf{E}^0 \right|^2 , \tag{2.14}$$

where $\alpha^M$ is the molecule's electric dipole-dipole polarizability, $Q_p$ is the normal mode coordinates for vibrational transition $p$, and $\mathbf{E}^0$ is the perturbing incident electric field. In SERS, where the molecule is adsorbed on to a plasmonic NP, this polarizability $\alpha^M$ should now reflect the polarizability of the total molecule-NP system (hereinafter represented as $\alpha^{\text{tot}}$). In order to understand the mechanisms of SERS, we often like to separate the contributions to $\frac{\partial \alpha^{\text{tot}}}{\partial Q_p}$, which has led to confusion and disagreement, into what is commonly referred to as the EMM and the CM. This separation is often made because surface plasmons, the driving force behind the SERS EMM, are accurately described using classical electrodynamics (ED)—though ideally one would treat the entire molecule-NP system using first principles.[111,112] In reality, the clear separation of this total polarizability into these two distinct contributions is not always possible.

We will proceed to discuss the EMM and CM by re-writing the SERS intensity as

$$I_p^{\text{SERS}} \propto \left| \frac{\partial \alpha^{\text{M'}}}{\partial Q_p} \cdot \mathbf{F}(\omega_S)\mathbf{F}(\omega_I) \cdot \mathbf{E}^0 \right|^2 , \tag{2.15}$$

where $\mathbf{F}(\omega_I)$ and $\mathbf{F}(\omega_S)$ are the enhancement of the incident and scattered fields, respectively, and constitute the EMM. The $\alpha^{\text{M'}}$ term describes the contribution to the total molecule-NP polarizability not accounted for by the EMM. All effects that contribute to the changing of the

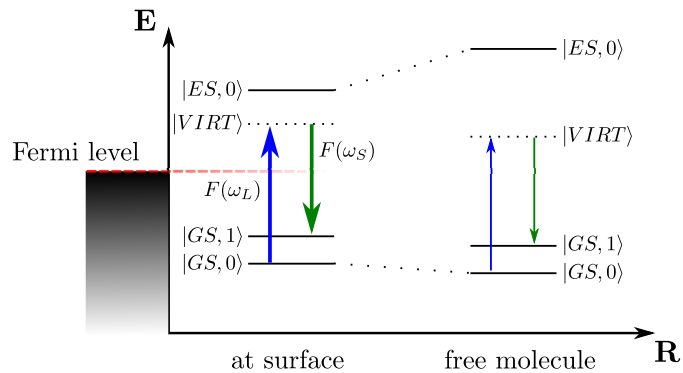


**Figure 2.3.** Illustration of the mechanisms of SERS. Abbreviations: ES, excited state; GS, ground state; VIRT, virtual state.

free-molecule polarizability $\alpha^{\mathrm{M}}$ to $\alpha^{\mathrm{M'}}$, such as changes to the electronic and geometric structure of the molecule, constitute the CM. A schematic of this is illustrated in Figure 2.3. In the next section, we will review a selection of the theoretical models used to simulate the EMM of SERS.

## 2.3 Theoretical Models of the Electromagnetic Mechanism

The EMM (sometimes referred to as the plasmonic theory) of SERS dates back to the late 1970s through the 1980s.[113–119] It originates from the classical interaction between the molecule and NP, solved using ED. As such, this mechanism can be derived without knowledge of the electronic structure of the molecule or the NP. The EMM has been reviewed a number of times (see for example Refs. 13,39,79,120). Here we will review the EMM theory by discussing two equivalent classical models (Silberstein's equations and the Gersten-Nitzan model), each with increasing complexity in the description of the molecule and NP. These models form the basis for the dressed-tensor formalism that is developed in Part II, and used throughout this dissertation. We also briefly introduce a hybrid classical-quantum mechanical method to describe SERS, which is expanded upon in Chapters 6 and 7 to describe other surface-enhanced spectroscopies.

### 2.3.1 Silberstein's equations

The simplest derivation of the EMM can be made using Silberstein's equations,[121,122] which is the solution of the addition of two isotropic polarizabilities. In these equations, we assume that the molecule and the NP are two point polarizable objects, with isotropic polarizability $\alpha^{\mathrm{M}}$ and $\alpha^{\mathrm{NP}}$, respectively, separated by some distance $R$. According to Silberstein's equations, the total system polarizability is given by

$$\alpha_{\parallel}^{\mathrm{tot}} = \frac{\alpha^{\mathrm{M}} + \alpha^{\mathrm{NP}} + 4\alpha^{\mathrm{M}}\alpha^{\mathrm{NP}}/R^3}{1 - 4\alpha^{\mathrm{M}}\alpha^{\mathrm{NP}}/R^6} \tag{2.16a}$$

and

$$\alpha_{\perp}^{\mathrm{tot}} = \frac{\alpha^{\mathrm{M}} + \alpha^{\mathrm{NP}} - 2\alpha^{\mathrm{M}}\alpha^{\mathrm{NP}}/R^3}{1 - \alpha^{\mathrm{M}}\alpha^{\mathrm{NP}}/R^6} \tag{2.16b}$$

where $\alpha_{\parallel}^{\text{tot}}$ and $\alpha_{\perp}^{\text{tot}}$ are the components of the total polarizability parallel and perpendicular to the separation axis, respectively. We now take the derivative with respect to normal mode coordinate $Q_p$, assuming that the polarizability of the NP is not affected by the normal modes of the molecule ($\frac{\partial \alpha^{\text{NP}}}{\partial Q_p} = 0$), which leaves the Raman polarizabilities as[41]

$$\frac{\partial \alpha_{\parallel}^{\text{tot}}}{\partial Q_p} = \frac{\partial \alpha^{\text{M}}}{\partial Q_p} \frac{\left(1 + 2\alpha^{\text{NP}}/R^3\right)^2}{\left(1 - 4\alpha^{\text{NP}}\alpha^{\text{M}}/R^6\right)^2} \tag{2.17a}$$

and

$$\frac{\partial \alpha_{\perp}^{\text{tot}}}{\partial Q_p} = \frac{\partial \alpha^{\text{M}}}{\partial Q_p} \frac{\left(1 - \alpha^{\text{NP}}/R^3\right)^2}{\left(1 - \alpha^{\text{NP}}\alpha^{\text{M}}/R^6\right)^2} \tag{2.17b}$$

Ignoring the terms in the denominators of Equation 2.17, which are contributions to the "image field" effect and will be discussed later, we are left with the parallel and perpendicular components of the local electric field enhancement ($E_{\parallel}$ and $E_{\perp}$), respectively. These lead to the following expressions for the SERS intensity:

$$I_{\parallel}^{\text{SERS}} \propto \left|\frac{\partial \alpha^{\text{M}}}{\partial Q_p}\right|^2 \left|E_{\parallel}\right|^4 \tag{2.18a}$$

and

$$I_{\perp}^{\text{SERS}} \propto \left|\frac{\partial \alpha^{\text{M}}}{\partial Q_p}\right|^2 \left|E_{\perp}\right|^4 \tag{2.18b}$$

which gives the familiar $|\mathbf{E}|^4$ EMM enhancement factor.

Using Silberstein's equations to simulate the SERS spectrum is equivalent to scaling the Raman spectrum by the $|\mathbf{E}|^4$ factor, with the largest enhancement for polarization along the NP-molecular axis. However, this scaling ignores the rich information that may be available in the observed SERS spectrum. Therefore, this method is only appropriate for molecules approximately described by isotropic polarizabilities, such as in Albrecht A-term scatterers, for example, where the polarizability is diagonal dominated and the relative mode intensities are not due to the tensorial nature of the polarizability-field interactions.[44] In all other cases, one would need a more rigorous method to account for the tensorial nature of the molecular polarizability and the local electric field in order to simulate the SERS mode selectivity.

### 2.3.2 Gersten-Nitzan model

Gersten and Nitzan[119] first outlined the electromagnetic theory of SERS, which takes into consideration the tensorial nature of the interactions. In this derivation, we start by writing the induced dipoles for both the molecule and NP as

$$\mu^{\text{M}} = \alpha^{\text{M}} \cdot (\mathbf{E}^0 + \mathbf{T}^{(2)} \cdot \mu^{\text{NP}}) \tag{2.19a}$$

and

$$\mu^{\text{NP}} = \alpha^{\text{NP}} \cdot (\mathbf{E}^0 + \mathbf{T}^{(2)} \cdot \mu^{\text{M}}) \tag{2.19b}$$

where $\mathbf{R}$ is the vector between the systems, and $\mathbf{T}^{(x)}$ are the interaction tensors,[123,124] generally defined as

$$\mathbf{T}^{(x)}(\mathbf{R}) = \nabla^x \frac{1}{|\mathbf{R}|}. \tag{2.20}$$

Solving Equation 2.19 leads to the effective polarizabilities of the molecule and NP, and finally to the following expression for the total Raman polarizability:

$$\begin{aligned}\frac{\partial \alpha^{\mathrm{tot}}}{\partial Q_p} = &\left(\mathbf{I} - \alpha^{\mathrm{M}} \cdot \mathbf{T}^{(2)} \cdot \alpha^{\mathrm{NP}} \cdot \mathbf{T}^{(2)}\right)^{-1} \cdot \frac{\partial \alpha^{\mathrm{M}}}{\partial Q_p} \cdot \Big[\mathbf{I} + \mathbf{T}^{(2)} \cdot \alpha^{\mathrm{NP}} \cdot \mathbf{T}^{(2)} \\ &\cdot \left(\mathbf{I} - \alpha^{\mathrm{M}} \cdot \mathbf{T}^{(2)} \cdot \alpha^{\mathrm{NP}} \cdot \mathbf{T}^{(2)}\right)^{-1} \cdot \alpha^{\mathrm{M}}\Big] \cdot \left(\mathbf{I} + \mathbf{T}^{(2)} \cdot \alpha^{\mathrm{NP}}\right) \\ &+ \left(\mathbf{I} - \alpha^{\mathrm{NP}} \cdot \mathbf{T}^{(2)} \cdot \alpha^{\mathrm{M}} \cdot \mathbf{T}^{(2)}\right)^{-1} \cdot \alpha^{\mathrm{NP}} \cdot \mathbf{T}^{(2)} \cdot \frac{\partial \alpha^{\mathrm{M}}}{\partial Q_p} \\ &\cdot \left[\mathbf{I} + \mathbf{T}^{(2)} \cdot \left(\mathbf{I} - \alpha^{\mathrm{NP}} \cdot \mathbf{T}^{(2)} \cdot \alpha^{\mathrm{M}} \cdot \mathbf{T}^{(2)}\right)^{-1} \cdot \alpha^{\mathrm{NP}} \cdot \left(\mathbf{I} + \mathbf{T}^{(2)} \cdot \alpha^{\mathrm{M}}\right)\right],\end{aligned} \tag{2.21}$$

where $\mathbf{I}$ is the identity matrix.

We may ignore terms of the form $\alpha \cdot \mathbf{T}^{(2)} \cdot \alpha \cdot \mathbf{T}^{(2)}$, which have been argued to be negligible in Ref. 41 since they are approximately $R^{-3}$ (in Ref. 119, they are referred to as the image field effect, which we will discuss later). This leads to

$$\frac{\partial \alpha^{\mathrm{tot}}}{\partial Q_p} \approx \left(\mathbf{I} + \alpha^{\mathrm{NP}} \cdot \mathbf{T}^{(2)}\right) \cdot \frac{\partial \alpha^{\mathrm{M}}}{\partial Q_p} \cdot \left(\mathbf{I} + \mathbf{T}^{(2)} \cdot \alpha^{\mathrm{NP}}\right). \tag{2.22}$$

This equation is different from Equation 1.10 in Ref. 119, and contains the additional term $\alpha^{\mathrm{NP}} \cdot \mathbf{T}^{(2)} \cdot \frac{\partial \alpha^{\mathrm{M}}}{\partial Q_p} \cdot \mathbf{T}^{(2)} \cdot \alpha^{\mathrm{NP}}$, which is the major SERS term and is responsible for the $|\mathbf{E}|^4$ enhancement. One can easily see that Equation 2.22 is similar to Equation 2.17, with the tensoral nature of $\alpha^{\mathrm{M}}$, $\mathbf{T}^{(2)}$, and $\alpha^{\mathrm{NP}}$ taken into account. This equation has been the most relevant when describing the EMM in SERS and leads directly into the dressed-tensor formalism developed in Part II of this dissertation.

### 2.3.3 Image field effect

The image field is an EMM effect resulting from the $\left(\mathbf{I} - \alpha \cdot \mathbf{T}^{(2)} \cdot \alpha \cdot \mathbf{T}^{(2)}\right)^{-1}$ terms in the Gersten-Nitzan equation (or the denominator in Silberstein's equations), and was considered by some early theories to be the major contributing factor in SERS.[113,125–127] This effect is the result of the fields reflected back and forth between the NP and the molecule, *ad infinitum*.

The Gersten-Nitzan model could be Taylor expanded to include the image field effect as follows

$$\begin{aligned}\frac{\partial \alpha^{\mathrm{tot}}}{\partial Q_p} = &\sum_{i,j=0}^{\infty} \left(\mathbf{I} + \alpha^{\mathrm{NP}} \cdot \mathbf{T}^{(2)}\right) \cdot \left(\alpha^{\mathrm{M}} \cdot \mathbf{T}^{(2)} \cdot \alpha^{\mathrm{NP}} \cdot \mathbf{T}^{(2)}\right)^i \cdot \frac{\partial \alpha^{\mathrm{M}}}{\partial Q_p} \\ &\cdot \left(\mathbf{T}^{(2)} \cdot \alpha^{\mathrm{NP}} \cdot \mathbf{T}^{(2)} \cdot \alpha^{\mathrm{M}}\right)^j \cdot \left(\mathbf{I} + \mathbf{T}^{(2)} \cdot \alpha^{\mathrm{NP}}\right).\end{aligned} \tag{2.23}$$

The case where $i = j = 0$ gives the Gersten-Nitzan formula without image effects, all other terms describe some order of the reflected field in the image field effect. Since the terms that depend on $i$ (or $j$) scale as $\left(R^{-3}\right)^i$, one can see that the image field depends strongly on distance between the molecule and the NP, and quickly becomes insignificant for $i, j > 1$. While the image field writen in this way quickly becomes impractical for simulating the image field effects, it allows for an easier understanding of the effect: the incident field induces a dipole in either the molecule or the NP, which reflects between the two systems $k$ times before driving the Raman activity, after which the scattered fields is reflected $j$ times before being detected in the far field.

This Taylor expansion form of the image field effect breaks down in the case where $\alpha^{\mathrm{M}}\mathbf{T}^{(2)}\alpha^{\mathrm{NP}}\mathbf{T}^{(2)} \approx 1$, and a more explicit incorporation of the image field is required. In the work of Masiello and coworkers,[128,129] the term "plasmon-dressed" is used to refer to the image field modified polarizability—and is not the same as the dressed-tensor formalism described later in this dissertation. Their model describes the image field coupling between the molecule (from first principles) and NP (from classical ED) using Green's function theory. Many other hybrid quantum mechanical (QM) / classical ED methods incorporate the image field effect,[130–140] often using a continuum model of the NP system. However, a method that include the image field effect (along with the EMM field enhancement) using an atomistic description of the NP system(s) has also been presented.[107,123,141–144] We will briefly review this method in the next subsection.

### 2.3.4 The discrete interaction model/quantum mechanical method

The discrete interaction model/quantum mechanical (DIM/QM) method[107,123,141–144] is a hybrid classical polarizable molecular mechanical / quantum mechanical method developed to describe surface-enhanced Raman scattering. This method describes the EMM of SERS by coupling the TDDFT quantum mechanical description of the molecule with the classical electrodynamics response of the nanoparticle. This is achieved, in the polarizability interaction model (PIM), by describing the atoms in the classical system as a collection of polarizable Gaussian charge distributions that were parametrized against a set of TDDFT calculations. These classical atoms interact with a nearby molecule through the DIM embedding operator $\hat{V}^{DIM}$ and the local field operator $\hat{V}^{loc}$. These operators are added to the time-dependent Kohn-Sham equations described in Equation 3.23, and are defined as

$$\hat{V}^{DIM}(\mathbf{r}, \omega) = \sum_j \sum_m \mu^{ind}_{m,\alpha}(\omega) T^{(1)}_{\alpha}(\mathbf{r}_m - \mathbf{r}_j) \tag{2.24}$$

and

$$\hat{V}^{loc}(\mathbf{r}, \omega) = \sum_j \sum_m \mu^{ext}_{m,\alpha}(\omega) T^{(1)}_{\alpha}(\mathbf{r}_m - \mathbf{r}_j) \tag{2.25}$$

where $\mu^{ind}$ and $\mu^{ext}$ are the induced and external DIM dipoles, $i, j, \ldots$ are QM electrons, and $m, n, \ldots$ denote DIM atoms. $T^{(1)}$ is the first-order interaction tensor between a QM electron and a DIM atom, defined in Equation 2.20. In most cases, these interaction tensors are screened by the error function,[141] which is equivalent to smearing out the point-dipole description of the DIM

atoms into Gaussian distributions. We explore the effects of this smearing of the DIM dipoles on the SERS enhancement in Chapter 5.

The DIM dipoles $\mu^{ind}$ can be thought of as an image field effect, described in the preceding subsection, and is due to the dipoles induced in the nanoparticle system by the ground state charge density of the QM molecule. The $\mu^{ext}$ dipoles, on the other hand, can be thought of as the perturbation of the nanoparticle system, responsible for the strong EMM fields, due to an external perturbation. These DIM dipoles may be obtained by solving a set of 3N complex linear equations

$$\mathbf{A}(\omega)\boldsymbol{\mu}(\omega) = \mathbf{E}(\omega) \tag{2.26}$$

where we have dropped the *ind* and *ext* superscripts for simplicity. For $\mu^{ind}$, $\mathbf{E}$ is the electric field due to the ground state charge density of the molecule, and for $\mu^{ext}$, $\mathbf{E}$ is the external perturbation. The components of the $\mathbf{A}$ matrix are given as

$$A_{mn,\alpha\beta}(\omega) = \begin{cases} \alpha^{-1}_{m,\alpha\beta}(\omega) & m = n \\ -T^{(2)}_{\alpha\beta}(\mathbf{r}_n - \mathbf{r}_m) & m \neq n \end{cases} \tag{2.27}$$

where $\alpha(\omega)$ is the aforementioned parametrized DIM atomic polarizability, taken to be isotropic, and $T^{(2)}$ is the second order interaction tensor.

This method, as mentioned, has been developed to describe SERS,[107,144] and we use it in Chapter 4 as a benchmark for the dressed-tensor formalism. We also expand upon the DIM/QM method in Chapters 6 and 7 to describe SEROA and plasmonic circular dichroism, respectively.

# Chapter 3
# Overview of Other Theoretical Methods Used

## 3.1 Kohn-Sham Density Functional Theory

In quantum mechanics, all information regarding a given system of electrons is contained in its wave function $\Psi(\mathbf{r}_1, \ldots, \mathbf{r}_N)$. This function depends on the spatial coordinates $\mathbf{r}$—within the Born-Oppenheimer approximation the nucleii are considered to be fixed and we have ignored the spin variable for simplicity—of each of the $N$ electrons in the system. We may (approximately) solve for $\Psi$ using Hartree-Fock or post-Hartree-Fock methods, but they are often prohibitively expensive owing to the $3N$ spatial coordinates of the system of electrons. Density functional theory (DFT) seeks to reduce the complexity of this problem by solving for the electron density $\rho(\mathbf{r})$, a function of just 3 spatial coordinates. Solutions utilizing the electron density had been in use since 1927,[145,146] but it was not until 1965 that Hohenberg and Kohn demonstrated their validity through two theorems.[147] The first theorem showed that the ground state wave function—and therefore all properties that depend on it—may be uniquely determined by the ground state electron density. The second theorem states that the exact ground state electron density may be found by minimizing the total-energy functional $E_{tot}[\rho]$. Unfortunately, this functional is not known, which leads to approximations for any practical applications of DFT.

One such widely used approximation is the Kohn-Sham (KS) method.[148] In this method, we use a reference system of non-interacting electrons that is defined to possess the same electron density as our system of interest. This allows us to separate the total-energy functional into

$$E_{tot}[\rho] = E_{NN} + T_s[\rho] + E_{ne}[\rho] + J[\rho] + E_{xc}[\rho] \tag{3.1}$$

where $E_{NN}$ is the nuclear-nuclear Coulomb energy, $T_s$ is the kinetic energy of our non-interacting electrons, $E_{ne}$ is the nuclear-electron Coulomb energy, and $J$ is the classical electron-electron Coulomb energy. The term $E_{xc}$ is the exchange-correlation (XC) energy and it contains the corrections to the kinetic energy due to interacting electrons, the corrections to the electron-electron Coulomb energy from self-interaction, the electron-electron exchange energy, and the electron-electron correlation energy. We may then describe these non-interacting electrons using some number $N_{orb}$ of orthogonal KS orbitals $\phi^{KS}$; the density of this system is therefore

$$\rho(\mathbf{r}) = \sum_{i=1}^{N_{orb}} n_i |\phi_i^{KS}(\mathbf{r})|^2 \tag{3.2}$$

where $n_i$ are the occupation numbers of these orbitals. This would, in turn, allow for exact definitions of $T_s$, $E_{ne}$ and $J$ using

$$E_{tot}[\rho] = E_{NN} + \sum_{i=1}^{N_{orb}} n_i \left\langle \phi_i^{KS} \left| \frac{-\nabla^2}{2} \right| \phi_i^{KS} \right\rangle + \int \nu_{nuc}(\mathbf{r})\rho(\mathbf{r})d\mathbf{r} + \frac{1}{2}\int \frac{\rho(\mathbf{r})\rho(\mathbf{r}')}{|\mathbf{r}-\mathbf{r}'|} d\mathbf{r}d\mathbf{r}' + E_{xc}[\rho] \tag{3.3}$$

where $\nu_{nuc}(\mathbf{r})$ is the nuclear Coulomb potential. Since $\rho$ is dependent on $\phi^{KS}$, we can minimize the total energy with respect to $\phi^{KS}$—under the constraint that all $\phi^{KS}$ are orthonormalized and that the density integrates to the correct number of electrons—leading to one-electron-like equations, termed the Kohn-Sham equations:

$$\begin{gathered} \left[ \frac{-\nabla^2}{2} + \nu_{nuc}(\mathbf{r}) + \int \frac{\rho(\mathbf{r}')}{|\mathbf{r}-\mathbf{r}'|} d\mathbf{r}' + \frac{\delta E_{xc}[\rho]}{\delta \rho(\mathbf{r})} \right] \phi_i^{KS}(\mathbf{r}) = \epsilon_i \phi_i^{KS}(\mathbf{r}); \quad i = 1, \cdots, N_{orb} \\ \hat{h}^{KS} \phi_i^{KS}(\mathbf{r}) = \epsilon_i \phi_i^{KS}(\mathbf{r}) \end{gathered} \tag{3.4}$$

where $\hat{h}^{KS}$ is the KS operator.

To solve for Equation 3.4, we usually expand our KS orbitals using some set of—not necessarily orthogonal—atomic orbitals (AOs) $\chi$ as

$$\phi_i(\mathbf{r}) = \sum_{\alpha}^{N_{ao}} C_{\alpha i} \chi_\alpha(\mathbf{r}) \tag{3.5}$$

where $\mathbf{C}$ is the molecular orbital (MO) coefficient matrix, $N_{ao}$ is the number of AOs used, and the Greek subscripts are AO indices. Consequently, we can express Equations 3.4 using matrices expressed within this AO basis, where the matrix $\mathbf{C}$ determines the density matrix $\mathbf{P}$ via $\mathbf{P} = \mathbf{C}\mathbf{C}^T$. The overlap between AOs $\mathbf{S}$ is defined as

$$S_{\alpha\beta} = \langle \chi_\alpha | \chi_\beta \rangle \tag{3.6}$$

and the "Fock matrix" $\mathbf{F}$ in AO basis is defined as

$$F_{\alpha\beta} = \langle \chi_\alpha | \hat{h}^{KS} | \chi_\beta \rangle \tag{3.7}$$

If we enforce the conditions that our MOs should be orthogonal, and that our density should integrate to the correct number of electrons, we end up with the following eigenvalue equations

$$(\mathbf{F} - \epsilon_i \mathbf{S})\, \mathbf{C}_i = 0 \tag{3.8}$$

where $\epsilon_i$ corresponds to the energy of the $i$th KS orbital. We should recognize that $\mathbf{F}$ is dependent on $\mathbf{P}$ (which in turn is dependent on $\mathbf{C}$), and therefore these equations need to be solved self-consistently.

KS-DFT is still exact in principle, however, approximations are needed for the XC energy

functional $E_{xc}$. The simplest approximation to $E_{xc}$ is the local density approximation (LDA), where the functional has been derived from a homogeneous electron gas and is only dependent on the local value of the electron density $\rho(\mathbf{r})$.[148–152] Improvements to the LDA functional, in the class of functionals called the generalized gradient approximations (GGAs), may be obtained by considering the gradient of the electron density $\nabla\rho(\mathbf{r})$.[153–157] Other classes of functionals include hybrid functionals, which include an amount of the exact Hartree-Fock exchange energy, and range-separated hybrid functionals, where the electron repulsion operator is partitioned into a short range interaction described by DFT exchange and a long range interaction described by Hartree-Fock exchange. Each of these functionals offers different advantages in the areas of efficiency and accuracy for various ground and excited state properties.[158–161] Despite the use of approximate XC functionals, the combined efficiency and accuracy of KS-DFT has made it the method of choice for describing the electronic ground and excited state properties of molecules.[162–171]

## 3.2 Subsystem Density Functional Theory

### 3.2.1 Frozen density embedding

In chemistry, we are often interested in understanding the behavior of a particular active site in some complex environment. Using the example of surface-enhanced spectroscopies, we may be interested in understanding how the quantum system of the molecule is affected by the (quantum) interactions with the plasmonic nanoparticle—which is particularly useful in understanding the chemical mechanism of SERS. To do this, we reduce the computational complexity of the systems that we are interested in by considering more manageable subsystems.[172–174] One such theory that includes the quantum interactions between each individual component of the supersystem is subsystem density functional theory (subsystem DFT).[175–178] This subsystem theory partitions the total system into individual subsystems on the basis of the electron density $\rho(\mathbf{r})$, while describing each individual subsystem—and their interactions with each other—using DFT.

In subsystem DFT, considering only two subsystems $A$ and $B$, the total density $\rho_{tot}(\mathbf{r})$ is divided as

$$\rho_{tot}(\mathbf{r}) = \rho_A(\mathbf{r}) + \rho_B(\mathbf{r}) \tag{3.9}$$

where $\rho_A(\mathbf{r})$ and $\rho_B(\mathbf{r})$ are the densities of subsystems $A$ and $B$, respectively. There need not be any restrictions to how this partition is made, however, one often restricts these densities so that they integrate to an integer number of electrons—which will be assumed for the remainder of this chapter. Similarly, the nucleii of the total system will also be partitioned into subsystem components. This allows the total energy $E_{tot}$ to be written as a functional of both $\rho_A$ and $\rho_B$, as

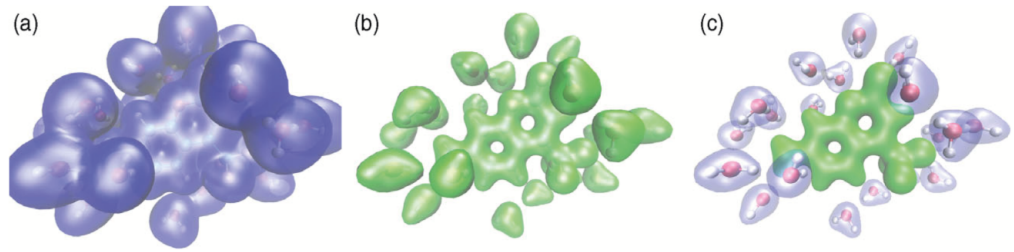


**Figure 3.1.** Schematic illustration of (a) conventional KS-DFT, (b) subsystem DFT, and (c) FDE for aminocoumarin C151 surrounded by 20 water molecules. Taken from Ref. 178.

$$\begin{aligned} E_{tot}[\rho_A, \rho_B] = E_{NN} &+ \int \{\rho_A(\mathbf{r}) + \rho_B(\mathbf{r})\} \left\{\nu^A_{nuc}(\mathbf{r}) + \nu^B_{nuc}(\mathbf{r})\right\} \\ &+ \frac{1}{2}\int \frac{\{\rho_A(\mathbf{r}) + \rho_B(\mathbf{r})\}\{\rho_A(\mathbf{r}') + \rho_B(\mathbf{r}')\}}{|\mathbf{r} - \mathbf{r}'|} d\mathbf{r}d\mathbf{r}' \\ &+ T_s[\rho_A] + T_s[\rho_B] + T_s^{nadd}[\rho_A, \rho_B] + E_{xc}[\rho_A] + E_{xc}[\rho_B] + E_{xc}^{nadd}[\rho_A, \rho_B] \end{aligned} \tag{3.10}$$

where $T_s^{nadd}$ and $E_{xc}^{nadd}$ are the the non-additive non-interacting kinetic energy and the non-additive XC energy, respectively. These terms are required as there is no guarantee that the $T_s$ and $E_{xc}$ functionals are additive with respect to the density—we will discuss this point with regards to the non-interacting kinetic energy later—and are defined as

$$T_s^{nadd}[\rho_A, \rho_B] = T_s[\rho_A + \rho_B] - T_s[\rho_A] - T_s[\rho_B] \tag{3.11}$$

and

$$E_{xc}^{nadd}[\rho_A, \rho_B] = E_{xc}[\rho_A + \rho_B] - E_{xc}[\rho_A] - E_{xc}[\rho_B] \tag{3.12}$$

One may then minimize $E_{tot}$ with respect to the density of each subsystem, where once again KS-DFT may be used to describe each subsystem.

One of the more popular applications of subsystem DFT has been frozen density embedding (FDE).[179] In FDE, one subsystem is identified as the active system (for the remainder of this chapter, we will assume this to be subsystem $A$) and is described by KS-DFT, while all others (subsystem $B$) are treated as the environment. The total energy is then minimized only with respect to the KS orbitals of subsystem $A$, while the density of subsystem $B$ ($\rho_B$) is kept frozen. A schematic of the differences between KS-DFT, subsystem DFT, and FDE is shown in Figure 3.1. This minimization leads to the following embedded KS equations

$$\left[\frac{-\nabla^2}{2} + \nu^{KS}_{eff}[\rho_A; \mathbf{r}] + \nu^{emb}_{eff}[\rho_A, \rho_B; \mathbf{r}]\right] \phi_i^A(\mathbf{r}) = \epsilon_i \phi_i^A(\mathbf{r}) \tag{3.13}$$

where $\phi_i^A$ are the KS orbitals of subsystem $A$, and $\nu^{KS}_{eff}$ and $\nu^{emb}_{eff}$ are the effective KS and embedding potentials, respectively, defined as

$$\nu_{eff}^{KS}[\rho_A;\mathbf{r}] = \nu_{nuc}^{A}(\mathbf{r}) + \int \frac{\rho_A(\mathbf{r}')}{|\mathbf{r}-\mathbf{r}'|}d\mathbf{r}' + \left.\frac{\delta E_{xc}[\rho]}{\delta\rho(\mathbf{r})}\right|_{\rho=\rho_A} \tag{3.14}$$

and

$$\nu_{eff}^{emb}[\rho_A,\rho_B;\mathbf{r}] = \nu_{nuc}^{B}(\mathbf{r}) + \int \frac{\rho_B(\mathbf{r}')}{|\mathbf{r}-\mathbf{r}'|}d\mathbf{r}' + \nu_T^{nadd}[\rho_A,\rho_B;\mathbf{r}] + \nu_{xc}^{nadd}[\rho_A,\rho_B;\mathbf{r}] \tag{3.15}$$

Here, we have introduced the non-additive kinetic potential (NAKP) $\nu_T^{nadd}$ and the non-additive XC potential $\nu_{xc}^{nadd}$ defined as

$$\nu_T^{nadd}[\rho_A,\rho_B;\mathbf{r}] = \left.\frac{\delta T_s[\rho]}{\delta\rho(\mathbf{r})}\right|_{\rho=\rho_{tot}} - \left.\frac{\delta T_s[\rho]}{\delta\rho(\mathbf{r})}\right|_{\rho=\rho_A} \tag{3.16}$$

and

$$\nu_{xc}^{nadd}[\rho_A,\rho_B;\mathbf{r}] = \left.\frac{\delta E_{xc}[\rho]}{\delta\rho(\mathbf{r})}\right|_{\rho=\rho_{tot}} - \left.\frac{\delta E_{xc}[\rho]}{\delta\rho(\mathbf{r})}\right|_{\rho=\rho_A} \tag{3.17}$$

These are simply the functional derivatives of the non-interacting kinetic and non-additive XC energy functionals, respectively, defined in Equations 3.11 and 3.12.

While the general subsystem DFT theory is exact in principle, the FDE theory only remains exact under specific conditions. To examine these conditions, we will consider $\rho_A^{target}$, which is the target density of the active subsystem $A$ that reproduces the exact total density of the system $\rho_{tot}^{exact}$ for any given frozen $\rho_B$; that is $\rho_A^{target}(\mathbf{r}) = \rho_{tot}^{exact}(\mathbf{r}) - \rho_B(\mathbf{r})$. In order to describe subsystem $A$ using KS-DFT, $\rho_A^{target}$ must be $\nu_s$-representable—that is, it must be representable as the density of the ground state of a reference system of non-interacting electrons. Only then can the minimization of the total energy with respect to $\rho_A$ (or $\phi^A$) be exact, within the limit of exact functionals. The $\nu_s$-representable $\rho_A^{target}$ requires that $\rho_A^{target}(\mathbf{r}) \geq 0$ everywhere in space. This condition is difficult to fulfill, particularly if $\rho_B$ is obtained from a simple isolated molecular calculation on subsystem $B$. In such cases, some have argued that the FDE functional is no longer variational.[180,181]

However, it was shown that any minimized $\rho_A$ can be thought of as the density that minimizes the total energy for any given environment density $\rho_B$.[182,183] In such cases, FDE yields an upper bound of the total energy. This total energy may be improved by an iterative "freeze-and-thaw" process, where the total energy is iteratively minimized with respect to each subsystem density. Therefore, FDE remains exact assuming that $\rho_B$ is carefully selected or that one performs freeze-and-thaw cycles when starting with an approximate $\rho_B$. The former case often requires a DFT calculation on the supersystem, from which an accurate $\rho_B$ may be obtained. This is useful for understanding the behavior of a particular active site in a complex environment, but requires that one is able to perform a DFT calculation on the supersystem. The freeze-and-thaw case may use any approximate starting $\rho_B$; this is particularly useful when one is unable to perform a DFT calculation on the supersystem, but the method still requires multiple subsystem calculations. Alternatively, one could reformulate the FDE equations such that the active system

$A$ is represented by a "density orbital", instead of its density.[180] This would allow $\rho_A^{target}$ to become negative—allowing for an exact theory outside of the aforementioned conditions—though no practical implementations of this method have ever been presented.

### 3.2.2 Kinetic energy density functionals and external orthogonality

In Equations 3.12 and 3.11, we introduced the non-additive XC ($E_{xc}^{nadd}$) and kinetic ($T_s^{nadd}$) energies, and stated that these are needed since the functionals that describe these energies are not necessarily additive with respect to the density. Using this definition, the total XC energy remains exact—within the XC energy functional approximation used—and we will not discuss the implications of the $E_{xc}^{nadd}$ further. As discussed earlier, the exact (non-interacting) kinetic energy in KS-DFT may be found from a set of orthogonal KS orbitals, written as $T_s[\{\phi\}]$. In the subsystem formalism, each individual subsystem is described by its own set of orthogonal KS orbitals, and therefore their exact kinetic energies may be found; these may be succinctly written as $T_s[\{\phi^A\}]$ and $T_s[\{\phi^B\}]$ for the $A$ and $B$ subsystems respectively. However, since there is no set of orthogonal orbitals to describe the supersystem, and there is no guarantee that the KS orbitals of subsystem $A$ are orthogonal to those of subsystem $B$, we cannot express the total kinetic energy as the sum of the kinetic energies of the individual subsystems. The $T_s^{nadd}$ term is, therefore, the additional kinetic energy of the supersystem not accounted for by the sum of each subsystem's kinetic energy. This also means that $T_s^{nadd}$ vanishes if the orbitals of $A$ and $B$ are orthogonal, a condition that is termed "external orthogonality" or EO.

Instead of expressing the kinetic energy as a functional of the KS orbitals, we could express the (non-interacting) kinetic energy as a functional of the electron density. These kinetic energy density functionals (KEDFs) have seen wide use in orbital-free (OF) DFT methods—an alternative to the more common KS-DFT—which circumvents the need for non-interacting reference systems by expressing the total energy as a pure density functional. These approximations to the KEDF often fail to describe any orbital structure in the electron density and their applications are limited. However, in FDE we already know most of the kinetic energy through $T_s[\{\phi^A\}]$ and $T_s[\{\phi^B\}]$, and only the non-additive component need to be estimated using approximate KEDFs

$$T_s[\rho_{tot}] = T_s[\{\phi^A\}] + T_s[\{\phi^B\}] + T_s^{nadd}[\rho_A, \rho_B] \tag{3.18}$$

where $T_s^{nadd}$ has been defined in Equation 3.11. For this reason, most available KEDFs are often sufficient for FDE applications. The simplest KEDF used in such applications is the local density approximation (LDA) to the KEDF termed the Thomas-Fermi (TF) functional, defined as

$$T_s^{TF}[\rho] = C_{TF} \int \rho^{5/3}(\mathbf{r}) d\mathbf{r} \tag{3.19}$$

where $C_{TF} = \frac{3}{10}(3\pi^2)^{2/3}$. One may also use the generalized gradient approximations (GGAs) to the KEDF, generally defined as[184]

$$T_s^{GGA}[\rho] = C_{TF} \int \rho^{5/3}(\mathbf{r}) F[s(\mathbf{r})] d\mathbf{r} \tag{3.20}$$

where $s(\mathbf{r})$ is the reduced density gradient

$$s(\mathbf{r}) = \frac{1}{2(3\pi^2)^{1/3}} \frac{|\nabla\rho(\mathbf{r})|}{\rho(\mathbf{r})^{4/3}} \tag{3.21}$$

and $F[s(\mathbf{r})]$ denotes the GGA enhancement factor. For the Thomas-Fermi LDA functional, this factor is simply 1. Other enhancement factors may be found in Ref. 184, with one of the most popular GGA KEDF used in FDE applications being the PW91k functional.[185,186]

There have been a handful of studies on the accuracy of these KEDFs for FDE applications, and it was found that the GGA KEDFs improve over the TF LDA KEDF for hydrogen bonded systems, though there was no particular GGA that outperformed the others.[184] In general, it was found that these KEDFs offer reasonable results for weakly bonded systems, such as for hydrogen bonded systems, systems with weak dative bonding, or ionic bonds.[184,187] However, they all fail for subsystems with covalent character. To rectify this, there have been methods developed to accurately calculate the embedding potentials.[188,189] These reconstructed potentials often require a KS-DFT calculation on the supersystem.

However, there has been an argument made by Henderson and co-workers that FDE, in the limit of non-orthogonal inter-subsystem KS orbitals (or lack of EO), is not an exact theory.[190,191] In their argument, they stated that the total electron density cannot be written as a sum of subsystem densities, or

$$\rho_{tot}(\mathbf{r}) \neq \rho_A(\mathbf{r}) + \rho_B(\mathbf{r}) \tag{3.22}$$

if the orbitals that describe $A$ and $B$ are not orthogonal. Since we cannot partition the density in this way, we cannot express $T_s^{nadd}$ and $E_{xc}^{nadd}$ as in Equations 3.11 and 3.12. Later, Jacob and co-workers showed that this inequality only holds true for densities $\rho_A$ and $\rho_B$ expressed in limited, linearly independent basis sets. For subsystems described using complete or linearly dependent basis sets, the density sum equality holds for subsystems with non-orthogonal KS orbitals, and the FDE non-additive energies are exactly defined by Equations 3.11 and 3.12.

One may circumvent these arguments of the inequality of density sums by ensuring that EO is enforced between subsystems. This ensures that the density sum equality holds—meaning that the definition of $E_{xc}^{nadd}$ is correctly defined in Equation 3.12—while removing the need for approximate KEDFs. Methods that enforce EO have been in use for decades, and have seen use in frozen-core approximations,[192] model potentials,[193] the Phillips-Kleinman pseudopotential approach,[194] and in the methods of Stoll and co-workers,[195] Mata and co-workers,[196] Henderson,[197] Hoffmann and co-workers,[191] and Miller and co-workers.[198–200] Miller and co-workers[198–200] and Hoffmann and co-workers[191] have shown that the supersystem KS-DFT may be exactly obtained from subsystem DFT, providing that there is EO. Hoffmann and co-workers[191] included EO as an additional constraint in the construction of Lagrangian, while the method of Miller and co-workers,[198–200] along with the reconstructed potential approach of Neugebauer and co-workers,[188,189] all require that the supersystem KS-DFT results are known *a priori*. Therefore, there is a need for a subsystem DFT method with EO, within the FDE framework, that does not require the supersystem KS-DFT as starting point. We develop such a method in Part III of this dissertation.

## 3.3 Subsystem Response Theory

### 3.3.1 Time-dependent density functional theory

The KS-DFT method presented in Section 3.1 is inherently a ground state theory. In order to determine excited state properties, such as excitation energies and polarizabilities, we need to employ the time-dependent (TD) extension to the KS equations, commonly referred to as time-dependent density functional theory (TDDFT). Runge and Gross showed, in an analogy to the ground state theorems presented by Hohenberg and Kohn,[147] that the time-dependent electron density may be uniquely determined by the time-dependent potential of the system.[201] This means that TDDFT, in the limit of exact functionals, is a formally exact theory.

In TDDFT, we solve for the time-dependent KS equations

$$\left[\frac{-\nabla^2}{2} + \nu_{nuc}(\mathbf{r}) + \int \frac{\rho(\mathbf{r}',t)}{|\mathbf{r}-\mathbf{r}'|}d\mathbf{r}' + \frac{\delta E_{xc}[\rho,t]}{\delta\rho(\mathbf{r})} + \delta\nu^{ext}(\mathbf{r},t)\right]\phi_i^{KS}(\mathbf{r},t) = i\frac{\partial}{\partial t}\phi_i^{KS}(\mathbf{r},t) \tag{3.23}$$

where we have included the time-dependence in the Coulomb and XC energies, and have introduced a time-dependent external perturbation $\delta\nu^{ext}$. This perturbation, within the dipole approximation, may be written as

$$\delta\nu^{ext}(\mathbf{r},t) = \hat{\mu}F(t) = \hat{\mu}\left[F_0 + F_\omega\cos(\omega t)\right] \tag{3.24}$$

where $\hat{\mu}$ is the dipole operator and $F(t)$ is an electric field. In order to solve these equations, we will re-write the one electron operator as $\hat{h} = \hat{h}^0 + \delta\nu^{ext}$. We can then use perturbation theory to solve for the linear response of the density $\delta\rho$, where we assume the density may be expanded as

$$\rho(\mathbf{r},t) = \rho_0(\mathbf{r},t) + \delta\rho(\mathbf{r},t) \tag{3.25}$$

where $\rho_0$ is the unperturbed density. This linear response of the density may be found from the response of the system due to the external perturbation, written as

$$\delta\rho(\mathbf{r},t) = \int\int \chi(\mathbf{r},\mathbf{r}',t-t')\delta\nu^{ext}(\mathbf{r}',t')d\mathbf{r}'dt' \tag{3.26}$$

where $\chi$ is the unknown response function of the system.

In order to simplify these expressions, we will switch to frequency-space and expand the density response using the ground state KS orbitals using

$$\delta\rho(\mathbf{r},\omega) = 2\sum_{ia}\delta P_{ia}(\omega)\phi_i(\mathbf{r})\phi_a(\mathbf{r}) \tag{3.27}$$

where subscripts $i$ and $a$ denote occupied and virtual KS orbitals, respectively, and $\delta\mathbf{P}$ is the linear response density matrix. The factor of 2 in Equation 3.27 is due to the fact that we are considering only closed-shell systems, which will be assumed for the remainder of this chapter. In this orbital space, Equation 3.26 may be written as

$$\delta P_{ia}(\omega) = \chi_{ia}(\omega)\delta\nu_{ai}^{ext}(\omega) \tag{3.28}$$

where, once again, the response function $\chi$ is unknown.

Analogous to ground state KS-DFT, we will consider the response function $\chi^s$ of a system of non-interacting electrons, which is defined as

$$\chi_{ai}^{s}(\omega) = \frac{\omega_{ia}}{(\omega + i\Gamma)^2 - \omega_{ia}^2} \tag{3.29}$$

where $\omega_{ia}$ is the orbital energy difference $\omega_{ia} = \epsilon_a - \epsilon_i$, and $\Gamma$ is a damping factor that has the meaning of the inverse of the lifetime of the excited states. This damping factor prevents a singularity when $\omega = \omega_{ia}$. To account for the interactions between electrons, we re-write Equation 3.28 as

$$\delta P_{ia}(\omega) = \chi_{ia}^{s}(\omega)\delta\nu_{ai}(\omega) \tag{3.30}$$

where the change in potential $\delta\nu_{ai} = \delta\nu_{ai}^{el} + \delta\nu_{ai}^{ext}$ has contributions from the change in the electron potential $\delta\nu_{ai}^{el}$ and the external perturbation $\delta\nu_{ai}^{ext}$. Assuming a linear response of the potential with respect to the change in the density, the matrix elements of $\delta\nu_{ai}^{el}$ are given as

$$\begin{aligned}\delta\nu_{ai}^{el} &= 2\sum_{jb}\int d\mathbf{r}\int d\mathbf{r}'\left[\phi_i(\mathbf{r})\phi_a(\mathbf{r})\left(\frac{1}{|\mathbf{r}-\mathbf{r}'|} + f_{xc}(\mathbf{r},\mathbf{r}',\omega)\right)\phi_j(\mathbf{r}')\phi_b(\mathbf{r}')\right]\delta P_{jb}(\omega) \\ &= 2\sum_{jb}\left(K_{ia,jb}^{Coul} + K_{ia,jb}^{XC}(\omega)\right)\delta P_{jb}(\omega)\end{aligned} \tag{3.31}$$

where $f_{xc}$ and $K^{XC}$ are the XC response kernel (in real space and orbital space), and $K^{Coul}$ is the Coulomb response kernel.

It should be noted that, like the XC energy functional, the XC response kernel is also unknown and must be approximated. This kernel is a nonlocal functional of both space (it depends on both $\mathbf{r}$ and $\mathbf{r}'$) and time (depending on both $t$ and $t'$), which makes it particularly difficult and expensive to calculate. A commonly used approximation is to remove the time dependence in $f_{xc}$, termed the adiabatic approximation, where $f_{xc}$ may be defined as the second functional derivative of the XC energy functional with respect to the density. For all applications in this dissertation, we also assume that $f_{xc}$ is also local in space and is derived from the LDA XC energy functional—this kernel is termed the adiabatic local density approximation (ALDA).

We can now express Equation 3.30 as

$$\delta P_{ia}(\omega) = \chi_{ia}^{s}(\omega)\left[\delta\nu_{ai}^{ext}(\omega) + 2\sum_{jb}K_{ia,jb}\delta P_{jb}(\omega)\right] \tag{3.32}$$

where we have grouped both response kernels together into $\mathbf{K}$. We observe that $\delta\mathbf{P}$ is on both sides of Equation 3.32, and therefore this equation needs to be solved self-consistently. Solutions

of $\delta\mathbf{P}$ allows us to define the electronic polarizability $\alpha_{\alpha\beta}$ as

$$\alpha_{\alpha\beta}(-\omega;\omega) = -\mathrm{Tr}\left[\mathbf{H}^{\alpha}\delta\mathbf{P}^{\beta}(\omega)\right] \tag{3.33}$$

where the sub- and superscript Greek letters are Cartesian directions, and $\mathbf{H}$ is the dipole moment matrix, given as

$$H^{\alpha}_{pq} = \langle\phi_p|\hat{\mu}_{\alpha}|\phi_q\rangle \tag{3.34}$$

where $p$ and $q$ are general orbital indices. These electronic polarizabilities may then be manipulated, using the short-time approximation, in order to obtain the transition polarizabilities needed to describe Raman scattering—as discussed in Chapter 2.

We may use the linear response of the density to obtain other response properties, for instance the quadrupole-dipole polarizability $\mathscr{A}$ may be defined as

$$\mathscr{A}_{\alpha\beta,\gamma}(-\omega;\omega) = -\mathrm{Tr}\left[\mathbf{Q}^{\alpha\beta}\delta\mathbf{P}^{\gamma}(\omega)\right] \tag{3.35}$$

where $\mathbf{Q}$ is the quadrupole moment matrix, obtained from

$$Q^{\alpha\beta}_{pq} = \langle\phi_p|\hat{\theta}_{\alpha\beta}|\phi_q\rangle \tag{3.36}$$

$\hat{\theta}$ is the (traceless) quadrupole moment operator defined as

$$\hat{\theta}_{\alpha\beta} = \frac{1}{2}\left(3\hat{r}_{\alpha}\hat{r}_{\beta} - \delta_{\alpha\beta}\hat{r}_{\alpha}\hat{r}_{\beta}\right) \tag{3.37}$$

Similarly, we may also consider an external perturbation that is inhomogeneous and expressible as $\delta\nu^{ext}(\mathbf{r},t) = \hat{\theta}F(t)$. This would allow us to define the dipole-quadrupole polarizability $A$ as

$$A_{\alpha,\beta\gamma}(-\omega;\omega) = -\mathrm{Tr}\left[\mathbf{H}^{\alpha}\delta\mathbf{P}^{\beta\gamma}(\omega)\right] \tag{3.38}$$

and the quadrupole-quadrupole polarizability $C$ as

$$C_{\alpha\beta,\gamma\delta}(-\omega;\omega) = -\mathrm{Tr}\left[\mathbf{Q}^{\alpha\beta}\delta\mathbf{P}^{\gamma\delta}(\omega)\right] \tag{3.39}$$

These polarizabilities are all needed for the dressed-tensor formalism with field gradient effects explored in Part II of this dissertation. There are other linear response polarizabilities that may be defined in a similar manner, using the appropriate quantum mechanical operator, some of which are used and defined in Chapters 6 and 7.

We may also re-write Equation 3.32 into the following matrix form[202,203]

$$\left[\Omega - \omega^2\right]\mathbf{F} = -\mathbf{S}^{-1/2}\delta\mathbf{v}^{ext} \tag{3.40}$$

where $\mathbf{F} = \mathbf{S}^{1/2}\delta\mathbf{P}$, and the elements of the matrices $\mathbf{S}$ and $\Omega$ are defined as

$$S_{ia,jb} = \frac{\delta_{ab}\delta_{ij}}{\omega_{ia}} \tag{3.41}$$

and

$$\Omega_{ia,jb} = \delta_{ab}\delta_{ij}\omega_{ia}^2 + 2\sqrt{\omega_{ia}}K_{ia,jb}\sqrt{\omega_{jb}} \tag{3.42}$$

This will allow us to solve for the excitation energies of the system. If $\omega$ corresponds to an excitation energy, the density response $\delta\mathbf{P}$ will diverge, and the term $\left[\Omega - \omega^2\right]^{-1}$ will have a singularly. We can therefore find these singularities by solving the following eigenvalue equations

$$\left[\Omega - \omega_k^2\right]\mathbf{F}_k = 0 \tag{3.43}$$

where $\omega_k$ is an excitation energy and $\mathbf{F}_k$ is the corresponding eigenvector.

### 3.3.2 Subsystem time-dependent density functional theory

Like the ground state properties, we may also partition the response of a system into subsystem components—referred to as subsystem TDDFT.[204,205] In such a theory, we assume that the total density response of the supersystem $\delta\rho_{tot}$ may also be separated into subsystem components[206]

$$\delta\rho_{tot}(\mathbf{r},t) = \delta\rho_A(\mathbf{r},t) + \delta\rho_B(\mathbf{r},t) \tag{3.44}$$

where $\delta\rho_A$ and $\delta\rho_B$ are the density response of subsystems $A$ and $B$, respectively. Using these definitions, we can re-write Equation 3.32 to account for these subsystem responses as

$$\delta\mathbf{P}^A(\omega) = \chi^s(\omega)\left[\delta\mathbf{v}^{ext}(\omega) + 2\mathbf{K}^{A,A}\delta\mathbf{P}^A(\omega) + 2\mathbf{K}^{A,B}\delta\mathbf{P}^B(\omega)\right] \tag{3.45}$$

with a similar expression for $\delta\mathbf{P}^B$. The response kernel $\mathbf{K}^{A,A}$ describes the changes to the potential on subsystem $A$ due to $\delta\rho_A$, while $\mathbf{K}^{A,B}$ describes the changes in the potential on subsystem $A$ due to $\delta\rho_B$.

There are two ways in which we can solve these subsystem response equations. The first, called uncoupled subsystem response theory, assumes that the density response of subsystem $B$ has no effect on subsystem $A$, and we can therefore ignore the $\mathbf{K}^{A,B}$ term. This is analogous to ground state FDE, where we once again assume that subsystem $B$—describing some environment—is frozen. In this case, we only need to consider the $\mathbf{K}^{A,A}$ response kernel. Like conventional TDDFT, this kernel will have contributions from the Coulomb and XC kernels. However, this kernel also needs to consider the changes to the non-additive XC and kinetic potentials as well. This kernel may therefore be written—in real space rather than orbital space for simplicity—as

$$K^{A,A}(\mathbf{r},\mathbf{r}') = \frac{1}{|\mathbf{r}-\mathbf{r}'|} + \left.\frac{\delta^2 E_{xc}[\rho]}{\delta\rho(\mathbf{r})\delta\rho(\mathbf{r}')}\right|_{\rho=\rho_{tot}} + \left.\frac{\delta^2 T_s[\rho]}{\delta\rho(\mathbf{r})\delta\rho(\mathbf{r}')}\right|_{\rho=\rho_{tot}} - \left.\frac{\delta^2 T_s[\rho]}{\delta\rho(\mathbf{r})\delta\rho(\mathbf{r}')}\right|_{\rho=\rho_A} \tag{3.46}$$

This uncoupled subsystem formalism has been successfully applied,[205,207–210] and approximately accounts for the environment or subsystem $B$ in the following ways: through the changes in the ground state orbitals and orbital energies of subsystem $A$; and through the changes in the potential on $A$ due to the non-additive kernels.

However, studies have shown that there are cases when these effects are insufficient at describing, even qualitatively, the response of the active subsystem $A$.[210] In such cases, the responses of both subsystems need to be coupled. This is analogous to the freeze-and-thaw method for ground state FDE, where now we iteratively solve for $\delta\mathbf{P}^A$ and $\delta\mathbf{P}^B$ until our results are self-consistent. In such cases, the response kernel that couples one subsystem to another is defined as

$$K^{A,B}(\mathbf{r},\mathbf{r}') = \frac{1}{|\mathbf{r}-\mathbf{r}'|} + \left.\frac{\delta^2 E_{xc}[\rho]}{\delta\rho(\mathbf{r})\delta\rho(\mathbf{r}')}\right|_{\rho=\rho_{tot}} + \left.\frac{\delta^2 T_s[\rho]}{\delta\rho(\mathbf{r})\delta\rho(\mathbf{r}')}\right|_{\rho=\rho_{tot}} \tag{3.47}$$

Using these definitions, we can then solve for the excitation energies or polarizabilities as described in Section 3.3.1.

Subsystem TDDFT, like subsystem DFT, requires the use of approximate KEDFs. The kinetic energy kernel in the ALDA is often used, where the kernel is described as

$$\frac{\delta^2 T_s[\rho]}{\delta\rho(\mathbf{r})\delta\rho(\mathbf{r}')} = \frac{10}{9} C_{TF}\rho^{-1/3}(\mathbf{r})\delta(\mathbf{r}-\mathbf{r}') \tag{3.48}$$

This non-additive kinetic energy kernel, like the ground state NAKP, is an approximate treatment for the non-orthogonality of the KS orbitals between systems. However, one would still expect that these approximate functionals will fail when the subsystems are strongly coupled.[206] In such cases, one may want to enforce EO between subsystems. Methods that the effects of non-orthogonal orbitals in TDDFT have been presented before,[211,212] but not within the general framework of subsystem TDDFT. We will continue to explore the implications of EO in subsystem TDDFT in Chapter 9.

# Part II

# The Dressed-Tensors Formalism

# Chapter 4
# Determining Molecular Orientation With Surface-Enhanced Raman Scattering Using Inhomogeneous Electric Fields

Chulhai, D. V.; Jensen, L. "*Determining Molecular Orientation with Surface-Enhanced Raman Scattering Using Inhomogenous Electric Fields*" *J. Phys. Chem. C* **2011**, *117*, 19622–19631

## Abstract

The inhomogeneous electric field near the metal surface of plasmonic nanoparticles allows molecular orientation to be determined from surface-enhanced Raman scattering (SERS). We illustrate this by simulating the effects of the field-gradient on the SERS spectrum of benzene and pyridine. To do this, we present an origin-independent formalism describing the effects of the local electric-field gradient in SERS. Using this formalism, we found that the field-gradient led to observation of Raman-inactive modes in benzene and allowed for extraction of orientation information from the SERS spectra of both benzene and pyridine. It was also observed that the SERS electromagnetic enhancement factor, when considering field-gradient effects, depends on the field-gradient magnitudes and is only approximately described by $|E|^4$ for certain modes. The field-gradient mechanism may also lead to a weakening of intensities as compared to a homogeneous local field. Thus, inclusion of field-gradient effects are crucial in understanding relative intensity changes in SERS.

## 4.1 Introduction

It is well known that the Raman scattering of molecules adsorbed onto metal surfaces that support plasmon resonances may be enhanced, a phenomenon that is referred to as surface-enhanced Raman scattering (SERS)[13,24,75,76]. In some cases, enhancement may be large enough ($> 10^8$) for resolution of single molecules, an effect referred to as single-molecule SERS (SMSERS)[9,19,81–84]. While the basic theory of SERS has been known for a while[13,39,40], the intricate details of the enhancement mechanisms are still being debated due to the complicated nature of the metal-molecule interface[12,41,42].

The SERS enhancement mechanisms may be broadly placed into two categories: the chemical mechanism (CM) and the electromagnetic (EM) mechanism. Enhancement under the CM may be further classified into a charge transfer (CT) mechanism where the incident light is in resonance with a charge transfer excitation between the metal-molecule system, a nonresonant chemical (CHEM) mechanism due to nonresonant interactions between the metal-molecule system, and a molecular resonance mechanism where the incident beam is in resonance with a molecular excitation[12,41]. The EM mechanism arises from the strong local electric field at the metal surface due to excitation of the surface plasmon[7,12,13,39–41,79]. This mechanism is largely independent of the molecule and known to be the major contributor to the SERS enhancement with an approximate enhancement factor of $|E|^4$, where $E$ is the local field enhacement[41,119,213].

Theoretical work[144,214] has shown that the magnitude of the local electric field can vary greatly over the space of a few nanometers. This feature of the local electric field, termed the local electric field-gradient (FG), is strongest for small nanoparticles and surface features described by small radii of curvature (near sharp tips, for example). In these systems, one should expect a significant contribution to the EM mechanism from the FG. This concept was first considered in the early 1980s in order to account for the observation of vibrational modes in the SERS of benzene and related molecules that are forbidden in normal Raman scattering (NRS).[35–38] Moskovits and coworkers[35–38] have argued that large FGs will contribute to the induced dipoles through the electric dipole-electric quadrupole polarizability ($A$) tensor (an effect that is sometimes referred to as quadrupolar-SERS or SEQRS). Since then, FG effects have been largely ignored until recently where descriptions of surface-enhanced Raman optical activity (SEROA), SERS through near-field optical microscopes (NSOM), and SMSERS necessitated such contributions. Janesko and Scuseria[215] have considered the local field and gradient from dipolar and quadrupolar spheres in generating dressed-polarizability tensors in order to describe SEROA. Jahncke and coworkers[216,217] have considered local fields that are functions of the normal coordinate of vibration in order to describe NSOM-SERS. Apkarian and coworkers[106] considered the FG and magnetic field around a nano-dumbbell in order to track the trajectory of a single molecule. Recently, Takase and co-workers demonstrated that FG effect can induce otherwise forbidden transition in SERS of carbon nanotubes.[218,219]

In this chapter, we derive an origin-independent formalism necessary to describe SERS due to inhomogeneous local electric fields. This formalism is similar to the dressed polarizability formalism presented by Janesko and Scuseria to describe SEROA, although their approach

was origin-dependent.[215] Origin-independence was achieved by recognizing that the fields and molecular properties need to be expanded around a common origin. We then used the local field and FG from a dipolar sphere in order to simulate the SERS spectra of benzene and pyridine. Early SERS on benzene[37,220] attributed the observation of normally forbidden modes to a FG effect, and selection rules for such observations were derived[35,36]. Here we verify these selection rules using the FG SERS formalism and show how it may be used to predict relative orientation of molecules with respect to the substrate surface. For pyridine, in addition to information about molecular orientation, we also show that the local FG may give rise to effects that are generally associated with a CM mechanism. Finally, we show that these FG effects are naturally included in simulations that account for the atomistic structure of the metal nanoparticle such as the recently developed atomistic discrete interaction method / quantum mechanics (DIM/QM) method.[123,143,144] Our results show the importance of the FG mechanism in interpreting SERS spectra.

## 4.2 Theory

### 4.2.1 SERS in an inhomogeneous electric field

The oscillating induced dipole, $\mu$, responsible for Raman scattering of a molecule in the vicinity of a metal nanoparticle is given by

$$\mu_\alpha = \alpha_{\alpha\beta} E_\beta + \frac{1}{3} A_{\alpha\beta\gamma} E_{\beta\gamma} + G_{\alpha\beta} B_\beta + \cdots \tag{4.1}$$

where $\alpha$, $A$, and $G$ are the electric dipole-dipole, electric dipole-quadrupole and electric dipole-magnetic dipole polarizabilities respectively. In order to describe Raman scattering, these polarizabilities should be understood to represent the transition polarizability tensors, i.e. derivatives of the polarizability tensors with respect to the vibrational normal mode. The fields perturbing the molecule are due to an incident plane wave field $E^{(0)}$ (described by frequency $\omega$ and propagation vector $n^{\mathrm{i}}$) and an inhomogeneous local field $E^{\mathrm{loc}}$, and may be written as

$$E_\alpha(r,t) = \left( E_\alpha^{(0)} + i\kappa |r| E_\alpha^{(0)} + \cdots + E_\alpha^{\mathrm{loc}} \right) e^{-i\omega t} \tag{4.2a}$$

$$E_{\alpha\beta}(r,t) = \left( i\kappa n_\beta^{\mathrm{i}} E_\alpha^{(0)} + \cdots + E_{\alpha\beta}^{\mathrm{loc}} \right) e^{-i\omega t} \tag{4.2b}$$

$$B_\alpha(r,t) = \left( \frac{\kappa}{\omega} \epsilon_{\alpha\beta\gamma} n_\beta^{\mathrm{i}} E_\gamma^{(0)} + \cdots - \frac{i}{\omega} \epsilon_{\alpha\beta\gamma} E_{\gamma\beta}^{\mathrm{loc}} \right) e^{-i\omega t} \tag{4.2c}$$

where $E_\alpha$, $E_{\alpha\beta}$, and $B_\alpha$ are the total electric field, electric FG and magnetic field perturbing the molecule respectively, and $\kappa = \omega/c$. The Einstein summation convention is employed for repeated indices.

For particles significantly smaller than the wavelength of light, we can ignore contributions on the order of $\kappa$ and higher. Using these fields, we re-write the induced dipole in terms of a

modified polarizability tensor $\alpha'$, defined as

$$\mu_\alpha^{\text{ind}} = \alpha_{\alpha\beta} E_\beta^{(0)} + \alpha_{\alpha\beta} E_\beta^{\text{loc}} + \frac{1}{3} A_{\alpha\beta\gamma} E_{\beta\gamma}^{\text{loc}} - \frac{i}{\omega} G_{\alpha\beta} \epsilon_{\beta\gamma\delta} E_{\gamma\delta}^{\text{loc}} \tag{4.3a}$$

$$= \left[ \alpha_{\alpha\gamma} \left( \delta_{\beta\gamma} + F_\gamma^{\text{loc},\beta} \right) + \frac{1}{3} A_{\alpha\gamma\delta} F_{\gamma\delta}^{\text{loc},\beta} - \frac{i}{\omega} G_{\alpha\gamma} \epsilon_{\gamma\delta\epsilon} F_{\delta\epsilon}^{\text{loc},\beta} \right] E_\beta^{(0)} \tag{4.3b}$$

$$= \alpha'_{\alpha\beta} E_\beta^{(0)} \tag{4.3c}$$

where $F_{\beta(\gamma)}^{\text{loc},\alpha}$ describes the local field (gradient) enhancement in the $\beta$ ($\gamma$) direction resulting from polarization in the $\alpha$ direction. This equation ignores terms on the order of $\kappa$ and higher. At the same order, $F_{\alpha\beta}^{\text{loc}}$ is symmetric ($F_{\alpha\beta}^{\text{loc},\gamma} = F_{\beta\alpha}^{\text{loc},\gamma}$) and there is no contribution to the local magnetic field; we will therefore ignore terms that are dependent on this field. Similarly, the quadrupole induced by an incident and local fields may be defined as

$$\theta_{\alpha\beta}^{\text{ind}} = \left[ \mathscr{A}_{\delta,\alpha\beta} \left( \delta_{\gamma\delta} + F_\delta^{\text{loc},\gamma} \right) + \frac{1}{3} C_{\alpha\beta,\delta\epsilon} F_{\delta\epsilon}^{\text{loc},\gamma} \right] E_\gamma^{(0)} \tag{4.4a}$$

$$= \mathscr{A}'_{\gamma,\alpha\beta} E_\gamma^{(0)} \tag{4.4b}$$

where $\mathscr{A}$ and $C$ are the molecule's electric quadrupole-dipole and electric quadrupole-quadrupole polarizabilities respectively.

The fields from the radiating dipole and quadrupole may also be enhanced by the plasmonic nanoparticle at the Raman-shifted frequency. This leads to an effective scattering polarizability tensor $\alpha''$ expressed as

$$\begin{aligned} \alpha''_{\alpha\beta} &= \left[ \delta_{\alpha\gamma} + F_\gamma^{\text{loc},\alpha}(\omega_S) \right] \alpha'_{\gamma\beta} + \frac{1}{3} F_{\gamma\delta}^{\text{loc},\alpha}(\omega_S) \mathscr{A}'_{\beta,\gamma\delta} \\ &= \left[ \delta_{\alpha\gamma} + F_\gamma^{\text{loc},\alpha}(\omega_S) \right] \left\{ \alpha_{\gamma\delta} \left[ \delta_{\beta\delta} + F_\delta^{\text{loc},\beta}(\omega_L) \right] + \frac{1}{3} A_{\gamma\delta\epsilon} F_{\delta\epsilon}^{\text{loc},\beta}(\omega_L) \right\} \\ &+ \frac{1}{3} F_{\gamma\delta}^{\text{loc},\alpha}(\omega_S) \left\{ \mathscr{A}_{\epsilon,\gamma\delta} \left[ \delta_{\beta\epsilon} + F_\epsilon^{\text{loc},\beta}(\omega_L) \right] + \frac{1}{3} C_{\gamma\delta,\epsilon\zeta} F_{\epsilon\zeta}^{\text{loc},\beta}(\omega_L) \right\} \end{aligned} \tag{4.5}$$

where $F^{\text{loc}}(\omega_L)$ and $F^{\text{loc}}(\omega_S)$ are the local field enhancements at the incident and Raman-shifted frequencies. The effective polarizability described here is similar to the dressed-polarizability tensor formalism of Janesko and Scuseria[215], with the inclusion of the quadrupole induced by the local field gradient (which is of the same order in $\kappa$) through the $C$-tensor. From Eq. 4.5, it is easy to show that we recover the free molecule polarizability tensor $\alpha''_{\alpha\beta} = \alpha_{\alpha\beta}$ within the limit of no local fields. In the formalism presented here, the polarization of the metal nanoparticle due to interactions with the molecule is neglected since these effects are generally small.[144]

The local fields from the nanoparticle (Eqs. 4.3 and 4.5) are applied at some fixed point in the molecule. This point, chosen for convenience, is the center-of-mass of the relevant molecule for results shown in this chapter. However, the resulting expression is origin-dependent since there

are no mutual cancellations of origin-dependent contributions from the $A$, $\mathscr{A}$ and $C$-tensors for fields coupled into the polarizability tensors. This is because these tensors describe the multipoles induced at the origin of the coordinate system of the molecule ($Q_M$) due to a field or FG, whereas the local fields are calcualted in a separate substrate coordinate system ($Q_S$). In order to maintain orgin-independence, we need a common-origin description of the local fields. This is achieved through a Taylor expansion of the fields about the center-of-mass (or about the vector in $Q_M$ that describes the change in gauge origin). The derivation and proof of this common-origin solution is available in Appendix D. This expansion of the local field coupled into the polarizability tensors leads to an origin-invariant expression of the effective dipole required for correctly describing inhomogeneous field effects in SERS.

Electric-field gradient effects are expected to be important for nanoparticles with a small radii of curvature such as atomic roughened surfaces, nano particles with sharp tips and junctions between different nanoparticles. To model this and obtain analytical expressions for the fields, we assume for simplicity a dipolar sphere model for the metal nanoparticle. Such a model neglects nonlocal and quantum effects which are expected to be of importance for nanostructures with small dimensions.[221–223] Such effects are likely to reduce the strength of the local field and thus will affect the ratio between the electric field and the FG. While the simple dipole model will not provide an accurate description of the absolute enhancements it can be used to determine the relative importance of the electric fields and FG. Furthermore, while the fields and field gradients in this work are obtained using the dipole approximation, the formalism presented remains valid for any fields obtained from complex geometries using classical electrodynamics simulations. In this dipolar model, the polarizability $\alpha^S$ of the metal nanoparticle depends on the radius of the sphere $a$ and a function $g$ of the frequency and dielectic constant and can be written as $\alpha^S = a^3 g$. Assuming a point-dipole approximation, the fields at the surface of the sphere (for $|R| = a$) may be expressed as $E \sim \alpha/|R|^3 = g$ and is independent of the sphere's radius. The FG at the surface, using the same model, is $\nabla E \sim \alpha/|R|^4 = g/a$ and is therefore dependent on the radius of the sphere. Larger spheres have smaller FG magnitudes than those for smaller spheres. We use this relationship to examine the SERS FG effects where a decrease on the sphere's radius results in an increase in its FG while the magnitude of the local field at the surface remains unchanged. It should be noted that the radius is used in this chapter to vary the field gradient to field strength ratios and is therefore a representation of the curvature of the local surface roughness responsible for these FG ratios; it is not the actual size of the metal nanoparticle. Also, for a dipolar model, it is easy to show that $B^{\text{loc}}_\alpha = -\frac{i}{\omega}\epsilon_{\alpha\beta\gamma}F^{\text{loc}}_{\gamma\beta} \propto 1/c$, which implies that local magnetic fields are 2-3 orders of magnitude weaker than the local electric FG (and within the quasi-static approximation, $B^{\text{loc}} = 0$ for $\kappa = 0$). As such, we have ignored contributions from the local magnetic field in the derivation of Eq. 4.5 and in simulations in this chapter.

## 4.3 Computational Details

All calculations presented in this work were performed using a local version of the Amsterdam Density Functional (ADF) program package.[165,224] The Becke-Perdew (BP86) XC-potential[153,154]

and an even-tempered quadruple-$\zeta$ slater type basis set with three polarization functions (ET-QZ3P) from the ADF basis set library were used unless stated otherwise. The vibrational frequencies and normal modes were calculated analytically within the harmonic approximation, where the BP86 functional results in harmonic frequencies of pyridine close to experimental results without the use of scaling factors[225]. Frequency dependent $\alpha$, $A$ and $C$-tensors were calculated using the AOResponse module implimented in ADF, with a excited state lifetime of $\Gamma = 0.1$ eV[50,63,111,225,226]. Tensor derivatives were calculated by numerical three-point differentiation with respect to Cartesian displacements.

Polarizability of the isotropic spheres were calculated using experimental frequency-dependent complex dielectric functions of silver at 354 nm, and is $\epsilon = -1.9858 + 0.2854i$.[227] We've also simulated fields from substrates using the discrete interaction model (DIM)[141,142] which uses atomistic electrodynamics. This model has been combined with time-dependent density functional theory (TDDFT) which also allows us to simulate linear-response properties of molecule/substrate complexes in what is termed the DIM/quantum mechanics (DIM/QM) method[123,143,144]. All simulated spectra have been broadened by a full width at half-maximum (fwhm) of 20 cm$^{-1}$.

The averaged Raman intensity may be calculated from the effective polarizability tensor similar to that of traditional Raman scattering. For linearly polarized incident light and a scattering angle of 90°, this is given as

$$\langle I_p \rangle = \frac{K_p}{45}\left(45\alpha_p''^2 + 7\gamma_p''^2 + 5\delta_p''^2\right) \tag{4.6}$$

where $\alpha_p''^2$, $\gamma_p''^2$ and $\delta_p''^2$ are invariants of the effective polarizability derivatives with respect to vibrational mode $p$, $(\alpha'')_p$. The effective polarizability derivatives need not be symmetric and therefore the tensor invariants are given by[2,66,67]

$$\alpha_p''^2 = \frac{1}{9}(\alpha''_{\alpha\alpha})_p(\alpha''^*_{\beta\beta})_p \tag{4.7}$$

$$\gamma_p''^2 = \frac{3}{4}\left[(\alpha''_{\alpha\beta})_p(\alpha''^*_{\alpha\beta})_p + (\alpha''_{\alpha\beta})_p(\alpha''^*_{\beta\alpha})_p\right] - \frac{1}{2}(\alpha''_{\alpha\alpha})_p(\alpha''^*_{\beta\beta})_p \tag{4.8}$$

$$\delta_p''^2 = \frac{3}{4}\left[(\alpha''_{\alpha\beta})_p(\alpha''^*_{\alpha\beta})_p - (\alpha''_{\alpha\beta})_p(\alpha''^*_{\beta\alpha})_p\right] \tag{4.9}$$

For Stokes scattering with an experimental set-up as described above, the parameter $K_p$ is given by[68]

$$K_p = \frac{\pi^2}{\epsilon_0^2}\left(\tilde{\nu_0} - \tilde{\nu_p}\right)^4 \frac{h}{8\pi^2 c\tilde{\nu_p}} \frac{1}{1 - \exp[-hc\tilde{\nu_p}/k_B T]} \tag{4.10}$$

where $\tilde{\nu_0}$ and $\tilde{\nu_p}$ are the frequencies of the incident light and of the $p$th vibrational mode respectively.

In order to describe the fields originating from a model substrate we will consider a sphere of isotropic, frequency-dependent polarizability $\alpha^S(\omega)$ located in some coordinate system $Q_S$. This polarizability is given as

$$\alpha^S(\omega) = a^3 \frac{\epsilon(\omega) - 1}{\epsilon(\omega) + 2} \tag{4.11}$$

where $\epsilon(\omega)$ is the material's complex, frequency-dependent relative dielectic function and $a$ is the radius of the sphere. The local field enhancement factors from this dipolar sphere are given as

$$F^{\beta}_{\alpha}(\omega; \mathbf{R}) = \left( \frac{3R_\alpha R_\gamma}{|R|^5} - \frac{\delta_{\alpha\gamma}}{|R|^3} \right) \alpha^S_{\gamma\beta}(\omega) \tag{4.12a}$$

$$F^{\delta}_{\alpha\beta}(\omega; \mathbf{R}) = \left( -\frac{15R_\alpha R_\beta R_\gamma}{|R|^7} + \frac{3(\delta_{\alpha\beta}R_\gamma + \delta_{\alpha\gamma}R_\beta + \delta_{\beta\gamma}R_\alpha)}{|R|^5} \right) \alpha^S_{\gamma\delta}(\omega) \tag{4.12b}$$

where $\mathbf{R}$ describes the vector separating the molecule and dipolar sphere. The common-origin expression of the local fields needed to maintain origin-invariance is included in Appendix D.

## 4.4 Results and Discussion

### 4.4.1 Enhancement factors in an inhomogeneous electric field

The EM enhancement in SERS is usually approximated as $|E'|^2|E|^2$, where $|E|^2$ is the local field enhancement of the incident field and $|E'|^2$ is the radiated field enhancement[41,119,213]. For simplicity, $E$ and $E'$ here represent the appropriate components of the local fields which depend on the relative orientation of the molecule with respect to these fields. For small Raman shifts, we may assume that $E' \sim E$, from which we obtain an approximate enhancement factor of $EF \sim |E|^4$. This factor, however, ignores the effects of an inhomogeneous local field or the presence of local magnetic fields. In traditional Raman scattering, we consider a plane-wave of frequency $\omega$ with electric FG and magnetic field contributions on the order of $i\kappa$ and $\kappa/\omega$, respectively. As such, the $A$ and $G$-tensors contribute negligibly to the induced dipoles and can safely be ignored (except in cases of Raman optical activity). However, near metal surfaces, the local electric FG is expected to be on the same order as the local electric field (see Eq. 4.2) and there would be a significant contribution to the induced dipoles from the $A$-tensor as well[36].

We have shown in Eq. 4.5 that by considering an inhomogeneous local field on the surface of a metal nanoparticle, we obtain an effective polarizability tensor of the form $\alpha'' \sim \alpha + A + \mathscr{A} + C$. The SERS intensities are proportional to the square of this effective polariability, or $I^{\text{SERS}} \propto |\alpha''|^2 \sim |\alpha + A + \mathscr{A} + C|^2$. This results in terms that resemble $|\alpha|^2$, $|A|^2$, $|\mathscr{A}|^2$, $|C|^2$, as well as a number of coupling terms (see Table 4.1). The $|\alpha|^2$ and $|A|^2$ terms can be thought of as being the Raman intensities resulting from dipoles induced by electric fields and FGs, whereas the $|\mathscr{A}|^2$ and $|C|^2$ terms are from the quadrupoles induced by the fields and FGs, respectively. The remaining terms describe the interference between these types of induced multipoles. Scattering from induced magnetic dipole moments due to the local field and gradient are ignored in this formalism since they scatter on the order of $\kappa$, but will become important in descriptions of SEROA[215]. The appropriate enhancement factors for these various contributors

**Table 4.1.** The terms contributing to the SERS intensity and their relevant enhancement factors

| Term | Enhancement |
|---|---|
| $\lvert\alpha\rvert^2$ | $\lvert E'\rvert^2 \cdot \lvert E\rvert^2$ |
| $\lvert A\rvert^2$ | $\lvert E'\rvert^2 \cdot \lvert\nabla E\rvert^2$ |
| $\lvert\mathscr{A}\rvert^2$ | $\lvert\nabla E'\rvert^2 \cdot \lvert E\rvert^2$ |
| $\lvert C\rvert^2$ | $\lvert\nabla E'\rvert^2 \cdot \lvert\nabla E\rvert^2$ |
| $\mathbf{Re}(\alpha A^\dagger)$ | $\lvert E'\rvert^2 \cdot E \cdot \nabla E$ |
| $\mathbf{Re}(\alpha \mathscr{A}^\dagger)$ | $E' \cdot \nabla E' \cdot \lvert E\rvert^2$ |
| $\mathbf{Re}(\alpha C^\dagger)$ | $E' \cdot \nabla E' \cdot E \cdot \nabla E$ |
| $\mathbf{Re}(A \mathscr{A}^\dagger)$ | $E' \cdot \nabla E' \cdot E \cdot \nabla E$ |
| $\mathbf{Re}(A C^\dagger)$ | $E' \cdot \nabla E' \cdot \lvert\nabla E\rvert^2$ |
| $\mathbf{Re}(\mathscr{A} C^\dagger)$ | $\lvert\nabla E'\rvert^2 \cdot E \cdot \nabla E$ |

$E$ and $E'$ are the field enhancement at the incident and Raman-shifted frequencies whereas $\nabla E$ and $\nabla E'$ are the field gradient enhancement at the incident and Raman-shifted frequencies, respectively.

to the SERS intensity are given in Table 4.1, where $E$ and $\nabla E$ are the field and FG enhancement factors respectively. This suggests that modes that are $\alpha$-tensor (Raman) active are enhanced as $|E|^4$. $|E|^2|\nabla E|^2$ is the appropriate enhancement factor for modes that are $A$-tensor active,[36] while $|\nabla E|^4$ is the relevant enhancement factor the $|C|^2$ terms. The interference terms may also contribute by either enhancing or weakening of the SERS intensities through the enhancement factors shown in Table 4.1.

### 4.4.2 SERS of benzene

SERS of benzene often serves as a model system for understanding adsorption of aromatic molecules on metal surfaces. This is also the prototypical system for investigating FG effects in SERS since vibrational modes normally forbidden in Raman scattering are observed for benzene on rough metal surface.[35–38] A typical SERS spectrum is shown in Figure 4.1[35,37,38,220,228–230]. In addition to the Raman-active $a_{1g}$ ($\nu_1$ and $\nu_2$), $e_{1g}$ ($\nu_{10}$) and $e_{2g}$ ($\nu_6$, $\nu_7$, $\nu_8$ and $\nu_9$) vibrational modes, Raman-inactive $a_{2u}$ ($\nu_{11}$), $e_{1u}$ ($\nu_{18}$, $\nu_{19}$ and $\nu_{20}$) and $e_{2u}$ ($\nu_{16}$ and $\nu_{17}$) modes are sometimes observed. The appearance of these modes have generally been attributed to a FG effect rather than a lowering of molecular symmetry or image charge effects[35–38]. The selection rules for these FG modes have also been considered[35,36]. Briefly, it states that modes that belong to representations that include a cubic transformation will be FG-active since the $A$-tensor transforms as the product of three translations. Benzene's high symmetry ($D_{6h}$) means that the modes that are enhanced by a local field ($a_{1g}$, $e_{1g}$, and $e_{2g}$) are distinct from those that are enhanced by the local FG ($a_{2u}$, $b_{1u}$, $b_{2u}$, $e_{1u}$, and $e_{2u}$)[36]. Included in the FG-active modes are the IR-active $a_{2u}$ and $e_{1u}$ modes, but we will not differentiate between FG-active/IR-active and FG-active/IR-inactive modes since the selection rules for IR are not, in general, related to those for FG SERS.

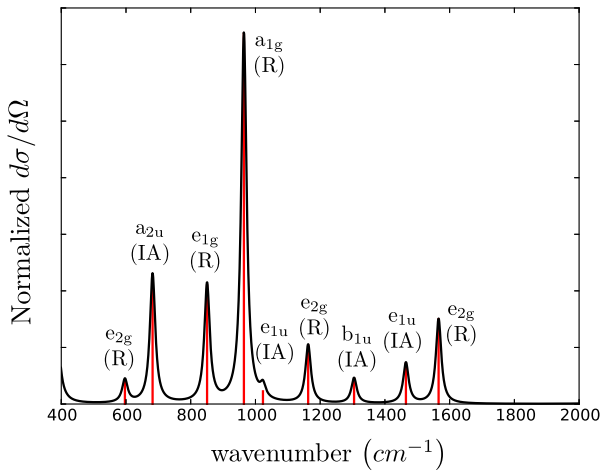


**Figure 4.1.** SERS spectrum of benzene on silver colloids excited at 488 nm. Indicated are the symmetry subgroup (assuming $D_{6h}$ symmetry) as well as the Raman selection rule, either Raman-active (R) or inactive (IA). Exerimental spectrum taken from Ref. 37

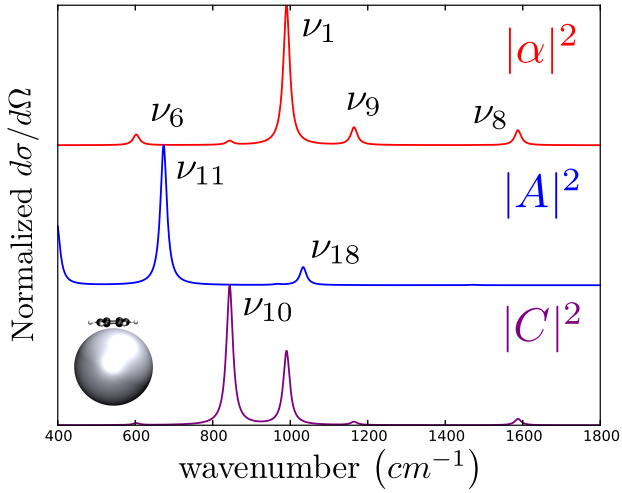


**Figure 4.2.** Contributions to the SERS of benzene flat on a surface from the local electric field ($|\alpha|^2$, *top*), the dipole-quadrupole terms ($|A|^2 + |\mathscr{A}|^2$, *middle*), and the quadrupole-quadrupole term ($|C|^2$, *bottom*).

We aim to show the FG surface selection rules by considering the contributions to the SERS of benzene, enhanced by the local electric field and gradient, in two different orientations. The local electric field contribution to the SERS spectrum of benzene parallel to the surface of the sphere (flat orientation) is described by the $|\alpha|^2$ term (shown in Figure 4.2 top) and resembles that of benzene's NRS spectrum. The relative intensity of the observed modes may be explained using surface selection rules with a greater enhancement of the $a_{1g}(\alpha_{zz})$ mode at 990 $cm^{-1}$ ($\nu_1$). (The surface normal runs along the $z$-axis for benzene parallel to the surface). The FG contribution to the SERS spectrum described by the $|A|^2 + |\mathscr{A}|^2$ terms leads to predicted FG-active modes.

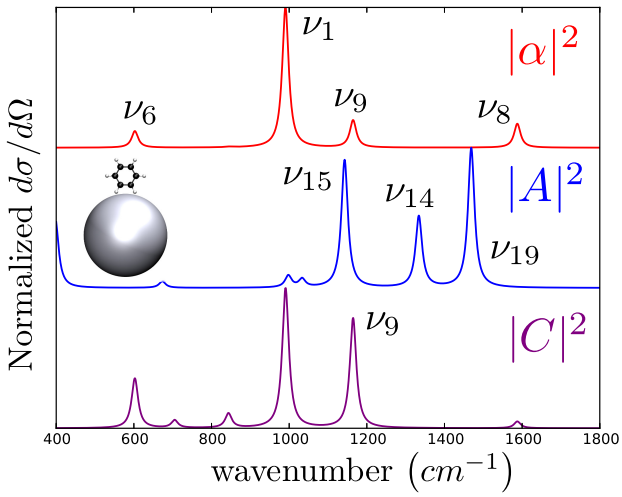


**Figure 4.3.** Contributions to the SERS of benzene perpendicular to a surface from the local electric field ($|\alpha|^2$, *top*), the dipole-quadrupole terms ($|A|^2 + |\mathscr{A}|^2$, *middle*), and the quadrupole-quadrupole term ($|C|^2$, *bottom*).

For benzene in the flat orientation, the Raman-inactive $\nu_{11}$ and $\nu_{18}$ are observable (Figure 4.2 middle). The relative intensities of these modes are as expected when considering FG surface selection rules with $\nu_{11}$ [$\mathrm{a_{2u}}(A_{zzz})$] being more intense than $\nu_{18}$ [$\mathrm{e_{1u}}(A_{zzx},A_{zzy})$]. These surface selection rules are also seen when the plane of the benzene ring is perpendicular to the substrate surface (vertical orientation, Figure 4.3 middle) where the Raman-inactive $\nu_{14}$, $\nu_{15}$ and $\nu_{19}$ are observable. Each of these modes contain large $A_{yyy}$ and/or $A_{xxx}$ components and are therefore expected to be enhanced for large FGs along the plane of the benzene ring. The $|C|^2$ contributions to the SERS intensity are plotted in the bottom spectra of Figures 4.2 and 4.3. While this term describes a field-gradient effect (the enhancement of the near field of an oscillating quadrupole induced by a field gradient), it selects modes that are typically Raman-active ($\nu_1$ and $\nu_{10}$ in a flat orientation and $\nu_1$, $\nu_6$ and $\nu_9$ in the vertical orientation). The local electric field-enhanced SERS of benzene in the vertical orientation (Figure 4.3 top) is very similar to the NRS and the field-enhanced SERS of flat benzene with small changes in relative intensities. Therefore, inclusion of the FG mechanism is essential for assignment of molecular orientation based on relative intensities. The $|\alpha|^2$, $|A|^2$ and $|C|^2$ contributions in Figures 4.2 and 4.3 were normalized, and their relative contributions to the observed SERS spectrum depend on the ratio of $\nabla E/E$. The interference terms are not shown. These terms are only significant when the appropriate polarizability tensor gradients describe the same mode. The Raman-active and FG-active modes in benzene are distinct, leading to little interference between the dipoles induced by the $\alpha$ and $A$ or $\alpha$ and $\mathscr{A}$ tensors. In general, the $\mathbf{Re}(\alpha A^\dagger)$ contribution for benzene is six orders of magnitude weaker than its $|\alpha|^2$ and $|A|^2$ contributions.

As we have shown, FG surface selection rules can give information about the relative orientation of the molecule with respect to the substrate surface (similar to the SERS suface selection rules). Alternatively, relative intensities of these FG modes can give information about the nature of the local electric field in the vicinity of the molecule. Based on these arguments one can deduce, for the

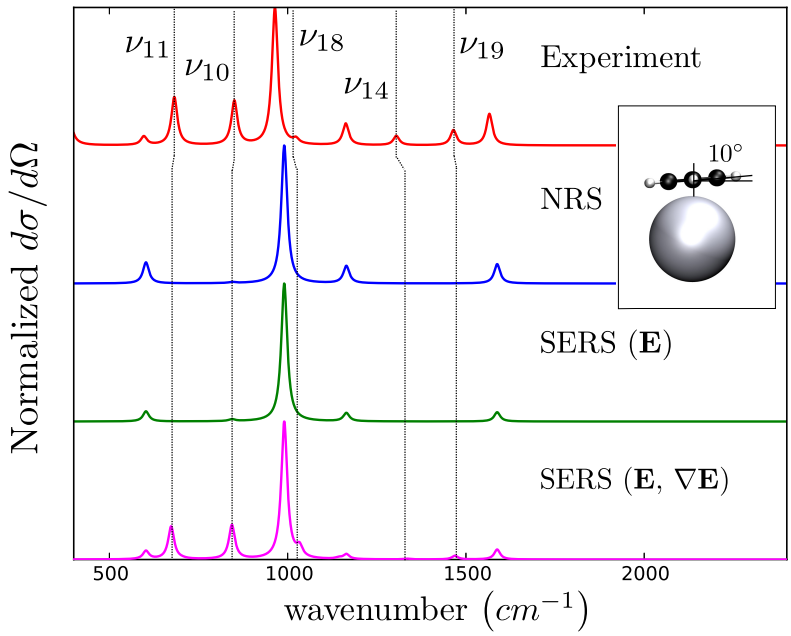


**Figure 4.4.** Simulated SERS of benzene titled at 10° with respect to the surface (orientation shown in inset). The radius of the substrate was taken to be 10 bohrs to reproduce the relative intensities seen in Figure 4.1.

experimental spectrum in Figure 4.1[37], an averaged ensemble orientation where benzene is tilted at some small angle. Indeed, we are able to reproduce the relative intensities of the FG modes in Figure 4.1 by assuming a tilt of $\sim 10°$ of the plane with respect to the surface, shown in Figure 4.4. We are able to correctly reproduce the experimental spectrum seen in Figure 4.1 with the modes in the region of 1100-1600 cm$^{-1}$ being weaker than those in the experimental spectrum. These modes may be weaker by comparison due to an over-estimation of the enhancement of $\nu_1$. The $\nu_{10}$ out-of-plane CH bending mode is particularly interesting since this is a Raman-active mode. However, in the model presented here, this mode is enhanced by a field-gradient effect through the $|C|^2$ term and is not observed for a homogeneous local field. The evidence presented here confirms that lowering of molecular symmetry is not required in order to observe Raman-inactive modes. Indeed, the intensity of modes that become Raman-active as a result of symmetry relaxation is generally very weak, and therefore a symmetry relaxation argument is usually insufficient to describe the intensities seen for Raman-inactive modes in experimental SERS.

### 4.4.3 SERS of pyridine

Another model system typically explored using SERS is pyridine adsorbed onto metal surfaces, where there is competition between the tendency to adsorb flat due to interactions with the $\pi$-system or upright (vertical) through interactions with the lone pair on the nitrogen. Pyridine possess $C_{2v}$ symmetry which means that, unlike benzene, there are no distinct FG modes; all modes are both Raman and FG-active. The observation of FG modes, however, can give information about the relative orientation of the pyridine molecule with respect to the surface through FG

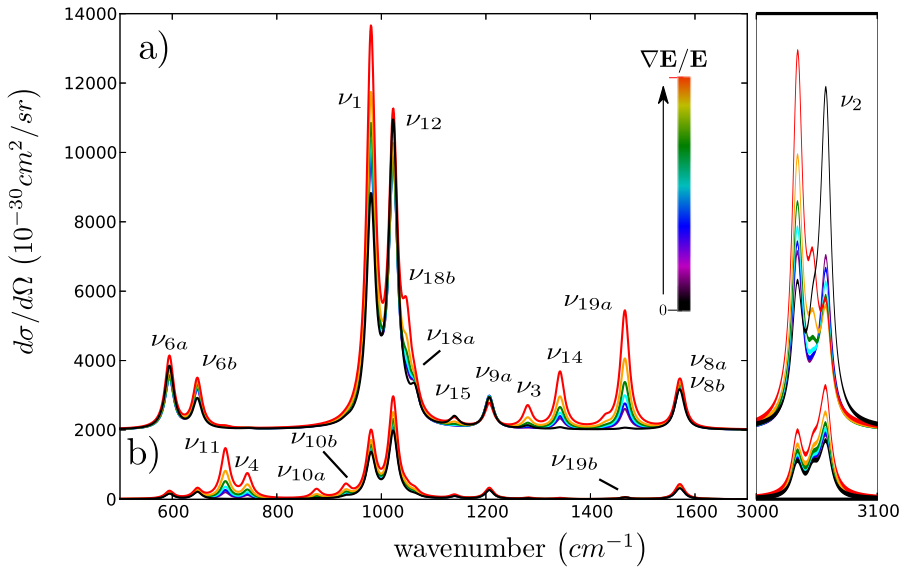


**Figure 4.5.** SERS of pyridine with the plane of the ring *a*) perpendicular, and *b*) parallel to the surface showing how the absolute intensities of each mode changes as we decrease the radius of the sphere from 40 bohrs (purple spectra) to 15 bohrs (red spectra), with the spectra enhanced by the local field only (black spectra) also shown.

surface selection rules. The exact orientation of pyridine on a metal surface is dependent on factors such as coverage, temperature, substrate, and electrochemical potential[35,231–236]. While there is evidence that pyridine binds through its nitrogen lone pair[4,237–239], scanning tunneling microscopy (STM) experiments[234–236] suggest that pyridine is primarily flat (or tilted) at low temperatures and coverages. For pyridine oriented vertically and considering only the local field enhancement, one would expect the $a_1(\alpha_{zz})$ modes to be the most intense, followed by the $b_2$ modes with the $b_1$, $a_2$ and $a_1(\alpha_{xx},\alpha_{yy})$ modes predicted to be very weak or unobservable. In the SERS spectrum of pyridine in this orientation (Figure 4.5*a*) enhanced by the local field only (black spectrum), we observe that the most intense peaks are the $a_1$ ring breathing modes $\nu_1$ and $\nu_{12}$, with contributions from $\nu_{6a}$, $\nu_{8a}$, $\nu_{9a}$ ($a_1$) and $\nu_{6b}$ and $\nu_{9b}$ ($b_2$). These are also the most intense modes in the NRS and the SERS spectra of pyridine flat on the surface (Figure 4.5*b*).

We then looked at the SERS spectra of pyridine with FG effects included. In order to visualize the changes caused by the FG terms in the spectra, we increase the $\nabla E/E$ ratio by decreasing the radius of the model substrate (from 40-15 bohrs for the spectra shown in Figure 4.5). This gives us a clear picture of the modes that are enhanced (or weakened) by the FG mechanism. For pyridine perpendicular to the surface (Figure 4.5*a*), we observe the largest enhancement due to the FG mechanism in $\nu_{19a}$ with contributions from $\nu_1$, $\nu_3$, $\nu_{6a}$, $\nu_{12}$, $\nu_{14}$, and $\nu_{18b}$. The most intense of these FG-enhanced modes ($\nu_{14}$ and $\nu_{19a}$) are also the modes enhanced by the FG mechanism for benzene in the same orientation (Figure 4.3 middle). Their relative intensities are therefore similarly described using FG surface selection rules, with the $a_1(A_{zzz})$ mode ($\nu_{19a}$) being more intense followed by the $b_2(A_{yzz})$ modes ($\nu_3$ and $\nu_{14}$). In this orientation, we also

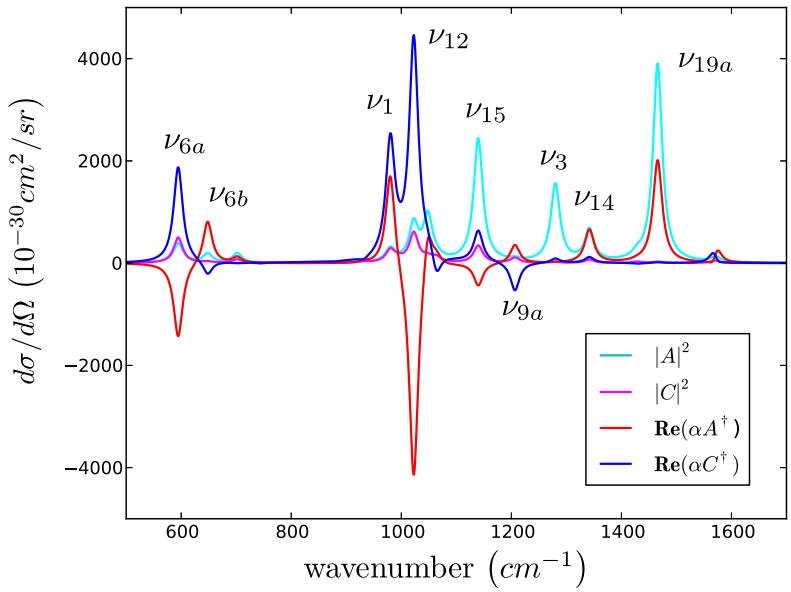


**Figure 4.6.** The major contributors (in addition to the $|\alpha|^2$ term) to the FG SERS spectrum of pyridine perpendicular to the surface of a 10 bohr radius sphere. The interference terms may result in either enhancement or weakening of modes.

observe weakening of $\nu_2$ and $\nu_{15}$ due to the FG mechanism. This is due to the interference between the multipoles induced by local fields and FGs described by the interference terms. The contribution from the $\mathbf{Re}(\alpha A^\dagger)$ and $\mathbf{Re}(\alpha \mathscr{A}^\dagger)$ terms (labeled as $\mathbf{Re}(\alpha A^\dagger)$ in Figure 4.6), for pyridine in this (vertical) orientation, is only an order of magnitude weaker than the $|\alpha|^2$ term and is the same order of magnitude as the $|A|^2$ terms and therefore contributes significantly to the observed spectrum (see Figure 4.6). This term weakens the intensity of $\nu_3$, $\nu_{6a}$, $\nu_{12}$ and $\nu_{15}$, while enhancing $\nu_{6b}$, $\nu_{14}$ and $\nu_{19a}$. The $|A|^2$ term, on the other hand, enhances $\nu_3$, $\nu_{14}$, $\nu_{15}$, $\nu_{18b}$ and $\nu_{19a}$. The $\mathbf{Re}(\alpha C^\dagger)$ contribution, which describes the interference between the dipoles induced by an electric field and the quadrupoles induced by an electric field gradient, shows an enhancement of $\nu_1$, $\nu_{6a}$, $\nu_{12}$, and $\nu_{15}$ and a weakening of $\nu_{9a}$. This suggests that $\nu_{6a}$, $\nu_{9a}$, $\nu_{12}$ and $\nu_{15}$ are either enhanced or weakened depending on the ratio of $\nabla E/E$. The results also indicate that the relative intensities of $\nu_{6a}$ and $\nu_{6b}$ and of $\nu_1$ and $\nu_{12}$ may change due to FG contributions. Understanding the relative behavior of $\nu_1$ and $\nu_{12}$ is particularly important since they are the characteristic modes of pyridine and their relative intensities change with change from NRS to SERS and also with change in electrode potential.

FG surface selection rules lead to a very different picture for pyridine lying flat on the surface (Figure 4.5*b*). In this orientation, the most intense FG modes are $\nu_4$ and $\nu_{11}$ ($b_1$), with $\nu_{10a}$ and $\nu_{10b}$ also observable. Surface selection rules predict that $b_1(A_{xxx})$ modes would be most intense for large FG perpendicular to the plane of the pyridine ring ($x$-axis). We also observe negligible contribution from the interference terms in this orientation, with intensities that are two orders of magnitude weaker than the $|\alpha|^2$ and $|A|^2$ terms. As such, we observe no weakening of modes in the presence of strong FGs.

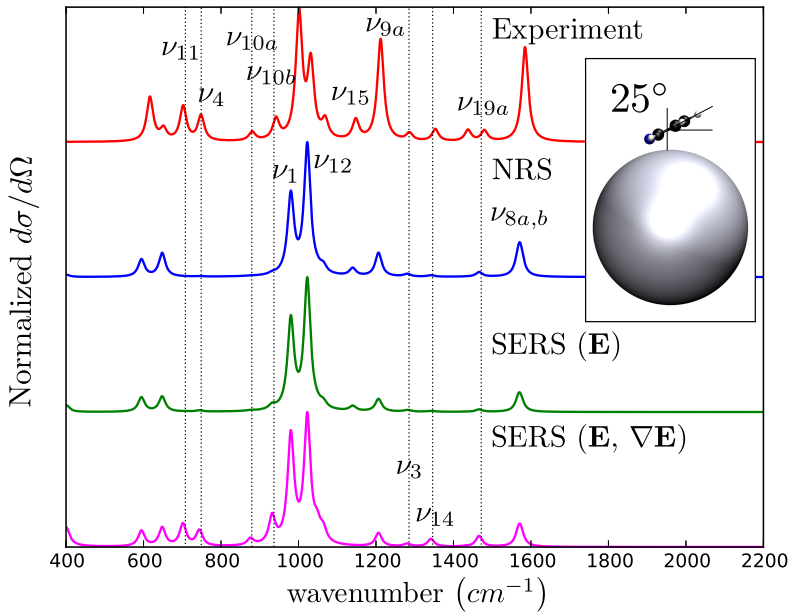


**Figure 4.7.** The SERS of pyridine on cold-deposited rough silver under vacuum[35] (*top*), and the simulated NRS and SERS spectra assuming a tilt angle of 25° with respect to the surface of a 15 bohr diameter sphere with contributions from only the local electric field, and both the local electric field and gradient.

The effects of the FG mechanism on the SERS of pyridine simulated in this chapter have been observed on electrodes at high negative potentials[240–242] and on low temperature roughened surfaces under vacuum[35]. Moskovits *et al.*[35] observed contributions from $\nu_4$, $\nu_{11}$, $\nu_{14}$, $\nu_{15}$, $\nu_{19a}$, and $\nu_{19b}$ in the SERS spectra of pyridine on cold-evaporated silver surfaces, which were absent in the SERS spectra of pyridine on silver colloids. The appearance of these modes have been attributed to the FG effect due to surface roughness. We have shown that a FG contribution to the EM mechanism is required to observe these modes (Figure 4.7) and that the relative intensity of $\nu_4$ and $\nu_{11}$ observed[35] suggests that pyridine is (nearly) flat on the surface for the majority of molecules in the ensemble. Figure 4.7 (top) shows the experimental data for pyridine on cold-deposited silver under vacuum[35] which we are able to reproduce (Figure 4.7 bottom) using the FG mechanism, by assuming a tilt angle of 25° and a high $\nabla E/E$ ratio (a 10 bohr dipolar sphere). We are able to reproduce most of the relative intensities observed with the exception of $\nu_1$ and $\nu_{12}$ (which is incorrectly described using the BP86 functional[243,244]) as well as the intensity of $\nu_{15}$. This argument of an (almost) flat orientation of pyridine on roughened silver electrode was also made by Creighton considering surface selection of the $\alpha$-tensor[240], and by STM experiments at low temperatures and coverages[234–236]. These modes disappear at higher temperatures[35] even though STM results show that pyridine remains in a flat or tilted orientation[234] indicating that observation of these modes may be due to roughness on an atomic level. The observation of these effects in the SERS spectra for pyridine on silver electrodes at high negative potentials may also be partially explained using FG arguments. Experiments have shown that increasing negative electrode potentials result in increase in the intensitiy of $\nu_4$, $\nu_{9a}$ and $\nu_{11}$ (among others)

and decrease in $\nu_{12}$[241,242]. These are all behaviors that are also observed (with the exception of $\nu_{9a}$) under a FG mechanism (see Figure 4.5). The intensity of $\nu_4$ and $\nu_{11}$ in particular suggests a (nearly) flat orientation in these experiments. Predicting orientation change with electrode potential using the FG mechanism is difficult, but one can show the relative behavior of all modes (with the exception of $\nu_{9a}$) if a small (fixed) tilt angle is assumed and the $\nabla E/E$ ratio is increased with increasing potential. Therefore, the behavior of these modes as seen in experiments are likely not entirely due to the CM mechanism and may be partially explained by an EM FG mechanism.

### 4.4.4 Field-gradient effects in atomistic models

The SERS spectra of benzene and pyridine simulated in this work (Figures 4.2, 4.3, 4.4, 4.5 and 4.7) suggest that radii of curvature on the order of 10-40 bohrs is needed to produce observable FG effects. These small radii of curvature indicates surface roughness on the order of a few atoms (previously suggested after observation of these forbidden modes in pyridine only at low temperatures[35]). This implies that an atomistic model may be required for a better description of the FG resulting from surface roughness. Quantum mechanical simulations of SERS based on the dipole-dipole polarzability for a supermolecule system (molecule plus small part the metal nanoparticle) already account implicitly for the FG effects.[41,245] However, this has not been demonstrated explicitly since such simulations also include contributions from the CM mechanism.

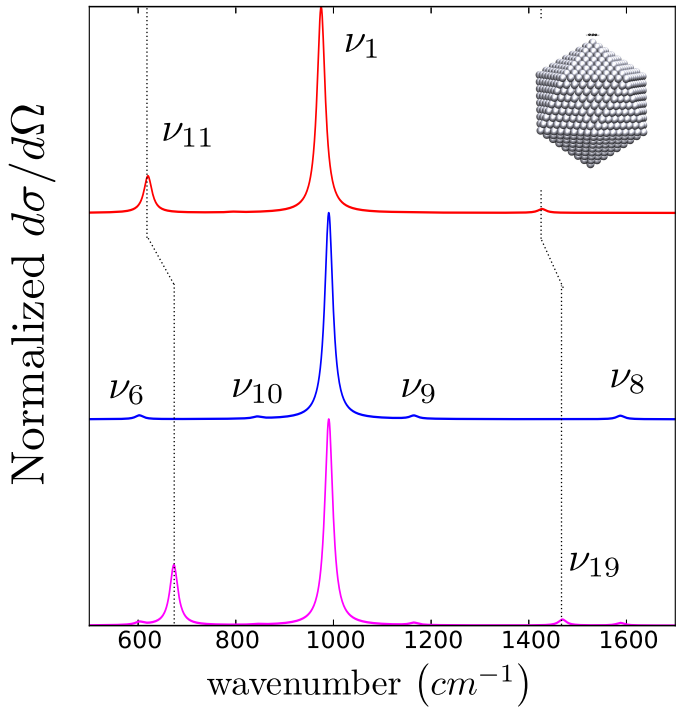


**Figure 4.8.** SERS spectrum of benzene sitting flat on the vertex of an $Ag_{2057}$ icosahedron (inset) simulated with *a*) the DIM/QM method, *b*) local field from the DIM system, and c) local field and gradient from the DIM system. The systems were excited at 488 nm which is far from the plasmon resonance of the $Ag_{2057}$ cluster and results in enhancement of the NRS spectrum by a factor of ∼10.

We will show that FG contributions are included in a supermolecule dipole-dipole polarzability using the DIM/QM model, which retains a detailed atomistic structure of the nanoparticle and provides a natural bridge between the electronic structure methods and the macroscopic electrodynamics description. Furthermore, since CM effects are not included in the DIM/QM model the spectral changes are only due to interactions between the molecule and an inhomogeneous electric field. We will examine the extreme case of benzene sitting flat on the vertex of an $Ag_{2057}$ icosahedron (inset in Figure 4.8). The small radius of curvature at the tip of the icosahedron ensures that the FG perpendicular to the plane of the ring in the vicinity of the molecule is very pronounced, and one would expect large enhancement of $\nu_{11}$. Figure 4.8*a* shows the SERS spectrum simulated using the DIM/QM method, whereas Figures 4.8*b* and *c* show the same system with the local field and gradient coupled in separately using Eq. 4.6. The local fields in Figures 4.8*b* and 4.8*c* are calculated using the DIM method and should be identical to those used in Figure 4.8*a* with the only difference being the way in which they are coupled. Figure 4.8*a* shows contributions from $\nu_{11}$ and $\nu_{19}$, which are Raman-inactive but FG-active. The intensities of Raman-active $\nu_6$, $\nu_8$, $\nu_9$ and $\nu_{10}$ are very weak. We are therefore only able to simulate these Raman-inactive modes after including the FG from the icosahedron (Figure 4.8*c*). It should also be noted that DIM/QM interaction[144] results in shifting of vibrational frequencies, as seen in Figure 4.8, which is not captured using Eq. 4.6. While benzene sitting flat on a surface tip may be unphysical, it clearly shows that the supermolecule polarizability calculated using the DIM/QM method includes contributions from local electric FG. In addition to this, DIM/QM allows us to account for the shift in vibrational frequencies due to substrate/molecule interactions.

Theoretically, the CM mechanism is elucidated from full QM calculations where the substrate is also treated using QM. However, since these results also contain effects of the FG, it becomes difficult to separate the two mechanisms based on these types of calculations. As we have shown in this chapter, a lot of the effects typically attributed to the CM mechanism for pyridine may also be explained by a FG mechanism.

## 4.5 Conclusion

In this work we derived an origin-independent SERS expression which includes the effects of the FG. We used this expression to simulate the SERS spectra of benzene and pyridine on model substrates and examined the effects of the FG. We found that we are able to correctly describe observed Raman-inactive modes in the SERS spectrum of benzene without lowering of molecular symmetry and that our results verified surface selection rules previously outlined for FG effects in SERS. We were also able to reproduce experimental results assuming a 10° tilt of the benzene plane with respect to the surface. For pyridine, we found that FG effects may lead to both enhancement and weakening of modes (the exact behavior is dependent on the FG to field strength ratio) and that we are able to describe modes observed in a low temperature, low coverage experiment by assuming a tilt angle of 25°. Also for pyridine, we observed that the FG mechanism correctly describes effects that are generally associated with the CM mechanism. Enhancement under the FG mechanism required surface roughness of atomic dimensions and we

showed that the DIM/QM (atomistic) method accounted for these effects in the calculation of the polarizability of the molecule-substrate complex. Electromagnetic hotspots in the junction between nanoparticles are typically only a few nm in dimensions and thus should have a small radii of curvature. Since hotspots are responsible for the largest enhancements in SERS we expect that FG effects should be considered. The results presented here demonstrate the importance of FG effects in understanding relative SERS intensities.

# Chapter 5
# Simulating Ensemble-Averaged Surface-Enhanced Raman Scattering

Chulhai, D. V.; Chen, X.; Jensen, L. "*Simulating Ensemble-Averaged Surface-Enhanced Raman Scattering*" *J. Phys. Chem. C* **2016**, DOI:10.1021/acs.jpcc.6b02159

## Abstract

The ability to simulate surface-enhanced Raman scattering (SERS) is a vital tool in elucidating the chemistry of molecules near the vicinity of plasmonic metal nanoparticles. However, typical methods do not include the dynamics of the molecule(s) of interest and are often limited to a single or few molecules. In this work, we combine molecular dynamics simulations with the dressed-tensor formalism to simulate the SERS spectra of Ag nanoparticles coated with a full monolayer of pyridine molecules. This method allows us to simulate the ensemble-averaged SERS spectra of more realistic large scale systems, while accounting for the organization of molecules in the hotspots. Through these simulations, we find that the preferential binding location and orientation of the molecules, the choice of electrodynamics method, and the inclusion of field gradient effects influence both the enhancement distribution and the spectral signatures. We also show that both the translational and rotational motions of a pyridine molecule near a nanoparticle junction may be effectively tracked through its SERS spectrum.

## 5.1 Introduction

One of the unique properties of plasmonic metal nanoparticles is their ability to enhance and concentrate the electromagnetic field at the surface of the particle. This leads to a large enhancement of the optical properties of molecules in the vicinity of the metal surface, which can be exploited in surface-enhanced spectroscopic techniques such as surface-enhanced Raman scattering (SERS).[13,24,75,76] Since its discovery[3] and identification[4,5], SERS has become a multi-disciplinary tool.[13,75,77–80] The large enhancement due to the metal particles enables the detection and identification of single molecules,[19,81–84] and a recent study has demonstrated that it is possible to achieve sub-nm resolution from the Raman imaging of individual molecules.[34]

The enhancement mechanism of SERS is now well understood, and results from a combination of the electromagnetic mechanism (EMM), due to the strong local field, and the chemical mechanism (CM), due to the specific interactions between the molecule and the surface.[12,13,24,41,75,76,246–248] The bulk of the enhancement comes from the EMM and it can be shown that SERS enhancement scales roughly as $|\mathbf{E}^{loc}|^4$, where $\mathbf{E}^{loc}$ is the local field experienced by the molecule.[213,249,250] However, a combination of the CM and the EMM is what leads to the observed SERS spectrum, which is often impossible to interpret without input from simulations. Thus, SERS provides unique opportunities and challenges for simulations due to the complex interplay between the CM and the EMM.

Typically, SERS may be simulated using either full quantum mechanical, using some small model metal cluster[12,41,225,243,251,252], or hybrid quantum/classical[107,130–140,253], where the molecule is described by quantum mechanics and the nanoparticle by classical electrodynamics, methods. The choice of method is determined by what is being explored—a full quantum mechanical description is needed to describe the quantum interactions between the molecule and nanoparticle necessary for describing the CM, while the hybrid methods are excellent at describing the EMM of SERS—and each has proved insightful in understanding the chemistry of molecules near metal substrates. However, these descriptions rarely extend beyond a single molecule. A full quantum mechanical description of the SERS of a large ensemble of molecules on a nanoparticle substrate is, at the present time, prohibitively expensive. Hybrid methods, on the other hand, could allow for the study of the effects of the EMM on ensemble SERS systems.

In addition, experiments have shown the ability to temporally track the SERS spectrum of a single molecule.[19,30,44,106,254] These single-molecule spectra are often characterized by large changes in both the SERS intensity and spectral signatures,[19,44,254–257] and these changes have been attributed to either the motion of the molecule about the hot-spot, or the change in the geometry of the excited state structure. While theory has shown that the orientational information of a single molecule may be reflected in its SERS spectrum,[106,258] there has not yet been any SERS model that naturally incorporates the dynamics of the molecule.

In this chapter, we will simulate the SERS spectra of several nanoparticle systems coated with a full monolayer of molecules by combining molecular dynamics (MD) simulations with the dressed-tensor formalism of SERS. Prior studies have demonstrated that the dressed-polarizability formalism[124,215,258] is an efficient method of simulating SERS spectra in inhomogeneous electric

fields by decoupling the calculations of the molecular properties from the calculation of the local field. The combination of these—MD simulations and dressed-tensors—models have allowed us to generate and analyze nearly 18 million SERS spectra. By calculating the SERS spectra of every molecule on the metal nanoparticles, we will be able to quantify the enhancement distributions, as well as simulate the ensemble-averged SERS spectrum, of these coated nanoparticles. This method will also allow us to explore how different aspects of the theoretical model affect the SERS of ensemble systems, such as including electron smearing, the explicit locations and orientations of attached molecules, and the gradient of the local electric field. This combined method also enables us to track the dynamics of a single molecule, and we will show how the molecule's translational and rotational motions are reflected in its SERS spectrum.

## 5.2 Computational Details

### 5.2.1 Molecular dynamics simulations

The pyridine (pyr) coated Ag nanoparticles used in this chapter were obtained from MD simulations using the Large-scale Atomic/molecular Massively Parallel Simulator (LAMMPS)[259,260]. The inter- and intra-molecular interactions of the pyr molecules were described by the general AMBER force field (GAFF)[261,262]. The force field responsible for the Ag-pyr interactions was parametrized through the embedded-atom-method (EAM) potential modified by a Morse potential and DFT-D2[263–265]. Full details on the optimization of this force field are included as Supporting Information.

In the initial structure, all pyr molecules were aligned perpendicular to the Ag(111) surface in order to generate a compact monolayer, and the coated nanoparticle was then immersed into a cubic box filled with pyr molecules. The surface coverage was set to $\sim$5.5 molecules/nm$^2$[266]. After the energy minimization, the whole system was slowly heated to 100 K and subsequently equilibrated to yield a condensed ligand shell around the Ag cluster. Then, NVE ensemble with a integration time step of 1 fs was employed, incorporated with velocity-rescale thermostat. The temperature was increased from 100 K to 800 K and annealed to 300 K gradually leading to the desorption of the excess ligands away from the Ag nanoparticle surface. Finally, the whole system was equilibrated under NVT at 300 K for 1 ns with an integration time step of 1 fs; the last 500 ps of which were used in the SERS simulations. During the MD simulations, the Ag nanoparticle was kept frozen to reduce computational cost.

### 5.2.2 The dressed-tensors formalism

The dressed-polarizability formalism,[124,215,248,258] which previously was shown to accurately simulate the SERS of pyr,[258] was used for all SERS simulations. In this formalism, the molecular transition polarizabilities are dressed as

$$\alpha_{\alpha\beta}^{D,(k)} = F_{\gamma}^{loc,\alpha}\left[\alpha_{\gamma\delta}^{(k)}F_{\delta}^{loc,\beta} + \frac{1}{3}A_{\gamma,\delta\epsilon}^{(k)}F_{\delta\epsilon}^{loc,\beta}\right] + \frac{1}{3}F_{\gamma\delta}^{loc,\alpha}\left[\mathcal{A}_{\gamma\delta,\epsilon}^{(k)}F_{\epsilon}^{loc,\beta} + \frac{1}{3}C_{\gamma\delta,\epsilon\zeta}^{(k)}F_{\epsilon\zeta}^{loc,\beta}\right] \tag{5.1}$$

where $\alpha^{(k)}$, $A^{(k)}$, $\mathcal{A}^{(k)}$, and $C^{(k)}$ are the electric dipole-dipole, dipole-quadrupole, quadrupole-dipole, and quadrupole-quadrupole transition polarizabilities, respectively, for normal mode $k$, and the Einstein summation convention is assumed for repeated Greek subscripts. The respective polarizabilities for each molecule being described were rotated to match their corresponding orientation in the nanoparticle reference frame. The $\mathbf{F}^{loc}$ terms are the local field enhancement matrices, where the superscripts describe the incident field direction and the subscripts describe the resulting field (or gradient) direction(s); for simplicity, these field enhancement matrices are assumed to be identical at both the incident and scattered frequencies.

These field enhancement matrices were calculated using two different atomistic electrodynamics methods: the discrete interaction model (DIM),[267] and the discrete dipole approximation (DDA).[268,269] In DIM, a Gaussian charge distribution is used to describe the atoms, and thus the interaction tensor is renormalized, which effectively screens the interactions at short distances.[142,267,270] In comparison, the bare unscreened interaction tensor is adopted in the DDA model, as the atoms are being treated as point charges. The screening of the interaction at short-range is essential for correctly describing the near field both in the vicinity of the nanoparticle and in the junction between nanoparticles.[267] To simplify the calculations of the field enhancement matrices, we have not included coordination dependence in DIM.[267]

### 5.2.3 Quantum mechanical calculations

All quantum mechanical calculations presented in this work were performed using a local version of the Amsterdam Density Functional (ADF) program package.[165,224] For the parameterization of the MD force field, the Becke-Perdew (BP86) XC-potential[153,154] and the triple-$\zeta$ with one polarization function (TZP) Slater type basis set from the ADF basis set library (keeping the 1s–3d core frozen for Ag) were used. Scalar relativistic effects were taken into account by adopting the zeroth-order regular approximation (ZORA)[271–273] and dispersion effects were accounted for by the DFT-D3 approach[274].

For the properties needed for the dressed-tensor simulations, the BP86 XC-potential[153,154] and an even-tempered quadruple-$\zeta$ slater type basis set with three polarization functions (ET-QZ3P) were used. Vibrational frequencies and normal modes were calculated analytically within the harmonic approximation, where the BP86 functional results in harmonic frequencies of pyr close to experimental results without the use of scaling factors[225]. Frequency dependent (at $\omega = 343.5$ nm) $\alpha$, $A$, $\mathcal{A}$, and $C$ tensors were calculated using the AOResponse module implemented in ADF, with an excited state lifetime of $\Gamma = 0.1$ eV[50,63,111,225,226]. The short-time approximation[55] was used to obtain transition polarizabilities, where tensor derivatives were calculated using numerical three-point differentiation with respect to Cartesian normal mode displacements.

## 5.3 Results and Discussion

### 5.3.1 Advantages and limitations

The dressed-tensor formalism is a hybrid quantum/classical method for simulating SERS; it uses polarizability tensors calculated with quantum mechanics to describe the molecule(s), and field enhancement matrices calculated with classical electrodynamics to describe the electromagnetic response of the nanoparticle. The polarizability tensors of any molecule of interest need to be calculated only once. The method may be applicable for both off- and on-resonance Raman scattering, providing that the relevant quantum mechanical description of the molecule is used to obtain the polarizability tensors. The field enhancement matrices need to be calculated for every individual molecule's position, but these are relatively inexpensive. This method also naturally separates the theories used to calculate the molecular polarizabilities and the local electric fields, which allows for the exploration of the effects of different electrodynamics methods. Coupling with MD simulations, which can provide a reasonable description of the dynamics of large scale systems, allows for either the efficient simulation of the ensemble-averaged SERS spectrum of realistic systems or the tracking of single molecules in motion via their SERS spectra.

However, we should point out that the method employed in this chapter also has its limitations. For each individual SERS spectrum, we only considered the interactions between the plasmonic substrate and the probe molecule in our simulations. All interactions with solvent molecules were ignored; although, one could include solvent molecules explicitly in the MD simulations, or consider their effects as a dielectric medium in the classical electrodynamics simulations. Additionally, we only considered the classical interactions between individual molecules and the plasmonic nanoparticle. All other molecule-nanoparticle interactions—not including the MD force field and classical electrodynamics field interactions—and all molecule-molecule interactions outside of the MD force field were ignored. This results in identical vibrational frequencies and transition polarizabilities for all molecules, requiring only one set of quantum mechanical calculations, and therefore significantly reduces the computational cost. It was also shown that there are charge-transfer (CT) transitions near the 343.5 nm excitation used in this chapter,[275] and these may significantly alter the resulting SERS spectrum. Accounting for these CT effects is beyond the limitations of the dressed-tensor formalism, though it was previously found that the SERS signatures resulting from the field gradient effects often resemble signatures attributed to a CT mechanism.[258] Finally, the SERS spectra were generated from trajectories of 500 ps; while this is much too short of a time-scale to capture the full dynamics in macroscopic SERS systems, the results still give insight into how the dynamics of these molecules affect their SERS spectra. This is particularly important since recent experimental studies have shown the ability to track the motion of single molecules via their SERS spectrum[19,30,254,276]

### 5.3.2 Analyzing hot-spots

We continue our discussion by considering how the hot-spots from different nanoparticle substrates affect the resulting SERS enhancement distribution. Figure 5.1 shows three Ag nanoparticle

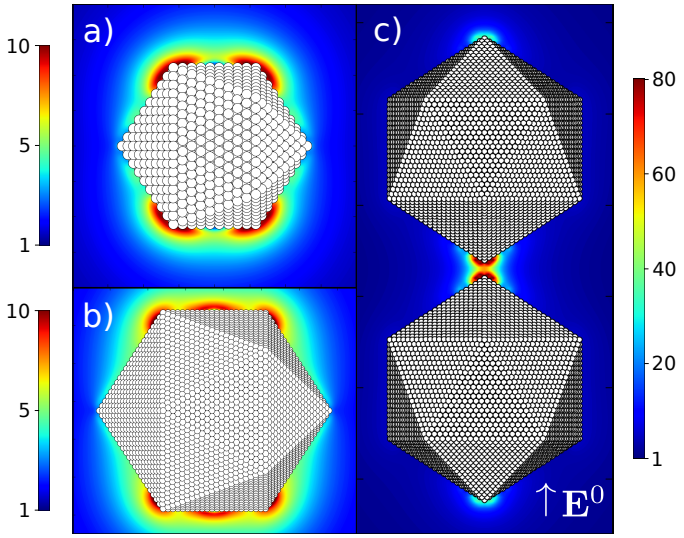


**Figure 5.1.** The local field enhancement along a cut plane for *(a)* the sm. monomer, *(b)* the lg. monomer, and *(c)* the dimer systems.

substrates: a small monomer icosahedron of 2869 atoms (hereinafter, sm. monomer); a large monomer icosahedron of 33153 atoms (hereinafter, lg. monomer); and a dimer system made up of two icosahedron monomers of 33153 atoms each. In this figure, we also show the local electric fields on a cut plane for the indicated incident field direction. Such figures are usually used to map the hot-spots in various substrates, and from this figure we observe that the properties of the hot-spots in these three substrate systems are very different. The hot-spots are near the vertices in the sm. monomer, near the vertices and edges in the lg. monomer, and in the junction between the monomers in the dimer system. The magnitude of the local electric field is also very different in these systems, as is expected, and is $\sim 4$ times larger in the dimer system than in the monomer systems. This image is very useful in determining the locations of—and the enhancement expected from—these hot-spots, though it neglects any information from the associated molecule(s).

An alternative method of mapping locations of hot-spots is presented in Figure 5.2. In this figure, we show a single snapshot in the MD trajectory for each of the three systems, where we color the individual molecules by their enhancement factors; the lowest enhancements are colored blue and the highest red. An advantage of this method is that it takes both the size and preferential binding orientation of the molecules into consideration. The information gained on the location of the hot-spots from Figure 5.2 are similar to those obtained from Figure 5.1; the largest enhancements occur near the vertices for the sm. and lg. monomer systems, and in the junction for the dimer system. However, the binding distance of the molecules and their orientations, which are both important determining factors, give us a better estimate of the enhancement we can expect for a pyr molecule in these hot-spots. Furthermore, it provides direct information about both the spatial distribution of and the organization of the molecules within the hot-spot, something that cannot be gained from the field-enhancement plots in Figure 5.1.

Additionally, we can use the statistics of the calculated enhancements over the entire MD

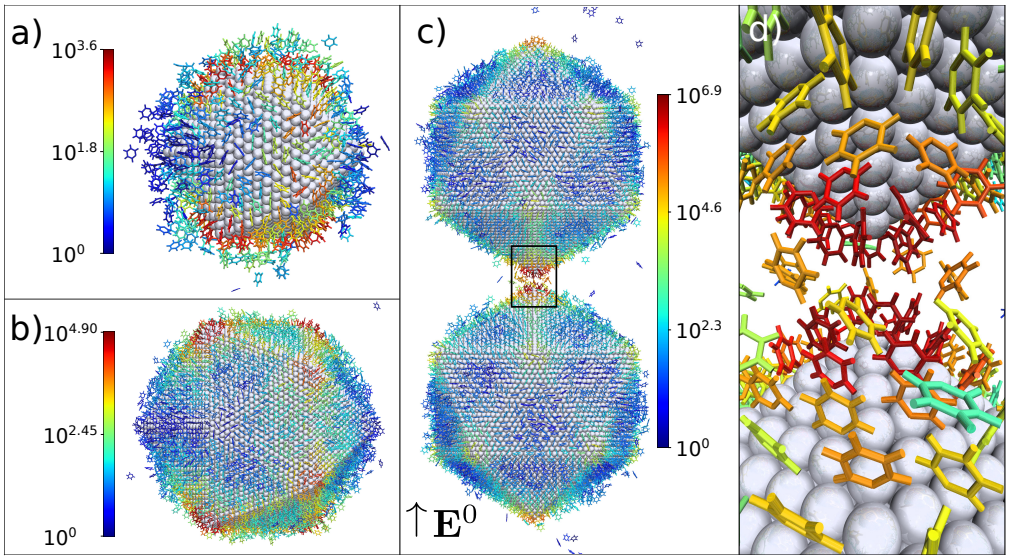


**Figure 5.2.** Individual molecules colored by their enhancement factors for *(a)* the sm. monomer, *(b)* the lg. monomer, *(c)* the dimer, and *(d)* a zoomed in region of the dimer system.

trajectory to quantify the hot-spot. In ref. 277, a truncated Pareto distribution (TPD) was used to fit the tail of the enhancement distribution in order to describe the nature of the hot-spot using three parameters. According to the TPD analysis, we can fit the tail of the enhancement distribution, on a log-log scale, to a straight line:

$$p(G) = A \cdot G^{-k} \tag{5.2}$$

where $G$ is the SERS enhancement and $p(G)$ is the enhancement probability density. $A$ and $k$ are two of the three parameters used to describe the hot-spot: $A$ is a representation of the (spatial) size of the hot-spot, while $k$ describes the sharpness of the hot-spot or how quickly, in spatial terms, the hot-spot decays. Note that our definitions of $A$ and $k$ are slightly different from those in ref. 277, and therefore the numbers obtained in this chapter should not be directly compared to those in the aforementioned paper. In particular, this interpretation of $A$ and $k$ assumes the description of a single hot-spot,[277] which does not apply to our monomer systems as seen from Figure 5.1. We will therefore only use these parameters as a way to quantify the general enhancement distribution (over all hot-spot regions) in our systems. In our analyses, we find that the margin of error is $\pm$ 1 for $A$ and $\pm$ 0.05 for $k$; these errors span the variations in A and k that may be obtained from choosing different enhancement bin sizes—all data presented were obtained with a (log) enhancement bin size of 0.2. The third parameter used to describe a hot-spot is the maximum measured enhancement $G_{max}$.

In Figure 5.3, we show the TPD analyses of the three nanoparticle systems; the values of $A$, $k$, $G_{max}$, and the average enhancement ($G_{avg}$) for these systems are included in Table 5.1. We observe very large $A$ and $k$ values—68 and 0.90, respectively—for the sm. monomer. These values result from a lack of a well-defined long-tail distribution of enhancement factors for this system,

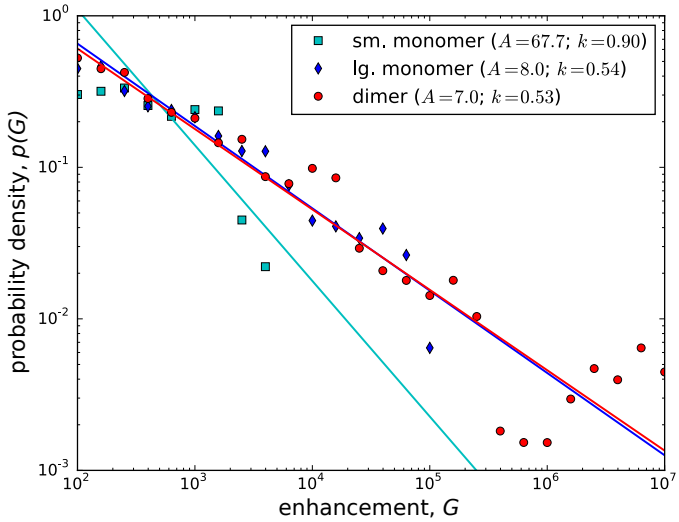


**Figure 5.3.** TPD analyses of the sm. monomer, lg. monomer, and dimer systems.

| system | $\log[G_{avg}]$ | $\log[G_{max}]$ | A | k |
|---|---|---|---|---|
| sm. monomer | 2.302 | 3.604 | 67.7 | 0.90 |
| lg. monomer | 3.104 | 4.953 | 8.0 | 0.54 |
| dimer | 4.318 | 6.949 | 7.0 | 0.53 |

**Table 5.1.** TPD enhancement distribution results from the different nanoparticle systems

and indicate a very large, but also very sharply decaying hot-spot—assuming that the system is comprised of a single hot-spot region. However, from Figure 5.2, we observe that there is no single hot-spot in this system; the largest enhancements are centered around the many vertices of the nanoparticle, giving the statistics of one very large hot-spot. Additionally, the difference between $G_{max}$ and $G_{avg}$ is small, resulting in a large $k$ value and giving the impression that these hot-spots are quickly decaying.

With an understanding of how the $A$ and $k$ values reflect the nature of the hot-spot regions, we will now look at the TPD results from the lg. monomer and dimer systems. Both these systems have similar enhancement distributions, with $A$ values of 8 and 7 for the lg. monomer and dimer systems, respectively, and with $k$ values of 0.54 and 0.53, respectively. These values are within their expected margins of error, suggesting that the enhancement distributions from these two very different substrate systems are, in fact, the same. However, both $A$ and $k$ describe the spatial distribution of the enhancements; since the dimer system is made up of two of the lg. monomer nanoparticles, one should expect the enhancement distributions—outside of the hotspot created by the junction in the dimer system—to be similar for both systems. The $G_{avg}$ and $G_{max}$ of these systems, on the other hand, are very different, and results from the larger enhancements in the dimer junction dominating its average enhancement. These enhancement distributions are also reflected in how much each molecule contributes to the ensemble SERS signal in each system,[278] the results of which are shown in Table S2 of the Supporting Information. They indicate that ∼90% of the signal is contributed by ∼33%, ∼14% and ∼1% of the molecules

in the sm. monomer, lg. monomer and dimer systems, respectively.

### 5.3.3 Distribution and spectral dependence on theoretical models

To understand how the theoretical model affects the resulting enhancement distribution and spectrum, we will examine three particular aspects: (1) electrodynamics method used in simulating the local electric field (that is, the DIM or DDA methods); (2) sampling method used (MD simulations or random sampling); and (3) field extension used in dressed-tensor formalism (homogeneous local field or both homogeneous field and its gradients). We will briefly examine how each of these influence both the SERS distribution, via the TPD results, and the resulting spectrum in the dimer nanoparticle system.

#### 5.3.3.1 The impact of the electrodynamics method on the SERS distribution

Classical electrodynamics are typically used to simulate the optical properties of metallic nanoparticles, but resent studies have shown that such a description fails for smaller (<10 nm) nanoparticles.[12,279–283] The failure of classical electrodynamics for these nanoparticles is due to a lack of treatment of the smearing of the electronic charge distribution over the particle surface; this effect is correctly captured in quantum mechanics and nonlocal electrodynamics.[267,284,285] This nonlocal effect is also thought to be important for simulating the local fields for nanoparticle dimers whose separations are <1 nm,[12,282] distances that are sometimes referred to as the tunneling regime. However, it is not yet clear to what extent the screening of the electric fields impact the SERS distribution of systems outside of this regime.

| model | $\log[G_{avg}]$ | $\log[G_{max}]$ | A | k |
|---|---|---|---|---|
| DIM (MD; E) | 4.32 | 6.95 | 7.0 | 0.53 |
| DIM (MD; E+FG) | 4.37 | 6.96 | 7.2 | 0.53 |
| DDA (MD; E) | 4.47 | 7.16 | 13.7 | 0.51 |
| DDA (MD; E+FG) | 4.71 | 7.58 | 9.8 | 0.47 |
| DIM (random; E) | 3.05 | 6.63 | 7.2 | 0.69 |
| DIM (random; E+FG) | 3.06 | 6.72 | 7.7 | 0.69 |
| DDA (random; E) | 3.13 | 6.68 | 42.1 | 0.80 |
| DDA (random; E+FG) | 3.16 | 7.29 | 41.9 | 0.80 |

**Table 5.2.** TPD enhancement distribution results from the different models

Examining how each of the DIM[141,142] and DDA[268] electrodynamics methods affect the TPD results should give us insight into the importance of nonlocal effects in these systems. The key difference between these two methods is that while the DDA method describes the interaction between point-dipole objects, the DIM method describes the interaction between Gaussian distribution of charges. Results from these methods are included in Table 5.2, with the corresponding graph shown as Figure S2 in the Supporting Information. The DDA method, at least for a homogeneous local electric field, results in uniformly larger field enhancements for (almost) all molecules when compared to the DIM method. This is reflected in the near parallel lines in Figure S2 and in their different $A$ values (7.0 and 13.7) but equivalent $k$ values (0.53 and 0.51) for the DIM and DDA methods, respectively. This is not surprising since most molecules

are bound to the surface and should, in the DIM method, experience near uniform screening of the local electric field when compared to the DDA method.

The results in Table 5.2 are also shown assuming either a homogeneous local field (E) or both a homogeneous local field and its gradient (E+FG). Note that the dimer system includes two atomically sharp tips, separated by 1 nm, and therefore magnifies the effects of the field gradient. We observe that the enhancement distribution for the DIM method is the same whether or not we take field gradients into consideration, with similar $A$, $k$, $G_{avg}$ and $G_{max}$ values. But in the DDA method, while both field expansions result in similar $k$ values (of $\sim$0.5), it results in very different $A$ , $G_{avg}$ and $G_{max}$ values. These differences are also due to the Gaussian charge distribution in DIM resulting in a screening of the electric fields at closer distances, which is where the field gradient is strongest, minimizing its overall impact. These results indicate that it is in fact the field gradient contributions to the local electric field that determines the enhancement distribution in the DDA method, while the enhancement distribution in the DIM method is primarily determined by its homogeneous local electric field contributions.

#### 5.3.3.2 The effect of sampling methods on the SERS distribution

A previous study dedicated to quantifying the enhancement distribution of SERS hot-spots[277] assumed that the molecular positions about the hot-spot were randomly sampled. The estimation of enhancement factors from local field plots, such as in Figure 5.1, also implicitly assumes random positioning of the molecule somewhere in the hot-spot region. However, the molecule's finite size and preferential binding orientation with respect to the surface influences its SERS enhancement. One should, therefore, expect that the SERS distribution of a particular molecule to also be dependent on its preferential binding location and orientation. In order to understand the extent of this dependency, we will compare the SERS distributions obtained from both MD and random sampling.

The data obtained from random sampling are also included in Table 5.2, with its graphical comparison with the MD sampled data shown in Figure S3 of the Supporting Information. The most obvious result from the random sampling methods is perhaps the much smaller $G_{avg}$ values, which are due to the probe molecules being randomly dispersed throughout the system rather than preferentially binding to the surface as observed in the MD simulations; on average, the molecules are farther away from the surface with random sampling. The smaller enhancement values from the random sampling—both $G_{avg}$ and $G_{max}$—are also due, in part, to the random orientation of the molecules. The pyr molecules from the MD sampling show a tendency for binding in an "upright" orientation, with the plane of the pyr ring perpendicular to the surface. This would lead to larger enhancements since the local field vector is also, at least in the hot-spot regions, perpendicular to the surface; as was previously shown,[258] pyr shows the strongest enhancements for local field vectors parallel to the plane of the molecule. The screening of the local fields (in the DIM method) also impacts the enhancement distribution differently with random sampling, which is illustrated in Figure S3 of the Supporting Information. As discussed earlier, the MD sampled distribution simulated with the DDA method can be seen as a uniform increase in the enhancement of (nearly) all molecules in the system when compared to the enhancement simulated

with the DIM method. This is not the case with the randomly sampled methods, since only the molecules closer to the substrate surface would be more enhanced by the DDA method—these are the fields most screened in the DIM method—resulting in larger $A$ and $k$ values.

#### 5.3.3.3 The SERS spectral signatures with field gradients

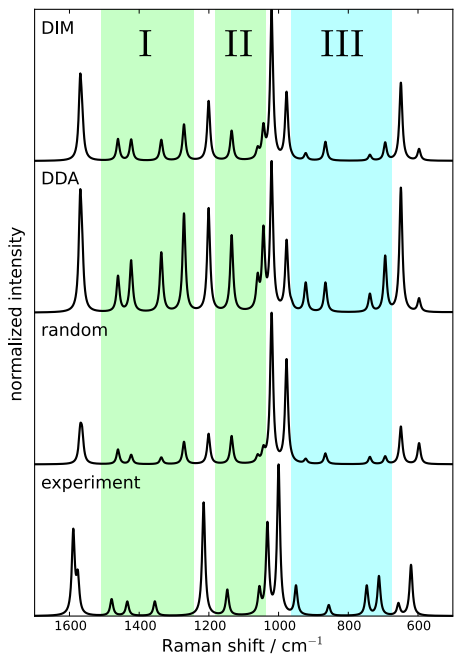


**Figure 5.4.** Ensemble SERS spectra calculated using the DIM and DDA methods with MD sampling, the DIM method with random sampling, and taken from experiment[35]. I, II and III indicate regions where the modes are most affected by the field gradient.

It is known that the local electric field at the surface of plasmonic nanoparticles may vary by orders of magnitude over the space of a few nanometers.[140,214,258] This gradient of the local electric field is strongest for surface features described by small radii of curvature, such as near sharp tips. They also result in a change of the Raman selection rules and often in the enhancement of Raman forbidden modes,[35–38,258] where ref. 258 has explicitly shown that the relative intensity of the field gradient modes may help to predict the orientation of the molecule(s) with respect to the surface. However, previous theoretical studies involving field gradients[124,215–217,258] have only considered single molecules, either in fixed orientations or orientationally averaged with respect to the nanoparticle surface. In order to understand how these field gradients influence the ensemble-averaged SERS spectrum, we will study the dimer nanoparticle system with its atomically sharp tips and strong field gradients.

In Figure 5.4, we show the resulting ensemble-averaged spectrum simulated using the DIM and DDA methods with MD sampling and using the DIM method with random sampling. We only show the spectra with field gradients included; this is because the (normalized) spectra are near identical when simulated with a homogeneous electric field. The data for the experimental

spectrum was taken from ref. 35, and is for pyr on roughened cold-evaporated silver under vacuum. This experimental spectrum clearly shows the enhancement of unexpected Raman modes that are attributed to large field gradients due to atomic-scale surface roughness. We also highlight three regions—I, II, and III—in Figure 5.4, which are regions where the modes are most affected by the field gradient. The modes in regions I and II are (usually) enhanced when pyr binds in an upright orientation, while those in region III are usually seen when pyr binds in a "flat" orientation, that is, when the plane of the pyr ring is parallel to the surface.[258]

In all three simulated cases in Figure 5.4, the ratio of the modes in regions I and II are larger than those in region III, while the opposite is true for the experimental spectrum. This is because the MD simulations resulted in the pyr molecules binding in an upright orientation, whereas the experimental data suggests that the pyr molecules are more flat; an angle of $\sim 25°$ between the molecular plane and the surface was calculated in ref. 258. Additionally, while the field gradient effects are clearly more significant in the DDA method than in the DIM method—due to the screening of the field gradient at closer distances in the DIM method—the relative intensity of the field gradient modes in the different regions remain the same in both methods. The random sampling method, on the other hand, shows very weak enhancements of the modes in the three regions. This is to be expected since fewer molecules are closer to the surface where the field gradients are stronger. Overall, one needs to be careful when comparing the intensities of the field gradient modes in the simulated spectra to those seen experimentally, as factors such as location, orientation, and screening of the electric field all influence the intensity of these modes.

### 5.3.4 Tracking single molecules

We also used the results from the MD simulations of the dimer system to track the SERS spectrum of a single molecule over the course of 100 ps, which is shown in Figure 5.5. This figure also includes the relative positions and orientations of this molecule at 400, 421, 436, 456, and 500 ps. This particular molecule was selected because it underwent the largest change in intensity over its calculated trajectory. Similar large changes in the SERS intensity have been observed in experiments, and are generally attributed to the diffusion of molecules across hot-spots.[19,30,254] The spectral changes we observe are of two types: intensity changes over a longer time scale (5–20 ps); and intensity changes on a shorter time-scale ($\sim$1 ps). We find that it is the translational motion of the molecule about the hot-spot that is responsible for the intensity changes over the longer time-scale. This is illustrated in Figure 5.5, and shows weaker intensities when the molecule is farther away from the dimer junction (at 400–418, 422–445 and 470–500 ps) and stronger intensities when the molecule is closer to the junction (at 418–422 and 445–470 ps).

In order to study the spectral changes over the shorter 1 ps time-scale, we will examine the SERS of the molecule in the region between 450–460 ps in Figure 5.6. This figure also includes the relative orientation of the molecule with respect to the dimer junction at each time step. These images clearly show that the spectral changes at the 1 ps time-scale are due to the rotational motion of the molecule. We observe that the intensity is lowest when the molecule flat on the surface—as seen at 450, 455, 457, and 459 ps. In these orientations, the field gradient modes that indicate at flat pyr molecule (at 738 and 922 $cm^{-1}$) are also sometimes visible; the spectrum at

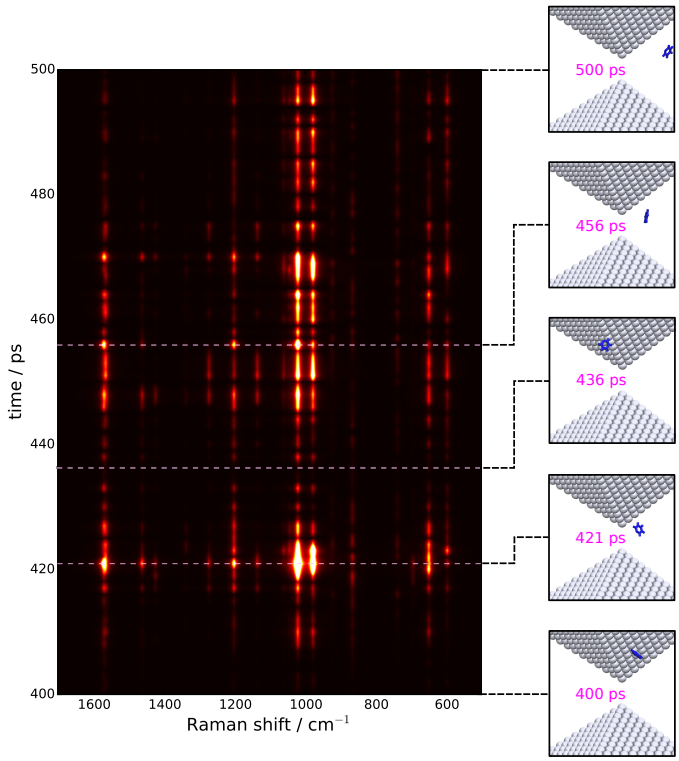


**Figure 5.5.** The SERS spectra of a single molecule over 100 ps *(left)* with its position and orientation relative to the dimer junction at selected times *(right)*.

459 ps is too weak to see these signatures. The brighter spectra indicate when the plane of the pyr molecule is perpendicular to the surface, or parallel to the local field vectors, and are of two types: an "upright" orientation, when the N-atom is pointing towards (or away from) the surface; and a "side" orientation, when the N-atom is pointing in a direction parallel to the surface. These two orientations are also distinctly seen in the spectral features through the intensity of the field gradient modes. The side orientations are clearly indicated by strong field gradient modes at 1060, 1135 and 1271 cm$^{-1}$ (at 451–454 ps), while the upright orientation is indicated by strong field gradient modes at 865 and 1458 cm$^{-1}$ (at 456 and 458 ps). The regular Raman modes at 597, 649, 977, 1019, 1200 and 1570 cm$^{-1}$ showed no distinct changes in relative intensity with respect to rotational motion.

Of course, there are lots of factors that would determine whether such rotational information may be obtained from SERS spectra. Some of these include obvious experimental challenges such as slowing rotational motion and having nanoparticle substrates designed with strong local electric field gradients. Additionally, the pyr molecule's Raman scattering was simulated off-resonance of any molecular excitations. It was shown that, when considering only the EMM mechanism of SERS, molecules on resonance that exhibit Franck-Condon (or A-term) scattering do not exhibit the same rotational asymmetry in its polarizability tensors[44], and therefore these rotational signatures may only be seen for Herzberg-Teller (or B-term) scatterers or non-resonant molecules. Yet, Figure 5.6 clearly shows that the rotational motion of a single molecule may be captured by

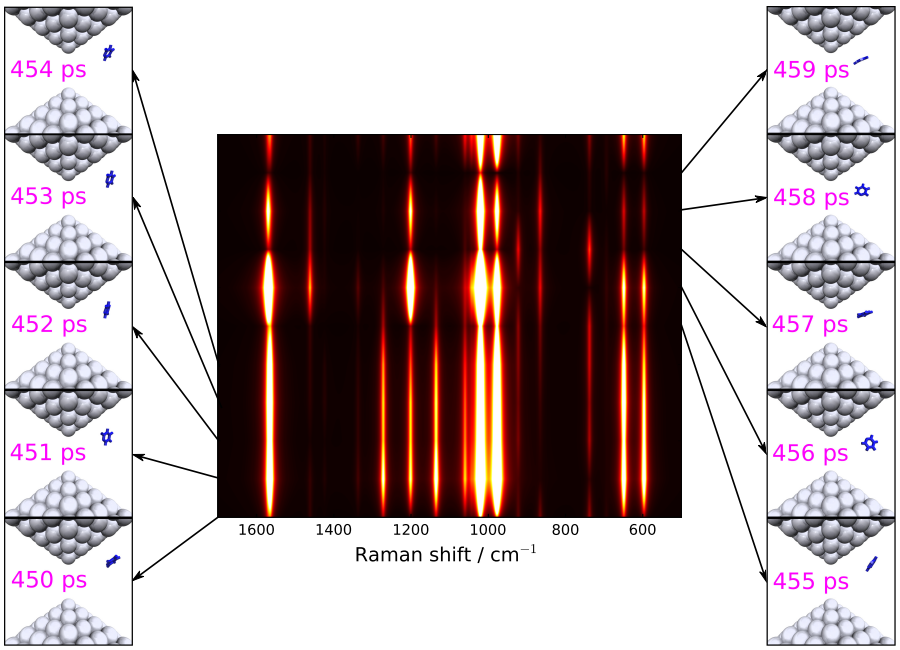


**Figure 5.6.** Single-molecule SERS spectra over 10 ps, showing how the orientation is reflected in the resulting spectrum

its SERS spectrum providing that the appropriate conditions are met.

## 5.4 Conclusion

In this chapter, we have combined MD simulations with the dressed-tensor formalism to simulate the SERS of ensemble systems over short time-scales. We have used the results obtained to examine the hot-spots of three model systems—a sm. monomer, a lg. monomer and a dimer nanoparticle system—by examining their respective enhancement distributions. We also showed that the location and orientation of the molecule, as well as whether or not field gradients were included in the simulations, all affected both the SERS enhancement distribution and the spectrum. We found that screening of the local electric fields was still important for a 1 nm dimer junction, and it also softened the effects of the field gradient, which is in better agreement with the weak field gradient effects seen experimentally. Finally, we presented the SERS trajectory of a single molecule, and showed how both translational and rotational information were reflected in its SERS spectrum. This chapter presents a comprehensive theoretical description of SERS on large scale systems, and explicitly show how single-molecule motion may be tracked via SERS spectroscopy.

# Chapter 6
# Simulating Surface-Enhanced Raman Optical Activity Using Atomistic Electrodynamics-Quantum Mechanical Models

Chulhai, D. V.; Jensen, L. "*Simulating Surface-Enhanced Raman Optical Activity Using Atomistic Electrodynamics-Quantum Mechanical Models*" *J. Phys. Chem. A* **2014**, *118*, 9069–9079

## Abstract

Raman optical activity has proven to be a powerful tool for probing the geometry of small organic and bio-molecules. It has therefore been expected that the same mechanisms responsible for surface-enhanced Raman scattering may allow for similar enhancements in surface-enhanced Raman optical activity (SEROA). However, SEROA has proved to be an experimental challenge and mirror-image SEROA spectra of enantiomers have so far not been measured. There exists a handful of theories to simulate SEROA, all of which treat the perturbed molecule as a point-dipole object. To go beyond these approximations, we present two new methods to simulate SEROA: the first is a dressed-tensors model that treats the molecule as a point-dipole and point-quadrupole object; the second method is the discrete interaction model / quantum mechanical (DIM/QM) model which considers the entire charge density of the molecule. We show that while the first method is acceptable for small molecules, it fails for a medium-sized one such as 2-Bromohexahelicene. We also show that the SEROA mode intensities and signs are highly sensitive to the nature of the local electric field and gradient, the orientation of the molecule, and the surface plasmon frequency width. Our findings give some insight into why experimental SEROA, and in particular observing mirror-image SEROA for enantiomers, has been difficult.

## 6.1 Introduction

Raman optical activity (ROA) measures the difference in the Raman intensities involving light of two different polarization states. The most common, incident circular polarization (ICP), measures the difference in Raman intensities due to right- and left-circularly polarized incident light. ROA measures vibrational optical activity, and is therefore able to detect structural information as it relates to the chirality of molecules.[286–288] Following the first theoretical treatments[289–291] and experimental observations[292,293], ROA has been routinely used to assign absolute configurations[294] of small chiral molecules and measure enantiomeric excess. The method can also be easily performed in aqueous environments, which makes it a powerful tool in modern biochemistry.[287,295] ROA may be used to study both the structure and dynamics of biomolecules *in situ* (for a recent overview, see ref. 295).

However, ROA is hindered by low signal intensities, which may be three or more orders of magnitude weaker than the already weak normal Raman scattering (NRS). These intensities may be enhanced by several orders of magnitude through surface-enhanced Raman scattering (SERS)-like mechanisms, termed surface-enhanced Raman optical activity (SEROA). SEROA is a unique technique in that it combines the powerful structural information of ROA with the strong enhancements known for SERS. However, the technique has proved to be difficult, with only a few experimental studies reported to date.[296–301]

There have been only a handful of theoretical treatments of SEROA. The earliest models were those by Efrima[302,303], who suggested that large ROA intensities may be observed for systems with large electric field-gradients and different phases of the field and field-gradient. Hecht and Barron[304,305] explored the effects of a surface fixed with respect to the laboratory frame. More recently, Janesko and Scuseria[215] proposed a "dressed-tensors" approach, where the molecular polarizabilities are "dressed" to account for the electromagnetic fields. Bouř and co-workers[306,307] later re-formulated this in matrix form that allows one to easily account for multiple substrates. Johnson and co-workers[308,309], expanding on the work done earlier by Kerker and co-workers for SERS,[116] used extended MIE theory to simulate the ROA excitation profiles of molecules near plasmonic nanoshells. These theories all treat the molecule as a point-polarizable dipolar object - either considering only the dipoles induced due to electric field gradients and magnetic fields, or the electric quadrupoles and magnetic dipoles induced due to electric fields only - where the relevant polarizabilities were calculated using quantum mechanics (QM) (or other appropriate methods) for the molecule in the absence of the nanoparticle. However, this approximation is expected to fail for molecules close to the nanoparticle surface where field-gradients are significant. For such systems, we assert that higher order terms describing the molecule are required.

Ideally, one should consider the molecule as a continuous charge distribution interacting with the plasmonic nanoparticle. This is accounted for naturally in full QM treatment of both the molecule and nanoparticle. We previously explored both the chemical and electromagnetic effects of SEROA using time-dependent density functional theory (TDDFT) by accounting for the finite lifetime of the excited states.[310] Janesko and Scuseria used TDDFT to further explore the chemical effects in SEROA by approximating the nanoparticles as $Au_2$ clusters.[311] In that

work, they showed that orientational averaging leads to a "wash-out" of the SEROA intensities. These methods, however, are intractable for realistically-sized nanoparticles (>1000 atoms). For such systems, a classical electrodynamics treatment of the nanoparticle(s) is warranted.

In this work, we present two methods that overcome the limit of assuming a point-dipole approximation of the molecule. The first is the discrete interaction model (DIM) / QM method,[107,123,143,144,312] where we treat the nanoparticle atomistically as a collection of interacting atomic polarizabilities. This method allows the entire charge density of the molecule to interact with the classical nanoparticle, with the response of the entire complex calculated within linear response (LR) TDDFT. DIM/QM have previously been used to simulate SERS[107,144] and here we extend this model to also describe SEROA. The second method is an extension of the dressed-tensors formalism[215,258], where we consider both the local electric field-gradient emanating from the nanoparticle, as well as a point-dipole and point-quadrupole expansion of the molecule. We will then explore the changes these different approximations have in the resulting SEROA spectrum, including enhancement factors, orientational averaging, and the effects of the plasmon frequency width. Finally, we conclude by highlighting the implications of the results presented here for experimental SEROA.

## 6.2 Theory

### 6.2.1 General ROA theory

The measured Raman optical activity depends on the experimental setup, and reflects a different relation between molecular properties. For spectra presented in this chapter, we will consider excitations off-resonance of any molecular transitions but on resonance with plasmonic modes. We will also (initially) ignore the difference in the frequencies of the incident and Raman-scattered radiation. Under such conditions, the ROA intensity for incident circular polarization (ICP) experimental setup with a back-scattered geometry is given by the far from resonance (FFR) expression[287,313,314]

$$I_p^R(\pi) - I_p^L(\pi) = K_p \left[ \frac{24\beta(G')_p^2 + 8\beta(A)_p^2}{45c} \right] \tag{6.1}$$

where $c$ is the speed of light, $\beta(G')_p^2$ is the anisotropic invariant of the product of the electric dipole-dipole ($\alpha^p$) and the electric dipole-magnetic dipole ($G'^p$) polarizability transition tensors, and $\beta(A)_p^2$ is the anisotropic invariant of the product of the electric dipole-dipole and electric dipole-quadrupole ($A^p$) transition tensors. These invariants are defined as

$$\beta(G')_p^2 = \mathbf{Im}\left( i\frac{3\alpha^p_{\alpha\beta}G'^{p*}_{\alpha\beta} - \alpha^p_{\alpha\alpha}G'^{p*}_{\beta\beta}}{2} \right) \tag{6.2}$$

$$\beta(A)_p^2 = \mathbf{Re}\left( \frac{1}{2}\omega\alpha^p_{\alpha\beta}\epsilon_{\alpha\gamma\delta}A^{p*}_{\gamma,\delta\beta} \right) \tag{6.3}$$

where $\epsilon_{\alpha\gamma\delta}$ is the Levi-Civita (anti-symmetric) tensor, $\omega$ is the angular frequency of the incident

light and **Re** and **Im** denotes the real and imaginary parts, respectively. The parameter $K_p$ depends on the incident and scattered light and is defined as

$$K_p = \frac{\pi^2}{\epsilon_0^2}(\tilde{\nu}_{in} - \tilde{\nu}_p)^4 \frac{h}{8\pi^2 c\tilde{\nu}_p} \frac{1}{1 - \exp[-hc\tilde{\nu}_p/k_B T]} \tag{6.4}$$

The Raman intensity for the same experimental setup is

$$I_p^R(\pi) + I_p^L(\pi) = K_p \left[ \frac{45\alpha_p^2 + 7\beta(\alpha)_p^2}{45} \right] \tag{6.5}$$

where $\alpha^2$ and $\beta(\alpha)^2$ are the isotropic and anisotropic invariants of the electric dipole-dipole polarizability, defined as

$$\alpha_p^2 = \frac{1}{9}\mathbf{Re}\left(\alpha_{\alpha\alpha}^p \alpha_{\beta\beta}^{p*}\right) \tag{6.6}$$

$$\beta(\alpha)_p^2 = \mathbf{Re}\left(\frac{3\alpha_{\alpha\beta}^p \alpha_{\alpha\beta}^{p*} - \alpha_{\alpha\alpha}^p \alpha_{\beta\beta}^{p*}}{2}\right) \tag{6.7}$$

The polarizability transition tensors $\alpha^p$, $A^p$, and $G'^p$ are approximated using a Placzek-like polarizability theory (we adopt a short-time approximation accounting for the finite lifetime of the excited states that are valid both on- and off-resonance.)[50,315–319] Within the Placzek-like approximation, the transition tensors are expanded in a Taylor series around the equilibrium geometry and can be expressed as geometric derivatives of the molecular properties as

$$\alpha_{\alpha\beta}^p = \left(\frac{\partial \alpha_{\alpha\beta}}{\partial Q_p}\right)_0 \tag{6.8}$$

$$A_{\alpha,\beta\gamma}^p = \left(\frac{\partial A_{\alpha,\beta\gamma}}{\partial Q_p}\right)_0 \tag{6.9}$$

$$G'^p_{\alpha\beta} = \left(\frac{\partial G'_{\alpha\beta}}{\partial Q_p}\right)_0 \tag{6.10}$$

where $Q_p$ is the normal mode of the $p$th vibration, and the unsuperscripted tensors are the electronic polarizability tensors.

### 6.2.2 DIM/QM in the modified velocity gauge

The DIM/QM method[107,123,143,144,312] represents the nanoparticle atomistically, allowing for the modeling of the influence of the local environment on the optical properties of the molecule, while treating the molecule as a charge density using density functional theory (DFT). The atomic resolution of the DIM method is therefore able to consider complex surfaces and nanoparticle geometries. The calculation of the electric dipole-dipole polarizability response in DIM/QM has been implemented in ADF using damped LR-TDDFT.[123,143,144] In this work, we implemented DIM/QM in the velocity gauge accounting for the perturbation due to the local electric fields

and the finite lifetime of the excited states. We also extended the DIM/QM framework to be able to calculate the electric dipole-quadrupole and electric dipole-magnetic dipole response tensors, including origin-dependent contributions from the local electric field, in order to calculate origin-invariant SEROA.

In order to modify the DIM/QM operators, we will start by considering the sum-over-states (SoS) expressions of the polarizability response tensors. However, it should be noted that actual response calculations were carried out using LR theory. The SoS expression for the DIM/QM electric dipole-dipole polarizability tensor in the length gauge (LG) is

$$\alpha^{\text{tot}}_{\alpha\beta}(\omega) = \langle\langle \hat{\mu}^{\text{tot}}_{\alpha}; \hat{\mu}^{\text{tot}}_{\beta} \rangle\rangle_{\omega+i\Gamma} \tag{6.11a}$$

$$= 2\sum_{n\neq 0} \frac{\omega_{n0}\langle\psi_0|\hat{\mu}^{\text{tot}}_{\alpha}|\psi_n\rangle\langle\psi_n|\hat{\mu}^{\text{tot}}_{\beta}|\psi_0\rangle}{\omega^2_{n0} - (\omega + i\Gamma)^2} \tag{6.11b}$$

where $\psi_0$ and $\psi_n$ are the electronic ground and excited state wave functions, $\hbar\omega_{n0} = E_n - E_0$ is the corresponding excitation energy, and $\Gamma$ is a damping factor to account for the finite lifetime of the excited states. $\hat{\mu}^{\text{tot}}$ is the total dipole operator, defined as

$$\hat{\mu}^{\text{tot}}_{\alpha}(\omega) = \hat{\mu}^{\text{QM}}_{\alpha} + \hat{V}^{\text{loc}}_{\alpha}(\omega) \tag{6.12}$$

where $\hat{\mu}^{\text{QM}}$ is the dipole operator of the molecule and $\hat{V}^{\text{loc}}$ is the frequency-dependent local field potential induced due to an external perturbation. It is defined as

$$\hat{V}^{\text{loc}}_{\alpha}(r_j, \omega) = -\sum_{m} \frac{r_{jm,\beta}\mu^{(\alpha)}_{m,\beta}(\omega)}{|r_{jm}|^3} \tag{6.13}$$

where $\mu^{(\alpha)}$ are the dipoles induced in the DIM system due to an external perturbation in the $\alpha$ Cartesian direction, and $m$ sums over each DIM atom.

We extend this to include the total electric dipole-quadrupole ($A^{\text{tot}}$) and electric dipole-magnetic dipole ($G'^{\text{tot}}$) response of the molecule-nanoparticle complex. These are defined as

$$A^{\text{tot}}_{\alpha,\beta\gamma}(\omega) = \langle\langle \hat{\mu}^{\text{tot}}_{\alpha}; \hat{\theta}^{\text{tot}}_{\beta\gamma} \rangle\rangle_{\omega+i\Gamma} \tag{6.14a}$$

$$= 2\sum_{n\neq 0} \frac{\omega_{n0}\langle\psi_0|\hat{\mu}^{\text{tot}}_{\alpha}|\psi_n\rangle\langle\psi_n|\hat{\theta}^{\text{tot}}_{\beta\gamma}|\psi_0\rangle}{\omega^2_{n0} - (\omega + i\Gamma)^2} \tag{6.14b}$$

$$G'^{\text{tot}}_{\alpha\beta}(\omega) = \mathbf{Im}\left[\langle\langle \hat{\mu}^{\text{tot}}_{\alpha}; \hat{m}^{\text{tot}}_{\beta} \rangle\rangle\right]_{\omega+i\Gamma} \tag{6.15a}$$

$$= -2\sum_{n\neq 0} \frac{(\omega + i\Gamma)\mathbf{Im}\left[\langle\psi_0|\hat{\mu}^{\text{tot}}_{\alpha}|\psi_n\rangle\langle\psi_n|\hat{m}^{\text{tot}}_{\beta}|\psi_0\rangle\right]}{\omega^2_{n0} - (\omega + i\Gamma)^2} \tag{6.15b}$$

where $\hat{\theta}^{\text{tot}}$ and $\hat{m}^{\text{tot}}$ are the total DIM/QM quadrupole and magnetic dipole operators respectively.

In DIM/QM, only the dipole operator is modified by the local fields. However, the $A$- and $G'$-tensors depend on the dipole operator and the choice of origin. $\hat{\theta}^{\text{tot}}$ and $\hat{m}^{\text{tot}}$ are therefore modified as

$$\hat{\theta}^{\text{tot}}_{\alpha\beta} = \hat{\theta}^{\text{QM}}_{\alpha\beta} + \frac{3}{2}R_\beta \hat{V}^{\text{loc}}_\alpha + \frac{3}{2}R_\alpha \hat{V}^{\text{loc}}_\beta - \delta_{\alpha\beta}R_\gamma \hat{V}^{\text{loc}}_\gamma \tag{6.16}$$

$$\hat{m}^{\text{tot}}_\alpha = \hat{m}^{\text{QM}}_\alpha - \frac{\omega}{2}\epsilon_{\alpha\beta\gamma}R_\beta \hat{V}^{\text{loc}}_\gamma \tag{6.17}$$

where $\mathbf{R}$ is the vector describing the molecule's center-of-nuclear-charge.

However, magnetic properties (such as $G'$) become origin-dependent under incomplete basis sets. Origin-invariant magnetic properties may be obtained using gauge-including atomic orbitals (GIAOs), which include a magnetic field-dependent phase factor.[320–322] Alternatively, response calculations may be performed in the velocity gauge[323,324] by employing the modified velocity gauge (MVG) formalism of Pedersen and co-workers.[325] In MVG, the static limit of the velocity gauge response needs to be subtracted from the frequency-dependent limit as[325]

$$\langle\langle \hat{A}^{LG}; \hat{B}^{LG} \rangle\rangle_\omega = \frac{1}{\omega^2}\left[\langle\langle \hat{A}^{VG}; \hat{B}^{VG} \rangle\rangle_\omega - \langle\langle \hat{A}^{VG}; \hat{B}^{VG} \rangle\rangle_0\right] \tag{6.18}$$

where $\hat{A}^{LG}$ and $\hat{B}^{LG}$ are general LG operators and $\hat{A}^{VG}$ and $\hat{B}^{VG}$ are their corresponding velocity gauge (VG) representations. When considering the finite lifetime of the excited states, the response tensors are complex and the MVG expression becomes

$$\langle\langle \hat{A}^{LG}; \hat{B}^{LG} \rangle\rangle_{\omega+i\Gamma} = \frac{1}{(\omega+i\Gamma)^2}\left[\langle\langle \hat{A}^{VG}; \hat{B}^{VG} \rangle\rangle_{\omega+i\Gamma} - \langle\langle \hat{A}^{VG}; \hat{B}^{VG} \rangle\rangle_0\right] \tag{6.19}$$

The derivation of the MVG expressions within damped response theory is described in Appendix F.

For consistency, we formulate all DIM/QM response tensors in the MVG formalism. The VG dipole operator of the molecule-nanoparticle complex is

$$\hat{\mu}^{\text{tot,VG}}_\alpha(\omega) = \hat{\nabla}^{\text{QM}}_\alpha + \hat{V}^{\text{loc,VG}}_\alpha(\omega) \tag{6.20}$$

where $\hat{V}^{\text{loc,VG}}$ is the VG form of the local field operator, defined as

$$\hat{V}^{\text{loc,VG}}(r,\omega) = \frac{1}{2}\left(\hat{\nabla}^2 \hat{V}^{\text{loc,LG}}(r,\omega)\right) + \left(\hat{\nabla}_\alpha \hat{V}^{\text{loc,LG}}(r,\omega)\right)\hat{\nabla}_\alpha \tag{6.21}$$

The operators $\hat{\theta}^{\text{VG}}$ and $\hat{m}^{\text{VG}}$ may be found in ref. 324. See Appendix F for derivation of $\hat{V}^{\text{loc,VG}}$. The total quadrupole and magnetic dipole VG operators ($\hat{\theta}^{\text{tot,VG}}$ and $\hat{m}^{\text{tot,VG}}$) are also modified by the local fields using eqs. 6.16 and 6.17 and $\hat{V}^{\text{loc,VG}}$. The MVG polarizability tensors can now be written using $\hat{\mu}^{\text{tot,VG}}$, $\hat{\theta}^{\text{tot,VG}}$, and $\hat{m}^{\text{tot,VG}}$ and using eq. 6.19. This MVG implimentation of DIM/QM therefore allows us to simulate gauge-invariant SEROA.

### 6.2.3 Dressed-tensors formalism

We extend the dressed-tensors formalism of Janesko and Scuseria[215] to include the quadrupoles induced by an electric field, gradient and magnetic field. This is an extension of a formalism that we recently presented to describe SERS due to inhomogeneous local fields.[258] We start by considering the dipole induced in the molecule due to all perturbing electric field, electric field gradient, and magnetic field. The dipole induced in the molecule is

$$\mu_\alpha^{\text{ind}} = \alpha_{\alpha\beta} E_\beta^{\text{in}} + \alpha_{\alpha\beta} E_\beta^{\text{loc}}(\mathbf{E}^{\text{in}}) + \frac{1}{3} A_{\alpha,\beta\gamma} E_{\beta\gamma}'^{\text{in}} + \frac{1}{3} A_{\alpha,\beta\gamma} E_{\beta\gamma}'^{\text{loc}}(\mathbf{E}^{\text{in}}) + G'_{\alpha\beta} B_\beta^{\text{in}} \tag{6.22}$$

where $\alpha$, $A$ and $G'$ are the electric dipole-dipole, electric dipole-quadrupole and electric dipole-magnetic dipole polarizabilities, respectively. $E$, $E'$ and $B$ are the perturbing electric field, electric field gradient, and magnetic field. The superscripts "in" and "loc" refer to the fields from the incident laser or the plasmonic local fields. Similarly, the induced quadrupole may be written as

$$\theta_{\alpha\beta}^{\text{ind}} = \mathscr{A}_{\gamma,\alpha\beta} E_\gamma^{\text{in}} + \mathscr{A}_{\gamma,\alpha\beta} E_\gamma^{\text{loc}}(\mathbf{E}^{\text{in}}) + \frac{1}{3} C_{\alpha\beta,\gamma\delta} E_{\gamma\delta}'^{\text{in}} + \frac{1}{3} C_{\alpha\beta,\gamma\delta} E_{\gamma\delta}'^{\text{loc}}(\mathbf{E}^{\text{in}}) + D_{\alpha\beta,\gamma} B_\gamma^{\text{in}} \tag{6.23}$$

and where $\mathscr{A}$, $C$ and $D$ are the electric quadrupole-dipole, electric quadrupole-quadrupole, and electric quadrupole-magnetic dipole polarizabilities, respectively.

The local fields, for a dipolar substrate, depend only on the incident electric field and may be defined as

$$E_\alpha^{\text{loc}}(E_\beta^{\text{in}}) = T_{\alpha\gamma}^{(2)}(\mathbf{R}) \alpha_{\gamma\beta}^{\text{NP}}(\omega_I) \tag{6.24a}$$

$$= E_\alpha^\beta(\mathbf{R}, \omega_I) \tag{6.24b}$$

$$E_{\alpha\beta}'^{\text{loc}}(E_\gamma^{\text{in}}) = T_{\alpha\beta\delta}^{(3)}(\mathbf{R}) \alpha_{\delta\gamma}^{\text{NP}}(\omega_I) \tag{6.25a}$$

$$= F_{\alpha\beta}^\gamma(\mathbf{R}, \omega_I) \tag{6.25b}$$

where $\alpha^{\text{NP}}(\omega_I)$ is the polarizability of the nanoparticle at the incident frequency $\omega_I$, and $\mathbf{R}$ is the vector describing the separation of the nanoparticle and the molecule. $T^{(x)}$ are the interaction tensors defined as $T^{(x)}(\mathbf{R}) = \nabla^x(1/|\mathbf{R}|)$.[123]

The dipoles and quadrupoles induced in the molecule may also induce dipoles in the plasmonic nanoparticle at the Raman-shifted frequency $\omega_S$. Therefore, the total dipole induced in the molecule-nanoparticle complex oscillating at $\omega_S$ is

$$\mu_\alpha^{\text{tot}} = \mu_\alpha^{\text{ind}} + \alpha_{\alpha\beta}^{\text{NP}}(\omega_S) T_{\beta\gamma}^{(2)}(\mathbf{R}) \mu_\gamma^{\text{ind}} + \frac{1}{3} \alpha_{\alpha\beta}^{\text{NP}}(\omega_S) T_{\beta\gamma\delta}^{(3)}(\mathbf{R}) \theta_{\gamma\delta}^{\text{ind}} \tag{6.26a}$$

$$= \mu_\alpha^{\text{ind}} + E_\beta^\alpha(\mathbf{R}, \omega_S)\mu_\beta^{\text{ind}} + \frac{1}{3}F_{\beta\gamma}^\alpha(\mathbf{R}, \omega_S)\theta_{\beta\gamma}^{\text{ind}} \tag{6.26b}$$

For simplicity, we will define $F_\beta^\alpha = \delta_{\alpha\beta} + E_\beta^\alpha$ and assume $\alpha^{\text{NP}}(\omega_S) \sim \alpha^{\text{NP}}(\omega_I)$. This allows us to ignore the frequency dependence of $F$. The complete expression for the total induced dipoles becomes

$$\begin{aligned}\mu_\alpha^{\text{tot}} = &\left(F_\gamma^\alpha \alpha_{\gamma\delta} F_\delta^\beta + \frac{1}{3}F_\gamma^\alpha A_{\gamma,\delta\epsilon}F_{\delta\epsilon}^\beta + \frac{1}{3}F_{\gamma\delta}^\alpha \mathscr{A}_{\epsilon,\gamma\delta}F_\epsilon^\beta + \frac{1}{9}F_{\gamma\delta}^\alpha C_{\gamma\delta,\epsilon\zeta}F_{\epsilon\zeta}^\beta\right)E_\beta^{\text{in}} \\ &+ \frac{1}{3}\left(F_\delta^\alpha A_{\delta,\beta\gamma} + \frac{1}{3}F_{\delta\epsilon}^\alpha C_{\delta\epsilon,\beta\gamma}\right)E_{\beta\gamma}^{'\text{in}} \\ &+ \left(F_\gamma^\alpha G'_{\gamma\beta} + \frac{1}{3}F_{\gamma\delta}^\alpha D_{\gamma\delta,\beta}\right)B_\beta^{\text{in}}\end{aligned} \tag{6.27}$$

We may now consider the dressed electric dipole-dipole polarizability $\alpha_{\alpha\beta}^D$, which describes the total dipoles induced in the $\alpha$ direction due to an incident electric field in the $\beta$ direction. This is found as

$$\alpha_{\alpha\beta}^D = F_\gamma^\alpha \alpha_{\gamma\delta} F_\delta^\beta + \frac{1}{3}F_\gamma^\alpha A_{\gamma,\delta\epsilon}F_{\delta\epsilon}^\beta + \frac{1}{3}F_{\gamma\delta}^\alpha \mathscr{A}_{\epsilon,\gamma\delta}F_\epsilon^\beta + \frac{1}{9}F_{\gamma\delta}^\alpha C_{\gamma\delta,\epsilon\zeta}F_{\epsilon\zeta}^\beta \tag{6.28}$$

Similarly, we take $A_{\alpha,\beta\gamma}^D$ to describe the total dipoles induced in the $\alpha$ direction due to an incident electric field gradient in the $\beta\gamma$ directions, and $G_{\alpha\beta}^{'D}$ to describe the total dipoles induced in the $\alpha$ direction due to an incident magnetic field in the $\beta$ direction. These dressed tensors are found as

$$A_{\alpha,\beta\gamma}^D = F_\delta^\alpha A_{\delta,\beta\gamma} + \frac{1}{3}F_{\delta\epsilon}^\alpha C_{\delta\epsilon,\beta\gamma} \tag{6.29}$$

$$G_{\alpha\beta}^{'D} = F_\gamma^\alpha G'_{\gamma\beta} + \frac{1}{3}F_{\gamma\delta}^\alpha D_{\gamma\delta,\beta} \tag{6.30}$$

We can also make the far from resonance approximation for the molecular polarizability tensors: $A_{i,jk} = \mathscr{A}_{i,jk}$, $C_{ij,kl} = C_{kl,ij}$, $G'_{ij} = -\mathscr{G}_{ji}$, and $D_{ij,k} = -\mathscr{D}_{k,ij}$, which (along with $\alpha^{\text{NP}}(\omega_I) \sim \alpha^{\text{NP}}(\omega_{\text{S}})$) leads to $A_{i,jk}^D = \mathscr{A}_{i,jk}^D$ and $G_{ij}^{'D} = -\mathscr{G}_{ji}^D$. As such, the SEROA intensity of the complex may be found using FFR theory in eq. 6.1 and the dressed polarizability tensors.

The dressed-tensors formalism in eqs. 6.28–6.30 are all origin-dependent, since the tensors $A$, $G'$, $\mathscr{A}$, $C$, and $D$ all depend on the choice of origin. However, we have found that a Taylor expansion of the local fields about the origin of the molecular frame (see ref. 258) accounting for the translation of some reference point (the CoNC in this case) leads to origin-invariant dressed tensors. This expansion is equivalent to defining the molecular origin as the CoNC. We have included the origin-dependence of the $C$- and $D$-tensors in Appendix F.

We also wish to point out that the electric field due to a point quadrupole is of the same order as the electric field gradient due to a point dipole, since both involve the $T^{(3)}$ interaction tensor. As such, a quadrupolar expansion of the molecule must be considered when accounting for the local electric field gradient. In this chapter, we will not generally differentiate between these two mechanisms, and may use either term to collectively describe them.

## 6.3 Computational Details

All calculations presented in this work were performed using a local version of the Amsterdam Density Functional (ADF) program package.[165,224,326] The Becke-Perdew (BP86) XC-potential[153,154] and a triple-$\zeta$ Slater-type basis set with two polarization functions (TZ2P) from the ADF basis set library were used unless stated otherwise. The vibrational frequencies and normal modes were calculated numerically within the harmonic approximation, where the BP86 functional results in harmonic frequencies of small molecules close to experimental results without the use of scaling factors[225]. Frequency dependent response tensors were calculated using a modified version of the AOResponse module implemented in ADF, with an excited state lifetime of $\Gamma = 0.1$ eV[50,63,111,225,226]. Tensor derivatives were calculated by numerical three-point differentiation with respect to Cartesian displacements. All simulated spectra have been broadened by a Lorentzian with a full-width at half-maximum (fwhm) of 20 $cm^{-1}$.

Nanoparticles in this chapter, unless stated otherwise, have been simulated using the discrete interaction model (DIM)[141,142], which treats the nanoparticle atomistically using classical electrodynamics. Icosahedral structures, which approximates spherical nanoparticles, were built from silver (111) unit cells. In this chapter, the polarizability interaction model (PIM) flavor of DIM was used, where the system is described as a collection of interacting polarizabilities. The frequency-dependent complex dielectric function of silver was obtained from Johnson and Christy[227].

## 6.4 Results and Discussion

### 6.4.1 SEROA with DIM/QM

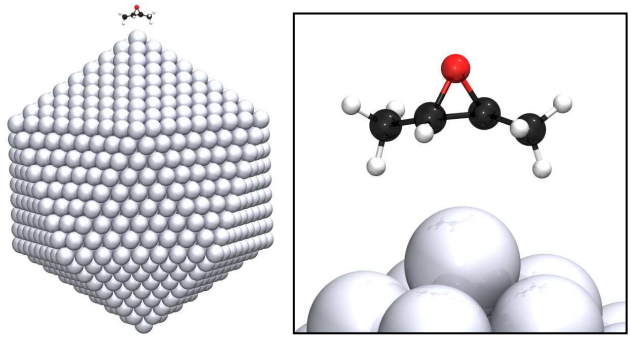

**Figure 6.1.** Orientation of (2S,3S)-*trans*-dimethyloxirane (DMO) on a $Ag_{2057}$ icosahedron. The distance between the CoNC of DMO and the nearest silver atom is 4.0 Å (7.6 $a_0$). The $Ag_{2057}$ cluster is ∼4 nm in diameter.

In order to test the origin-invariance of the DIM/QM calculated spectra, we examined the SEROA of (2S,3S)-*trans*-dimethyloxirane (DMO) on a $Ag_{2057}$ cluster for the molecule

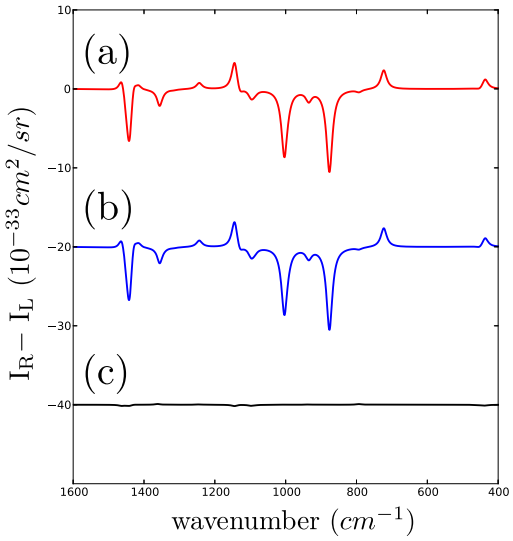


**Figure 6.2.** The SEROA of DMO on a $Ag_{2057}$ cluster excited at 343 nm for the molecule *(a)* at the center of nuclear charge, and *(b)* translated a vector (5,3,1) Å, calculated using MVG. The spectrum in *c* is the difference between *a* and *b*. Spectra have been offset for clarity.

centered at its center of nuclear charge (CoNC) (see Figure 6.1 for orientation) and for the same system translated a vector (5,3,1) Å. The system was excited at 343 nm, which is the DIM simulated plasmon resonance of the silver cluster chosen, and would therefore produce the largest enhancements to the SERS and SEROA spectra. The SEROA of these systems are presented in Figure 6.2, where the Figure 6.2*a* is the CoNC SEROA and Figure 6.2*b* is the SEROA of the translated complex. Figure 6.2*c* is the difference between these two spectra, which clearly shows that the calculated spectra are origin-invariant (a requirement of any observable), even though the individual tensor components of $A$ and $G'$ remain origin-dependent. Origin-invariance is obtained through mutual cancellation of origin-dependent contributions.

Figure 6.3 shows the SEROA of DMO on $Ag_{2057}$ calculated using DIM/QM with and without local field enhancements. The DIM/QM spectrum in Figure 6.3*a* contains only the "image field" effect, which accounts for the mutual polarization of the two sub-systems. This results in minor changes to the ROA spectrum. The local field contribution on the other hand (Figure 6.3*b*), commonly referred to as the electromagnetic (EM) enhancement mechanism in SERS, results in large enhancements of the ROA signal. The current implementation of DIM/QM ignores most effects related to the "chemical mechanism". The small "image field" effect along with an absence of chemical effects, suggests that the dressed-tensors formalism should agree with the results simulated using DIM/QM, providing that an acceptable multipolar expansion of the molecule is considered.

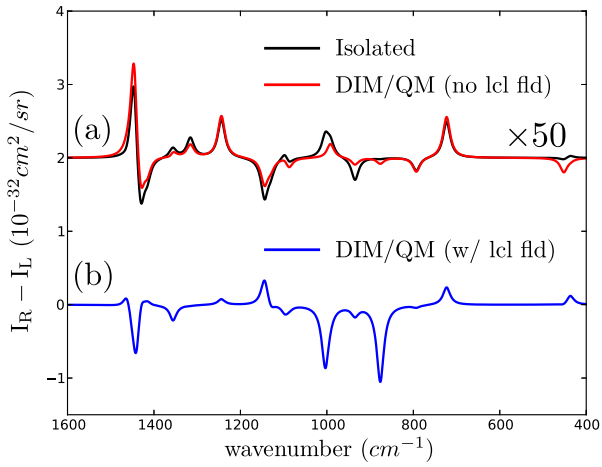


**Figure 6.3.** The *(a)* ROA and SEROA of DMO on $Ag_{2057}$ without enhancement from local fields, and *(b)* with enhancements from local fields.

### 6.4.2 SEROA using dressed tensors

In order to test the quadrupolar expansion of the dressed-tensors formalism, we simulate the SEROA of DMO on $Ag_{2057}$ (orientation the same as in Figure 6.1) with dressed tensors and compare it to the results obtained using DIM/QM. These results are shown in Figure 6.4, where we graph the unenhanced ROA (Figure 6.4*a*), the dressed-tensors dipolar-expansion (Figure 6.4*b*), the dressed-tensors quadrupolar expansion (Figure 6.4*c*), and the DIM/QM (Figure 6.4*d*) simulated SEROA of DMO. For a small molecule like DMO, the dressed-tensors formalism reproduces the DIM/QM spectrum reasonably well once the field-gradient (quadrupolar) contributions are taken into consideration. This suggests that even for a molecule as small as DMO, one needs to consider a quadrupolar expansion as well as the inhomogeneous nature of the local electric field to correctly simulate the response of the system.

Since the dressed-tensors formalism may be used to accurately describe the SEROA of DMO, we used it to explore a number of SERS and SEROA phenomena. One such application is exploring the effects of orientational averaging due to strong local fields. Janesko and Scuseria have explored the effects of the chemical mechanism on orientationally averaged SEROA.[311] In that paper, they showed that the chemical effect leads to a weakening of SEROA intensities when compared to those of a fixed molecule-substrate orientation. We observe the same effects in SEROA due to the EM mechanism both with and without field-gradient effects. Because the SEROA mode selectivity and intensity signs all depend on the specific molecule/nanoparticle orientation, we define the SERS and SEROA enhancement factors as

$$EF^{\text{SERS/SEROA}} = \frac{\sum_p |I_p^{\text{SERS/SEROA}}|}{\sum_p |I_p^{\text{NRS/ROA}}|} \tag{6.31}$$

where $p$ sums over all modes in the region of the molecule under consideration (400-1800 $cm^{-1}$).

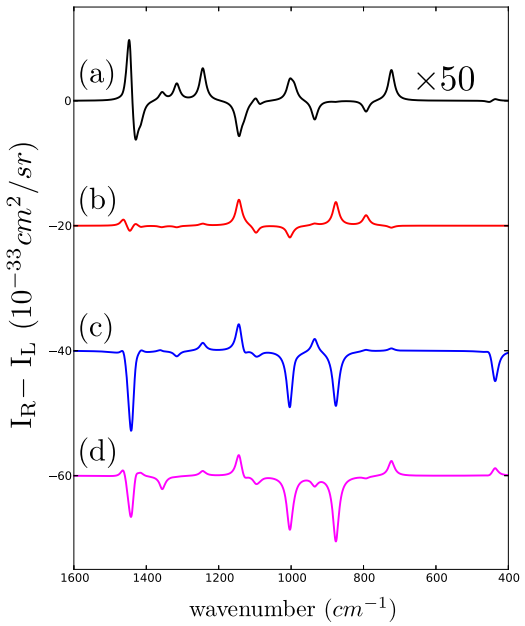


**Figure 6.4.** The ROA ($a$), and the SEROA ($b$, $c$ and $d$) spectra of (2S,3S)-*trans*-DMO on a $Ag_{2057}$ cluster excited at 343 nm. The spectra in $b$ and $c$ were simulated using the dressed-tensors formalism, where $b$ neglects all terms due to a local electric field-gradient. The spectrum in $d$ was simulated using DIM/QM with the same substrate and orientation as the complexes in $b$ and $c$.

In orientational averaging, we assume that the molecule may bind in any orientation with respect to the surface with equal probability of sampling all orientations. Figure 6.5 shows the SERS enhancements as a function of the separation of the molecule and nanoparticle for both a fixed-orientation and orientationally-averaged molecule, while Figure 6.6 shows the same for the SEROA enhancements. From Figure 6.5, we observe that both the inclusion of the field-gradient effects as well as orientational averaging lead to larger SERS enhancement. This is expected since the field-gradient effect leads to relaxed Raman selection rules,[35–38,258] leading to more modes becoming Raman-active. The effect is increased upon orientational averaging since it allows more orientations to be sampled where specific modes are preferentially enhanced. For SEROA, however, we observe that while a fixed orientation leads to SEROA signals that are more intense than those of unenhanced ROA, the changes in mode signs and intensities lead to weakened SEROA intensities upon orientational averaging (compared to the intensities of a fixed-orientation). This effect is independent of the nature of the local electric field or multipolar expansion assumed for the molecule. We also observe $EF^{\mathrm{SEROA}} < 1$ (SEROA intensities that are weaker than unenhanced ROA, see Figure 6.6) upon orientational averaging. These weakening factors are found for orientationally averaged systems with very small perturbing local electric fields, and results from sign changes in the SEROA intensity for different orientations. The results show that, like the chemical mechanism[311], the EM enhancement mechanism also results in weaker SEROA intensities upon orientational averaging. Therefore, SEROA experiments should be performed on fixed-orientation molecules to maximize observed intensities.

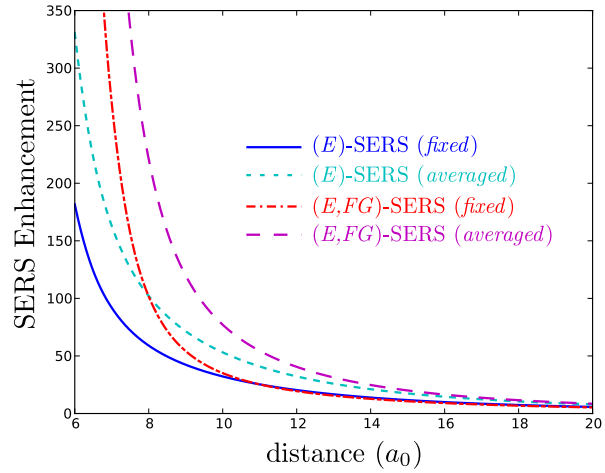


**Figure 6.5.** The SERS enhancement for DMO on $Ag_{2057}$ as a function of the separation of the molecule from the nanoparticle. Enhancement shown for fixed orientation (*fixed*) and orientationally averaged (*averaged*) systems, assuming a homogeneous local electric field ($E$) or a local electric field and gradient ($E$,$FG$). The $x$-axis measures the separation of the CoNC and the nearest silver atom (in atomic units).

Figures 6.5 and 6.6 also give us insight into the SERS and SEROA enhancement factor dependence on the local field gradient magnitudes. It is well established[41,119,213] that the SERS enhancement may be approximated as $|E|^4$, where $E$ is the local field enhancement. Similarly, using the terms from the dressed-tensors and DIM/QM formalisms, one obtains an approximate SEROA enhancement factor of $E^3$. Because the field gradient varies with the distance $R$ from the surface as $R^{-4}$, the SERS enhancement dependence on the field gradient varies as $R^{-16}$, whereas the SEROA field gradient enhancement varies as $R^{-12}$. This implies that the field gradient is only significant in SERS for molecules very close to the nanoparticle surface, while in SEROA, the field gradient has a greater effect over larger distances. For fixed orientation DMO separated 16 $a_0$ (8.5 Å) from the $Ag_{2057}$ cluster, we observe significant contribution to the SEROA from the field gradients but vanishingly small contributions to the SERS spectrum. These relationships change with orientational averaging, where we observe that most field gradient effects in SEROA are negated upon averaging.

### 6.4.3 SEROA dependence on plasmon width

For simplicity, we have so far used the $\omega_S = \omega_I$ approximation, which is valid for broad plasmons. If we consider the change in the polarizability of the nanoparticle at the incident and Raman-shifted frequencies (which is especially important for nanoparticles with narrow plasmon widths), then the FFR ROA theory is no longer applicable. Even if we are not exciting (near) a molecular transition, using $\alpha^{NP}(\omega_S) \neq \alpha^{NP}(\omega_I)$ results in different dressed Roman- and script-type polarizability transition tensors. Under these conditions, we therefore apply the unrestricted ROA formalism outlined by Nafie[314]. For backscattered Raman and ICP-ROA, these unrestricted intensities are given by

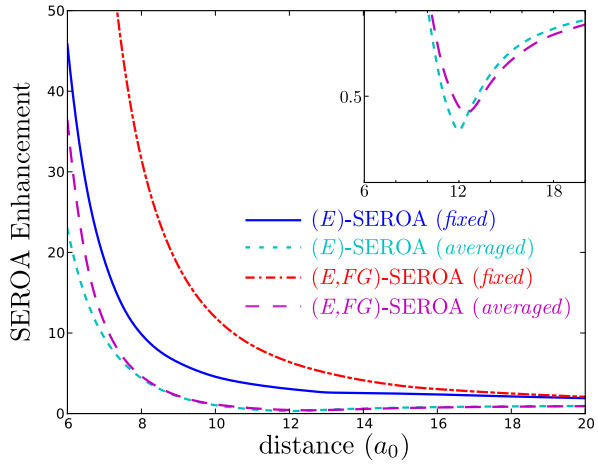


**Figure 6.6.** The SEROA enhancement for DMO on $Ag_{2057}$ as a function of the separation of the molecule from the nanoparticle. Enhancement shown for fixed orientation (*fixed*) and orientationally averaged (*averaged*) systems, assuming a homogeneous local electric field ($E$) or a local electric field and gradient ($E$,$FG$). The inset shows the enhancement region between 0–1 (weakening) that occurs for an orientationally averaged system.

$$I_p^R(\pi) + I_p^L(\pi) = K_p \left[ \frac{45\alpha_p^2 + 7\beta_S(\alpha)_p^2 + 5\beta_A(\alpha)_p^2}{45} \right] \tag{6.32}$$

$$\begin{aligned} I_p^R(\pi) - I_p^L(\pi) = \frac{K_p}{45c} \big[ & 90\alpha G'_p + 14\beta_S(G')_p^2 + 10\beta_A(G')_p^2 + 2\beta_S(A)_p^2 - 2\beta_A(A)_p^2 \\ & +90\alpha\mathscr{G}_p - 10\beta_S(\mathscr{G})_p^2 + 10\beta_A(\mathscr{G})_p^2 + 6\beta_S(\mathscr{A})_p^2 - 2\beta_A(\mathscr{A})_p^2 \big] \end{aligned} \tag{6.33}$$

where the symmetric ($\beta_S$) and anti-symmetric ($\beta_A$) anisotropic invariants are all defined in ref. 314.

The dressed-tensors formalism allows us to easily account for the changes in the nanoparticle's polarizability, and we are able to define dressed Roman- and script-type tensors as

$$A^D_{\alpha,\beta\gamma} = F^\alpha_\delta(\omega_S) A_{\delta,\beta\gamma} + \frac{1}{3} F^\alpha_{\delta\epsilon}(\omega_S) C_{\delta\epsilon,\beta\gamma} \tag{6.34a}$$

$$\mathscr{A}^D_{\alpha,\beta\gamma} = \mathscr{A}_{\delta,\beta\gamma} F^\alpha_\delta(\omega_I) + \frac{1}{3} C_{\beta\gamma,\delta\epsilon} F^\alpha_{\delta\epsilon}(\omega_I) \tag{6.34b}$$

$$G'^D_{\alpha\beta} = F^\alpha_\gamma(\omega_S) G'_{\gamma\beta} + \frac{1}{3} F^\alpha_{\gamma\delta}(\omega_S) D_{\gamma\delta,\beta} \tag{6.35a}$$

$$\mathscr{G}^D_{\alpha\beta} = \mathscr{G}_{\alpha\gamma} F^\beta_\gamma(\omega_I) + \frac{1}{3} \mathscr{D}_{\alpha,\gamma\delta} F^\beta_{\gamma\delta}(\omega_I) \tag{6.35b}$$

We may still assume that there are no molecular transitions near the excitation frequency, where

the FFR equalities hold true for the "undressed" molecular tensors ($A_{i,jk} = \mathscr{A}_{i,jk}$, $C_{ij,kl} = C_{kl,ij}$, $G'_{ij} = -\mathscr{G}_{ji}$, and $D_{ij,k} = -\mathscr{D}_{k,ij}$).

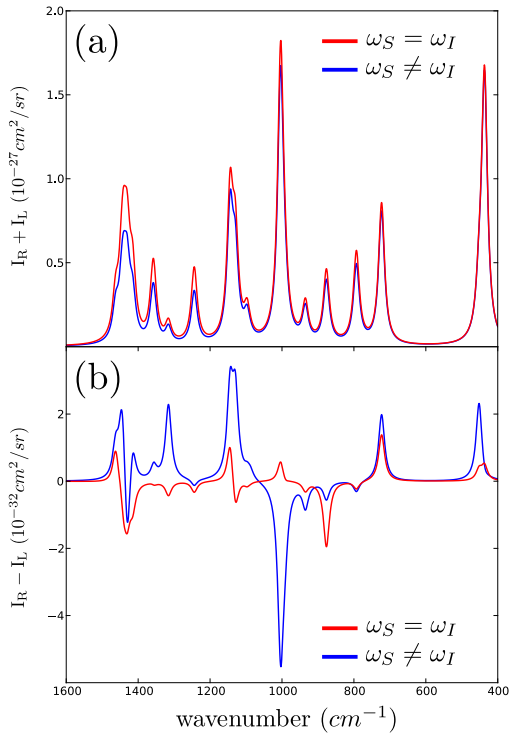


**Figure 6.7.** The difference in ($a$) SERS and ($b$) SEROA of DMO accounting for the difference in polarizability of the substrate at $\omega_I$ and $\omega_S$ for a plasmon fwhm of 0.5 eV.

We used these dressed tensors and the unrestricted equations to simulate the SERS and SEROA of DMO using a Drude model for the plasmon of a dipolar sphere. The model plasmon has a fwhm of 0.5 eV and we excite the system at the plasmon resonance (343 nm or 3.61 eV). We simulate the SERS and SEROA under two conditions: the first assumes that $\omega_S = \omega_I$, and the second accounts for the difference in $\omega_S$ and $\omega_I$. The results show that the effects are negligible in SERS (see Figure 6.7$a$), with the intensities at higher wavenumbers being less enhanced (the scattered fields are only weakly able to excite the plasmons). However, the results are much more complex for SEROA (Figure 6.7$b$). We find that spectrum looks very different when accounting for the plasmon width. This difference is seen at both low and high wavenumbers with changes in both intensity and sign of individual modes. In general, we see that accounting for the difference in incident and Raman-shifted frequencies resulted in a general increase in the SEROA intensities, this is the opposite of what is observed in SERS. This is because the Roman- and script-type tensors are different; the Roman-type tensors (describing the dipoles due to an incident field gradient or magnetic field) are enhanced at $\omega_S$, whereas the script-type tensors (describing the quadrupoles or magnetic dipoles due to an incident electric field) are enhanced at $\omega_I$. These differences mean that there is not a perfect cancellation of terms in the unrestricted formalism and

the larger intensities are due to the additional terms that are not present in the FFR equation. This effect, therefore, is specific to the scattering geometry, molecule and its orientation, and the plasmon width, and would require careful control when trying to reproduce experimental data.

### 6.4.4 SEROA of bromohexahelicene

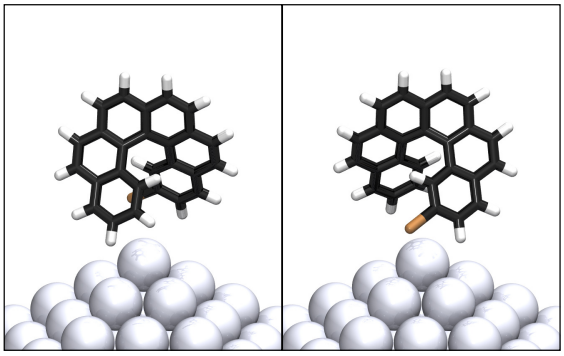

**Figure 6.8.** The orientation of (+)2Brhh *(left)* and (-)2Brhh *(right)* on the $Ag_{21k}$ cluster.

To test the limitations of our two methods, we simulated the SEROA of the two enantiomers of 2-Bromohexahelicene (2Brhh) on a 10 nm diameter (21127 atoms) silver icosahedron (Figure 6.8 shows their respective orientations). We chose 2Brhh because simulations of its ROA were recently shown to reproduce experimental results quite accurately[327] (see Figure F.1 in Appendix F for the ROA of (+/-)2Brhh). Additionally, observing mirror-image SEROA for enantiomers has been an on-going experimental challenge. We aim to add to this discussion by simulating the SEROA of both enantiomers of 2Brhh on silver nanoparticles. The DIM/QM simulations also demonstrate the method's ability to simulate the SEROA of a medium-sized molecule on a realistically-sized nanoparticle with atomic resolution.

Figure 6.9 shows SEROA simulation of the enantiomers of 2Brhh on $Ag_{21127}$ using the dressed-tensors (Figure 6.9*a*) and DIM/QM (Figure 6.9*b*) methods. We observe large differences in total SEROA intensities using the three methods. The dressed-tensors dipolar approximation resulted in intensities that are $\sim 55$ times weaker than those from the DIM/QM method. The dressed-tensors quadrupolar approximation, while producing relative intensities that are very similar, resulted in a two-fold increase in intensities over those from the dipolar approximation. This implies that both terms contribute about equally to the total SEROA intensities. However, the large intensity differences between the dressed-tensors and DIM/QM methods suggest that higher order multipoles need to be considered for a medium-sized molecule like 2Brhh. Such expansions would require higher order polarizability responses in its dressed-tensors expression, which would quickly become infeasible. For such systems, a method that considers the entire charge density of the molecule (like DIM/QM) is required.

Even though the dressed tensors resulted in spectra that are an order of magnitude different from those by DIM/QM, the two methods still reproduced spectra with similar relative intensities in the 1200 and 1350 $cm^{-1}$ regions. The major observed differences are the shift in vibrational

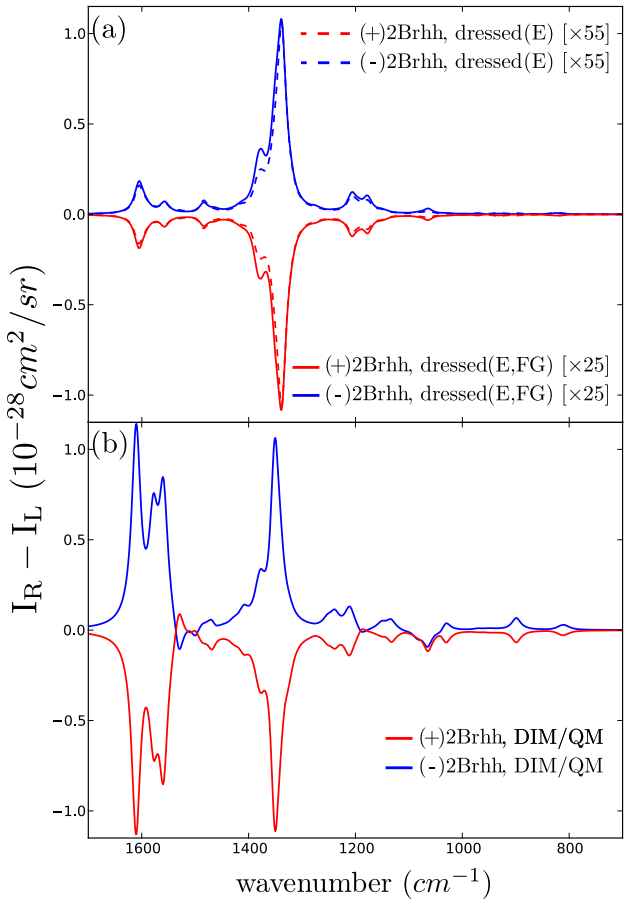


**Figure 6.9.** SEROA of (+/-)2Brhh simulated using (*a*) the dressed tensors with (solid lines) and without (dashed lines) the quadrupolar expansion, and (*b*) the DIM/QM method.

frequencies (caused by the molecule interacting with the surface through the DIM/QM force field[144]), the large intensities of the three modes $\sim 1600$ cm$^{-1}$, and the break in mirror-image SEROA for the two enantiomers at $\sim 1070$ cm$^{-1}$. The modes at 1065 and 1084 cm$^{-1}$ are in-plane C-H bending modes in the region near the bromine atom, whereas the modes at 1559, 1578 and 1611 cm$^{-1}$ are all C-C stretches. The changes in relative intensities observed for these modes are due to the geometry changes caused by the DIM/QM force field. We explored the effects of these geometry changes by considering the ROA of the DIM/QM optimized 2Brhh, while ignoring polarization and plasmonic effects from the DIM system. The results (see Figure F.2 in Appendix F) show large changes in the relative intensities of these modes when compared to the modes $\sim 1350$ cm$^{-1}$ and to the corresponding modes in the gas-phase optimized structure.

The spectra in Figure 6.9 all produced (near) mirror-image SEROA for the two enantiomers of 2Brhh. We may further explore the limitations of observing mirror-image SEROA for enantiomers due to the EM mechanism using the dressed-tensors formalism. This is important since mirror-image SEROA of enantiomers have not yet been shown experimentally. We have found that mirror-

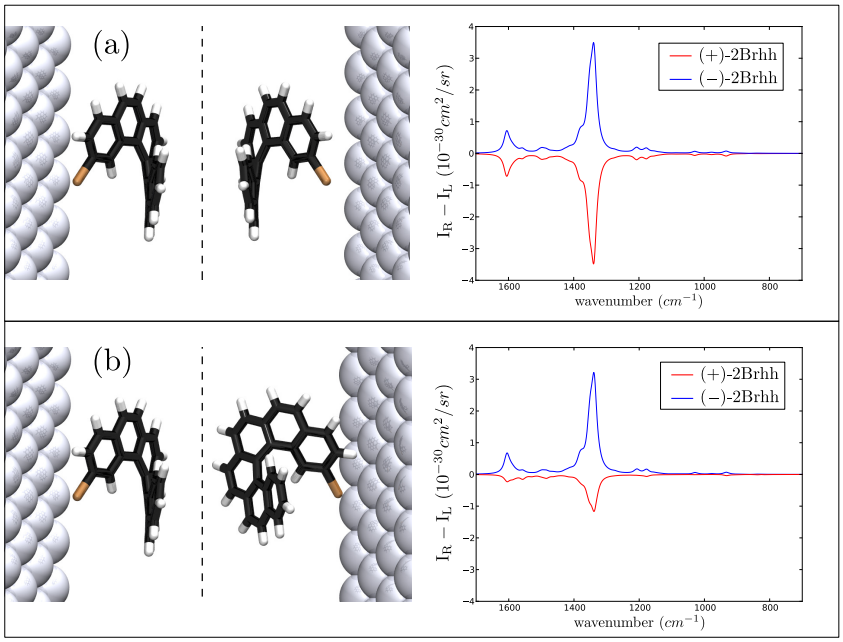


**Figure 6.10.** SEROA for the two enantiomers of 2Brhh on a flat surface calculated using the dressed-tensors formalism for *(a)* structures that preserve mirror symmetry, and *(b)* structures that break mirror symmetry. The (+)-2Brhh enantiomer in *b* has been rotated an Euler angle $(15°, 15°, 15°)$ compared to that in *a*.

image SEROA may only be observed when the mirror symmetry for the molecule-nanoparticle complex is preserved. We show an example of this in Figure 6.10, where we simulate the SEROA of the two enantiomers of 2Brhh on a flat surface. To model the flat surface, we considered an electric field and gradient component perpendicular to the surface. The orientations shown in Figure 6.10*a* preserves mirror symmetry and results in mirror-image SEROA. Any deviation from such orientations or change in the local electric field strengths for one enantiomer but not the other leads to a break in the mirror symmetry of the complex and very different SEROA spectra, as shown in Figure 6.10*b* where the (+)-2Brhh enantiomer was rotated through a small Euler angle of $(15°, 15°, 15°)$. These results imply that in order to observe mirror-image SEROA, one needs to ensure that the molecules of both enantiomers bind in geometries that preserves their mirror symmetry on surfaces that supports local electric fields that are (near) identical. These experimental conditions are difficult to fulfill, giving us some insight into why observing mirror-image SEROA for enantiomers continues to be a challenge.

## 6.5 Conclusion

In conclusion, we have developed two methods to simulate SEROA which go beyond the point-dipole approximation of the molecule. The first is a point-dipole and point-quadrupole dressed-

tensors approximation which is valid for small molecules, but which fails to describe the SEROA of large molecules. The second DIM/QM method describes the molecule as a complete charge distribution, while accounting for an atomistic description of the nanoparticle, and may be used for large molecules and nanoparticles. The DIM/QM method have been implemented using the MVG so as to ensure gauge-invariant results. We have used these methods to explore some phenomena as it relates to SEROA, and have found that for a fixed orientation, the field-gradients induces significant change in the SEROA spectrum and are effective over larger surface-molecule separation than in SERS, but these effects are minimized with orientational averaging. We also showed that orientational averaging and the EM mechanism leads to weakened SEROA intensities, and may even lead to SEROA intensities that are weaker than those of unenhanced ROA. We have found that the SEROA mode intensities and signs are highly sensitive to the molecular orientation, local electric field and gradient strengths, and plasmon widths, all of which makes experimental SEROA challenging.

# Chapter 7

# Plasmonic Circular Dichroism of 310- and alpha-Helix Using a Discrete Interaction Model / Quantum Mechanics Method

Chulhai, D. V; Jensen, L. "*Plasmonic Circular Dichroism of 310- and α-Helix Using a Discrete Interaction Model / Quantum Mechanics Method*" *J. Phys. Chem. A* **2014**, *119*, 5218–5223

## Abstract

Plasmonic circular dichroism (CD) of chiral molecules in the near field of plasmonic nanoparticles (NPs) may be used to enhance molecular CD signatures or to induce a CD signal at the plasmon resonance. A recent few-states theory explored these effects for model systems, and showed an orientation-dependence of the sign of the induced CD signal for spherical NPs. Here, we use the discrete interaction model / quantum mechanical (DIM/QM) method to simulate the CD and plasmonic CD of the $3_{10}$- and $\alpha$-helix conformations of a short alanine peptide. We find that the interactions between the molecule and the plasmon lead to significant changes in the CD spectra. In the plasmon region, we find that the sign of the CD depends strongly on the orientation of the molecule as well as specific interactions with the NP through image dipole effects. A small enhancement of the CD is found in the molecular region of the spectrum, however, the molecular signatures may be significantly altered through interactions with the NP. We also show that the image dipole effect can result in induced plasmonic CD even for achiral molecules. Overall, we find that the specific interactions with the NP can lead to large changes to the CD spectrum that complicates the interpretation of the results.

## 7.1 Introduction

Circular dichroism (CD) is an optical technique that measures the difference in the absorption of left- and right-circularly polarized light. It is also commonly referred to as electronic CD (ECD) when associated with the electronic absorption spectrum of a molecule. CD is most commonly used to identify the secondary structure of proteins, such as differentiating between $\alpha$-helix, $\beta$-sheet, and random coil,[328] or even between the $3_{10}$-helix and the $\alpha$-helix.[329,330] Plasmonic CD is a term generally used to describe the measure of CD signals of plasmonic nanoparticles (NPs) either by themselves or in the presence of chiral molecules. Applications of plasmonic CD range from the enhancement of CD signals in chiral molecules[331] to the design of novel devices.[332,333]

There are a number of mechanisms by which a plasmonic NP (or collection of NPs) may induce or enhance a CD signal.[334] CD signals may be observed for NPs with chiral shapes,[335] for a collection of NPs in a chiral arrangement,[336] for NPs built from chiral crystal structures, or for achiral NPs interacting with chiral molecules.[331,337,338] For a recent review on the types of plasmonic CD, see ref. 334. In this chapter, we will focus on the enhancement of CD signals of chiral molecules due to the near field (local field) effect of achiral plasmonic NPs.

Govorov and co-workers[339,340] developed a few-states theory to simulate the plasmonic CD of model systems. In this method, the plasmonic CD may be written as[339]

$$CD_{\text{molecule-NP}} = \sum_n \left( a_n \cdot \mathbf{Im} \left[ (\hat{P} \cdot \vec{\mu}^n) \cdot \vec{m}^n \right] + b_n \cdot \mathcal{F}(\vec{\mu}^n, \vec{m}^n) \right) \tag{7.1}$$

where $n$ sums over all excited states with transition electric and magnetic dipoles $\vec{\mu}^n$ and $\vec{m}^n$, and where the coefficients $a_n$ and $b_n$ depend on the geometry and material of the NP(s), on the energy of the incident light frequency, and on excited state $n$. $\hat{P}$ is the local field enhancement matrix, and the function $\mathcal{F}$ depends on the material of the NP(s) and the geometry of the complex. The first term in eq. 7.1 is a local field enhancement of the transition dipole moment, and is responsible for enhancing CD signatures at the molecular resonances. The second term is primarily responsible for the induced CD signal at the plasmon resonance. This theory was applied to model chiral systems (including a 4-state $\alpha$-helix model) near spherical monomer and dimer NPs, where an opposite-sign behavior of the CD signals induced at the plasmon resonance was observed for orthogonal transition dipole moments.[339,340] While successful in describing the plasmon included CD, this model neglects specific interactions between the molecule and the nanoparticle. Recent work by Li *et al.*[341] used a quantum mechanics capacitance molecular mechanics (QMCMM) model to study the CD of helicon molecules adsorbed on metal surfaces. This work showed that the CD depends strongly on the orientation of the molecule relative to the surface. The QMCMM model accounted for the specific interactions between the molecule and the surface, but did not include plasmon effects in the simulations. Thus, there is a need for models that account for both the specific interactions with the metal surface and the plasmon response of the NP to accurately model plasmonic CD.

In this chapter, we will explore the plasmonic CD near (quasi-)spherical NPs for realistic molecular systems by adapting the discrete interaction model / quantum mechanics (DIM/QM)

method[107,123,124,143,144,258,312] to describe the CD of the molecule-NP complex. This method couples a (time-dependent) density functional theory ((TD)DFT) description of the molecule with an atomistic electrodynamics model of the NP. The TDDFT description allows us to go beyond the few-states model description of a molecule, while the atomistic description of the NP allows us to simulate surface defects and arbitrarily shaped NPs. DIM/QM has previously been used to simulate a variety of plasmon-molecule interactions such as surface-enhanced Raman scattering (SERS)[107,144] and surface-enhanced Raman optical activity (SEROA).[124] We will explore the CD and plasmonic CD of the $3_{10}$- and $\alpha$-helix conformations of Alanine$_{20}$ (Ala$_{20}$) near a 17 nm diameter (quasi-)spherical silver NP. This choice of system is similar to the model system studied by Govorov[339,340] and thus will allow for a qualitative comparison with the predictions from that simple few-states model.

## 7.2 Theory

The CD spectrum, in terms of $\Delta\epsilon$ (in units of 1 mol$^{-1}$ cm$^{-1}$), is given as[342]

$$\Delta\epsilon(\omega) = \frac{[\theta(\omega)]}{3298.8} \tag{7.2}$$

where $[\theta(\omega)]$ is the frequency-dependent molar ellipticity of the molecule. This term (in units of deg cm$^2$/dmol) may be obtained from the imaginary part of the complex frequency-dependent optical rotation parameter $\tilde{\beta}(\omega)$ (in atomic units) as

$$[\theta(\omega)] = 1.343 \times 10^{-6} \bar{\nu}^2 \mathbf{Im}\left[\tilde{\beta}(\omega)\right] \tag{7.3}$$

where $\bar{\nu} = \omega/(2\pi c)$ is the frequency in wave numbers. The optical rotation parameter, $\tilde{\beta}$, is obtained from

$$\tilde{\beta}(\omega) = -\frac{1}{3\omega}\sum_{\alpha}\tilde{G}'_{\alpha\alpha} \tag{7.4}$$

where $\tilde{G}'$ is the imaginary part of the electric dipole–magnetic dipole response tensor, broadened by a phenomenological damping factor. We point out that, unlike ref. 342, we define $\tilde{\beta}$ in terms of $\tilde{G}'$ and not $\tilde{G}$, where $\tilde{G}' = i\tilde{G}$.

We recently implemented the calculation of $\tilde{G}'$ within the DIM/QM method[124] in order to simulate the SEROA of molecules. This implementation of $\tilde{G}'$ in the DIM/QM framework was done in the modified velocity gauge (MVG)[325] in order to calculate the gauge origin-independent tensors needed for SEROA. It should be noted that $\tilde{\beta}$ depends on the trace of $\tilde{G}'$, which should be origin-independent for a finite basis set in any gauge. Briefly, the DIM/QM implementation of $\tilde{G}'$ is as follows

$$\tilde{G}'_{\alpha\beta}(\omega,\Gamma) = \frac{2}{(\omega+i\Gamma)^2}\sum_{n\neq 0}\left[\frac{\omega_{n0}\mathbf{Im}\left[\langle 0|\hat{\mu}_\alpha^{\mathrm{tot,VG}}|n\rangle\langle n|\hat{m}_\beta^{\mathrm{tot,VG}}|0\rangle\right]}{\omega_{n0}-(\omega+i\Gamma)^2} - \frac{\mathbf{Im}\left[\langle 0|\hat{\mu}_\alpha^{\mathrm{tot,VG}}|n\rangle\langle n|\hat{m}_\beta^{\mathrm{tot,VG}}|0\rangle\right]}{\omega_{n0}}\right] \tag{7.5}$$

where $\Gamma$ is a damping factor that has the meaning of the inverse of the lifetime of the excited states.[226] The operators $\hat{\mu}^{\mathrm{tot,VG}}$ and $\hat{m}^{\mathrm{tot,VG}}$ are the total electric dipole and magnetic dipole operators in the velocity gauge (VG). In DIM/QM, these operators are modified by the local fields (generated by the NP at incident frequency $\omega$) perturbing the molecule, and are defined as

$$\hat{\mu}_\alpha^{\mathrm{tot,VG}} = \hat{\mu}_\alpha^{\mathrm{QM,VG}} + \hat{V}_\alpha^{\mathrm{loc,VG}} \tag{7.6a}$$

$$\hat{m}_\alpha^{\mathrm{tot,VG}} = \hat{m}_\alpha^{\mathrm{QM,VG}} - \frac{\omega}{2}\epsilon_{\alpha\beta\gamma}R_\beta\hat{V}_\gamma^{\mathrm{loc,VG}} \tag{7.6b}$$

where the Einstein summation convention is assumed for repeated indices, the superscript "QM" indicates the quantum mechanical operators, and $\mathbf{R}$ is the vector describing the molecule's center of nuclear charge. The operator $\hat{V}^{\mathrm{loc,VG}}$ is the local field operator in the VG, defined as

$$\hat{V}_\alpha^{\mathrm{loc,VG}}(\mathbf{r},\omega) = \frac{1}{2}\sum_i^{N_{NP}} T^{(3)}_{\beta\beta\gamma}(\mathbf{r}-\mathbf{R}_i)\mu^{(\alpha)}_{i,\gamma}(\omega) + \sum_i^{N_{NP}} T^{(2)}_{\beta\gamma}(\mathbf{r}-\mathbf{R}_i)\mu^{(\alpha)}_{i,\gamma}(\omega)\hat{\nabla}_\beta \tag{7.7}$$

The index $i$ runs over all classical atoms located at $\mathbf{R}_i$, where $\mu_i^{(\alpha)}(\omega)$ is the dipole induced at atom $i$ due to an external perturbation in the $\alpha$ Cartesian direction at incident frequency $\omega$. The tensors $T^{(x)}(\mathbf{R})$ are the interaction tensors defined as $T^{(x)}(\mathbf{R}) = \nabla^x(1/|\mathbf{R}|)$.[123]

## 7.3 Computational Details

All calculations presented in this work were performed using a local version of the Amsterdam Density Functional (ADF) program package.[165,326,343] The Becke-Perdew (BP86) XC-potential[153,154] and a triple-$\zeta$ Slater-type basis set with one polarization function (TZP) from the ADF basis set library were used. The core orbitals (C[1s], N[1s], O[1s]) were frozen. Structures for the $3_{10}$- and $\alpha$-helix conformations of the (S)-$\mathrm{Ala}_{20}$ polypeptide were obtained from Jacob and co-workers.[344] Frequency-dependent response tensors were calculated using a modified version of the AOResponse module implemented in ADF, with an excited state inverse lifetime of $\Gamma = 0.1$ eV[50,63,111,225,226]. The absorption and CD spectra were then generated within the 170–400 nm window, with a 0.1 eV resolution. An icosahedral structure of 104,223 silver atoms ($\mathrm{Ag}_{104k}$) was used to approximate a ∼17 nm diameter spherical NP, where the frequency-dependent complex dielectric function of silver was obtained from Johnson and Christy[227]. For the DIM/QM simulations the polarizability interaction model (PIM) form of DIM was used, where the NP is described as a collection of interacting polarizabilities.[107]

## 7.4 Results and Discussion

We chose to study the $3_{10}$- and $\alpha$-helix peptide in order to understand how the CD of molecules is perturbed by interactions with a plasmonic NP. The $\alpha$-helix is characterized by a hydrogen bond between the residues $i$ and $i+4$, whereas the $3_{10}$-helix has hydrogen bonds between the residues $i$ and $i+3$. This difference in the hydrogen bond network makes the $3_{10}$-helix longer than the $\alpha$-helix for identical residue sequences. The gas-phase optimized structures used in this chapter were taken from the work of Jacob and co-workers.[344] The dihedral angles of the central residues in the $\alpha$-helix were found to be ($\phi = -60°$, $\psi = -42°$), which is close to the dihedral angles of an ideal $\alpha$-helix of ($\phi = -57°$, $\psi = -47°$). For the $3_{10}$-helix, the dihedral angles of ($\phi = -63°$, $\psi = -19°$) were also found to be in good agreement with that of an ideal $3_{10}$-helix of ($\phi = -74°$, $\psi = -4°$). As discussed in the introduction, CD can in certain cases be used to distinguish between these two types of helical structures.[329,330]

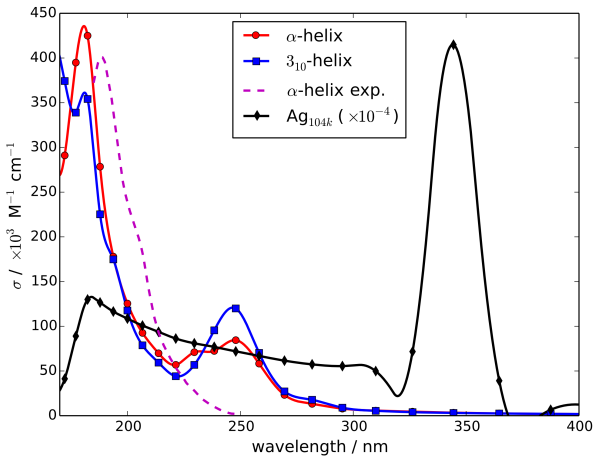


**Figure 7.1.** Simulated absorption spectra of the $3_{10}$- and $\alpha$-helix conformations of $Ala_{20}$, and of the $Ag_{104k}$ NP. Also included is an example of the absorption of an $\alpha$-helix (taken from ref. 345).

In Figure 7.1, we show the absorption spectra of the $3_{10}$- and $\alpha$-helix conformations of $Ala_{20}$. Both systems produce very similar absorption spectra, with maxima at 180 nm and smaller features at 190, 230 and 250 nm. The maxima at 180 nm with the corresponding shoulders at 190 and 230 nm are in good agreement with what is observed experimentally (see, for example, ref. 345), and correspond to a $\pi\pi^*$ and two $n\pi^*$ transitions, respectively. The differences in excitation energies between experiment and simulation are likely due to an absence of solvent effects. The absorption at 250 nm is not observed in experiments and may be attributed to either spurious low-lying excited states[346] or the single geometry for each helical structure sampled here; the latter being more likely because of the significant oscillator strength of the 250 nm transition. Ideally, one should Boltzmann average over all low-energy conformations of the molecule, which is beyond the scope of this work. Kaminský and co-workers have shown that averaging over MD simulations is necessary to achieve converged band profiles.[347] We also include the absorption

spectrum of the $Ag_{104k}$ NP in Figure 7.1. The absorption spectrum of the NP is dominated by a strong band at 344 nm, which is characteristic of the plasmon resonance in spherical Ag NP's. Since this band does not overlap with any of the molecular transitions, it allows us to examine both the changes in the molecular CD signatures and the nature of the CD induced at the plasmon resonance.

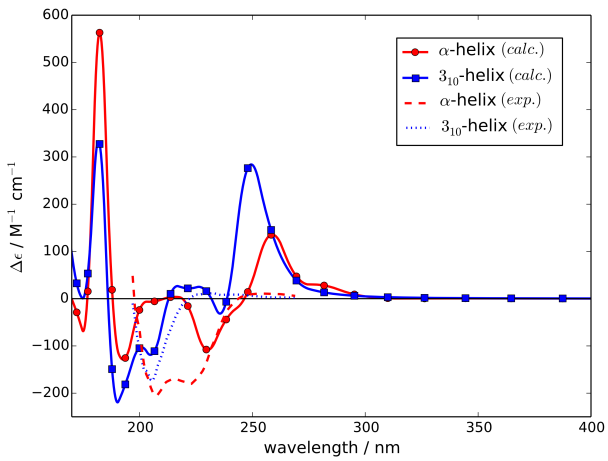


**Figure 7.2.** Simulated CD spectra of $\alpha$- and $3_{10}$-helices. Also included are the experimental CD spectra of the $\alpha$- and $3_{10}$-helix conformations of a polypeptide between 200–250 nm (taken from ref. 330).

We plot the CD spectra of the two helical structures of $Ala_{20}$ in Figure 7.2. The absorption maxima at 180 nm correspond to large positive CD in both molecules, whereas the absorption shoulders at 190 and 230 nm result in negative CD intensity. The ellipticity ratio between the 230 and 190 nm CD bands ($[\theta]_{230}/[\theta]_{190}$) is proposed to be about 0.4 for the $3_{10}$-helix and about 1.0 for the $\alpha$-helix.[329,330,345,348] We observe the same trend, with this ratio estimated as 0.1 for the $3_{10}$-helix and 1.0 for the $\alpha$-helix simulated here. In general, the calculated CD spectra for both the $3_{10}$- and $\alpha$-helices are in good agreement with experimental results, with the exception of the CD band at 250 nm which, like the absorption observed in this region, is not observed experimentally.

In Figure 7.3, we show the parallel and perpendicular orientations of the helices with respect to the $Ag_{104k}$ NP. The helices are arranged with their N terminus towards the silver surface in the perpendicular configurations. We have also included in Figure 7.3 the magnitude of the perturbing electric fields at the plasmon resonance frequency (344 nm), where $|\mathbf{E}| = |\mathbf{E}^{ext} + \mathbf{E}^{loc}|$, for an external perturbation perpendicular to the surface of the NP. This shows that, on average, the parallel orientations "feel" a much larger electric field than the perpendicular orientations. It is also clear from the figure that the electric field varies significantly over the dimensions of the helices, especially, for the perpendicular orientations. Therefore, it becomes crucial to account for the inhomogeneous electric field perturbing the helices. We showed previously[124,258] that the DIM/QM local field operator (used in eq. 7.7) accounts for this inhomogeneous nature of the local electric field through dipolar-multipolar (NP-molecule) interactions.

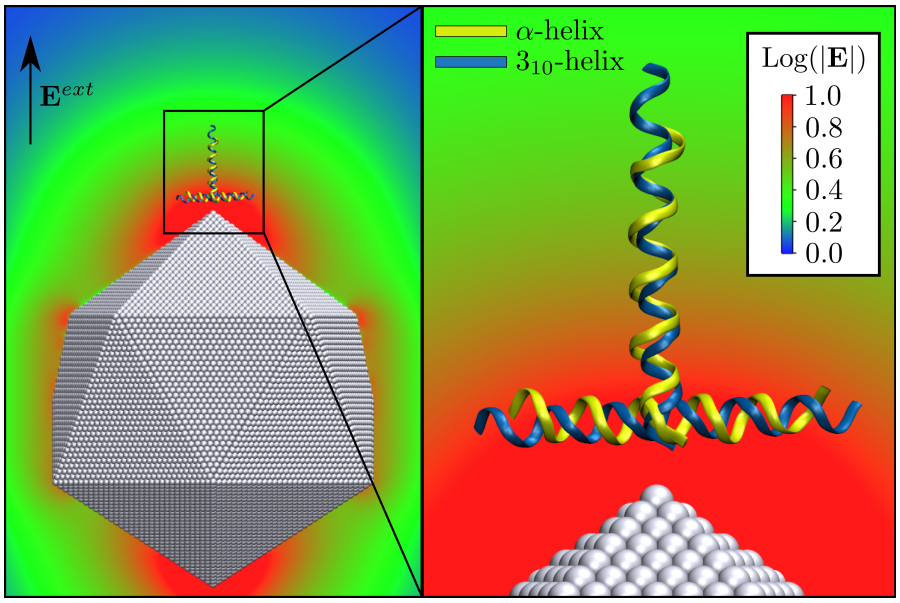


**Figure 7.3.** Orientations of the $3_{10}$- and $\alpha$-helix conformations of $Ala_{20}$ with respect to $Ag_{104k}$. $\mathbf{E}^{ext}$ marks the direction of the external perturbing field (at the plasmon resonance, 344 nm), and $\mathbf{E} = \mathbf{E}^{ext} + \mathbf{E}^{loc}$, where $\mathbf{E}^{loc}$ is the local electric field.

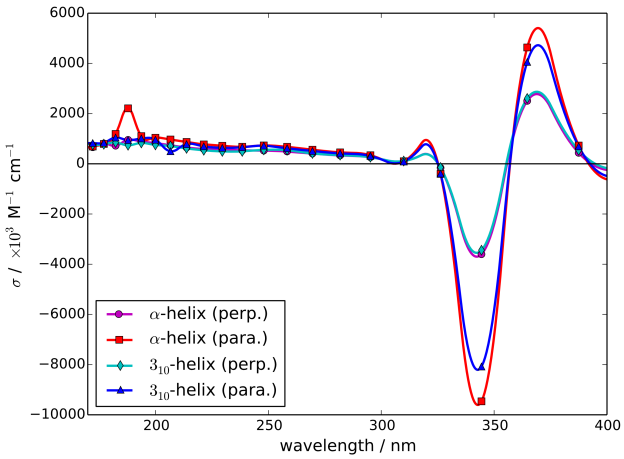


**Figure 7.4.** Simulated absorption spectra for $3_{10}$- and $\alpha$-helices on $Ag_{104k}$ for both the perpendicular (perp.) and parallel (para.) orientations.

Figure 7.4 shows the absorption spectra of the two $Ala_{20}$-$Ag_{104k}$ complexes, where the absorption at ∼350 nm gives us an indication of the coupling strength between the molecule and the plasmon excitation in the NP. We point out that the absorption simulated here is the molecular contribution to the absorption of the metal-molecule complex, and it contains both the absorption induced into the molecule by the NP and that induced into the NP by the molecule. It is important to note that the molecular contribution to the total absorption can be both

negative and positive (only the total absorption of the system has to be positive) as it contains both constructive and destructive terms.[143] For both helices in both orientations, the molecular absorption spectra show a negative band at 344 nm and a positive band at 354 nm. These features would lead to a red-shift of the plasmon excitation if the NP was covered with the molecules. We observe that the parallel orientations are more strongly coupled to the NP than the perpendicular orientations, which is expected based on the average local electric fields "felt" by the helices in these orientations as illustrated in Figure 7.3. We also observe that both helices have similar coupling strengths for the perpendicular orientations, whereas in the parallel orientations, the $\alpha$-helix is more strongly coupled than the $3_{10}$-helix. This may also be explained in terms of average fields "felt" by the helices, where the ends of the longer $3_{10}$-helix extend into regions of much weaker local electric fields.

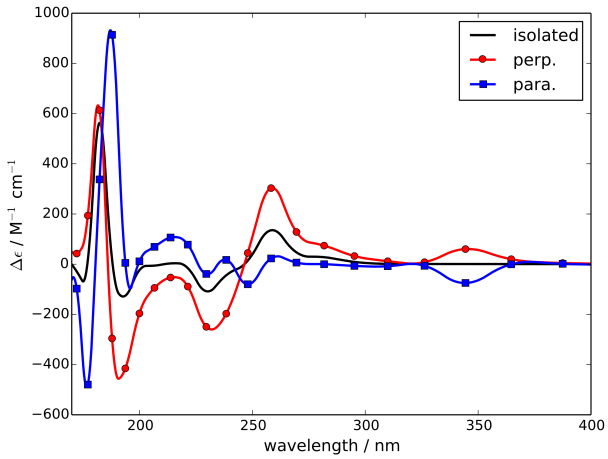


**Figure 7.5.** Simulated CD spectrum (isolated) and plasmonic CD spectrum for $\alpha$-helix on $Ag_{104k}$ in both the perpendicular (perp.) and parallel (para.) orientations.

Figure 7.5 shows the CD spectrum and plasmonic CD spectrum of the $\alpha$-helix. We observe that, in the region below 300 nm, there is a small enhancement (about a factor of 2) over the isolated CD signal. This is because the NP has a non-zero absorption in this region, resulting in small local electric fields that couple into (and enhance) the molecule's transition dipole moments. However, the enhancement factors are not identical for the two orientations (at the same incident frequency). The seemingly erratic behavior of the plasmonic CD may be attributed to a combination of a shift in excitation energies[123], a preferential enhancement of transition dipoles parallel to the local electric fields, and an orientation-dependent rotation of the transition electric dipoles with respect to the transition magnetic dipoles (discussed below). These lead to a very complicated plasmonic CD in the region below 300 nm, thus making it difficult to retain molecular signatures. We see this in Figure 7.5, where the plasmonic CD signatures of the parallel orientation is unrecognizable as being those from an $\alpha$-helix, and the ellipticity ratio for the perpendicular orientation (0.6) is very different from that of the isolated molecule (1.0). We also observe a non-zero CD signal at the plasmon frequency (344 nm), which is of comparable

strength to the CD of the isolated molecule. We observe that, as predicted by the few-states model in ref. 339, the signs of these induced CD at the plasmon resonance are different for the parallel and perpendicular orientations of the $\alpha$-helix.

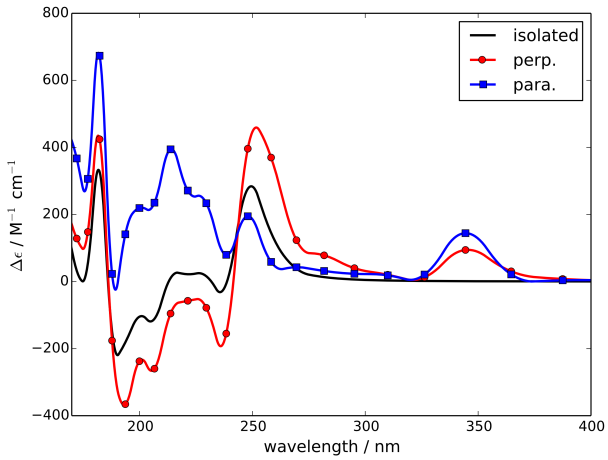


**Figure 7.6.** Simulated CD spectrum (isolated) and plasmonic CD spectrum for $3_{10}$-helix on $Ag_{104k}$ in both the perpendicular (perp.) and parallel (para.) orientations.

We plot the CD spectrum and plasmonic CD spectrum of the $3_{10}$-helix in Figure 7.6. The plasmonic CD spectra behave similarly to those of the $\alpha$-helix in the region below 300 nm; we observe a small enhancement of the CD signals, the CD molecular signatures of the $3_{10}$-helix is unidentifiable in the parallel orientation, and the ellipticity ratio in the perpendicular orientation (0.5) is very different from that of the isolated molecule (0.1). However, unlike what was observed for the $\alpha$-helix, we observe the same sign for the CD signals induced at the plasmon resonance. This seems, at first, contradictory to the prediction of the few-states model in ref. 339. However, the DIM/QM method varies from that method in three important ways, any of which may have resulted in this difference: First, the functional form of the major contributing term for the CD induced at the plasmon in ref. 339 was derived for a spherical NP. The atomistic DIM/QM method allows any arbitrarily shaped NP to be simulated. While this opposite-sign relation may hold true for orthogonal transition electric dipoles near spherical NPs, the behavior may be more complex for other NP shapes. However, we used icosahedral NPs which are approximate spherical and is therefore less likely an explanation for the same-sign CD observed. Second, the functional form of the metal-molecule interaction has been truncated at the dipole-dipole limit in ref. 339. As we have shown,[124,258] the DIM/QM method implicitly includes interactions with higher order multipoles, which may have led to the differences observed here. Third and finally, the same-sign CD signal observed here may be due to the "image field" effect, absent in the model in ref. 339. The image field is the perturbation by the "image" dipoles induced in the NP by the charge distribution of the molecule (both in the ground state and excited state), and may cause a rotation of the transition dipoles of the molecule. This, in turn, may lead to a change in the angle between the transition electric and magnetic dipoles. In ref. 339, the angle between

$\vec{\mu}^{0n}$ and $\vec{m}^{n0}$ is fixed for all orientations, and may only be effectively changed through the local field enhancement matrix (which is not the term responsible for inducing CD at the plasmon resonance). In DIM/QM, this angle will be dependent on the orientation of the molecule through the image field perturbation, and result in differences in the CD spectra for the parallel and perpendicular orientations (even without the plasmonic local fields). In fact, we observe image field induced CD signals that are 3.5 times larger (1.4 versus 0.4 $M^{-1}$ $cm^{-1}$) for the $3_{10}$-helix versus the $\alpha$-helix at the plasmon resonance frequency for the parallel orientations.

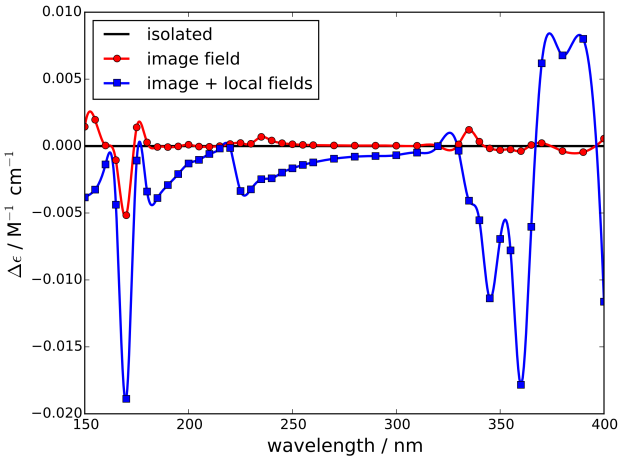


**Figure 7.7.** Simulated CD spectrum and plasmonic CD spectrum of achiral pyridine on $Ag_{147}$ showing the effects of the image and local fields.

To further explore this effect, we show an example of the image field rotating $\vec{\mu}^{0n}$ with respect to $\vec{m}^{n0}$ in Figure 7.7, where we plot the plasmonic CD spectrum of pyridine (pyr) on a $Ag_{147}$ NP. We chose pyr because it is a small achiral molecule with strong oscillator strengths. Being achiral, $\vec{\mu}^{0n}$ is orthogonal to $\vec{m}^{n0}$ for all $n$, and we observe zero CD signal for the isolated molecule. We then calculated the "plasmonic" CD of the gas-phase $C_{2v}$ optimized (achiral) pyr on $Ag_{147}$, without the contributions from the local fields (that is, only the image field effect is considered). We observed a non-zero CD in the region of strong absorption (∼170 nm), indicating that the angle between $\vec{\mu}^{0n}$ and $\vec{m}^{n0}$ has changed. This implies that while pyr is achiral, the molecule and it's image field together are not, and we may observe plasmonic CD for achiral molecules attached to achiral NPs. One would expect that, for a perfectly reflecting surface, this would not be true since we have introduced a mirror-plane symmetry into the molecule-image complex. The observed image field induced CD signals are small, and the inclusion of the local fields enhances these signals by a factor comparable to that observed for $Ala_{20}$ on $Ag_{104k}$ in the same spectral region. The region of the CD spectrum around the plasmon resonance of the $Ag_{147}$ cluster also shows significant induced plasmonic CD. The fact that multiple bands are seen around the plasmon excitation in the CD spectrum is simply due to the small size of the $Ag_{147}$ cluster, which leads to a splitting of the plasmon excitation.

## 7.5 Conclusion

In conclusion, we have used the DIM/QM method to calculate complex optical rotation tensors, enabling us to simulate the plasmonic CD spectrum of molecule-NP complexes. We used this method to calculate the plasmonic CD of the $3_{10}$- and $\alpha$-helical conformations of $Ala_{20}$ on $\sim$17 nm diameter icosahedral NPs. We observe small plasmonic enhancement of the CD signatures of the molecules, and these signatures are sometimes unrecognizable for specific orientations. In both helical structures, we observe a CD signal induced at the plasmon resonance. However, we do not observe opposite-sign CD signal at the plasmon frequency for orthogonal orientations of the $3_{10}$-helix. We propose that this observation is likely due to an "image field" effect, and show that this effect is also able to induce a CD signal for achiral molecules attached to achiral NPs.

# Part III

# An Exact Subsystem Density Functional Theory

# Chapter 8
# Frozen Density Embedding with External Orthogonality

Chulhai, D. V.; Jensen, L. "*Frozen Density Embedding with External Orthogonality in Delocalized Covalent Systems*" *J. Chem. Theory Comput.* **2015**, *11*, 3080–3088

## Abstract

Frozen density embedding (FDE) has become a popular subsystem density functional theory (DFT) method for systems with weakly overlapping charge densities. The failure of this method for strongly interacting and covalent systems is due to the approximate kinetic energy density functional (KEDF) – though the need for approximate KEDFs may be eliminated if each subsystem's Kohn-Sham (KS) orbitals are orthogonal to the other, termed external orthogonality (EO). We present an implementation of EO into the FDE framework within the Amsterdam Density Functional program package, using the level-shift projection operator method. We generalize this method to remove the need for orbital localization schemes and to include multiple subsystems, and we show that the exact KS-DFT energies and densities may be reproduced through iterative freeze-and-thaw cycles for a number of systems, including a charge delocalized benzene molecule starting from atomic subsystems. Finally, we examine the possibility of a truncated basis for systems with and without charge delocalization, and found that subsystems require a basis which allows them to correctly describe the supermolecular delocalized orbitals.

## 8.1 Introduction

A combination of the calculation expense of large systems and the fact that most chemistry is centered around a smaller subsystem has led to the development of subsystem methods.[349] In these methods, each subsystem may be either treated with the same or different theoretical descriptions. Among the most common subsystem approaches are combined quantum mechical/molecular mechanics methods,[172,350,351] which enable one to focus on the region of interest using quantum mechanics while having an approximate classical description of the environment. Another approach that has gained popularity recently is subsystem density functional theory (subsystem DFT),[175–178] in which each subsystem is treated using Kohn-Sham (KS) DFT.

Subsystem DFT allows for intuitive partitioning of the supermolecular system via the real-space electron density $\rho(\mathbf{r})$. This supermolecular system density is divided into the region of interest (the active/embedded subsystem, hereinafter $\rho_I(\mathbf{r})$) and the environment (hereinafter $\rho_{II}(\mathbf{r})$). The total energy functional is then minimized under the constraint of a fixed number of electrons for each subsystem. The most common implementation of subsystem DFT is frozen density embedding (FDE),[179] in which one subsystem ($\rho_{II}(\mathbf{r})$) is kept frozen while the total energy is minimized with respect to changes in the other subsystem density ($\rho_I(\mathbf{r})$). Minimization of total energy with respect to the supermolecular density is achieved through freeze-and-thaw cycles, where the roles of subsystems $I$ and $II$ are iteratively interchanged.

FDE is exact in principle, though approximations for the exchange-correlation (XC) functional and the kinetic energy density functionals (KEDF) have to be made for practical calculations. In particular, the KEDF contributes to the embedding potential via the nonadditive kinetic potential (NAKP) defined as

$$\nu_T[\rho_I, \rho_{II}; \mathbf{r}] = \frac{\delta T_s[\rho]}{\delta \rho(\mathbf{r})} - \frac{\delta T_s[\rho_I]}{\delta \rho_I(\mathbf{r})} \tag{8.1}$$

where $T_s$ is the KEDF. Available approximations to the KEDF are acceptable only for FDE subsystems with weakly overlapping densities, but break down in the region of strongly overlapping densities and subsystems with a covalent character.[184,187,188] These failures are generally attributed to the non-exactness of available KEDFs, although it has been shown that inter-subsystem KS orbitals orthogonality is needed to ensure that the density sum relationship of subsystems ($\rho(\mathbf{r}) = \rho_I(\mathbf{r}) + \rho_{II}(\mathbf{r})$) is upheld.[190] Therefore, even for the exact KEDF, the resulting NAKP may still lead to incorrect results unless subsystem KS orbitals are both internally (with respect to orbitals of the same subsystem) and externally (with respect to orbitals of the other subsystem) orthogonal. In addition, external orthogonality (EO) ensures that $\nu_T = 0$ and therefore removes the dependence on approximate KEDFs.[352]

Methods that enforce EO between subsystems have been in use for decades, such as in frozen-core approximations[192], the Phillips-Kleinman pseudopotential approach[194], and the methods of Stoll and co-workers[195], Mata and co-workers[196], and Henderson[197]. Manby, Miller and co-workers recently introduced EO into subsystem DFT and wave function theory in DFT embedding through the use of a level-shift projection operator.[198–200] This method requires that

the supermolecular KS-DFT results are known *a priori*, and requires further MO localization schemes. For both covalent and non-covalent systems, they showed that this method reproduces the supermolecular KS-DFT energies exactly in the supermolecular basis[198,200] and accurately in a truncated basis.[199]. Hoffman and co-workers implemented a method where EO is included as a constraint to the coupled KS Lagrangian,[191] which consequently removes the need for an initial supermolecular calculation. For non-covalent systems of varying interaction strengths, they showed that the supermolecular KS-DFT energies, densities, and potential energy curves are exactly reproduced by their subsystem formalism in the supermolecular basis, and well approximated in an extended monomer basis.

In this chapter, we present a flexible implementation of EO into the FDE framework[208,353] in the Amsterdam density functional (ADF) program suite.[165,326,343] We generalize the Miller and co-workers projection operator method[198,199] to include any starting subsystem KS orbitals represented in any basis set. This allows one, in the spirit of conventional FDE, to start with monomer subsystem KS orbitals and iterate through successive freeze-and-thaw cycles to achieve converged results, similar to the constrained Lagrangian approach[191]. We show that this implementation exactly reproduces the KS-DFT energies and densities for a number of systems of varying density overlaps. This projection operator method is more easily extended to describe multiple subsystems, and we show that the exact KS-DFT density of a charge delocalized benzene molecule can be obtained from isolated atomic starting subsystems. We also examine the effects of basis set truncation for a number of covalent systems, including systems with large charge delocalization, in order to assess the viability of a truncated basis in subsystem DFT for such systems.

## 8.2 Theory

The FDE Kohn-Sham equation (sometimes called the Kohn-Sham equation with constrained electron density[179]) is given as

$$\left[-\frac{\nabla^2}{2} + \nu_{\text{eff}}^{\text{KS}}[\rho_I;\mathbf{r}] + \nu_{\text{eff}}^{\text{emb}}[\rho_I,\rho_{II};\mathbf{r}]\right]\phi_i^I(\mathbf{r}) = \epsilon_i\phi_i^I(\mathbf{r}); \qquad i = 1,\ldots,N_I \tag{8.2}$$

where $\rho_I$ and $\rho_{II}$ are the embedded ($I$) and frozen ($II$) subsystem densities (with $N_I$ and $N_{II}$ number of electrons), respectively, $\phi^I$ are the KS orbitals for subsystem $I$, $\nu_{\text{eff}}^{\text{KS}}$ is the KS effective potential for subsystem $I$, and $\nu_{\text{eff}}^{\text{emb}}$ is the effective embedding potential due to the frozen $\rho_{II}$, written as

$$\nu_{\text{eff}}^{\text{emb}}[\rho_I,\rho_{II};\mathbf{r}] = \nu_{II}^{\text{nuc}}(\mathbf{r}) + \int \frac{\rho_{II}(\mathbf{r}')}{|\mathbf{r}-\mathbf{r}'|}d\mathbf{r}' + V_{\text{XC}}^{\text{nadd}}[\rho_I,\rho_{II};\mathbf{r}] + \nu_T[\rho_I,\rho_{II};\mathbf{r}] \tag{8.3}$$

where the first and second terms on the right hand side are the nuclear and electron Coulombic potentials, respectively, $V_{\text{XC}}^{\text{nadd}}$ is the nonadditive contribution to the XC potential, and $\nu_T$ is the NAKP defined eariler.

The NAKP is present because the KS orbitals of subsystem $II$ are not necessarily orthogonal to those of subsystem $I$. In the case where these subsystems are mutually orthogonal, then $\nu_T = 0$ and we do not require approximate KEDFs. In this work, we enforce EO by implementing the level-shift projection operator introduced in ref. 198. We expand on this method by allowing for any starting subsystem MOs, any level of basis set overlap between subsystems, and iterative freeze-and-thaw cycles. This removes the need for a starting supermolecular calculation and MO localization. We modify the Fock matrix of the embedded system in the AO basis using the projection operator as

$$f_{\alpha\beta}^{\mathrm{EO}} = f_{\alpha\beta}^{\mathrm{FDE}(\nu_T=0)} + \mu P_{\alpha\beta}^{II} \tag{8.4}$$

where $\alpha$ and $\beta$ are the AO indices of subsystem $I$. The first term on the right hand side is the conventional FDE Fock matrix without a NAKP contribution, and $\mu\mathbf{P}^{II}$ is a term which raises energy of the $i$th orbital in subsystem $II$ to $\epsilon_i^{II} + \mu$, where $\mu$ is a scaling parameter and $\mathbf{P}^{II}$ is the projection operator of subsystem $II$. The orbitals are forced to be perfectly orthogonal in the limit $\mu \to \infty$, however a large number ($10^4 < \mu < 10^8$) is usually used in practical applications. The projection operator is defined as

$$\begin{aligned} P_{\alpha\beta}^{II} &= \langle \chi_\alpha^I | \left\{ \sum_{i\in II} |\phi_i^{II}\rangle\langle\phi_i^{II}| \right\} |\chi_\beta^I\rangle \\ &= \sum_{\tau,\upsilon} \langle \chi_\alpha^I | \chi_\tau^{II}\rangle \gamma_{\tau\upsilon}^{II} \langle \chi_\upsilon^{II} | \chi_\beta^I\rangle \\ &= \left[\mathbf{S}^{I,II}\gamma^{II}\mathbf{S}^{II,I}\right]_{\alpha\beta} \end{aligned} \tag{8.5}$$

In this equation, $\{\chi^I\}$ and $\{\chi^{II}\}$ are the set of AOs describing subsystems $I$ (with AO indices $\alpha$ and $\beta$) and $II$ (with AO indices $\tau$ and $\upsilon$), respectively, $\{\phi^{II}\}$ is the set of KS orbitals of subsystem $II$ (with density matrix $\gamma^{II}$), and $\mathbf{S}^{I,II}/\mathbf{S}^{II,I}$ are the overlap matrices between the AOs of the two subsystems. The density matrix $\gamma^{II}$ is symmetric and $\left(\mathbf{S}^{I,II}\right)^T = \mathbf{S}^{II,I}$, which ensures that the projection operator, and therefore the modified Fock matrix, is Hermitian. Since $\{\chi^I\}$ and $\{\chi^{II}\}$ may span any subset of the supermolecular basis set $\{\chi^S\}$, we will refer to the case where $\{\chi^I\} \cap \{\chi^{II}\} = \emptyset$ as the monomer basis implementation (FDE(EO,m)), $\{\chi^I\} = \{\chi^{II}\} = \{\chi^S\}$ as the supermolecular basis implementation (FDE(EO,s)), and $\{\chi^I\} \cap \{\chi^{II}\} = \{\chi^O\} \neq \{\chi^S\}$ as an extended monomer implementation (FDE(EO,e), where $\{\chi^O\} \neq \emptyset$ describes the overlap region).

We also extend this projection operator to describe multiple frozen subsystems, where $\rho_{II}(\mathbf{r}) = \sum_{i\in II} \rho_i(\mathbf{r})$. In such a calculation, each frozen subsystem will be comprised of its own set of KS orbitals, spanning their own AO basis, and we rewrite eq. 8.4 as

$$f_{\alpha\beta}^{\mathrm{EO}} = f_{\alpha\beta}^{\mathrm{FDE}(\nu_T=0)} + \mu \left( \sum_{i\in II} P_{\alpha\beta}^{i} \right) \tag{8.6}$$

This ensures that subsystem A is mutually orthogonal to each frozen subsystem. Note that this does not necessarily ensure orthogonality between different frozen subsystems. Mutual orthogonality between all subsystems is achieved through freeze-and-thaw cycles, ensuring that

each subsystem is orthogonal to all others.

## 8.3 Computational Details

All calculations presented in this work were performed using a local version of the Amsterdam Density Functional (ADF) program package,[165,326,343] with the Becke-Perdew (BP86) exchange-correlation (XC) potential.[153,154] The QZ4P basis set was used for the water dimer, $FHF^-$, $BH_3NH_3$, ethane and benzene systems, while the TZ2P basis set was used for all other systems. All geometries were first optimized using the BP86 XC functional. The Thomas-Fermi (TF) local density approximation to the NAKP[145,146] was used for all conventional FDE calculations. For all external orthogonality calculations, the subsystems' KS orbitals are orthogonalized using a level-shift parameter of $\mu = 10^6\ E_h$. This was found to be reasonable since values $> 10^7\ E_h$ generally lead to numerical instabilities and values $< 10^2\ E_h$ were insufficient at achieving external orthogonality.[198] All density manipulations were performed numerically on a cubic grid of 0.1 Å spacing, with the densities calculated using pyADF[354]. Other ADF specifications include: integration threshold = 8.0; self-consistent field energy convergence criterion = $10^{-8}$.

The typical workflow using our implementation of EO into the FDE framework (FDE(EO)) within ADF is as follows: (1) Identify the subsystems of the supermolecular system. (2) Determine which atoms constitute the overlap region. (3) Calculate (and save) the KS orbitals of each subsystem, using "ghost" or empty AOs for atoms that are not a part of this subsystem but are included in the overlap region. (4) Perform an FDE(EO) calculation using the KS orbital information for each starting subsystem.

## 8.4 Results and Discussion

### 8.4.1 Exact KS-DFT results

**Table 8.1.** Energy errors for FDE(cft) using the TF NAKP and EO methods.

| System | Method | KE / $E_h$ | XC / $E_h$ | Coulomb / $E_h$ | Total / $E_h$ |
|---|---|---|---|---|---|
| $H_2O$–$H_2O$ | TF | -0.005 475 74 | 0.002 046 65 | -0.001 073 68 | -0.004 502 77 |
| | EO | -0.000 000 03 | 0.000 000 01 | 0.000 000 05 | 0.000 000 03 |
| F–H–$F^-$ | TF | 0.031 478 52 | 0.000 197 19 | -0.059 215 52 | -0.027 539 81 |
| | EO | 0.000 000 49 | -0.000 000 06 | -0.000 000 18 | 0.000 000 25 |
| $BH_3NH_3$ | TF | -0.044 359 39 | -0.015 477 93 | 0.042 474 37 | -0.017 362 95 |
| | EO | 0.000 000 20 | -0.000 000 01 | 0.000 000 04 | 0.000 000 23 |
| $C_2H_6$ | TF† | -3.811 613 27 | 0.246 893 16 | 4.540 666 11 | 0.975 946 00 |
| | EO | 0.000 000 06 | 0.000 000 01 | 0.000 000 05 | 0.000 000 12 |

†These values were obtained after 50 freeze-and-thaw cycles.

We show that the EO method within the FDE framework with converged freeze-and-thaw (cft) cycles exactly reproduces the supermolecular Kohn-Sham results by comparing the energies

and densities of four systems that vary in their amount of density overlap. These systems were previously used to explore the effectiveness of a reconstructed NAKP,[188] and include hydrogen bonded systems (water dimer and $FHF^-$), a doner-acceptor system ($BH_3NH_3$), and a covalent system (ethane). In Table 8.1, we show the energy differences between FDE with converged freeze-and-thaw iterations (using the TF NAKP and EO) and that of the supermolecular KS-DFT calculation for these systems. For these methods, the total XC energy is taken as the sum of the XC energy of the individual subsystems plus that of the nonadditive XC energy ($E_{\mathrm{XC}}[\rho_I, \rho_{II}] = E_{\mathrm{XC}}[\rho_I] + E_{\mathrm{XC}}[\rho_{II}] + E_{\mathrm{XC}}^{\mathrm{nadd}}[\rho_I, \rho_{II}]$). By definition, this is the XC energy of the sum of densities $\rho_I + \rho_{II}$. The total non-interacting KE for the EO method is taken as the sum of the non-interacting KE of the individual subsystems ($T_S^{\mathrm{EO}}[\rho_I, \rho_{II}] = T_S[\{\phi^I\}] + T_S[\{\phi^{II}\}]$), whereas for the TF method the nonadditive KE is also added ($T_S^{\mathrm{TF}}[\rho_I, \rho_{II}] = T_S[\{\phi^I\}] + T_S[\{\phi^{II}\}] + T_S^{\mathrm{nadd}}[\rho_I, \rho_{II}]$. For the TF method, the error in the KE varies from -5.4 $mE_h$ in the water dimer to -3.8 $E_h$ in the case of ethane. This is expected since the TF (and generally most NAKPs) approximation is only accurate in the limit of weakly overlapping densities. This leads to incorrect densities and consequently large errors in the XC and Coulomb energies for the systems with a stronger covalent character. However, fortuitous cancellation of errors often results in a total energy error that is always smaller than that of the non-interacting KE. When EO is enforced, all energies are numerically identical (within 0.5 $\mu E_h$) to those of the KS-DFT results. The projection operator DFT-in-DFT embedding was shown to produce sub-$\mu E_h$ energy errors for systems where the subsystems were obtained from localization of the MOs of the supermolecular system,[198] whereas these results show that the same level of accuracy is obtained from isolated starting subsystems using the iterative freeze-and-thaw method.

**Table 8.2.** Integrated absolute density difference ($\Delta^{\mathrm{abs}}$, in $e$) for FDE(TF,s,cft), FDE(EO,s,2ft) and FDE(EO,s,cft) methods.

| System | Active | TF | TF+cft | EO | EO+2ft | EO+cft |
|---|---|---|---|---|---|---|
| $H_2O$–$H_2O$ | $I$ | 0.1019 | 0.0371 | 0.1168 | 0.0001 | 0.0000 |
| | $II$ | 0.1166 | | 0.0784 | 0.0000 | |
| F–H–$F^-$ | F–H | 0.5736 | 0.1154 | 0.5936 | 0.0021 | 0.0000 |
| | $F^-$ | 0.7174 | | 0.4544 | 0.0021 | |
| $BH_3NH_3$ | $BH_3$ | 0.7433 | 0.4724 | 0.8357 | 0.0110 | 0.0000 |
| | $NH_3$ | 0.6423 | | 0.3693 | 0.0033 | |
| $C_2H_6$ | $CH_3^+$ | 1.7171 | †4.0116 | 1.8818 | 0.0711 | 0.0000 |
| | $CH_3^-$ | 1.3109 | †3.9072 | 0.7973 | 0.0145 | |

†These values were not converged after 50 freeze-and-thaw cycles.

We compare the density error between the FDE methods and that of the KS-DFT density using the integrated absolute density difference[188,352,355–357] ($\Delta^{\mathrm{abs}} = \int \left|\rho^{\mathrm{KS}}(\mathbf{r}) - \rho^{\mathrm{FDE}}(\mathbf{r})\right| d\mathbf{r}$) for the four systems in Table 8.2. We include results for regular FDE and FDE(cft) for both methods, as well as FDE with two freeze-and-thaw cycles (2ft) for the EO method. For the water dimer, subsystem $I$ is the water molecule whose hydrogen atom is involved in a hydrogen bond with

the oxygen lone pair of subsystem $II$. The $\Delta^{\text{abs}}$ values for the FDE(TF,s) method starting with each subsystem $I$ and $II$ are 0.10 and 0.12 $e$, respectively. These are both acceptable values for $\Delta^{\text{abs}}$,[188,357] and we will therefore use $\Delta^{\text{abs}} < 0.15\ e$ as our $\Delta^{\text{abs}}$ threshold. Our results with the TF NAKP closely resemble those from an earlier study[188] with the PW91k NAKP[185], and we will therefore not examine them in detail. In summary, the TF NAKP can only describe the water dimer (both regular FDE and FDE(cft) approaches) and $FHF^-$ (only the FDE(cft) approach) systems, but fails for the $BH_3NH_3$ and ethane systems. In addition, the iterative freeze-and-thaw method failed to converge for the strongly interacting (covalent) ethane system,[184] and the results shown in Table 8.1 were taken after 50 cycles. Using the bare FDE method with EO, that is, without freeze-and-thaw, we found that the $\Delta^{\text{abs}}$ values were comparable to those obtained with the TF NAKP. This is expected since the error is dominated by the frozen subsystem. However, we observe numerically identical densities in the FDE(cft) calculations. We also include the results from the FDE(2ft) method to show that this convergence of density is rapid, requiring an average of 16 iterations for the ethane molecule and 7 iterations for the other systems with a convergence criterion of $10^{-8}\ E_h$. For all systems, FDE(EO,2ft) was sufficient to yield acceptable density errors with $\Delta^{\text{abs}}$ comparable to (and often significantly better than) those of the water dimer with FDE(TF,ctf). As the results indicate, the supermolecular KS-DFT densities are exactly obtained from iterative freeze-and-thaw calculations with EO, and yields acceptable density errors for covalent systems in as few as two freeze-and-thaw cycles.

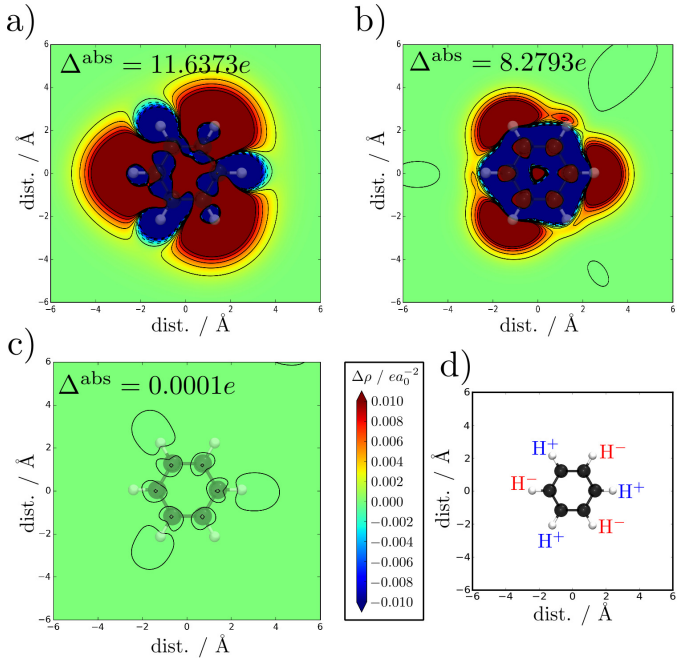


**Figure 8.1.** The density difference (integrated over the perpendicular axis not shown) for a benzene molecule, using (a) the sum of subsystem densities, (b) FDE(TF,s,30ft), and (c) FDE(EO,s,30ft). The molecular coordinates and location of the $H^-$ and $H^+$ subsystems are shown in (d).

We also show that the EO method allows for multiple subsystems and any arbitrary

partitioning of the density by reconstructing the exact KS-DFT density of benzene from atomic subsystems. In Figure 8.1, we show the density difference integrated over the perpendicular axis ($\Delta\rho = \int \left(\rho^{\mathrm{KS}} - \rho^{\mathrm{FDE}}\right) dz$, in units of $ea_0^{-2}$) of a benzene molecule for the FDE(TF, s, 30ft) and FDE(EO, s, 30ft) methods, each starting from atomic subsystem densities. In order to construct closed-shell subsystems, the six H atomic subsystems are instead represented as three $H^-$ and three $H^+$ ions, with their respective positions given in Figure 8.1d. These positions are reflected as the large positive and negative regions in the difference density in Figure 8.1a, with a calculated $\Delta^{\mathrm{abs}} = 11.6373\ e$. The TF NAKP only slightly improves upon the sum of subsystems description, with a $\Delta^{\mathrm{abs}} = 8.2793\ e$ (Figure 8.1b). This model is not expected to be qualitatively correct for such a system, and seems to push the electron density towards the carbon and hydrogen nucleii, and away from the benzene ring. With the EO method, however, we clearly see (Figure 8.1c) that the density is identical to that of the KS-DFT density, with a $\Delta^{\mathrm{abs}}$ value of 0.0001 $e$. The benzene system shown here was only converged to $\sim 10^{-7}\ E_h$ after 50 freeze-and-thaw iterations, which may be due to the delocalized nature of the system and the number of subsystems used. These results show the robustness of our implementation of the EO method, and that it allows one to arbitrarily (limited to closed-shell subsystems in the current implementation) divide any, even delocalized, supermolecular system.

### 8.4.2 Effects of basis set truncation

To reduce the cost of the FDE(EO) method it is therefore desirable to truncate the number of AOs in the overlap region of each subsystem. We study the effects of different levels of a truncated basis set on a series of alkene compounds, with 6 to 20 carbon atoms and 1 to 9 conjugated double bonds. The compounds with one double bond are of the general form $CH_3(CH_2)_nCH{=}CH(CH_2)_nCH_3$ ($n$ = 1,2,3,4,5), where each subsystem is $CH_3(CH_2)_nCH$. These systems are hereinafter referred to as the "alkane-like" systems. The compounds with multiple conjugated double bonds are of the general forms $CH_2(CH)_nCH_2$ ($n$ = 4,8,12,16) or $CH_3(CH)_nCH_3$ ($n$ = 6,10,14,18), with identical starting subsystems of the form $CH_2(CH)_n$ ($n$ = 2,4,6,8) or $CH_3(CH)_n$ ($n$ = 3,5,7,9), respectively. The optimized geometry of these systems are included in the Supporting Information. We chose these systems since they enable one to cut across a covalent (double) bond to obtain two identical closed shell starting subsystems. These hydrocarbon chains allow for the exploration of EO in a truncated basis for systems with localized (in the alkane-like systems) and delocalized (in the conjugated alkenes) electrons.

We compare the energy ($|\Delta E| = |E^{\text{KS-DFT}} - E^{\mathrm{EO}}|$), density ($\Delta^{\mathrm{abs}}$), and dipoles ($|\Delta\mu| = |\mu^{\text{KS-DFT}} - \mu^{\mathrm{EO}}|$) to that of the supermolecular KS-DFT results in Figures 8.2, 8.3, and S1 in the Supporting Information, respectively. These figures show the results after 5 freeze-and-thaw iterations (5ft); we found that increasing to 10 iterations provided no significant improvements on these properties. In these figures, m denotes the FDE(EO,m) method and e$x$ denotes a level of the extended monomer basis expansion, where $x$ denotes the number of carbon atoms and its associated hydrogen(s) whose AOs are included in the overlap region. We show an example of this truncation naming convention for one subsystem of $C_{16}H_{20}$ in Figure 8.4. It should be clear from this that e3 denotes the supermolecular basis in the six carbon chains, e4 is the supermolecular

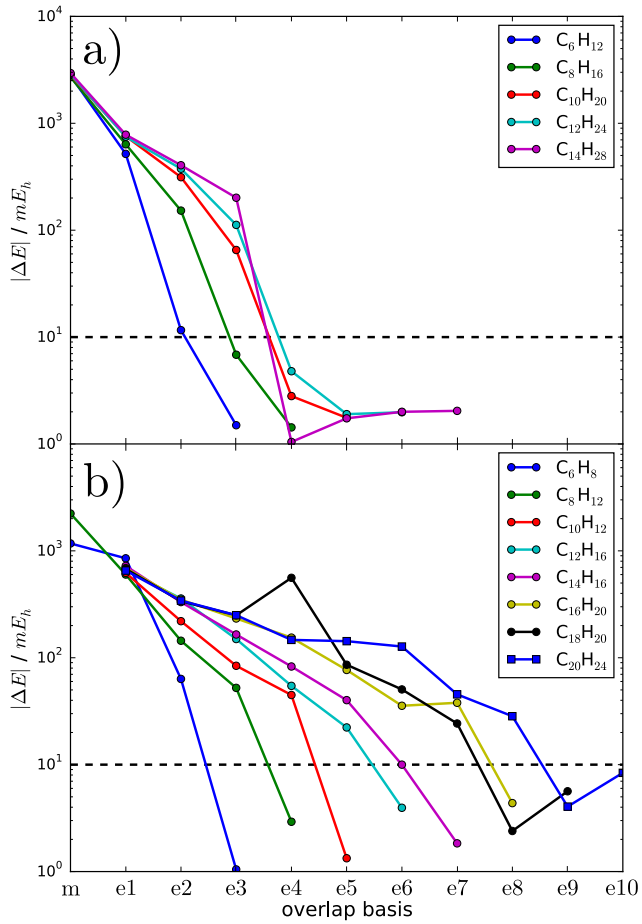


**Figure 8.2.** $|\Delta E|$ in the FDE(EO,5ft) method with different levels of basis set overlap for (a) alkane-like systems, and (b) conjugated alkenes. The dashed line is the energy difference threshold of 10 $mE_h$.

basis in the eight carbon chains, and so on.

Based on the (acceptable) total energy errors obtained with the FDE(TF,cft) method for the water dimer and $FHF^-$ systems (in Table 8.1), we will consider values of $|\Delta E| < 10\ mE_h$ as our energy difference threshold. This is represented as the dashed line in Figure 8.2. We observe that only the supermolecular basis yields acceptable energies for the conjugated alkenes (with the exception of e8 for $C_{18}H_{20}$ and e9 for $C_{20}H_{24}$), whereas different levels of the extended monomer basis yields acceptable energies for the alkane-like systems. In addition to the supermolecular basis, the e3 basis results in acceptable energies for $C_8H_{16}$; the e4 for $C_{10}H_{20}$; e4 and e5 for $C_{12}H_{24}$; and e4, e5, and e6 for $C_{14}H_{28}$. These results indicate that an e4 level of truncation (which corresponds to including AOs from all nucleii $< 5.7$ Å away for these systems) is required to obtained acceptable energies in alkane-like systems (without electron delocalization). However, for the delocalized conjugated alkenes, only the supermolecular basis results in acceptable energies.

Similar results are obtained for density difference (Figure 8.3), with a threshold value of $\Delta^{\text{abs}} < 0.15$. Only the supermolecular calculations results in acceptable density errors in the

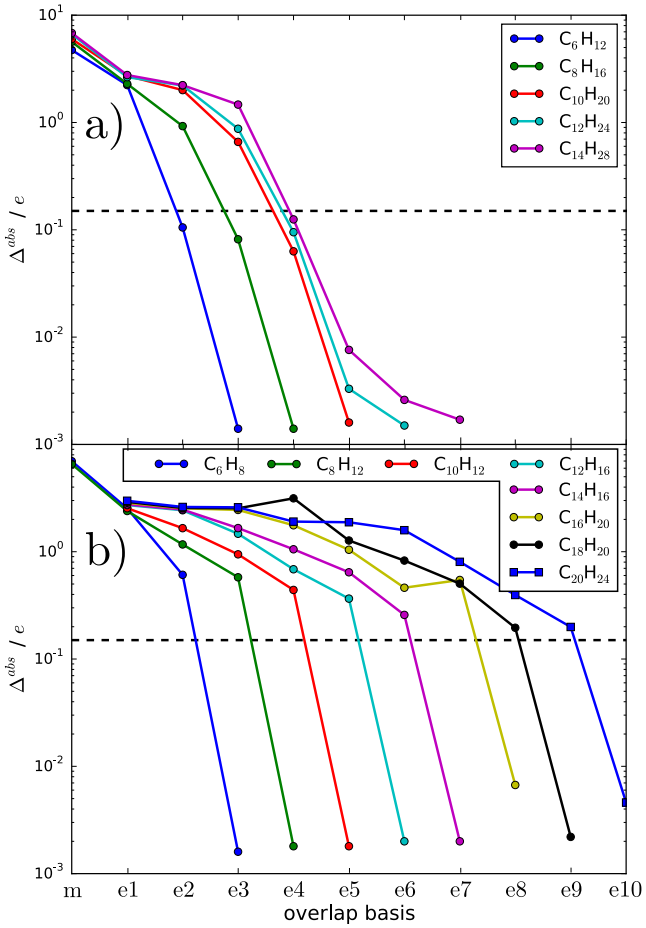


**Figure 8.3.** $\Delta^{\text{abs}}$ for the FDE(EO,5ft) method with different levels of basis set overlap for (a) alkane-like systems, and (b) conjugated alkenes. The dashed line is the $\Delta^{\text{abs}}$ threshold of 0.15 $e$.

conjugated alkene systems. For the alkane-like systems, a number of truncated basis yielded acceptable densities: the e2 for $C_6H_{12}$, e3 for $C_8H_{16}$, e4 for $C_{10}H_{20}$, e4 and e5 for $C_{12}H_{24}$, and e4; e5; and e6 for $C_{14}H_{28}$. For dipoles (Figure S1), with an acceptable threshold of $|\Delta\mu| < 0.25$ $D$, the same level of basis set truncation yields acceptable for the alkane-like systems, while the only the supermolecular basis (and e4 truncation for $C_{10}H_{12}$) yields acceptable dipole errors for the conjugated alkenes. We note that e7 for $C_{16}H_{20}$ and e4 for $C_{18}H_{20}$ appear as outliers in the trend of improving energy, density and dipole errors with increasing levels of basis set truncation. The reason for this is uncertain, and may be due to the quality of the starting subsystem. We point out that most of the conjugated alkenes starting subsystems were converged to $\sim 0.1$ $E_h$ after 100 SCF iterations, yet this does not seem to affect the results of the FDE(EO,5ft) calculations (except for the two truncations mentioned above).

The large errors in some levels of the extended basis truncation may be attributed to the $\mu$-dependence of these truncated systems, as was explored in ref. 199, where $|\Delta E|$ changes of two

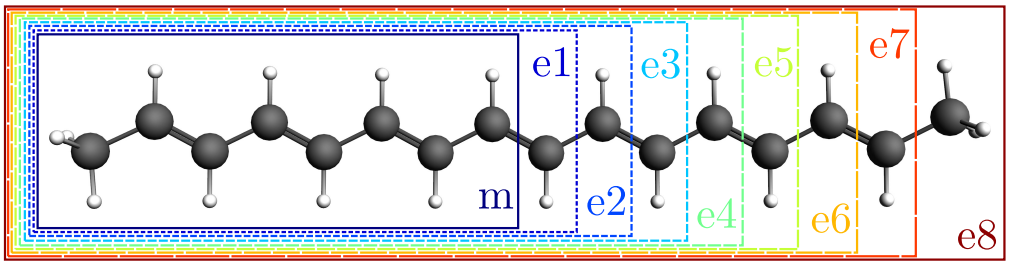


**Figure 8.4.** An example of the basis set truncation used for one subsystem of $C_{16}H_{20}$.

orders of magnitude and greater were observed for $\mu$ values ranging between $10^2$–$10^8$. In that paper, it was found that projecting only the MOs that are localized within the AO space of the active subsystem removes the $\mu$-dependence, and subsequently led to a reduction in the energy error of the truncated systems. In Figure 8.5, we plot the energy differences of the different levels of basis set truncations for the two 10-Carbon ($C_{10}H_{20}$ and $C_{10}H_{12}$) systems. We observe no strong dependence of $|\Delta E|$ on the $\mu$-parameter for any of the extended monomer basis truncation, with very little change between $\mu$ values of $10^4$–$10^8$. The only exception to this is in the monomer basis truncations, for which there are no MO localization counterpart since there are no common AOs describing both subsystems. We will continue to explore the reasons for the large errors seen in some levels of the extended monomer basis truncation, particularly as it relates to the results seen for the conjugated alkenes, in the remainder of this chapter.

The failure of an FDE(EO) method with an extended monomer truncated basis for the conjugated alkenes may be attributed to three factors: (1) insufficient overlap basis to achieve orthogonality between subsystems, (2) insufficient (mutual) polarization of subsystems, and (3) insufficient AO space for subsystems to accurately reproduce supermolecular MOs. We propose that the extent of subsystem MO orthogonality obtained may be assessed through the value of the "overlap energy", defined as

$$E^{\text{ovrlp}}[\phi^I, \phi^{II}] = \mu \text{tr}\left(\gamma^I \mathbf{P}^{II}\right) \tag{8.7}$$

This value was shown to be the first order perturbative correction to the total energy of the system,[198] and we will use it as a measure of the extent of orthogonality attained between subsystem MOs. Mathematically, this value measures the overlap between the subsystem MOs, and is exactly zero for perfectly orthogonal MOs. We explore the overlap energy at successive freeze-and-thaw iterations for an alkane-like system ($C_{14}H_{28}$ in Figure 8.6a) and a conjugated alkene ($C_{18}H_{20}$ in Figure 8.6b). In this figure, a half cycle corresponds to the thawing of the initially frozen subsystem, and an $E^{\text{ovrlp}}$ value of $10^{-6}$ $E_h$ is effectively zero with $\mu = 10^6$ $E_h$. In the $C_{14}H_{28}$ system, we found that the e4, e5, and e6 truncation were sufficient at reproducing acceptable energy, density and dipoles errors (Figures 8.2, 8.3, and S1), but only the e5 and e6 truncation were suffcient at producing perfectly orthogonal MOs. The e4 truncation was sufficient to enforce orthogonality of one subsystem MOs with respect to the other, but not the other way around. Note that, although the initial subsystems are identical, we choose one subsystem to be

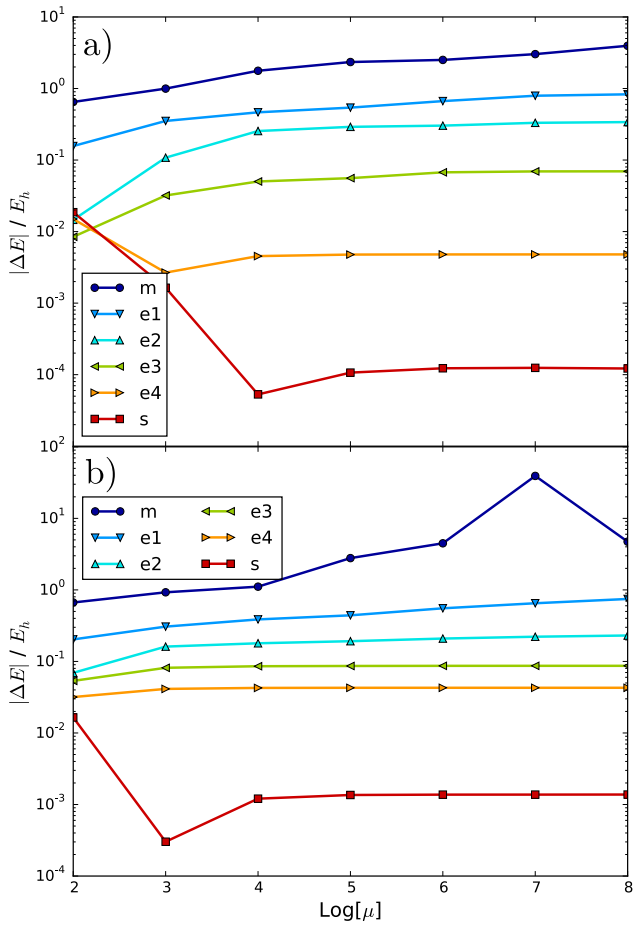


**Figure 8.5.** The dependence of the $|\Delta E|$ on the $\mu$-parameter for different levels of truncations in (a) $C_{10}H_{20}$, and (b) $C_{10}H_{12}$.

the starting active subsystem, which can lead to asymmetrical results. For the $C_{18}H_{20}$ system, the e7 and e8 truncations were sufficient at achieving orthogonality between subsystem MOs. This suggests that a lack of EO is not the reason for large energy, density and dipole errors observed for this molecule at these truncation levels. We can also rule out insufficient polarization since increasing to 10 freeze-and-thaw cycles did not improve on these errors. Therefore, we can conclude that the inability of the e7 and e8 truncations of this system to reproduce the KS-DFT energy, density and dipole is due to an inability of the spatially limited subsystem basis at describing the delocalized supermolecular MOs.

There are other ways in which one may truncate the basis set of the overlap region, while maintaining the spatial distributions of AOs. We examined the effects of reducing the quality of overlapping AOs, from TZ2P to DZP, while maintaining a TZ2P description of remaining AOs. This was done by simply changing the basis type of the ghost atoms in the overlap region. We show these results in Figure 8.7, along with the results of supermolecular basis and the extended monomer basis that is one level below the supermolecular basis (that is, e2 for $C_6H_8$, e3 for $C_8H_{12}$,

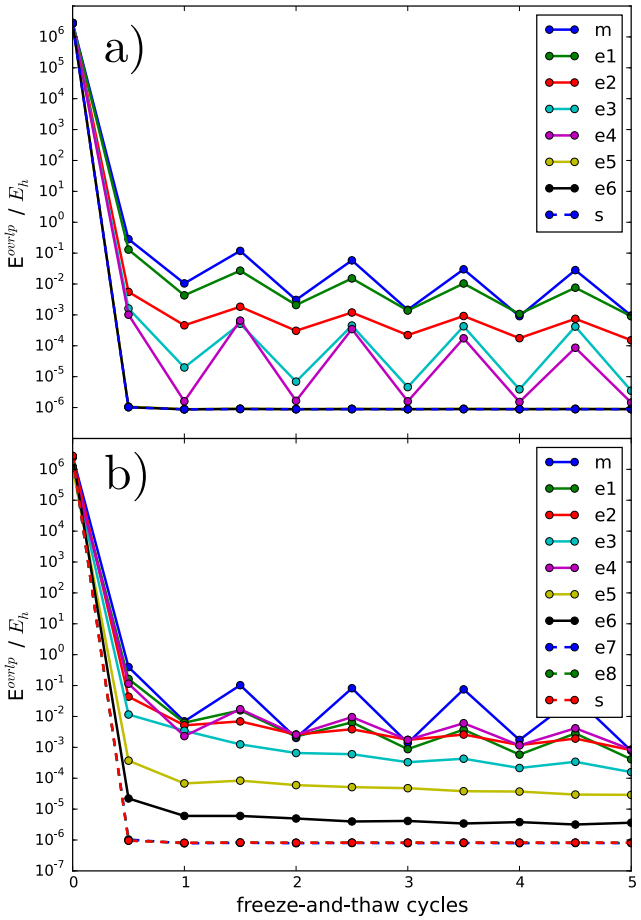


**Figure 8.6.** $E^{\mathrm{ovrlp}}$ at successive freeze-and-thaw cycles for (a) $C_{14}H_{28}$ and (b) $C_{18}H_{20}$.

e4 for $C_{10}H_{12}$, and so on). This DZP truncation yields acceptable energy and density errors for all systems, while large dipole errors were only observed for the $C_{18}H_{20}$ and $C_{20}H_{24}$ systems. The dipole errors for these alkene chains are particularly sensitive to the chain length, since they rely on the addition of large dipole vectors of the individual subsystems to yield the (almost) zero dipole vector of the supermolecular system. These results clearly show that reducing the quality of the overlap basis is a better basis set truncation strategy in delocalized systems, rather just including the set of nearby AOs.

Additionally, the DZP truncation is much more efficient in reducing the number of AOs when compared to the extended monomer strategy. The DZP truncation resulted in a 25 % reduction of the supermolecular AOs for all systems, whereas the extended monomer basis resulted in an 8 % reduction for the $C_{20}H_{24}$ system to a maximum of 20 % reduction for the $C_6H_8$ system (see Figure S2 in the Supporting Information). We note that a further reduction to a SZ basis set for the overlap region resulted in errors that were comparable to the extended monomer strategy. This reduction in AOs results in a significant reduction in computation time (Figure S3

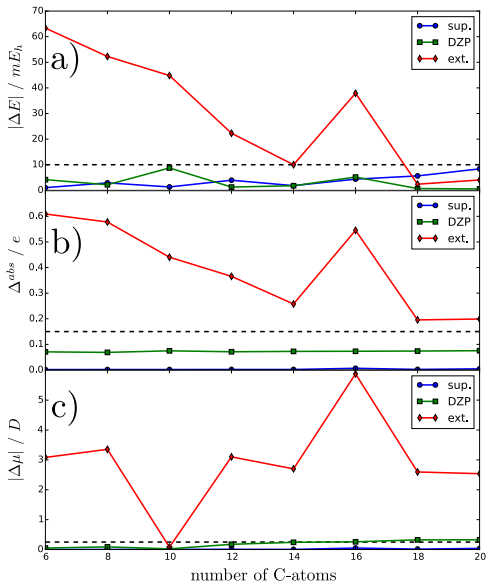


**Figure 8.7.** Results from the supermolecular basis (sup.), truncated basis with DZP overlap (DZP), and the extended monomer basis that is one level below that of the supermolecular basis (ext.) showing the (a) absolute energy difference, (b) integrated density difference, and (c) absolute dipole difference for the conjugated alkenes.

in the Supporting Information), and is more efficient than the ineffective extended monomer-type truncation. However, we point out that these methods are still more expensive than the supermolecular KS-DFT calculations. The effectiveness of these embedding methods will therefore depend on eliminating the need for iterative freeze-and-thaw cycles and/or increasing the number of basis functions truncated. Olsen and co-workers[358] have implemented a strategy that eliminates the need for mutual polarization through iterative freeze-and-thaw cycles by using a classical polarizable force field. Additionally, one may employ the dual truncation strategy of reducing the number of atoms in the overlap region as well as the quality of these overlap AOs when working with non-covalent systems or covalent systems with localized charge distributions.

## 8.5 Conclusion

In this chapter, we presented an EO implementation into the FDE framework within ADF. This method is a generalized form of the level-shifting projection operator method of Miller and co-workers, extended to include any (and multiple) starting subsystem KS orbitals. We showed that the KS-DFT densities and energies are exactly reproduced with iterative freeze-and-thaw cycles for a number of systems with a range of overlapping density strengths. We also showed that the exact density of a charge delocalized system (benzene) is exactly reconstructed from atomic subsystems. Finally, we examined the limits of a truncated basis for such a method and found that, while including only the nearest AOs works well for alkane-like systems, only the supermolecular basis reproduced the exact supermolecular KS-DFT results in charge delocalized

systems. For such systems, we found that reducing the quality of the overlap basis to be a more effective and efficient strategy.

# Chapter 9
# External Orthogonality in Subsystem Time-dependent Density Functional Theory

Chulhai, D. V.; Jensen, L. "*External Orthogonality in Subsystem Time-dependent Density Functional Theory*" *Phys. Chem. Chem. Phys.* **2016**, DOI:10.1039/c6cp00310a

## Abstract

Subsystem density functional theory (subsystem DFT) is a DFT partitioning method that is exact in principle, but depends on approximations to the kinetic energy density functional (KEDF). One may avoid the use of approximate KEDFs by ensuring that the inter-subsystem molecular orbitals are orthogonal, termed external orthogonality (EO). We present a method that extends a subsystem DFT method, that includes EO, into the time-dependent DFT (TDDFT) regime. This method therefore removes the need for approximations to the kinetic energy potential and kernel, and we show that it can accurately reproduce the supermolecular TDDFT results for weakly and strongly coupled subsystems, and for systems with strongly overlapping densities (where KEDF approximations traditionally fail).

## 9.1 Introduction

The computational limitations of modeling large systems, along with the fact that most of chemistry is centered around a smaller subsystem or active site, have led to the development of subsystem methods.[349] One very popular subsystem method is subsystem density functional theory (subsystem DFT).[175–178] Subsystem DFT is a partitioning method that separates the supermolecular system via the real-space electron density ($\rho(\mathbf{r})$), where each subsystem is treated using Kohn-Sham (KS) DFT and is exact in the limit of exact functionals. In such a method, the total energy of the system is minimized under the constraint that the number of electrons for each subsystem remains fixed. The most common subsystem DFT scheme is frozen density embedding (FDE),[179] where the total energy is minimized with respect to one active/embedded subsystem ($\rho_A(\mathbf{r})$) while the remaining environment subsystem(s) ($\rho_B(\mathbf{r})$) is "frozen". Minimization of the total energy with respect to all subsystem densities is achieved through freeze-and-thaw cycles, where the roles of subsystems A and B are iteratively interchanged. The excited states formulation of FDE within the time-dependent DFT (TDDFT) framework, sometimes referred to as subsystem TDDFT or FDE-TDDFT, has also been developed.[204–206] There have been two general implementations of FDE-TDDFT: the first only accounts for the changes in the orbitals and orbital energies that stem from the embedding potential—the response of the environment is neglected—termed "uncoupled" FDE-TDDFT or FDEu; the second includes coupling to the environment response and is termed "coupled" FDE-TDDFT or FDEc.

Although FDE is an exact theory, approximations to the exchange-correlation (XC) functional and the kinetic energy density functional (KEDF) have to be made for practical applications. Available KEDFs are acceptable only for subsystems with weakly overlapping densities, and have been shown to fail for other systems.[184,187,188] Similarly, the subsystem TDDFT response depends on approximations for the XC and kinetic energy kernels. Alternatively, one may circumvent the need for approximate KEDFs by ensuring that the KS orbitals are both internally (with respect to the KS orbitals on the same subsystem) and externally (with respect to the KS orbitals of the other subsystems) orthogonal. Methods that enforce external orthogonality (EO) include frozen-core approximations,[192] model potentials,[193] the Phillips-Kleinman pseudopotential approach,[194] and the methods of Stoll and co-workers,[195] Mata and co-workers,[196] and Henderson.[197] In particular, Manby, Miller and co-workers,[198–200] Hoffmann and co-workers,[191] and the authors of this paper[359] have shown that the supermolecular KS-DFT ground-state density and energy may be exactly obtained from subsystem DFT, providing that there is EO. More recently, Neugebauer and co-workers[188,189] have eliminated the need for approximate KEDFs through the use of reconstructed potentials, and extended this into the subsystem TDDFT regime. Using this method, they have shown that accurate local excitation energies (when compared to supermolecular TDDFT) may be obtained through a subsystem TDDFT method.[189]

Recently, we presented a method that enforces EO in conventional FDE calculations, which we termed FDE-EO,[359] that is based on the level-shift projection operator method of Manby and co-workers.[198–200] The FDE-EO method represents a flexible implementation of EO, since one can start with any approximate solution of the individual subsystems, and iterate through

freeze-and-thaw cycles in order to obtain the converged supermolecular KS-DFT results; the supermolecular KS-DFT results do not need to be known *a priori*. The FDE-EO method proved to be very robust, and reproduced supermolecular KS-DFT ground-state densities and energies for systems ranging from weakly interacting to covalently bonded.

In this paper, we expand the FDE-EO method into the subsystem TDDFT regime. We do this by examining the first order response of the EO level-shift projection operator, and explore its behavior on a selection of model systems. These model systems have been chosen in order to test the FDE-EO response formalism in the limits where traditional subsystem TDDFT methods start to fail, in particular, in the limit of strongly overlapping densities and systems with charge-transfer-like excitations. The rest of this paper is organized as follows: we first present a brief background on subsystem TDDFT and the FDE-EO method, before describing the the FDE-EO subsystem response method; we then examine the behavior of the $\mu$-parameter on the excitation energies; Finally, we apply the FDE-EO subsystem response method to the LiH, He-dimer, 2-aminopyridine–methanol, and benzaldehyde-dimer model systems.

## 9.2 Theory

### 9.2.1 Subsystem TDDFT

In this subsection, we will briefly outline the supermolecular and subsystem TDDFT methods. More detailed derivations may be found in refs 206 and 203. We use the subscripts $i$, $j$, ... for occupied molecular orbitals (MOs), subscripts $a$, $b$, ... for virtual MOs, subscripts $p$, $q$, ... for general MOs, and subscripts $\alpha$, $\beta$, ... for atomic orbitals (AOs). We have also dropped the spin indices for simplicity, and present results using only closed-shell restricted subsystems. The theory is presented here for two subsystems, A and B, but is easily generalizable to multiple subsystems.

In the TDDFT framework, the excitation energies may be obtained from the following set of eigenvalue equations

$$\Omega \mathbf{F}_k = \omega_k^2 \mathbf{F}_k \tag{9.1}$$

where $\omega_k$ corresponds to an excitation energy of the system with the corresponding eigenvector $\mathbf{F}_k$. The four-index matrix $\Omega$ is defined as

$$\Omega_{ia,jb} = \delta_{ij}\delta_{ab}\omega_{ia}^2 + 2\sqrt{\omega_{ia}} K_{ia,jb} \sqrt{\omega_{jb}} \tag{9.2}$$

where the coupling matrix $\mathbf{K}$ in turn is defined as

$$K_{ia,jb}(\omega) = \int d\mathbf{r} \int d\mathbf{r}' \phi_i(\mathbf{r})\phi_a(\mathbf{r}) \left[ \frac{1}{|\mathbf{r}-\mathbf{r}'|} + f_{xc}(\mathbf{r},\mathbf{r}',\omega) \right] \phi_j(\mathbf{r}')\phi_b(\mathbf{r}') \tag{9.3}$$

The first term in brackets in eqn 9.3 is the Coulomb kernel, while $f_{xc}$ is the XC kernel and is often approximated by the adiabatic local density approximation (ALDA). This coupling matrix determines the change in electronic potential ($\delta\nu$) due to a change in electron density ($\delta P$) through

$$K_{ia,jb} = \frac{\delta \nu_{ai}}{\delta P_{jb}} \tag{9.4}$$

For the subsystem theory, we will consider subsystems A and B ($\rho_{tot}(\mathbf{r}) = \rho_A(\mathbf{r}) + \rho_B(\mathbf{r})$). In subsystem DFT, the total potential on active subsystem A due to an environment subsystem B is

$$\nu^{\mathrm{A(B)}}(\mathbf{r}) = \nu^{\mathrm{nuc}}(\mathbf{r}) + \int \frac{\rho_{tot}(\mathbf{r}')}{|\mathbf{r}-\mathbf{r}'|} + \nu_{\mathrm{xc}}[\rho_{tot};\mathbf{r}] + \nu_T[\rho_{tot};\mathbf{r}] - \nu_T[\rho_A;\mathbf{r}] \tag{9.5}$$

where the terms on the right-hand side of eqn 9.5 are the nuclear potential, the Coulomb potential, the XC potential, and the two terms that constitute the non-additive kinetic potential (NAKP), respectively. $\nu_T$ is the kinetic potential, which is taken as the functional derivative of the KEDF.

Like the ground-state density, the density response is also partitioned into subsystem contributions ($\delta\rho_{tot}(\mathbf{r}) = \delta\rho_A(\mathbf{r}) + \delta\rho_B(\mathbf{r})$). The corresponding change in potential due to the respective density responses are

$$\frac{\delta \nu^{\mathrm{A(B)}}(\mathbf{r})}{\delta \rho_A(\mathbf{r}')} = \frac{1}{|\mathbf{r}-\mathbf{r}'|} + f_{xc}[\rho_{tot};\mathbf{r},\mathbf{r}'] + f_T[\rho_{tot};\mathbf{r},\mathbf{r}'] - f_T[\rho_A;\mathbf{r},\mathbf{r}'] \tag{9.6}$$

and

$$\frac{\delta \nu^{\mathrm{A(B)}}(\mathbf{r})}{\delta \rho_B(\mathbf{r}')} = \frac{1}{|\mathbf{r}-\mathbf{r}'|} + f_{xc}[\rho_{tot};\mathbf{r},\mathbf{r}'] + f_T[\rho_{tot};\mathbf{r},\mathbf{r}'] \tag{9.7}$$

where the first two terms in both eqns 9.6 and 9.7 are the Coulomb and XC kernel (evaluated for the total system density). $f_T$ is the kinetic energy kernel, where once again the ALDA form, the second functional derivative of the Thomas-Fermi (TF) KEDF, is most commonly used.

These results allow us to separate the coupling matrix $\mathbf{K}$ into two parts: a part that depends only on the response of the same subsystem ($\mathbf{K}^{\mathrm{A,A}} \equiv \frac{\delta v^{\mathrm{A}}}{\delta \rho_A}$), and a part that depends on the response of the other subsystem ($\mathbf{K}^{\mathrm{A,B}} \equiv \frac{\delta v^{\mathrm{A}}}{\delta \rho_B}$). This, in turn, allows us to partition the eigenvalue equations (eqn 9.1) into

$$\begin{pmatrix} \Omega^{\mathrm{A,A}} & \Omega^{\mathrm{A,B}} \\ \Omega^{\mathrm{B,A}} & \Omega^{\mathrm{B,B}} \end{pmatrix} \begin{pmatrix} \mathbf{F}_k^{\mathrm{A}} \\ \mathbf{F}_k^{\mathrm{B}} \end{pmatrix} = \omega_k^2 \begin{pmatrix} \mathbf{F}_k^{\mathrm{A}} \\ \mathbf{F}_k^{\mathrm{B}} \end{pmatrix} \tag{9.8}$$

For FDEu, one only needs to solve the eigenvalue equations that depend only on the response of one subsystem ($\Omega^{\mathrm{A,A}}\mathbf{F}_k^{\mathrm{A}} = \omega_k^2\mathbf{F}_k^{\mathrm{A}}$ and $\Omega^{\mathrm{B,B}}\mathbf{F}_k^{\mathrm{B}} = \omega_k^2\mathbf{F}_k^{\mathrm{B}}$).[205,206] If the responses of the respective subsystems are strongly coupled, which are needed for FDEc calculations, then one needs to solve the full eqn 9.8.[206] An approximate method for the solution of eqn 9.8 has been presented in ref 206, where the coupled solutions may be approximated from an incomplete set of solved FDEu eigenvalues and eigenvectors. We employ the same strategy in this paper for the solution of the coupled excitations for the larger systems (2-aminopyridine–methanol and benzaldehyde-dimer).

### 9.2.2 The FDE-EO method

The FDE-EO method used in this paper was initially presented in ref 359, and was based on earlier work by Manby and co-workers.[198] In such a method, the MOs of subsystem B are projected on to subsystem A using a level-shift projection operator. The FDE-EO Fock matrix is then modified with this projection operator (hereinafter called the EO "potential", $V^{\mathrm{EO}}$) as

$$F^{\mathrm{EO}}_{\alpha\beta} = F^{\mathrm{FDE}(\nu_T\,=\,0)}_{\alpha\beta} + V^{\mathrm{EO,A(B)}}_{\alpha\beta} \tag{9.9}$$

where $F^{\mathrm{FDE}(\nu_T\,=\,0)}$ is the conventional FDE Fock operator in AO basis with the NAKP set to zero (there is still a contribution from the non-additive XC potential).

The EO potential is defined as[359]

$$V^{\mathrm{EO,A(B)}}_{\alpha\beta} = \mu \sum_{\gamma,\delta\in\mathrm{B}} S^{\mathrm{A,B}}_{\alpha\gamma} P^{\mathrm{B}}_{\gamma\delta} S^{\mathrm{B,A}}_{\delta\beta} \tag{9.10}$$

where $\mu$ is a scaling parameter, $S^{\mathrm{A,B}}_{\alpha\gamma}$ is an AO overlap matrix element between subsystems A and B, and $P^{\mathrm{B}}_{\gamma\delta}$ is a density matrix element of subsystem B.

In our implementation of the FDE-EO method, one only needs to start with approximate KS orbitals for each subsystem. This is done by performing a ground-state KS-DFT calculation on each isolated subsystem, which could be done in either the monomer basis or the supermolecular basis using "ghost" orbitals. One then performs an FDE calculation, projecting the orbitals of all the frozen MOs on to the active/embedded subsystem. This process is repeated through iterative freeze-and-thaw cycles until the total energy of the system is self-consistent.

### 9.2.3 The EO coupling matrix

The EO potential can also be expressed in the MO basis ($^{\dagger}$see the ESI for derivation) as

$$V^{\mathrm{EO,A(B)}}_{pq} = \mu \sum_{r,s\in\mathrm{B}} S^{\mathrm{A,B}}_{pr} P^{\mathrm{B}}_{rs} S^{\mathrm{B,A}}_{sq} \tag{9.11}$$

where $S^{\mathrm{A,B}}_{pr}$ is an element of MO overlap matrix between subsystems A and B, and $P^{\mathrm{B}}_{rs}$ is a density matrix element for subsystem B in MO basis. We can now use the EO operator in MO basis to derive the EO coupling matrix $\mathbf{K}^{\mathrm{EO;A,B}}$ as

$$\begin{aligned} K^{\mathrm{EO;A,B}}_{(ia)_A,(jb)_B} &= \delta V^{\mathrm{EO,A(B)}}_{ia} / \delta P^{\mathrm{B}}_{jb} \\ &= \mu S^{\mathrm{A,B}}_{ij} S^{\mathrm{B,A}}_{ba} \end{aligned} \tag{9.12}$$

This EO contribution to the coupling matrix is then added to the Coulomb and XC kernel contributions as presented in eqn 9.3. Since the same approximation to the XC kernel is used in both the subsystem and supermolecular TDDFT, we will not consider the effects of the particular choice of XC kernel in this paper. We also point out that the EO coupling matrix for a subsystem with itself is zero, since $K^{\mathrm{EO;A,A}} = \delta V^{\mathrm{EO,A(B)}} / \delta P^{\mathrm{A}} = 0$.

For perfectly orthogonal inter-subsystem MOs, the term $S_{pq}^{\mathrm{A,B}} = 0$. However, this is only true for $\mu \to \infty$. For finite $\mu$, we find inter-subsystem (occupied) MO overlaps on the order of $S_{ij}^{\mathrm{A,B}} = \mathcal{O}(\mu^{-1})$. We find it beneficial to calculate the MO overlaps analytically using $S_{ij}^{\mathrm{A,B}} = [(\mathbf{C}^{\mathrm{A}})^T \mathbf{S}^{\mathrm{A,B}} \mathbf{C}^{\mathrm{B}}]_{ij}$, where $\mathbf{C}^{\mathrm{A/B}}$ are the MO coefficient matrices for subsystems A/B, and $\mathbf{S}^{\mathrm{A,B}}$ is the AO overlap matrix between subsystems A and B. Additionally, since only the occupied MOs are projected on to each other subsystem, there is no guarantee that the inter-subsystem virtual MOs are orthogonal. In fact, we find similar virtual orbital space (possibly varying only in sign) for subsystems described using the supermolecular basis. Therefore, the EO coupling term in eqn 9.12, since it is scaled by $\mu$, becomes significant in the coupled response. One may also think of the EO coupling matrix as a first order correction to the coupled response due to a finite $\mu$, similar to that of the ground-state energy,[198] which should vanish for perfectly orthogonal inter-subsystem MOs.

## 9.3 Computational Details

The TDDFT extensions of the FDE-EO method have been implemented into a modified version of the Amsterdam Density Functional (ADF) program package.[165,326,360] All calculations presented in this work were performed using the Vosko–Wilk–Nair (VWN)[151] form of the local density approximation (LDA) XC potential. The triple-$\zeta$ with one polarization function (TZP) basis set from the ADF basis set library[361] was used for all systems except the helium-dimer, where a double-$\zeta$ (DZ) basis set was used. Geometry optimizations for the 2-aminopyridine–methanol system and the benzaldehyde monomer were also performed with the above described level of theory. All monomer subsystems have been expanded in the supermolecular basis for all subsystem DFT calculations. The Thomas-Fermi (TF) LDA to the NAKP[145,146] and the TF ALDA to the kinetic energy kernel were used for all conventional FDE calculations. For all FDE-EO calculations (except where stated), the subsystems' KS orbitals are orthogonalized using a level-shift parameter of $\mu = 10^6$ $\mathrm{E}_h$. All absorption stick spectra were broadened by Lorentzians with a full-width at half-maxima (fwhm) of 0.1 eV.

## 9.4 Results and Discussion

### 9.4.1 Dependence on $\mu$-parameter

We will first examine the nature of the $\mu$-parameter and its effects on both the ground and excited state properties of a system. Since we are enforcing external orthogonality, the results should agree exactly with that of the supermolecular KS-DFT. However, this is true only in the limit of infinite $\mu$. In practical applications, errors are introduced from the finite value of $\mu$. For the ground-state energy, it has been shown[198] that the error introduced due to a finite $\mu$ may be corrected (to first order using perturbation theory) by $\mu \mathrm{Tr}[\mathbf{P}^{\mathrm{A}} \mathbf{V}^{\mathrm{EO,A(B)}}]$, where $\mathbf{P}^{\mathrm{A}}$ and $\mathbf{V}^{\mathrm{EO,A(B)}}$ are the density matrix of subsystem A and the projection operator of subsystem B onto A (in AO basis) introduced earlier. This term has been used as a measure of the orthogonality achieved

between subsystems[359] and has been termed the "overlap energy". When corrected with this overlap energy, it was found that the total energy from the EO method agrees with that from KS-DFT (to within $10^{-11}$ $E_h$) for $10^2 \leq \mu \leq 10^7$ $E_h$.[198]

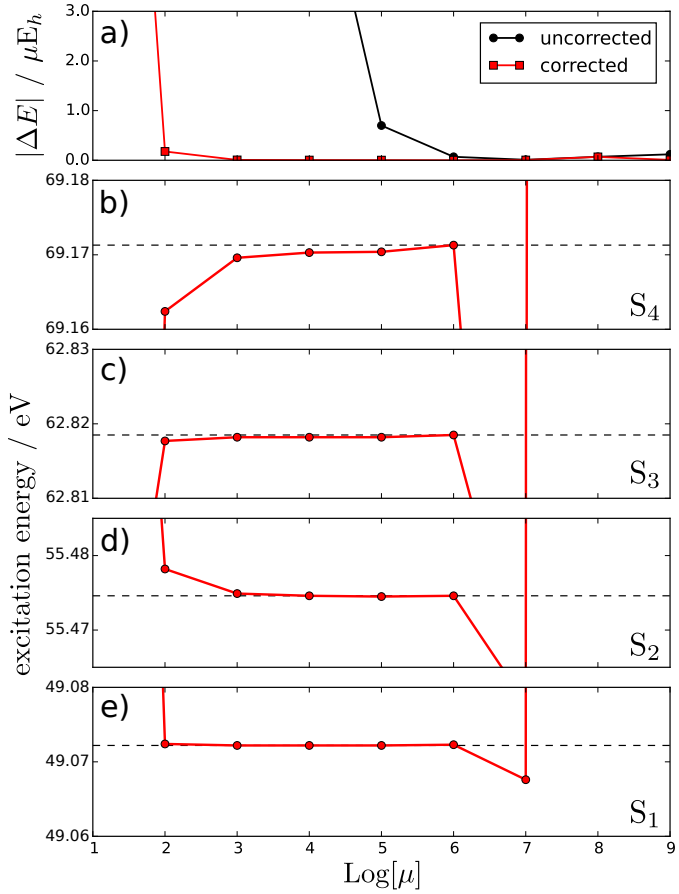


**Figure 9.1.** Stability of (a) the absolute energy difference (with respect to a supermolecular KS-DFT result), and (b–e) excitation energies of the four transitions of a He-dimer with respect to the $\mu$-parameter.

Using a model He-dimer system with a 1 Å separation, we plot both the absolute ground-state energy difference (between the EO method and supermolecular KS-DFT) and the excitation energies as a function of the value of the $\mu$-parameter in Fig. 9.1. Fig. 9.1a shows both the uncorrected and corrected (with the overlap energy) absolute energy differences. For the uncorrected energies, we find sub-microhartree ($\mu E_h$) differences for all $10^5 \leq \mu \leq 10^9$ $E_h$. When corrected with the overlap energy, this range extends to $10^2 \leq \mu \leq 10^9$ $E_h$, spanning seven orders of magnitude.

We also show the transition energies of the four excited states of the He-dimer ($S_1$, $S_2$, $S_3$, and $S_4$) in Fig. 9.1b–e. These subsystems are strongly coupled (a point that will be discussed later in this paper) and the results shown here have been calculated using the FDEc-EO method. As previously mentioned, the FDEc-EO method (using the EO coupling matrix in eqn 9.12) can also be thought of as a correction to the response due to a finite $\mu$. Additionally, since

the inter-subsystem occupied MO overlaps are dependent on the choice of $\mu$-parameter for the ground-state calculation, the same value of $\mu$ must be used for both ground-state and coupled excited states calculations. Using the FDEc-EO method, we find that the excitation energies are stable (to within 0.002 eV) for the range $10^3 \leq \mu \leq 10^6$ $E_h$ (spanning three orders of magnitude).

For all the remaining calculations in this paper, we will use $\mu = 10^6$ $E_h$, since this value lies within the stable ranges for both ground-state and excited state energies, as well as producing the smallest correction to the ground-state energy.

### 9.4.2 LiH

In order to study the effect of the EO method on the excitation of uncoupled subsystems, we examined the LiH molecule. This model system is made up of two closed-shell subsystems with two electrons each ($Li^+$ and $H^-$). This construction leads to inter-subsystem excitation energies that are well separated—all excitations for the $Li^+$ subsystem are greater than 48 eV with the current level of theory. We note that the ground-state properties of this system are incorrectly described by the FDE-TF method; we find FDE-TF energy errors (compared to KS-DFT) of 0.04 $E_h$ at 6 Å separation, which increases to 0.12 $E_h$ at 1 Å. For the FDE-EO method, we find ground-state (uncorrected) energies that are within 0.1 $\mu E_h$ of the KS-DFT results for all separation distances. Therefore, the LiH system represents a model (uncoupled) system for which conventional FDE-TF fails, but for which FDE-EO is able to describe correctly.

In Fig. 9.2, we plot the five lowest excitation energies of the $H^-$ subsystem of LiH (excitations $S_2$ and $S_3$ are degenerate) against inter-subsystem separation using three methods: supermolecular TDDFT, FDEu-TF, and FDEu-EO. These five excitations are all less than 10 eV, and are therefore uncoupled from the $Li^+$ subsystem excitations. We also performed the coupled calculations using both the FDEc-TF and FDEc-EO methods, but since the excitations are uncoupled, those results are near identical to the uncoupled results and we do not include them here. We observe that the FDEu-TF method shows no qualitative agreement with the supermolecular TDDFT results, even at 6 Å separation. This is due to the incorrect electronic structure of the ground-state system obtained by the FDE-TF method, as evidenced by the large ground-state energy errors ($> 0.01$ $E_h$). One should naturally expect that if conventional FDE fails for the ground-state electronic structure of a system, so too will its TDDFT extension. It was previously found that the kinetic potential for the frozen subsystem is incorrect at large inter-subsystem separations,[362] leading to badly described orbitals (and consequently incorrect response properties), and a correction was thus presented. We found that this correction had little effect on the LiH system (see Fig. S1$^\dagger$) for the distances examined. At longer separation distances, an unrestricted formalism is needed to correctly describe the supermolecular system—which is beyond the scope of this work.

For the FDEu-EO method, on the other hand, we observe good quantitative agreement with supermolecular TDDFT results at all separation distances. At 1 Å separation, the mean absolute error (MAE) for the excitation energies using the FDEu-EO method (for all 40 excitations) is 0.01 eV, which decreases to 0.0004 eV at 6 Å. Note that the only contributions to the response kernel in the FDEu-EO method are the Coulomb and XC kernels, and therefore the correct response of these uncoupled systems depend entirely on the accuracy of the ground-state electronic structure.

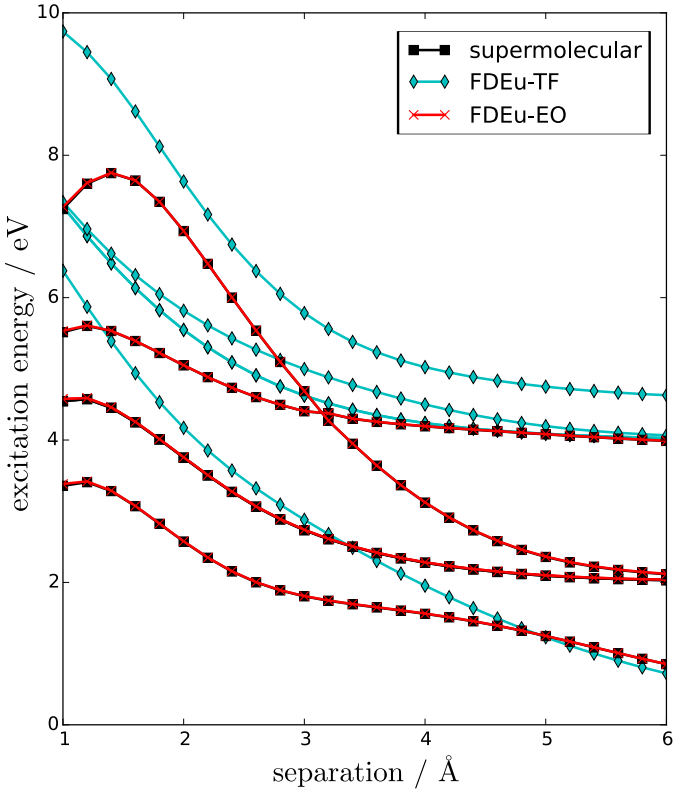


**Figure 9.2.** Excitation energies of the five lowest transitions of LiH with respect to inter-atomic separation. Energies are plotted for the supermolecular TDDFT, the FDEu-TF, and the FDEu-EO methods.

### 9.4.3 He-dimer

We study the case of a strongly coupled model system in Fig. 9.3, where we plot the excitation energies of the He-dimer against inter-atomic separation. This system is constructed from two atomic He subsystems with two electrons each. We chose a small basis set (DZ) so that we could correctly monitor all excitations; in the DZ basis, each monomer has one (local) excitation at 59.06 eV in the monomer basis, and three excitations in the supermolecular basis (at 27.58, 59.06, and 151.61 eV at 4 Å separation). The transition at 59.06 eV is a local excitation (which is the same as the transition observed with the monomer basis) and the transitions at 27.58 and 151.61 eV are charge-transfer-like in nature. We acknowledge that these monomer excitations (in the supermolecular basis) are weakly dependent on atomic separation due to the size of the basis set chosen (DZ) and basis set superposition error. In the supermolecular system, there are four excitations. At 4 Å separation, these are: degenerate charge-transfer-like excitations at 50.88 eV, and degenerate local excitations at 59.08 eV. This model system was chosen because the inter-subsystem response couplings are strong, and we observe excitation energy splits of 5.88 and 4.88 eV for the charge-transfer-like and local sets of excitations, respectively, at 1 Å separation using the supermolecular TDDFT method.

We now examine the excitations using the different subsystem TDDFT methods. In the

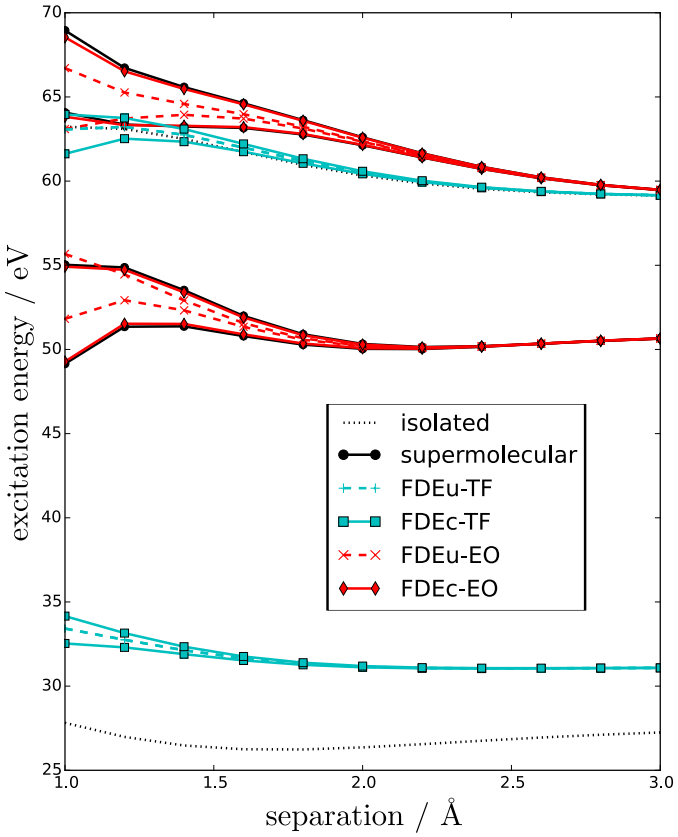


**Figure 9.3.** Excitation energies of a He-dimer as a function of atomic separation.

subsystem methods, there are a total of six excitations (three from each subsystem in the supermolecular basis), two of which should be fictitious due to the available orbital space. In the EO method, these fictitious excitations are shifted to very high energies (on the order of $\mathcal{O}(\mu)$ $E_h$) since the orbitals involved in these transitions are not orthogonal to all the occupied orbitals of supersystem. The methods based on the approximate TF KEDF make no such correction, and as such, we find that these methods fail to correctly describe the charge-transfer-like excitations even at large inter-atomic separations. The local degenerate excitations at ∼59.06 eV, however, is correctly described by both the FDEu-TF and FDEu-EO methods, as expected, with an MAE of 0.0001 eV. But as the inter-atomic distance decreases, the TF methods start to fail (see Fig. 9.3) and result in errors of 2.49 and 4.99 eV for the two coupled local excitations at 1 Å separation. The FDEc-EO method, on the other hand, correctly captures both the local and charge-transfer excitations, with an MAE (for all excitations) of 0.2 eV at 1 Å separation, which improves to 0.07 eV at 1.6 Å separation. We should point out that the EO contribution to the inter-subsystem coupling matrix, and not the Coulomb or XC kernels, is responsible for the strong coupling observed; we show the results of this system without including the EO coupling matrix in Fig. S2$^{\dagger}$. We acknowledge that an MAE of 0.2 eV (at 1 Å) is still very large; this error may be due to numerical inaccuracies (since the occupied MO overlaps are $\mathcal{O}(\mu^{-1})$ and is being scaled by $\mu$), or

to eqn 9.12 being a correction to first order only in the subsystem response with near-orthogonal orbitals caused by a finite $\mu$.

We also observe in Fig. 9.3 that the excitation energies obtained from the FDEu-EO method are not degenerate at <2.0 Å separations, while the FDEu-TF excitation energies remain degenerate. This is because, at these distances, the occupied MOs involved in these "degenerate" excitations start to overlap and are no longer orthogonal. In order to maintain orthogonality between all occupied MOs, the EO method therefore shifts the energy of these occupied orbitals relative to each other, causing the excitation energies for their respective transitions to shift. Since this is not accounted for in the TF KEDF, the FDEu-TF excitation energies remain degenerate. The further splitting between the FDEu-EO and FDEc-EO methods (and indeed, between the FDEu-TF and FDEc-TF methods) is then due to the coupling between the two sets of excitations.

### 9.4.4 2-aminopyridine–methanol

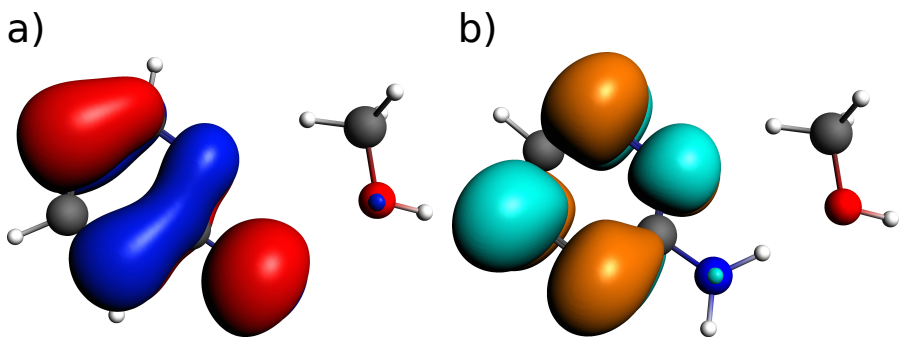


**Figure 9.4.** Isosurface plots of the (a) $\pi$ and (b) $\pi^*$ orbitals (value = $\pm$ 0.03 a.u.) involved in the 2-aminopyridine–methanol transition analyzed in this paper.

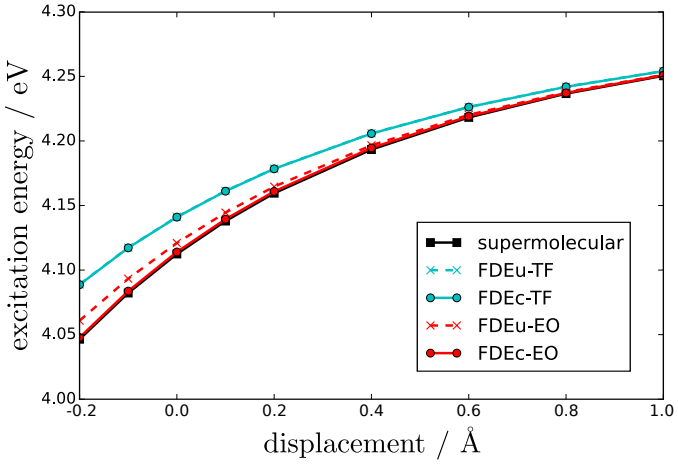


**Figure 9.5.** Excitation energy of the lowest singlet $\pi \rightarrow \pi^*$ transition in the 2-aminopyridine–methanol system as a function of hydrogen bond displacement.

As a test on a more realistic weakly-coupled system, and to compare our results with that of the reconstructed NAKP method,[189] we examined the lowest singlet $\pi \rightarrow \pi^*$ transition in a 2-aminopyridine–methanol system. The system is divided into a 2-aminopyridine and a methanol subsystem, where the orbitals that contribute to the analyzed transition are shown in Fig. 9.4. This transition is therefore a local excitation centered on the 2-aminopyridine subsystem. Significant solvent effects have been observed for this transition in earlier studies.[189,363] Fig. 9.5 plots the energy of this transition with respect to the hydrogen bond displacement (from the equilibrium geometry) while keeping the individual subsystem geometries fixed; a displacement of 0 Å represents the equilibrium hydrogen bond length of 1.77 Å. In ref 189, the subsystem excitation energy of this transition has been analyzed using FDEu for the excited state response with the TF, PW91k,[185,186] and a reconstructed kinetic potential[188] for the ground-state calculation. In that paper, it was found that the PW91k NAKP resulted in an error of 0.03 eV at the equilibrium distance (in the monomer basis), compared to 0.02 eV for the TF NAKP and 0.003 eV for the reconstructed potential.[189]

We find that, at the equilibrium geometry, the FDE-TF/FDEu-TF methods (in the supermolecular basis) resulted in an error of 0.03 eV with respect to the supermolecular TDDFT results; this is consistent with the results obtained in ref 189. The results from the FDEc-TF method are also near-identical to those of the FDEu-TF method (Fig. 9.5), suggesting that this system is uncoupled using this level of theory. The FDEu-EO and FDEc-EO methods resulted in errors of 0.009 and 0.002 eV at the equilibrium geometry, respectively; these errors are also comparable to those obtained with the reconstructed potential, though we should point out that we use the supermolecular basis compared to the monomer basis in ref 189. At a displacement of -0.2 Å, the observed errors are 0.01 and 0.001 eV for the FDEu-EO and FDEc-EO methods, respectively. A noteworthy observation is that this transition is (weakly) coupled to the methanol response, as evidenced by the small differences between the excitation energies obtained from the FDEu-EO and FDEc-EO methods, whereas the FDEu-TF/FDEc-TF methods show it to be uncoupled; the lowest excitation in the methanol subsystem is at 5.3 eV.

### 9.4.5 Benzaldehyde-dimer

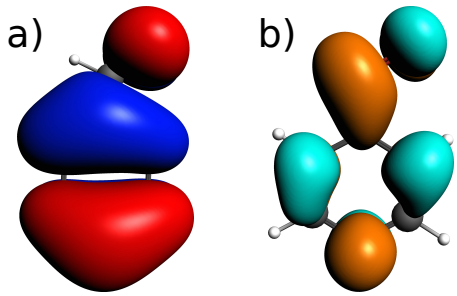


**Figure 9.6.** Isosurface plots of the (a) $\pi$ and (b) $\pi^*$ orbitals (value = $\pm$ 0.03 a.u.) involved in the local transition of the benzaldehyde subsystems examined.

We also examined the strongly coupled local transitions in a benzaldehyde-dimer. The

benzaldehyde-dimer system is made up of two identical benzaldehyde subsystems, separated by the axis that runs perpendicular to the benzene ring. This system has been previously used to test the implementation of the coupled subsystem excitations method presented in ref 206. The local excitation examined is the lowest $\pi \rightarrow \pi^*$ transition with a significant oscillator strength ($f = 0.23$), which is found at 4.921 eV (in the monomer basis). The $\pi$ and $\pi^*$ orbitals involved in this local transition are shown in Fig. 9.6 for the benzaldehyde monomer.

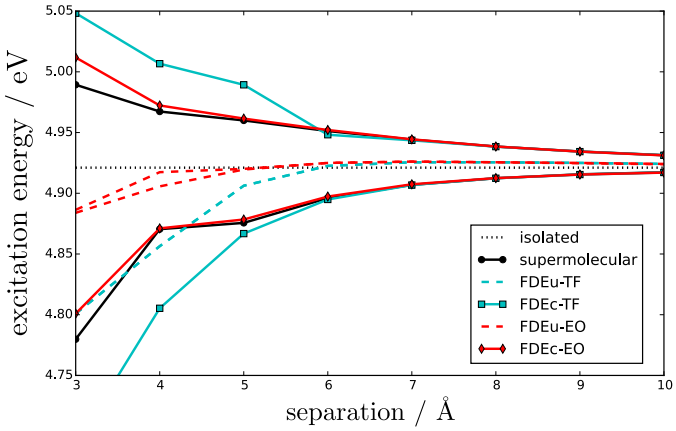


**Figure 9.7.** Excitation energies of the coupled $\pi \rightarrow \pi^*$ local excitation as a function of the benzaldehyde-dimer inter-planar separation.

We plot the excitation energies for for these coupled transitions as a function of the benzene-plane separation in Fig. 9.7. In the supermolecular TDDFT results, we observe that there is a weak coupling between these transitions at 10 Å, with a splitting of the excitation energies of 0.014 eV; this splitting increases to 0.210 eV at 3 Å separation. For the uncoupled methods, we again find that the excitations for the FDEu-TF methods are degenerate, while those in the FDEu-EO method are split—the occupied orbitals in the FDE-EO method are shifted in energy in order to maintain orthogonality when there is significant overlap between the MOs. For the FDEc-TF method, we find good qualitative agreement with respect to the supermolecular TDDFT results, which was also found from the studies in ref 206. However, good quantitative agreement is only found for separations of 6 Å and greater. At 6 Å separation, we observe errors of 0.003 and 0.001 eV for the upper and lower transitions, respectively, which are reduced to less than 0.0001 eV at 10 Å. For separations of 5 Å and below, the FDEc-TF method over-estimates the coupling, with an energy splitting of 0.355 eV (compared to 0.210 eV in supermolecular TDDFT) at 3 Å. The explanation of this over-estimation in ref 206 was due to the coupling of charge-transfer-like excitations in the supermolecular TDDFT results, which were not accounted for in the FDEc-TF method since the subsystems were calculated in the monomer basis. We used the supermolecular basis for all subsystem calculations, which should account for these charge-transfer-like excitations, however, as was observed in the case of the He-dimer, these charge-transfer-like excitations are incorrectly described due to an incorrect description of the ground-state electronic structure using FDE-TF. The over-estimation of the coupling, therefore, represents a more general failure of the TF approximation to the NAKP and the kinetic energy kernel. Using the FDEc-EO method, we

observe good quantitative agreement at all distances, with errors of 0.022 eV and 0.021 eV for the upper and lower transitions, respectively, at 3 Å separation, which are reduced to 0.005 and 0.001 eV at 4 Å, and to less than 0.0001 eV at 10 Å. Interestingly, the energy splitting between the transitions at 3 Å using the FDEc-EO method is 0.211 eV compared to 0.210 eV in the supermolecular TDDFT calculations.

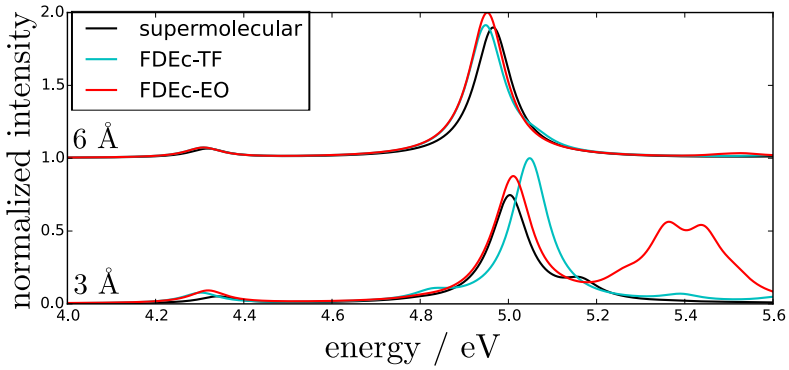


**Figure 9.8.** Absorption spectra of the benzaldehyde calculated using the supermolecular TDDFT, FDEc-TF, and FDEc-EO methods at 6 Å (top) and 3 Å (bottom) separations.

We also considered the accuracy of the FDEc-TF and FDEc-EO methods in calculating the oscillator strengths of the respective transitions. In Fig. 9.8, we plot the absorption spectra of the benzaldehyde-dimer (where the sticks spectra have been broadened by Lorentzians with fwhm of 0.1 eV) at 3 and 6 Å separation. We note good agreement from both methods for the absorption spectra below 5 eV. We will consider the oscillator strength of the previously described $\pi \rightarrow \pi^*$ transition (examined in Fig. 9.7), which has an oscillator strength of $f = 0.27$ at 3 Å and $f = 0.45$ at 10 Å. In the FDEc-TF method, we observe errors in the oscillator strengths of 0.10 and 0.01 at 3 and 10 Å separations, respectively. The FDEc-EO method performs better at closer distances with an error of 0.04 at 3 Å, but is comparable at farther separations with an error of 0.02 at 10 Å. Over all distances, both methods yielded MAEs of 0.04. Above 5 eV, the absorption spectra vary significantly from that of the supermolecular TDDFT results. One would expect that at these higher energies, there are a lot of strongly coupled excitations, and there may be an insufficient number of uncoupled excitations calculated from each subsystem to correctly reproduce the supermolecular TDDFT results.

## 9.5 Conclusion

We have extended the FDE-EO ground-state method, which enforces inter-subsystem MO orthogonality through the use of the level-shifting projection operator, into the TDDFT regime. This TDDFT formulation also depends on a $\mu$-parameter, and we have found stable excitation energies for parameters varying three orders of magnitude ($10^3$–$10^6$). Like conventional subsystem TDDFT methods, we show that the FDE-EO TDDFT extension can also be separated into "uncoupled" (FDEu-EO) and "coupled" (FDEc-EO) methods, ignoring or accounting for the

response of other subsystems, respectively. We show that these methods can accurately reproduce the supermolecular TDDFT results, particularly where conventional subsystem TDDFT methods fail (such as in systems with strongly overlapping densities or with charge-transfer-like excitations) by exploring the LiH, He-dimer, 2-aminopyridine–methanol, and benzaldehyde-dimer systems. While the method in this paper does not improve on computational costs, it does represent an accurate subsystem formulation of TDDFT that does not depend on approximate KEDFs.

# Part IV

# Using Theory to Elucidate Experimental Observations

# Chapter 10
# The Tip-enhanced Raman Scattering of H2TBPP Monolayer

Chiang, N.; Jiang, N.; Chulhai, D.V.; Pozzi, E.A.; Hersam, M.C.; Jensen, L.; Seideman, T.; Van Duyne, R.P. "*Molecular-Resolution Interrogation of a Porphyrin Monolayer by Ultrahigh Vacuum Tip-Enhanced Raman and Fluorescence Spectroscopy*" *Nano Lett.* **2015**, *15*, 4114–4120. (adapted from)

## Abstract

Tip-enhanced Raman scattering (TERS) of a self-assembled porphyrin monolayer on Ag(111) is studied using an ultrahigh vacuum scanning tunneling microscope (UHV-STM). Through selectively exciting different Q-bands of *meso*-tetrakis-(3,5-ditertiarybutylphenyl)-porphyrin (H2TBPP), chemical information regarding different vibronic excited states is revealed by a combination of TERS and time-dependent density functional theory simulations. It is found that the TERS spectra reflect specific vibronic excitations for a monolayer of flat-lying H2TBPP.

## 10.1 Introduction

Porphyrins are of great interest in the fields of chemistry, physics, biology, and medicine due to their natural abundance and distinct electronic, photonic, and catalytic properties.[364] Ordered porphyrin adlayers formed by selfassembly have been extensively investigated in the past.[365–370] The most widely used technique for studying such self-assembled porphyrin systems is scanning tunneling microscopy (STM),[368–372] with more recent emphasis placed on experiments done under ultrahigh vacuum (UHV) conditions.[373–376] However, STM alone is insufficient at revealing much of the rich chemical information on these systems. A combination of optical spectroscopy and STM allows one to overcome this limitation.

Raman scattering is a spectroscopic technique that uses photon excitation, and is capable of studying vibrational, rotational, and other low-frequency modes of molecules. The introduction and subsequent growth of surface-enhanced Raman spectroscopy (SERS) has helped scientists overcome the detection related issue of low Raman cross-sections for organic molecules.[4,80] In SERS, the incident and Raman scattered light is amplified by the localized surface plasmon resonance (LSPR) supported on nanostructured noble metal substrates. Amplification occurs through large enhancements to the electromagnetic (EM) fields[377] that are capable of reaching single-molecule sensitivity under favorable circumstances.[19,30,81]

Similarly, Raman scattering from only a few molecules on a surface can be enhanced by a highly confined EM field created by optically exciting the LSPR of the tip-sample junction in an STM, or an atomic force microscope (AFM), with plasmonically active noble metal tips.[30,31] This technique is known as tip-enhanced Raman scattering (TERS).[32,33] UHV and low-temperature environments have also been incorporated into TERS to increase the stability of molecules and to obtain spectra with higher signal-to-noise ratios.[32,45,378,379] Recent advances in TERS have shown the capability of single-molecule imaging[379] as well as improving spatial resolution below 5 nm.[380,381] For example, Dong, Hou, and co-workers have reported an impressive subnanometer TERS image of a single molecule.[34]

In this chapter, we present a series of TERS spectra, recorded under UHV conditions, of a self-assembled *meso*-tetrakis(3,5-ditertiarybutylphenyl)- porphyrin (H2TBPP) monolayer grown on a single crystal Ag(111) surface. Excitation wavelengths were chosen to coincide as closely as possible with the different Q-band vibronic transition energies. The spectroscopic differences in the obtained TERS spectra are explained by time-dependent density functional theory (TDDFT) simulated resonance Raman spectra (RRS), and surface-enhanced resonance Raman scattering (SERRS), resulting from these different vibronic transitions.

## 10.2 Computational Details

The optimized geometry and normal modes of $H_2$TBPP were obtained with the B3LYP/6-311G* level of theory using NWChem.[382,383] Vibrational frequencies were scaled by a factor of 0.98 to account for missing anharmonicity in the simulations. The resonance Raman scattering of $H_2$TBPP was simulated using a time-dependent wave packet formalism.[384] The Franck-Condon

factors and the transition dipole derivatives (needed for the Herzberg-Teller contributions) were obtained from three-point numerical differentiation of the excited states energies and transition dipoles, respectively, along mass-weighted normal mode coordinates. The excited states lifetime parameters for a high-temperature Brownian oscillator solvent model[385,386] were optimized to best match the solution-phase absorption spectrum. All simulated Raman spectra were broadened by Lorentzians with full width at half maxima of 7.0 $cm^{-1}$.

The dressed-polarizability formalism,[215,258] as outlined in Part II, was used to simulate SERRS, where the molecular polarizabilities are dressed as

$$\alpha^{D,(k)}_{\alpha\beta} = \mathbf{E}^{a}_{\mathrm{loc},\gamma}(\omega_S)\alpha^{(k)}_{\gamma\delta}\mathbf{E}^{\beta}_{\mathrm{loc},\delta}(\omega_L) \tag{10.1}$$

where $\alpha^{(k)}$ is the transition polarizability for normal mode $k$, and $\mathbf{E}_{\mathrm{loc}}$ represents the local field enhancement matrices at the incident ($\omega_L$) and scattered ($\omega_S$) frequencies. These matrices generally depend on the orientation of the molecule with respect to the surface. However, on the basis of the STM images (Figure 1), results for parallel orientations (porphyrin rings parallel to the surface) best represent the experimental data.

## 10.3 Correctly Describing the Tip-enhanced Raman Scattering of H2TBPP

A typical porphyrin molecule exhibits multiple vibronic transitions in the near-UV and visible region. At 419 nm, $H_2$TBPP shows a strong transition to the third and fourth electronically excited states, known as the Soret band (data not shown). It also has four weak absorption bands peaks at 515, 549, 593, and 649 nm. These bands are denoted as $Q_y$(1,0), $Q_y$(0,0), $Q_x$(1,0), and $Q_x$(0,0), respectively, which indicate transitions to the two lowest electronic excited states (Figure 10.1a). The TDDFT-simulated absorption spectrum is in good agreement with the measured absorption in ethanol, with the only exception being the $Q_y$(1,0) band, which is slightly blueshifted. The observed blue shift is likely due to Duschinksy rotations[387] or frequency anharmonicity,[388] absent in the theory used here. However, we cannot rule out solvent and surface effects or interactions with other molecules as possible sources for the observed discrepancy. Figure 10.1b shows the tip-engaged and tip-retracted TERS spectra, along with the resonant SERS (SERRS) spectrum of R6G. Figure 10.1c shows six of the normal modes that have significant contributions to the spectra observed in Figure 10.1b.

Figure 10.2a shows a series of TERS spectra using different excitation wavelengths, along with corresponding TDDFT calculated spectra. We account for the blue shift of the $Q_y$(1,0) transition in the TDDFT-simulated absorption spectrum (Figure 10.1a) by shifting the excitation wavelengths in the TDDFT-simulated SERRS, thereby retaining relative overlap with this band. Specifically, we used 508 and 525 nm as the excitation wavelengths in the TDDFT calculations to remain congruent with the experimental data acquired with 514.5 and 532 nm excitations, respectively. Table 10.1 shows the TDDFT calculated excited states properties, including the x- ($\mu^{0n}_x$) and y- ($\mu^{0n}_y$) components of the transition dipole moments, and the homogeneous broadening

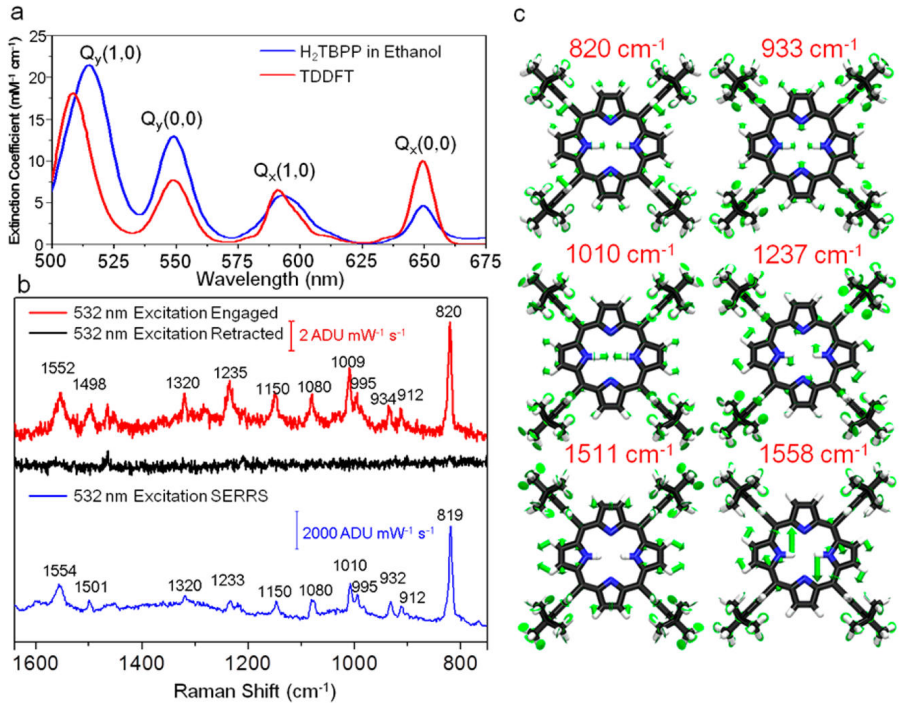


**Figure 10.1.** (a) Absorption spectrum of $2.5 \times 10^{-6}$ M of $H_2$TBPP in ethanol (blue) and TDDFT calculated spectrum (red). (b) UHV-TERS tip-engaged (red) and tip-retracted (black) spectra of $H_2$TBPP monolayer on Ag(111) with 532 nm excitation (0.1 V, 500 pA, 180 s) and SERS spectrum of $H_2$TBPP adlayer on AgFON substrate with 532 nm excitation (10 s). (c) Selected TDDFT calculated Raman active normal modes of an $H_2$TBPP molecule.

**Table 10.1.** TDDFT calculated excited states properies used for the simulation of the RRS and TERS of $H_2$TBPP

| | $\Delta E$ used$^a$ (calc.) (eV) | $\mu_x^{0n}$ (D) | $\mu_y^{0n}$ (D) | $\Gamma^a$ (cm$^{-1}$) |
|---|---|---|---|---|
| $S_1(Q_x)$ | 1.9097 (2.1765) | 1.0343 | 0.0021 | 120.0 |
| $S_2(Q_y)$ | 2.2584 (2.3247) | -0.0009 | 1.1639 | 250.0 |
| $S_3(B_x)$ | 3.0765 (3.1352) | -8.3296 | -0.0097 | 700.0 |
| $S_4(B_y)$ | 2.9591 (3.2539) | -0.0130 | 10.5358 | 300.0 |

$^a$The values of $\Delta E$ and $\Gamma$ used best reproduced experimental data. For the high-temperature Brownian oscillator solvent model, a value of $\kappa = 0.1$ was used for all states.

factor ($\Gamma$), used in the simulated plasmonically enhanced resonance Raman spectra.

The TERS spectra were similar for all excitations, except in the region from 1200–1400 cm$^{-1}$. Additionally, the 1010 cm$^{-1}$ Raman mode was stronger when exciting the $Q_y$(1,0) transition, while the 819 cm$^{-1}$ mode had the highest relative intensity when using 532 nm excitation. These spectral differences are explained by the theory of resonance Raman spectroscopy as follows. For the $Q$(0,0) bands (561 and 594 nm excitation), $H_2$TBPP molecules were excited to the ground vibrational state ($\nu = 0$) of the corresponding electronically excited states, $S_1$ for the $Q_x$ transitions and $S_2$ for the $Q_y$ transitions, as indicated in Figure 10.2, panel b. For the $Q$(1,0)

transitions, the molecules were also excited to the first vibrational excited state of a specific normal mode in that electronic excited state. A top-down waterfall plot (Figure 10.2c) shows a TDDFT-simulated resonance Raman excitation profile in the region of the $Q_y$(1,0) and the $Q_y$(0,0) transitions. The figure shows that each normal mode has a maximum at the $Q_y$(0,0) excitation (∼550 nm) and another maximum at the $Q_y$(0,0) energy plus the energy of the corresponding $\nu = 1$ state. In the experimental results, the 532 nm excitation (525 nm in TDDFT calculation) is closer to the $\nu = 1$ resonance of the 819 $cm^{-1}$ mode, while the 514.5 nm excitation (508 nm in TDDFT calculation) is in better resonance with $\nu = 1$ for the 1554 $cm^{-1}$ mode.

TERS with 633 nm excitation, in resonance with the $Q_x$(0,0) band, was not observed since the fingerprint spectral region of the Raman signal was covered by the strong fluorescence of $H_2$TBPP. However, TDDFT simulated Raman excitation profile in the $Q_x$ region (Figure 10.3) shows similar behavior as in the $Q_y$ region.

## 10.4 Conclusion

In conclusion, we have explained the differences in the UHV-TERS spectra of $H_2$TBPP from different excitation energies using a combination of the dressed-tensors theory with RRS transition polarizabilities. We found that these spectral differences are due to being on resonance with different vibronic transitions as we excite the $Q_y$ transitions of $H_2$TBPP. We expect a similar behavior for the $Q_x$ transitions, but the TERS at these frequencies were quenched by the strong fluorescence of the molecule, and were not observed.

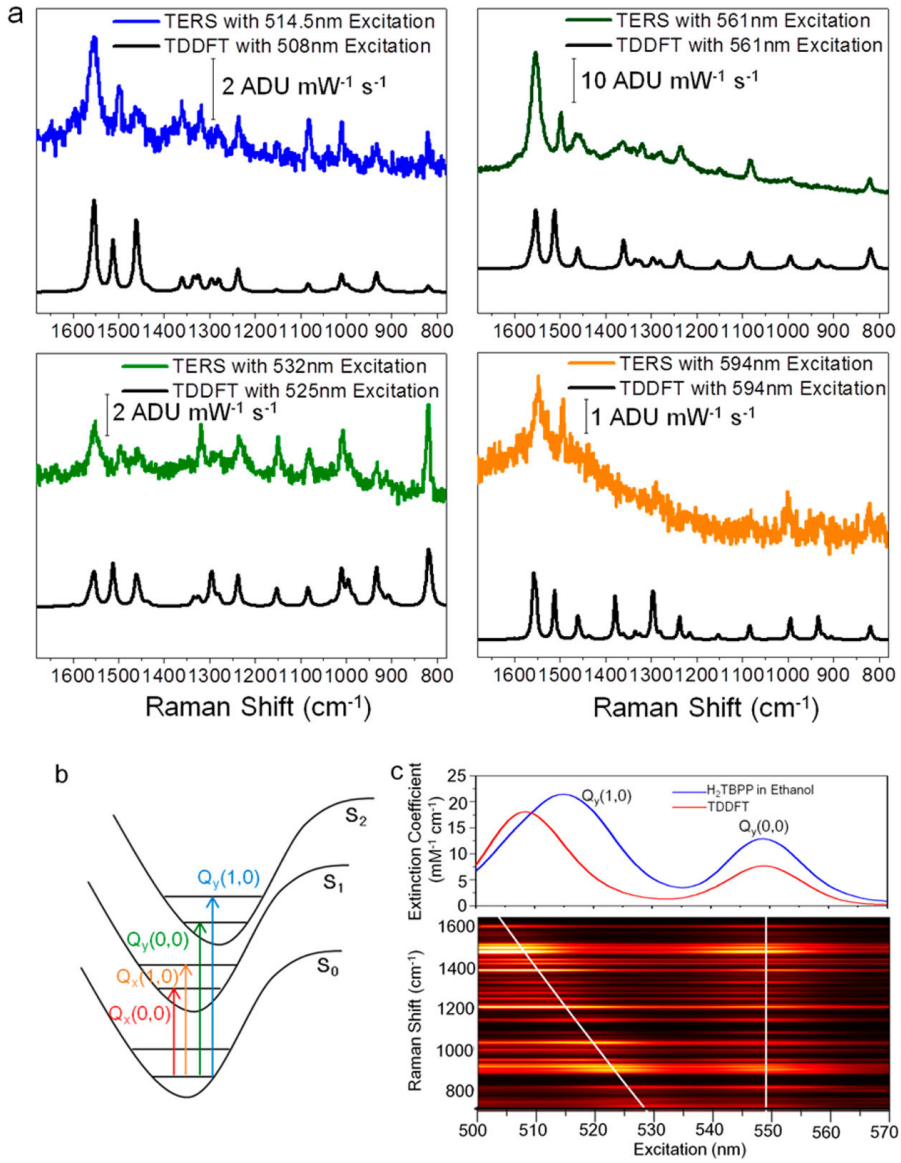


**Figure 10.2.** (a) UHV-TERS spectra of $H_2$TBPP adlayer on Ag(111) with 514.5, 532, 561, and 594 nm excitation, and the corresponding TDDFT simulations of plasmonically enhanced Raman spectra with polarization of the excitation parallel to the tip axis. (b) Schematics of the resonance Raman process of $H_2$TBPP. (c) TDDFT simulated excitation profile for resonance Raman spectra of $H_2$TBPP with excitation from 500–570 nm; the white lines are the corresponding $Q_y(1,0)$ and $Q_y(0,0)$ excitation energies for each vibrational mode.

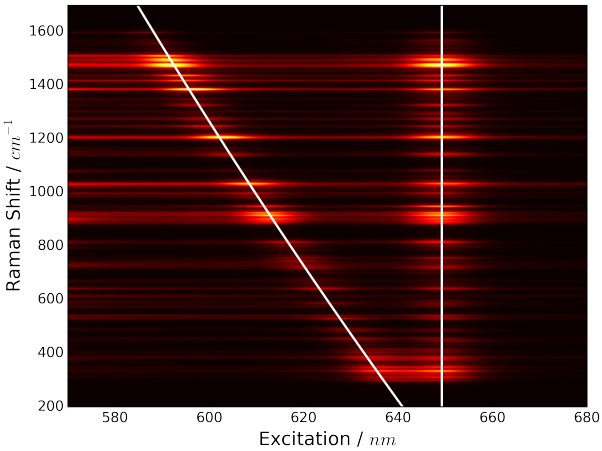


**Figure 10.3.** TDDFT simulated excitation profile for the resonance Raman spectra of $H_2$TBPP with excitation from 570–680 nm; the white lines are the corresponding $Q_x(1,0)$ and $Q_x(0,0)$ excitation energies for each vibrational mode.

# Chapter 11
# The Origin of Relative Intensity Fluctuations in Single-Molecule Tip-Enhanced Raman Spectroscopy

Sonntag, M.D.; Chulhai, D.; Seideman, T.; Jensen, T.; Van Duyne, R.P. "*The Origin of Relative Intensity Fluctuations in Single-Molecule Tip-Enhanced Raman Spectroscopy*" *J. Am. Chem. Soc.*, **2013**, *135*, 17187–17192. (adapted from)

## Abstract

An explanation of the relative intensity fluctuations observed in single-molecule Raman experiments is described utilizing both single-molecule tip-enhanced Raman spectroscopy and time-dependent density functional theory calculations. Theoretical calculations provide convincing evidence that the fluctuations are not the result of diffusion, orientation, or local electromagnetic field gradients but rather are the result of subtle variations of the excited-state lifetime, energy, and geometry of the molecule. These variations in the excited-state properties will provide information on adsorbate-adsorbate and adsorbate-substrate interactions and may allow for inversion of experimental results to obtain these excited-state properties.

## 11.1 Introduction

In 1997, two independent reports observing single-molecule surface-enhanced Raman spectroscopy (SMSERS) contributed to a renaissance in SERS.[81,82] Nie and Emory reported the observation of SERS spectra from single rhodamine 6G (R6G) molecules adsorbed on citrate-reduced Ag nanoparticles that were electrostatically immobilized on glass in an ambient environment. Strong intensity fluctuations occurred on the second time scale and were attributed to surface diffusion of molecules into and out of the electromagnetic enhancing hot spot.[254] Independently, Kneipp and co-workers observed SMSERS of crystal violet (CV) in citrate-reduced Ag nanoparticle aggregates in solution, the signal demonstrating a Poisson distribution of intensities corresponding to 0, 1, 2, or 3 molecules in the hot-spot.

Similarly, reports of single-molecule tip-enhanced Raman spectroscopy (SMTERS) have generated a tremendous amount of interest due to its ability to probe chemical information on the nanometer scale.[30,34,379,389,390] The combination of scanning tunneling microscopy (STM) with Raman spectroscopy can overcome the low sensitivity and diffraction limited spatial resolution associated with Raman spectroscopy as well as the limited chemical sensitivity associated with STM. TERS employs the use of a nanometallic tip to both localize and enhance the incident electric field.

After the initial SMSERS observations one of the major questions involved the nature of the sporadic intensity fluctuations (i.e., blinking), specifically what is their origin. There have been many reports studying blinking, demonstrating that the blinking dynamics are dependent on temperature,[254,255,391,392] excitation intensity,[256,257] and environment.[19,254,391] While the blinking dynamics have been demonstrated to be dependent on temperature, no changes in the relative intensities were observed during thermal heating of the sample during illumination.[254] Additionally, the fluctuations themselves have been treated with many models.[81,256,257,393–395]

In general, it appears that blinking is caused by diffusion of the molecule on the surface into and out of the hot spot. Previous work in both SMSERS and SMTERS utilized an isotopically edited extension of the bianalyte technique, which demonstrates strong evidence of a diffusion mechanism.[19,30] To date, multiple papers on SMSERS have focused on fluctuations both in peak intensity and spectral position, using statistical analysis to claim observance of single-molecule behavior. Within the TERS literature, similar fluctuations in intensity have also been used as a basis for identifying single-molecule behavior.[389,390] Fluctuations in the line shape and spectral position can also make characterization of samples difficult, as molecular decomposition and photobleaching are possible.[396,397]

Although dramatic changes in the Raman intensity and frequency of the Raman modes have been discussed at length (see above), more subtle changes are often evident in the Raman spectrum of single molecules. Large relative intensity fluctuations between individual modes within a single spectrum, along with changes in linewidths, have been observed during the course of the experiment. There are several possible explanations for this behavior based on the properties of the molecule and the hot-spot itself. For example, in ambient conditions, a water meniscus forms in the tip-sample junction allowing the molecule to diffuse and sample different

polarizations, orientations, enhancement factors, etc. In this chapter, we will explore the origin of these relative intensity fluctuations. This information may be used to gain some insight into the adsorbate-adsorbate and/or adsorbate-substrate interactions.

## 11.2 Computational Details

The time-dependent wave packet formalism of the resonance Raman scattering (RRS) tensor ($\alpha$), considering only the ground ($G$) and one resonantly excited ($E$) state, may be written as[398] (see also Equation 2.7)

$$\left(\alpha_{\alpha\beta}\right)_{\mathrm{p}} = \left(\mu_{\alpha}^{\mathrm{GE}}\right)\left(\mu_{\beta}^{\mathrm{GE}}\right) \times L[E^{\mathrm{EG}}, \omega_p, \Delta_p, \Gamma] \tag{11.1}$$

where Greek subscripts refer to Cartesian directions, $\mu^{\mathrm{EG}}$ is the transition dipole moment between the ground and resonantly excited state, $L$ is a line shape function that depends on $E^{\mathrm{EG}}$ (the energy difference between $G$ and $E$), $\omega_p$ (the frequency of the of vibrational mode $p$), $\Delta_p$ (the mode-dependent displacement between ground- and excited-state potential minima in ground-state dimensionless coordinates), and $\Gamma$ (a spectral broadening parameter that is related to the lifetime of $E$). This equation also assumes the Condon approximation (no vibrational coordinate dependence on $\mu^{\mathrm{EG}}$). Within these approximations, the RRS spectrum may be simulated exactly providing that $\mu^{\mathrm{EG}}$, $E^{\mathrm{EG}}$, $\omega_p$, $\Delta_p$, and $\Gamma$ are known.

Simulations of the RRS of R6G were previously obtained using parameters calculated from a time-dependent density functional theory (TDDFT) method as outlined previously.[30] Geometry optimization, normal modes, and excited-state energy calculations were performed in NWChem[382] using the B3LYP/6-311G* level of theory. Vibrational frequencies were scaled by a factor of 0.98. Dimensionless displacements were obtained from a three-point numerical differentiation of excited state energies along mass weighted vibrational coordinates. The lifetime parameter was estimated from solution-phase R6G RRS experimental results and found to be $\sim$500 cm$^{-1}$. These parameters were shown to accurately simulate experimental ensemble RRS spectra of R6G.

In single-molecule observations, these parameters may vary reflecting the exact local environment of the molecule. To examine this possibility, we fitted simulated spectra using a least-squares method to experimental data allowing for small changes in the molecular parameters. Both experimental and simulated spectra were normalized (to the mode at $\sim$1658 cm$^{-1}$), and the least-squares minimization was performed using a multidimensional downhill simplex algorithm[399] allowing for variations in $\Delta_p$, $E^{\mathrm{EG}}$, and $\Gamma$. Calculated values (described above) were used as starting points in the simplex algorithm, with values of $E^{\mathrm{EG}}$ allowed to vary within $\pm$25 nm of the initial value (532 nm) and $\Gamma$ between 50–1500 cm$^{-1}$. The $\Delta_p$ of 10 selected modes were allowed to vary within $\sim$40% of their initial values. These modes (at $p$ = 616, 772, 1195, 1298, 1356, 1515, 1561, 1579, 1607, and 1658 cm$^{-1}$) were selected because they were the largest contributors to the RRS spectrum in the region under examination (400–1800 cm$^{-1}$). The $\Delta_p$ of the remaining modes were kept fixed at their calculated values.

## 11.3 Results and Discussion

We show the time series plot of the TERS spectra of a single R6G molecule in Figure 11.1. This plot clearly shows large changes in the relative intensities of the normal modes with time. Of these modes, we highlight the vibrations at 608, 771, 1362, and 1651 $\text{cm}^{-1}$ (see Figure 11.2). The majority of these vibrations are concentrated on the xanthene ring; however each mode contains slightly different normal mode character. It is possible that differing adsorption geometries could cause certain modes to be preferentially enhanced or damped. A more complete understanding of the relationship between different modes and the integrated intensities can be gained by examining the intensity changes across the entire experimental data set.

We have shown, in Chapter 4, that the orientation dependence of molecules with respect to the surface in SERS may be approximated using

$$I^{\text{SERS}} \propto \left|\mathbf{F}^{\text{loc}}(\omega_L) \cdot \mathbf{R}^T \cdot \alpha \cdot \mathbf{R} \cdot \mathbf{F}^{\text{loc}}(\omega_S)\right|^2 \tag{11.2}$$

where $\mathbf{F}^{\text{loc}}$ is the local field enhancement, $\alpha$ is the Raman tensor, and $\mathbf{R}$ is some rotation matrix.[34,106,400] The $\omega_L$ and $\omega_S$ indicate the incident and scattered frequencies, respectively. This formalism can describe similar fluctuations observed in SMSERS experiments in which the relative intensities and peak positions are the result of molecular reorientation inside the hot spot.[106,401] However, this approximation cannot be used to correctly describe the relative mode intensities of the SERRS (TERRS) of Franck-Condon (A-term) scatterers resonantly excited to a single excited state, such as R6G. In such molecules, the resonance Raman tensor $\alpha$ (calculated using the time-dependent formalism presented in eq 11.1) depends on the line shape function $L$ which is independent of rotation; orientation-dependence stems from rotation of a vector (the transition dipole) that, in the Condon approximation, is mode-independent.

While this results in orientation-independent relative intensities, the SERRS intensities calculated using the above equation will, however, result in largest enhancements for transition dipoles aligned with the local field vectors. Going beyond the Condon approximation, inclusion of the first Herzberg-Teller ($B$) term results in some orientation dependence of the SERRS spectrum for R6G, but its contribution is minor, with features that are 1–2 orders of magnitude weaker than the total intensity, and therefore is an unlikely explanation for the fluctuations observed in the SMTERS experiments. A similar argument could be made for field gradient effects since the electric dipole-quadrupole tensor contains the same line shape function. A more rigorous theoretical treatment would be required to account for fluctuations of individual modes in SERRS and TERRS. In particular, one would need to determine the orientation- and site-dependent coupling of the excited state (and therefore the properties that depend on this state, such as $\mu^{\text{EG}}$, $E^{\text{EG}}$, $\Delta_p$, and $\Gamma$) with the plasmonic surface.

Alternatively, one may be able to "invert" experimental data in order to obtain these excited-state properties.[402,403] Generic algorithms may be used to accurately obtain these parameters through nonlinear least-squares minimization, assuming that a good initial "guess" was first made. In this chapter, we use the results of full TDDFT calculations as an initial guess in a multidimensional downhill simplex algorithm[399] in order to obtain optimized parameters.

**Table 11.1.** Parameters used to reproduce experimental spectra obtained from least-squares minimization of excited-state properties

| parameter | calcd | 09 | 32 | 37 | 50 | 52 | 57 |
|---|---|---|---|---|---|---|---|
| $\Gamma$ ($cm^{-1}$) | – | 545 | 1727 | 1159 | 654 | 601 | 489 |
| $E^{EG}$ (nm) | 534 | 542 | 557 | 527 | 524 | 522 | 538 |
| $\Delta_{616}$ | -0.245 | -0.294 | -0.164$^{\dagger}$ | -0.205 | -0.190$^{\dagger}$ | -0.274 | -0.274 |
| $\Delta_{772}$ | -0.163 | -0.181 | -0.155 | -0.166 | -0.201 | -0.157 | -0.186 |
| $\Delta_{1195}$ | -0.098 | -0.089 | -0.111 | -0.089 | -0.093 | -0.101 | -0.093 |
| $\Delta_{1298}$ | -0.141 | -0.151 | -0.193$^{\dagger}$ | -0.153 | -0.196$^{\dagger}$ | -0.176$^{\dagger}$ | -0.160 |
| $\Delta_{1356}$ | 0.180 | 0.161 | 0.158 | 0.173 | 0.170 | 0.167 | 0.177 |
| $\Delta_{1515}$ | -0.143 | -0.162 | -0.158 | -0.169 | -0.146 | -0.146 | -0.150 |
| $\Delta_{1561}$ | 0.145 | 0.140 | 0.130 | 0.158 | 0.117 | 0.130 | 0.126 |
| $\Delta_{1579}$ | 0.120 | 0.142 | 0.118 | 0.123 | 0.103 | 0.127 | 0.127 |
| $\Delta_{1607}$ | 0.047 | 0.052 | 0.065$^{\dagger}$ | 0.052 | 0.053 | 0.048 | 0.054 |
| $\Delta_{1658}$ | -0.199 | -0.168 | -0.174 | -0.151$^{\dagger}$ | -0.198 | -0.177 | -0.176 |

Calculated values were obtained using the B3LYP/6-311G* level of theory. Values that are more than 20% different from the calculated values are labeled with a †.

Figure 11.3 shows the comparison between six frames of the experimental TERS and simulated RRS with optimized parameters of R6G. These frames were chosen because they show intense features at different regions in their respective spectrum. The spectra in Figure 11.3 show the accuracy of the minimization algorithm, where we were able to simulate the relative intensities of the 10 modes under consideration for each experimental spectrum. The values used for the simulated spectra in Figure 11.3 are listed in Table 11.1. The top row indicates the particular spectrum number in the experimental data set that is being modeled. Both the calculated and optimized parameters are shown for each mode corresponding to the six spectra shown.

The results indicate that the large fluctuations in relative intensities observed experimentally may be reproduced theoretically assuming small fluctuations in excited-state properties. In particular, these large changes were reproduced assuming small changes (usually <20%) in the dimensionless deltas. These changes are reasonable as they reflect changes in the excited-state bond lengths of a picometer or less. These changes are averaged out in ensemble measurements but become important in single-molecule observations. This implies that quantitative analysis of the relative intensities from single-molecule experiments is difficult at best. By summing all of the single-molecule spectra obtained in Figure 11.1, we obtain a spectrum, shown in Figure 11.4, that resembles the ensemble spectrum in both SERS and TERS experiments in which the relative intensities across the spectrum are roughly similar.[30,404]

## 11.4 Conclusion

We have determined an explanation of the large relative intensity fluctuations present in single-molecule TERS spectra. In principle, these conclusions should also be generalizable to other experiments such as single-molecule SERS; however, that data must still be examined. Theoretical calculations have ruled out orientation and field gradient as the cause of these effects. Matching

of the theoretical spectra to the experimentally obtained fluctuations was achieved by allowing for small variations (<20%) in the lifetime, energy, and geometry of the excited state. The ability to invert experimental measurements to obtain molecular properties of the excited state of the molecule can provide detailed information on the interactions between adsorbates and the surface.

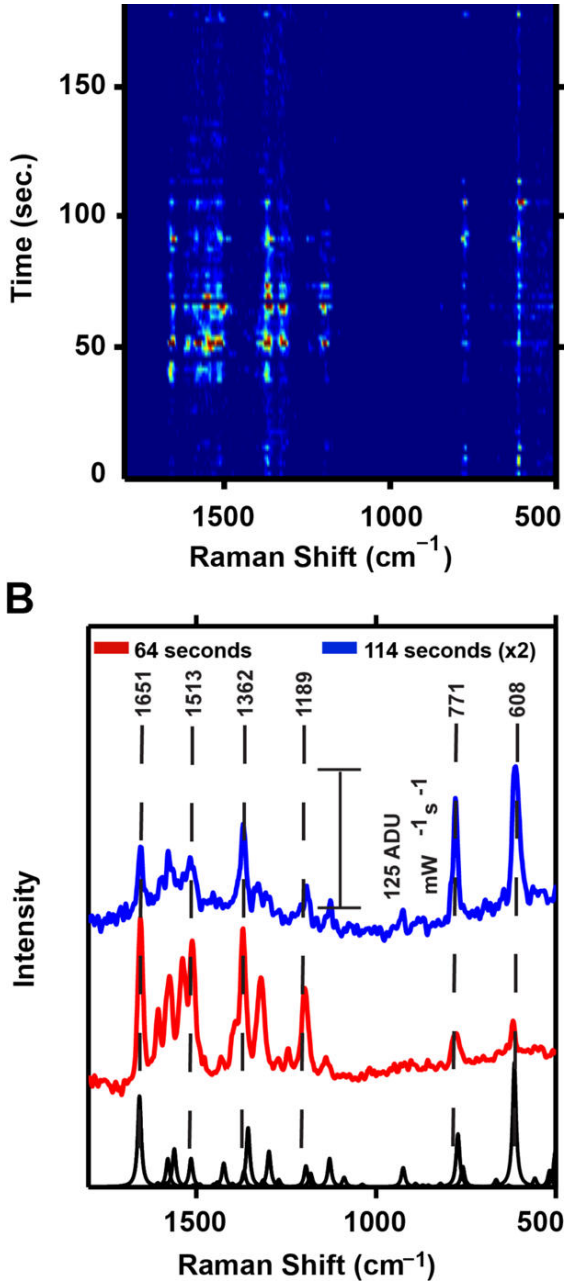


**Figure 11.1.** (A) Time series waterfall plot of spectra taken continuously under single-molecule conditions. The false color represents signal intensity, where red is highest and blue is lowest. (B) Two representative spectra illustrating the large changes in relative intensity along with the theoretical spectrum.

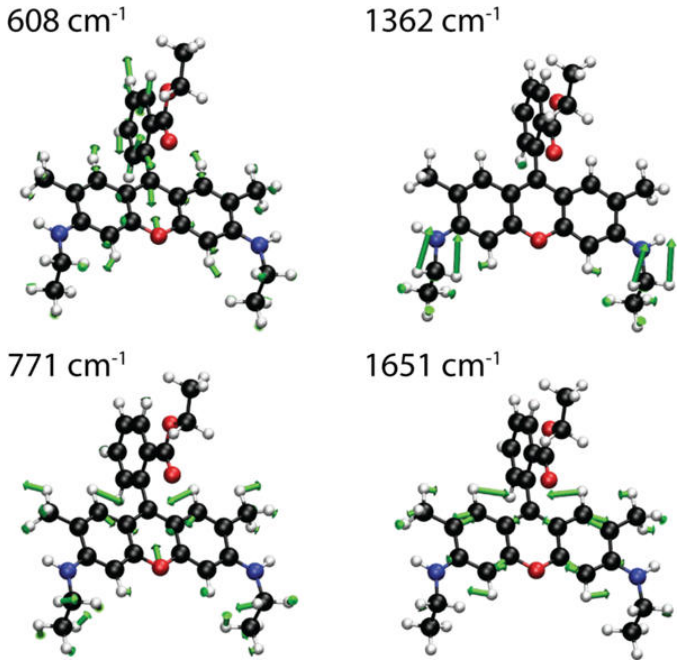


**Figure 11.2.** Visual depiction of the normal modes of the four most intense vibrations in the TERS spectrum of R6G

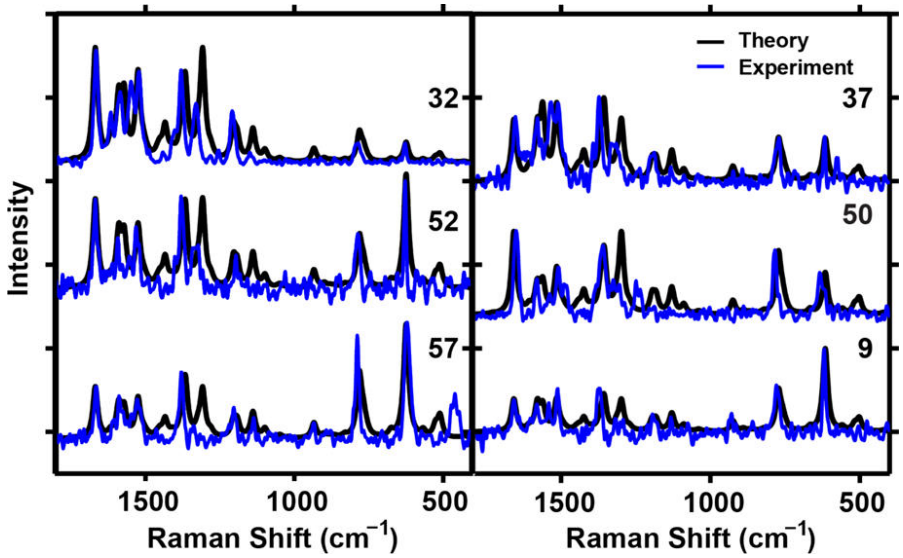


**Figure 11.3.** Plot of the experimental and theoretical spectra. The fluctuations can be reproduced by allowing for small changes in the properties of the molecule. Different frames show certain regions of the spectrum dominating the total intensity.

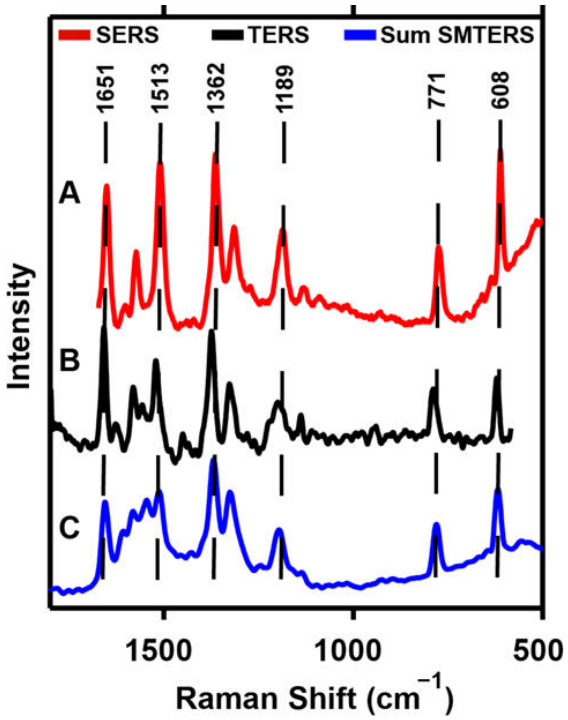


**Figure 11.4.** Plot of ensemble (A) SERS and (B) TERS and (C) sum of the single-molecule TERS spectra.

# Chapter 12
# Binding Orientation of Rhodamine-6G From Tip-Enhanced Raman Spectroscopy

Klingsporn, J.M.; Jiang, N.; Pozzi, E.A.; Sonntag, M.D.; Chulhai, D.; Seideman, T.; Jensen, L.; Hersam, M.C.; Van Duyne, R.P. "*Intramolecular Insight into Adsorbate–Substrate Interactions via Low-Temperature, Ultrahigh-Vacuum Tip-Enhanced Raman Spectroscopy*" *J. Am. Chem. Soc.* **2014**, *136*, 3881–3887. (adapted from)

## Abstract

Tip-enhanced Raman spectroscopy (TERS) provides chemical information for adsorbates with nanoscale spatial resolution, single-molecule sensitivity, and, when combined with scanning tunneling microscopy (STM), Ångstrom-scale topographic resolution. Performing TERS under ultrahigh-vacuum conditions allows pristine and atomically smooth surfaces to be maintained, while liquid He cooling minimizes surface diffusion of adsorbates across the solid surface, allowing direct STM imaging. Low-temperature TER (LT-TER) spectra differ from room-temperature TER (RT-TER), RT surface-enhanced Raman (SER), and LT-SER spectra because the vibrational lines are narrowed and shifted, revealing additional chemical information about adsorbate-substrate interactions. As an example, we present LT-TER spectra for the rhodamine 6G (R6G)/Ag(111) system that exhibit such unique spectral shifts. The high spectral resolution of LT-TERS provides intramolecular insight in that the shifted modes are associated with the ethylamine moiety of R6G. LT-TERS is a promising approach for unraveling the intricacies of adsorbate-substrate interactions that are inaccessible by other means.

## 12.1 Introduction

Understanding the nature of molecular adsorption geometries and the attendant adsorbate-surface interactions is of fundamental importance in the development of technologies such as dye-sensitized solar cells, organic photovoltaics, heterogeneous catalysts, and molecular electronics. Adsorbate-surface interactions are inherently heterogeneous because of the number of crystallographically distinct surface sites available as well as the various adsorbate-adsorbate interactions possible. Scanning tunneling microscopy (STM) and atomic force microscopy (AFM) provide unprecedented detail about these interactions at the single-molecule (SM) and single-site level for "flat" molecules. Such direct high-resolution imaging is compromised for molecules that have complex 3D adsorption geometries. Tip-enhanced Raman spectroscopy (TERS), on the other hand, is an established tool for surface science that can probe the details of adsorbate-surface interactions for individual molecules adsorbed at individual surface sites.

TERS, unlike surface-enhanced Raman spectroscopy (SERS), utilizes a controllable hot spot formed at the tip-sample junction. This hot spot allows nanofocusing of the electromagnetic (EM) field to provide nanoscale spatial resolution. The high EM field intensity at the tip-sample junction provides enhancements of the Raman signals that are sufficient to provide ultrahigh sensitivity down to the SM level.[30,34,379,390,405] While most of the work in the TERS field has concentrated on studies performed under ambient conditions,[406–410] performing TERS in ultrahigh vacuum (UHV) can minimize contamination and maximize STM spatial resolution. The first TERS experiment performed in UHV[379] showed SMTERS spectra that were dominated by a single vibrational mode for brilliant cresyl blue (BCB) dye molecules deposited from solution on Au(111). The first multivibrational mode UHV-TERS experiment, along with complete UHV sample preparation,[378] was performed for copper phthalocyanine (CuPc) on Ag(111). The recent report of UHV-TERS at 80 K for the *meso*-tetrakis(3,5- di-tert-butylphenyl)porphyrin (H2TBPP)/Ag(111) system has further energized this field with its demonstration of sub-nanometer spatial resolution.[34] However, the effect of temperature on the TERS signal has not yet been quantified.

Here we present and analyze low-temperature (LT) (19 K), UHV ($<2 \times 10^{-11}$ Torr) TERS of single molecules and clusters of rhodamine 6G (R6G) adsorbed and immobilized on a Ag(111) surface. Previous LT Raman studies have demonstrated the additional advantage of reduced line widths compared with room temperature (RT), which is evidently dominated by increased vibrational dephasing times.[411–413] Further, a UHV, near-field, variable-temperature SERS study of R6G reported that the background signal narrowed and decreased at LT.[414] We now demonstrate analogous line width narrowing in TERS upon cooling to 19 K as well as informative spectral shifts that are observed in LT-TERS compared with RT-TERS and SERS at both temperatures. Analysis of these spectral shifts using the potential energy distributions (PEDs) of their respective vibrational modes has provided additional information about the specific structural moieties interacting with the Ag(111) surface. This insight has allowed us to postulate a plausible adsorption geometry for R6G on Ag(111). Overall, LT-TERS of a small number of molecules with minimal motional averaging is a significant advance in the study of molecules interacting with surfaces.

## 12.2 Computational Details

The resonance Raman scattering (RRS) of R6G was simulated using a time-dependent wave packet formalism as was described briefly in Chapter 11 and in more detail elsewhere.[30,398] Briefly, optimized geometries, normal modes, and excitation energies were obtained at the B3LYP/6-311G* level of theory using NWChem.[382] Vibrational frequencies were scaled by a factor of 0.98. Dimensionless displacements were obtained from three-point numerical differentiation of the excited-state energies along mass-weighted vibrational coordinates. Normal mode distributions were calculated from mass-weighted normal mode vectors. The molecule was first divided into seven regions (two ethylamine, two methyl, one ethyl ester, one phenyl, and one xanthene). The vibrational PEDs were then determined by considering the magnitudes of the normal mode vectors and the regions to which the corresponding atoms belong.

## 12.3 Spectral Shifts in LT-TERS

Because of the limited information given by STM, we turned to spectroscopy in order to elucidate the nature of the adsorbate-substrate interactions. Figure 12.1 depicts LT-TERS, along with both RT- and LT-SERS and RT-TERS of R6G. We also include the calculated spectrum of free R6G in this figure. Several differences between LT-TERS and the other spectra can be clearly observed. These differences permit some adsorbate-surface structural properties to be deduced. The focus will be on the following: (1) the observed Raman line shapes; and (2) the unique spectral shifts observed only in LT-TERS.

The observed Raman line shapes may be explained by three mechanisms: (1) the number of molecules being observed; (2) the diffusion of molecules in and around the hot-spot; and (3) the temperature-dependent Raman line width. In contrast to the TERS spectra, the SERS spectra contain contributions from all of the molecules within the laser probe volume, resulting in a highly ensemble-averaged signal. On the other hand, the TERS signal is due only to molecules within the TERS enhancing region. The exact size of this enhancing region has been under debate, however, we approximate that $10^9$ molecules are probed in SERS.[378] In contrast, if we consider a typical Ag probe morphology,[397] the TERS signal originates from no more than $10^4$ R6G molecules. However, as shown with SERS, a few molecules in the region of highest field strength (that is, the hot spot) will dominate the signal.[415] Under this assumption, the lower bound for the number of R6G molecules in the TERS enhancing region would be only a few molecules. Because of varied geometries and adsorption sites possible, one would expect a normal distribution of mode frequencies, resulting in the observed broad, Gaussian-shaped bands in SERS spectra collected at both temperatures (Figure 12.1). While RT-TERS drastically reduces the number of molecules in comparison to SERS, the rapid diffusion of R6G molecules at RT results in motional averaging as the molecules move in and out of the hot-spot—this also results in Gaussian-shaped bands for RT-TERS. Finally, and perhaps most significantly, molecules are immobilized during LT studies, and experience constant adsorption configurations. In addition, we expect that the stationary molecules adopt one of a finite number of local minimum-energy configurations on the periodic

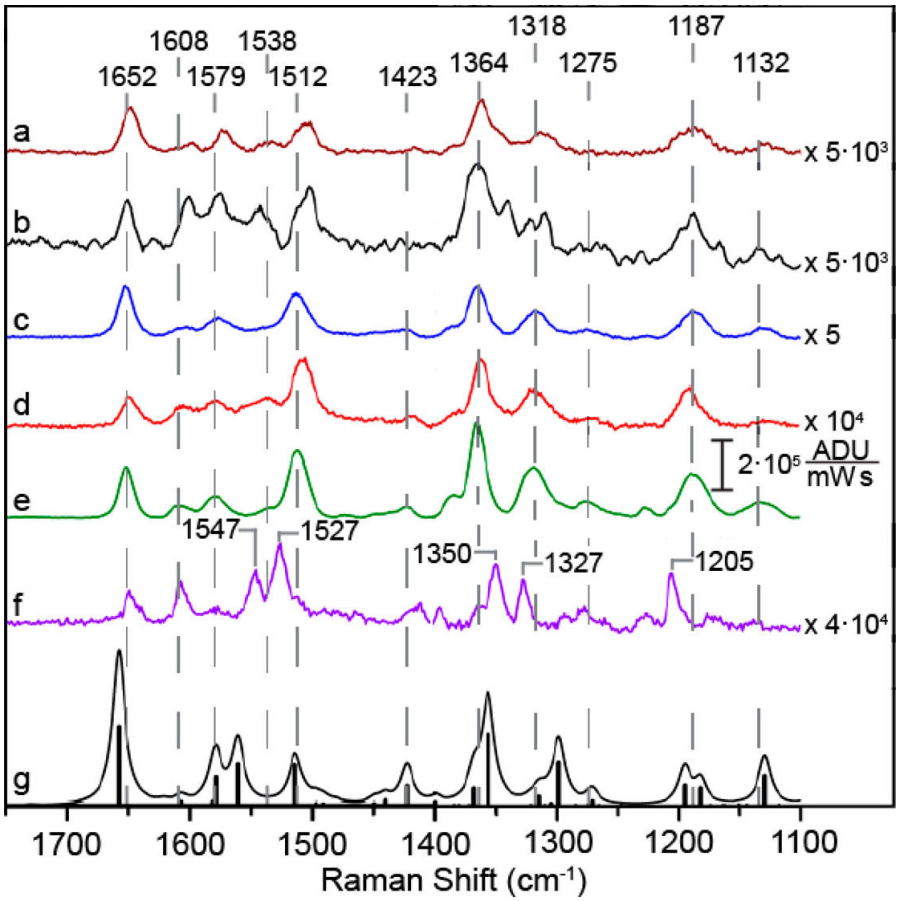


**Figure 12.1.** Spectral comparisons for R6G on silver surfaces: (a) ambient SM RT-SERS on Ag colloids (brown), (b) ambient SM RT-TERS on a smooth Ag film (black), (c) RT-UHV-SERS on AgFON (blue), (d) RT-UHV-TERS on Ag(111) (red), (e) LT-UHV-SERS on AgFON (green), (f) LT-UHV-TERS on Ag(111) (violet), and (g) TDDFT calculated Raman spectrum of free R6G.

substrate. As a result, the distribution of adsorption geometries and therefore individual mode frequencies is decreased in LT-TERS. Additional narrowing in LT-TERS is afforded through the intrinsic temperature dependence of the Raman line width. It has been shown that SMSERS line widths are temperature-dependent through anharmonic coupling between the molecular vibrations of the adsorbate and the phonons of the silver surface, resulting in an increase in the vibrational dephasing relaxation time.[411] A more detailed discussion on the line shapes from RT and LT SERS and TERS may be found in Ref. 45 and its Supporting Information.

These effects all lead to line width narrowing in LT-TERS, which increases the information content available in a collected spectrum. Although there is no standard definition of spectral resolution in Raman spectroscopy,[416] an intuitive one is that in a fixed spectral region, the number of resolvable lines increases with decreasing line width. This is clearly observed in Figure 12.1, in which 12 peaks are resolved in the range 1100–1450 $cm^{-1}$ in LT-TERS compared with eight peaks in RT-TERS.

Along with the observed line width narrowing, multiple LT-TERS peaks are shifted with respect

**Table 12.1.** Major peaks for LT-TERS[a] and theoretically calculated frequencies and PEDs for the moieties present in R6G

| experimental | | theoretical | | | | | |
|---|---|---|---|---|---|---|---|
| position $cm^{-1}$ | shifted Y/N | position $cm^{-1}$ | methyl % | xanthene % | ethylamine % | phenyl % | ester % |
| 614 | N | 616 | 3.5 | 39.2 | 6 | 51.1 | 0.1 |
| 775 | N | 772 | 16.8 | 42.3 | 39.7 | 1.1 | 0.2 |
| 1132 | Y | 1129 | 13.5 | 27.5 | 40.5 | 16.1 | 2.4 |
| 1205 | Y | 1195 | 0.4 | 61.2 | 38.3 | 0.1 | 0 |
| 1274 | N | 1271 | 0.7 | 70 | 17.5 | 9.3 | 2.5 |
| 1327 | Y | 1321 | 3.8 | 11.7 | 84.4 | 0 | 0 |
| 1350 | Y | 1367 | 0.2 | 4.7 | 93.9 | 1.2 | 0 |
| 1423 | N | 1424 | 37.9 | 30.3 | 17.1 | 14.5 | 0.2 |
| 1527 | Y | 1515 | 11.8 | 28.2 | 58.1 | 1.8 | 0.1 |
| 1547 | Y | 1535 | 6.8 | 38.6 | 54.5 | 0 | 0 |
| 1579 | N | 1582 | 0.1 | 6.9 | 1.9 | 90.8 | 0.4 |
| 1608 | N | 1607 | 0 | 3.6 | 0 | 96.2 | 0.2 |
| 1652 | N | 1658 | 8.9 | 89.6 | 1.3 | 0 | 0.2 |

[a]For each peak, the entry in the second column indicates whether the peak is shifted with respect to the other spectra.

to both the RT-TERS and the RT/LT-SERS spectra shown in Figure 12.1. The eigenvectors for the normal modes of interest are shown in Figure 12.2. Additionally, Figure 12.1 also compares both RT/LT-SERS and -TERS spectra to previously reported SMTERS and SMSERS spectra.[19,30] The SM spectra appear to remain consistent with the RT-SERS, LT-SERS, and RT-TERS spectra but greatly differ from the LT-TERS spectra. Both blue and red mode shifts of up to 20 $cm^{-1}$ are observed for multiple LT-TERS modes, while other modes remain un-shifted. The unique spectral characteristics observed for LT-TERS combined with a careful theoretical interpretation provide further insight into the molecular orientation of R6G on the Ag(111) surface. Table 12.1 summarizes the major peaks and indicates whether they are shifted in the LT-TERS spectrum, and it also provides the corresponding theoretical PEDs (see Appendix I for the PEDs of all normal modes).

The peaks located at 1132, 1205, 1327, 1350, 1527, and 1547 $cm^{-1}$ in the LT-TERS spectrum show frequency shifts compared with both RT/LT-SERS and RT-TERS. As shown by highlighted cells in Table 12.1, all of these peaks have a unique similarity in that each mode is characterized theoretically to have a PED that involves approximately localized vibrations on the ethylamine moieties or on the xanthene ring and ethylamine moieties. For example, the peak observed at 1205 $cm^{-1}$ is shifted with respect to the other spectra and has a PED showing 61% xanthene character and 38% ethylamine character. The modes at 1132, 1327, 1350, 1527, and 1547 $cm^{-1}$ also show large shifts and have PEDs showing large xanthene ring and/or ethylamine character. The rest of the major peaks do not exhibit such shifts. Comparing these unshifted modes with their PED values in Table 12.1 shows that they have either high phenyl ring character or are highly delocalized modes with contributions from most of the internal coordinates of R6G. An

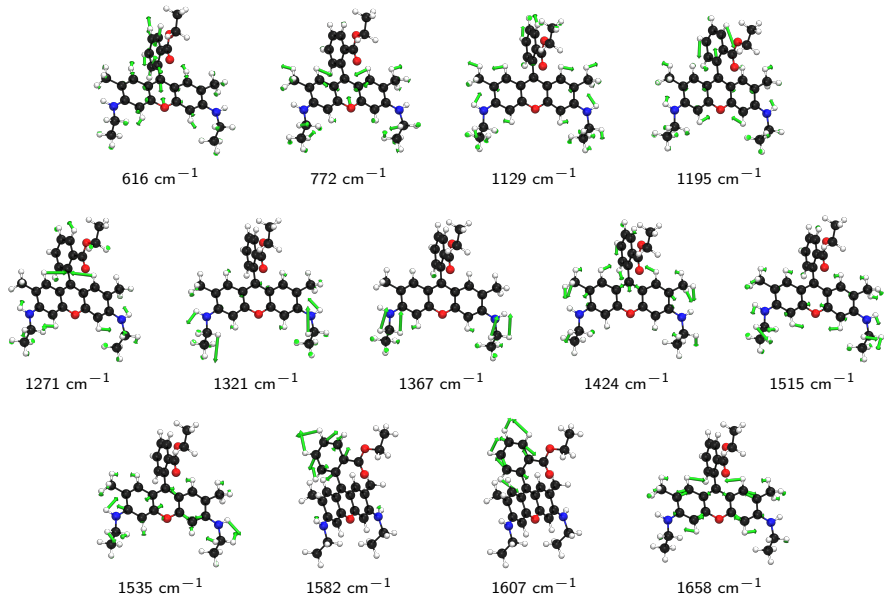


**Figure 12.2.** Illustration of the eigenvectors of the normal modes of R6G examined in this Chapter

example of an unshifted, phenyl-ring-localized mode is the peak located at 1608 cm$^{-1}$. The unshifted xanthene-ring-localized mode at 1652 cm$^{-1}$ is worthy of note. This mode only has 1% ethylamine character and is therefore effectively decoupled from the Ag(111) surface. An in-depth discussion of the characteristics of the R6G vibrations will not be presented here, as it has been thoroughly covered previously.[19,30,44]

An alternative explanation for the observed peak shifts might lie in the strength of molecule–molecule interactions. In other words, we consider the possibility that the dimers, trimers, and larger aggregates observed in STM images of R6G on Ag(111) at LT may explain the shifted peaks in LT-TERS. However, since one would expect similar aggregation properties in LTSERS in this case, the absence of such shifts decreases the likelihood of this scenario. Furthermore, because multiple R6G aggregation states are observed in the STM images, we would expect to see either inhomogeneously broadened or many more peaks in LT-TERS as a result of varying molecule–molecule interactions. We thus conclude that intramolecular interactions are not a significant contributor to the peak shifts observed in LT-TERS.

Understanding the unique spectral characteristics observed for LT-TERS in comparison with the other spectra presented here requires an interpretational hypothesis. We hypothesize that the moieties in closest proximity to the surface exhibit the greatest perturbation in the observed Raman frequency. Under this hypothesis, the orientation of R6G on the Ag(111) substrate can be further understood on the basis of the unique spectral characteristics observed. Using the

above hypothesis and the observation that all of the modes localized on the ethylamine moieties or xanthene ring modes coupled to the ethylamine moieties exhibit spectral shifts, we propose that the ethylamine moieties of adsorbed R6G interact with the Ag(111) surface. Therefore, the molecule is likely oriented with the R6G molecule situated edgewise along its xanthene moiety with its ethylamine substituents against the Ag(111) surface.

## 12.4 Conclusion

LT-TERS performed in UHV provides additional insight into the adsorption properties of molecules on surfaces. According to the PEDs obtained by time-dependent density functional theory (TD-DFT) calculations on the free R6G molecule, the spectral shifts observed in LT-TERS for certain modes are attributed to their proximity and coupling to the surface. Specifically, we postulate that R6G adsorbs to Ag(111) along its xanthene edge with the ethylamine moieties in close proximity to the surface. Overall, we conclude that LT-TERS enables improved understanding of adsorbate-substrate interactions and thus has the potential to influence the design of future molecular devices.

# Part V

# Summary and Outlook

# Chapter 13
# Summary and Outlook

## 13.1 Dissertation Summary

This dissertation focused on developing new theoretical tools in order to describe and understand the spectral changes observed in surface-enhanced Raman scattering (SERS) and other surface-enhanced spectroscopies. The development of these new methods drew inspiration from each of the main mechanisms of SERS, namely the electromagnetic mechanism (EMM), and the chemical mechanism (CM). As such, this dissertation was presented in four parts, the first of which focused on introducing the main ideas and theoretical models used throughout.

In the second part, "The Dressed-Tensors Formalism", we developed methods to describe SERS, surface-enhanced Raman optical activity (SEROA), and surface-enhanced circular dichroism that were based on the EMM. It was demonstrated that the inhomogeneity of the local fields generated by surface plasmons may significantly alter both the Raman and Raman optical activity signatures, and, in the case of SERS, these signatures may contain information regarding the relative orientation of the molecule with respect to the nanoparticle's surface. For SEROA, we found that the spectral signatures are highly sensitive to the inhomogeneity of the local fields, the orientation of the molecule, and the surface plasmon frequency width, which all give insight into why mirror image SEROA for enantiomers are yet to be observed. We found that the surface-enhanced circular dichroism of the $\alpha$- and $3_{10}$-helices resulted in significantly complicated molecular signatures, and the structure of the proteins could no longer be identified from the spectra. We further showed that the dressed-tensors formalism can efficiently simulate the SERS of ensemble systems, and, when coupled with molecular dynamics simulations, show that the time-lapse of a single-molecule SERS spectrum may contain information of the translational and rotational motions of the molecule.

The third part, "An Exact Subsystem Density Functional Theory", focused on developing a new theoretical method to understand the CM of SERS. This method considers the quantum mechanical interaction between two subsystems—such as between a molecule and a plasmonic nanoparticle—exactly within the limit of density functional theory (DFT), by the use of a projection operator embedding method. We implement this new method within the frozen density embedding (FDE) framework, and showed that it exactly reproduces the ground state energies and densities of the supermolecular system. In particular, we showed that the method was robust enough to exactly reproduce the supermolecular electron density of benzene, starting from

atomic subsystems. We also extended this model into time-dependent DFT (TDDFT) in order to describe the response properties of each subsystem, and showed that the theory reproduces the supermolecular excitation energies of weakly and strongly coupled subsystems, and for subsystems with strongly overlapping densities.

In the fourth part, "Using Theory to Elucidate Experimental Observations", we used theoretical models—including models developed in this dissertation—in order to describe the spectral signatures observed from experimental SERS and tip-enhanced Raman scattering (TERS). We showed that changes in the spectral signatures of a monolayer of *meso*-tetrakis(3,5-ditertiarybutylphenyl)-porphyrin (H2TBPP) with respect to changes in the incident laser frequency reflect the excitation of specific vibronic transitions in the molecule. We also noted that the orientation dependence of the SERS spectrum as predicted in the first part of this dissertation is only applicable for non-resonant and Herzberg-Teller scatterers. In the case of the single-molecule TERS of Franck-Condon scatterers, we show that large changes in the relative intensity of the signal may be due to picometer changes in the excited state geometry of the molecule. Finally, we illustrated that, in low-temperature TERS studies, the molecule's interactions with the nanoparticle's surface may induce shifts in the observed normal mode frequencies. We showed that these shifts contain information of the binding orientation of the molecule, and in the case of rhodamine-6G, we find that the molecule bind to the surface along its xanthene/ethylamine moieties.

## 13.2 Future Directions for the Dressed-Tensors Formalism

As developed and explored in Part II of this dissertation, the dressed-tensors formalism is a very efficient method of accounting for the effects of the local electric field responsible for surface-enhanced spectroscopies. The method, as developed so far, has many potential applications in describing the SERS or surface-enhanced Raman optical activity (SEROA) of single molecules or even ensembles of millions of molecules. Below, we will present several potential theoretical extensions and applications of the methods developed in Part II.

### 13.2.1 Field gradient effects in non-linear spectroscopies

The dressed-tensors formalism presented in Part II focused on accounting for an inhomogeneous local field for the linear SERS and SEROA spectroscopies. We also, briefly, explored how the formalism may be expanded to account for non-linear surface-enhanced spectroscopies in Appendix B. There, we showed how the dressed-tensors with a homogeneous local field may be applied to any general second and third order response tensors—however, these expressions do not account for the gradient of the local field. Having a model to describe the various surface-enhanced non-linear spectroscopies is particularly important as we have already seen examples of surface-enhanced hyper-Raman scattering (SEHRS), surface-enhanced coherent anti-Stokes Raman scattering (SECARS), surface-enhanced femto-second stimulated Raman scattering (SE-FSRS), and surface-enhanced sum-frequency generation (SESFG). As such, developing the

dressed-tensors formalism to include field gradients is sorely needed. Below, we show how this may be done for a few of these non-linear surface-enhanced spectroscopies.

Perhaps the simplest extension of the dressed-tensor formalism would be to describe SECARS. Coherent anti-Stokes Raman scatter (CARS) is a four photon process that depends on the third order susceptibility tensor $\chi^{(3)}$. In vibrationally resonant CARS, this tensor may be approximated as products of the linear response polarizabilities $\alpha_{\alpha\beta}$, as

$$\chi^{(3)}_{\alpha\beta\gamma\delta}(-2\omega_1-\omega_2;\omega_1,-\omega_2,\omega_1) \approx \sum_p \frac{\partial\alpha_{\alpha\beta}(\omega_1)}{\partial Q_p}\frac{\partial\alpha_{\gamma\delta}(\omega_1)}{\partial Q_p}\frac{2}{[\omega_p-(\omega_1-\omega_2)-i\epsilon]} + \text{c.c.} \tag{13.1}$$

where $\omega_1$ and $\omega_2$ corresponds to the incident laser frequencies, $p$ sums over all vibrational states with frequency $\omega_p$, $\epsilon$ is the inverse lifetime of the vibrational states, and c.c. denotes the complex conjugate. Because this non-linear susceptibility may be written as products of linear polarizabilities, one would expect that the tensor may be dressed in the same way. Specifically, the dressed $\chi^{(3)}$ with field gradients may be obtained from dressed $\alpha_{\alpha\beta}$ with field gradients as outlined in Equations 4.5 and D.6.

In the case of SEHRS, which depends on the hyperpolarizability derivatives in the Placzek approximation, the dressed hyperpolarizability $\beta^{tot}$ may be obtained as

$$\begin{aligned}
\frac{\partial\beta^{tot}_{\alpha\beta\gamma}}{\partial Q_p} &= \left[\delta_{\alpha\delta}+F^{\alpha}_{\delta}\right]\frac{\partial\beta^{\mu\mu\mu}_{\delta,\epsilon,\zeta}}{\partial Q_p}\left[\delta_{\beta\epsilon}+F^{\beta}_{\epsilon}\right]\left[\delta_{\gamma\zeta}+F^{\gamma}_{\zeta}\right] \\
&+\frac{1}{3}\left[\delta_{\alpha\delta}+F^{\alpha}_{\delta}\right]\frac{\partial\beta^{\mu\mu\theta}_{\delta,\epsilon,\zeta\eta}}{\partial Q_p}\left[\delta_{\beta\epsilon}+F^{\beta}_{\epsilon}\right]F^{\gamma}_{\zeta\eta} \\
&+\frac{1}{3}\left[\delta_{\alpha\delta}+F^{\alpha}_{\delta}\right]\frac{\partial\beta^{\mu\theta\mu}_{\delta,\epsilon\eta,\zeta}}{\partial Q_p}F^{\beta}_{\epsilon\eta}\left[\delta_{\gamma\zeta}+F^{\gamma}_{\zeta}\right] \\
&+\frac{1}{3}F^{\alpha}_{\delta\eta}\frac{\partial\beta^{\theta\mu\mu}_{\delta\eta,\epsilon,\zeta}}{\partial Q_p}\left[\delta_{\beta\epsilon}+F^{\beta}_{\epsilon}\right]\left[\delta_{\gamma\zeta}+F^{\gamma}_{\zeta}\right] \\
&+\frac{1}{9}\left[\delta_{\alpha\delta}+F^{\alpha}_{\delta}\right]\frac{\partial\beta^{\mu\theta\theta}_{\delta,\epsilon\eta,\zeta\kappa}}{\partial Q_p}F^{\beta}_{\epsilon\eta}F^{\gamma}_{\zeta\kappa} \\
&+\frac{1}{9}F^{\alpha}_{\delta\eta}\frac{\partial\beta^{\theta\mu\theta}_{\delta\eta,\epsilon,\zeta\kappa}}{\partial Q_p}\left[\delta_{\beta\epsilon}+F^{\beta}_{\epsilon}\right]F^{\gamma}_{\zeta\kappa} \\
&+\frac{1}{9}F^{\alpha}_{\delta\eta}\frac{\partial\beta^{\theta\theta\mu}_{\delta\eta,\epsilon\kappa,\zeta}}{\partial Q_p}F^{\beta}_{\epsilon\kappa}\left[\delta_{\gamma\zeta}+F^{\gamma}_{\zeta}\right] \\
&+\frac{1}{27}F^{\alpha}_{\delta\eta}\frac{\partial\beta^{\theta\theta\theta}_{\delta\eta,\epsilon\kappa,\zeta\lambda}}{\partial Q_p}F^{\beta}_{\epsilon\kappa}F^{\gamma}_{\zeta\lambda}
\end{aligned} \tag{13.2}$$

where the superscripts $\mu$ and $\theta$ describe the dipole or quadrupole quantum mechanical operator used to define the electronic hyperpolarizability $\beta$, and the field enhancement matrices $\mathbf{F}$ have been defined elsewhere. The hyperpolarizabilities—and generally all other non-linear response tensors—defined with the quadrupole operator are not freely available (as far as the authors are aware) in any computational package, and would need to be implemented. Similarly, one will

need to derive the dressed-tensors formalism and implement the codes needed to generate the respective non-linear tensors, in order describe other non-linear surface-enhanced spectroscopies with an inhomogeneous local field.

### 13.2.2 Octopole response in surface-enhanced Raman scattering

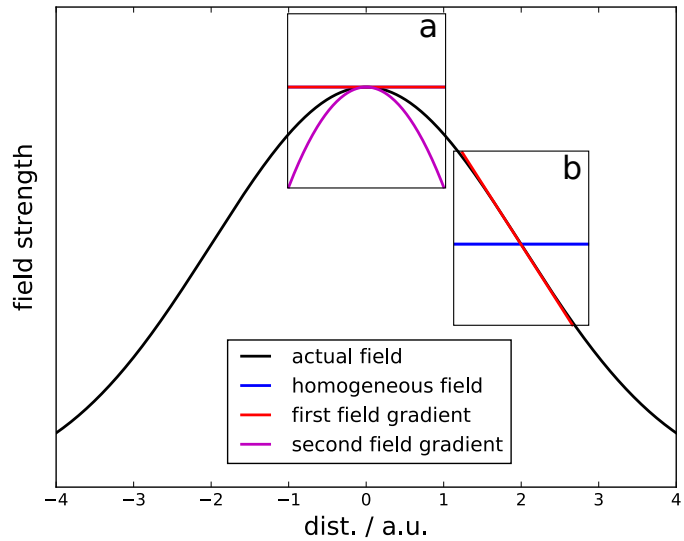


**Figure 13.1.** The inhomogeneity of the local field in a symmetric junction as described by a homogeneous electric field, its first gradient, and its second gradient approximations. Boxes $a$ and $b$ represent the finite size of some small molecule.

In Chapter 4, we considered the effects of the gradient of the local electric field perturbing the molecule. We needed to do this since, over the finite size of the molecule, the value of the local electric field could vary considerably. In Figure 13.1, we show a typical field distribution expected from a symmetric dimer nanoparticle junction. Boxes $a$ and $b$ represent the finite size of some small molecule, and we show how accurate a homogeneous field, the first field gradient, and the second field gradient are at describing the local fields perturbing the molecule. We can see that if the molecule is away from the center of the junction, the field gradient approximation can accurately describe the local fields. However, if the molecule is nearer to the center of the junction, such an approximation fails. This is particularly important since the fields are strongest in the center of the junction, and molecules positioned here would contribute the most to the SERS signal as shown in Chapter 5. As such, we may want to consider the second gradient of the local field—which, in Figure 13.1, is shown to qualitatively reproduce the inhomogeneity of the local field across a molecule in the center of the junction.

Inclusion of the second field gradient would include additional terms to Equations 4.5 and D.6 that are due to the octopole moment $\Omega$ linear response tensors. This dressed tensor formalism may have terms that look like

$$
\begin{aligned}
\frac{\partial \alpha^{tot}}{\partial Q_p} &= \mathbf{E}\cdot\chi^{\mu\mu}\cdot\mathbf{E} + \frac{1}{3}\mathbf{E}\cdot\chi^{\mu\theta}\cdot\nabla\mathbf{E} + \frac{1}{9}\mathbf{E}\cdot\chi^{\mu\Omega}\cdot\nabla^2\mathbf{E} \\
&+ \frac{1}{3}\nabla\mathbf{E}\cdot\chi^{\theta\mu}\cdot\mathbf{E} + \frac{1}{9}\nabla\mathbf{E}\cdot\chi^{\theta\theta}\cdot\nabla\mathbf{E} + \frac{1}{27}\nabla\mathbf{E}\cdot\chi^{\theta\Omega}\cdot\nabla^2\mathbf{E} \\
&+ \frac{1}{9}\nabla^2\mathbf{E}\cdot\chi^{\Omega\mu}\cdot\mathbf{E} + \frac{1}{27}\nabla^2\mathbf{E}\cdot\chi^{\Omega\theta}\cdot\nabla\mathbf{E} + \frac{1}{81}\nabla^2\mathbf{E}\cdot\chi^{\Omega\Omega}\cdot\nabla^2\mathbf{E}
\end{aligned}
\tag{13.3}
$$

where we have simplified all the linear transition polarizabilities as $\chi$, with superscripts $\mu$, $\theta$, and $\Omega$ to symbolize the dipole, quadrupole and octopole operators used to obtained them. $\mathbf{E}$, $\nabla\mathbf{E}$, and $\nabla^2\mathbf{E}$ are also simplified versions of the field, field gradient, and second field gradient enhancement matrices. Such a term is rather complex, and would require that all of the octopole linear transition tensors are also available.

### 13.2.3 Tip-enhanced Raman imaging of molecular vibrations

Recently, Dong, Hou and co-workers have observed TERS signals from a single molecule of *meso*-tetrakis(3,5-ditertiarybutylphenyl) porphyrin (H2TBPP) that were spatially confined to sub-nanometer length scales.[34] They also found that the confinement of the TERS signals were unique to the particular vibrational mode responsible for the scattering. There have been many proposed mechanisms for this effect,[417–420] which includes a highly (spatially) confined plasmon field[418–420] and strong field gradients.[419] The models developed in Part II of this dissertation are uniquely poised to solve this question. While the dressed-tensors formalism may not be able to accurately describe a spatially confined plasmon field that is on the same length scale of the molecule begin probed, the discrete interaction model / quantum mechanics method, developed in Chapters 6 and 7 for optical activity, couples the local field into the quantum mechanical operators—essentially, it accounts for all orders of the local field gradient. Therefore, it should be able to answer whether the observed sub-nanometer TERS images were in fact due to a confined plasmon field.

Preliminary results are shown in Figure 13.2. In this figure, we see that an atomically sharp tip (Figure 13.2*c*), which produces a very confined plasmon field, results in TERS features that are on the Ångstrom length scale and are reflective of the particular molecular vibration (Figure 13.2*a*). A broader tip (Figure 13.2*d*) with a less confined field does not show the same types of features (Figure 13.2*b*). Of course, water is a non-resonant Raman scatterer and these preliminary results may not necessarily be applicable for the resonant H2TBPP molecule. In particular, the molecular resonance probed in H2TBPP for TERS applications is often the $Q_y(1,0)$ vibronic transition.[34,43] As such, one would need to carefully consider how the localized plasmonic fields couple into the molecule's excitation energies and transition dipole moment operators.

### 13.2.4 Molecule-molecule interactions in ensemble surface-enhanced Raman scattering

In Chapter 5, we generated the ensemble-averaged spectrum of a full monolayer of pyridine molecules on Ag nanoparticle systems. In these systems, we dressed each molecule's polarizabilities

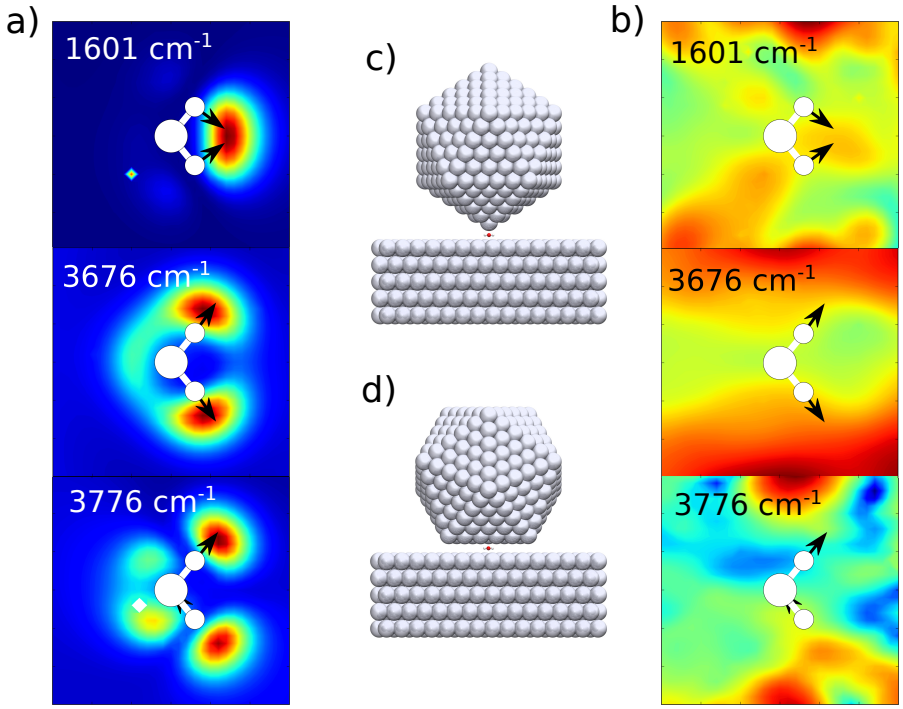


**Figure 13.2.** Sub-nanometer TERS intensities for *(a)* a confined plasmon field, and *(b)* a broad plasmon field. The fields for *a* and *b* were generated by the TERS systems illustrated in *c* and *d*, respectively. TERS intensities are plotted on a log scale.

by accounting for the local field from the bare nanoparticle. However, it was shown that molecules binding to the surface of a nanoparticle can greatly disrupt the local field.[267] In order to account for these interactions—using the simplest approximation—we would need to account for the molecule-molecule and molecule-nanoparticle interactions by either approximating the molecule, or its individual atoms, as point-polarizable objects. Generating disrupted fields by this approximation should be straight forward with the discrete interaction model, albeit computationally expensive since one would require the fields for every time-step in the molecular dynamics simulations. Obtaining disrupted fields in an efficient manner remains a challenge.

## 13.3 Future Directions for the Exact Subsystem Density Functional Theory

In Part III, we presented an exact subsystem density functional theory (subsystem DFT), which includes external orthogonality in the frozen density embedding method (FDE-EO), so that we may be able to exactly model and analyze, through the use of subsystems, the chemical mechanism (CM) of SERS. The method cannot yet model these mechanisms in a black box manner, and we propose the following possible extensions and applications.

### 13.3.1 Applications to few-states resonant Raman scattering

We show, in Chapter 9, that we are able to correctly reproduce the excitation energies and transition dipole moments of strongly coupled systems using the subsystem DFT method. These properties should be sufficient for calculating the transition polarizabilities needed to describe resonant Raman scattering, using the method of Albrecht and co-workers.[52–54,64] We should, in theory, be able to analyze the effects of plasmon-exciton coupling,[143,421–428] and charge-transfer resonances[12,75,243,251] in SERS with the methods developed herein.

### 13.3.2 Calculation of general response properties

The FDE-EO method developed so far is only able to calculate coupled subsystem excitations (see Chapter 9 and Ref. 429). In order to simulate the Raman scattering and other linear and non-linear spectroscopies, we need to extend the method to be able to calculate the polarizability and other response tensors. The generalization of the frozen density embedding (FDE) method to calculate these properties has been presented previously.[204–206,430,431] Accounting for external orthogonality (EO) in the the calculation of linear response properties may include substituting the EO response kernel, as defined in Equation 9.12, with the non-additive kinetic response kernel as presented in Ref. 431. Though, special care may be needed when calculating the diagonal matrix $\mathbf{S}$ in Equation 9 of Ref. 431, as our inter-subsystem molecular orbitals are now (nearly) orthogonal.

As far as the authors are aware, no subsystem formalism has yet been presented for non-linear response properties within time-dependent density functional theory (TDDFT). It is therefore a significant challenge to not only present a subsystem TDDFT method for non-linear response, but to also extend this to in include EO.

# Appendices

# Appendix A
# Fixed-frame and Orientationally-averaged Raman Scattering

## A.1 Electric and Magnetic Multipole Radiation Fields

Light scattering from molecules can be assumed to originate from the radiation of time-varying electric and magnetic multipole moments.[313] These time-varying multipole moments are derived from oscillating charge $\rho$ and current $\mathbf{J}$ densities

$$\begin{aligned} \rho(t) &= \rho^{(0)} e^{-i\omega t} \\ \mathbf{J}(t) &= \mathbf{J}^{(0)} e^{-i\omega t} \end{aligned} \tag{A.1}$$

where $\omega$ is the frequency of these oscillations. The scalar potential, $\phi$, may be evaluated at some vector $\mathbf{R}$ away, where $t' = t - |\mathbf{R} - \mathbf{r}|/c$, as

$$\begin{aligned} \phi(\mathbf{R}, t) &= \frac{1}{4\pi\epsilon_0} \int \frac{\rho^{(0)} e^{i(\kappa|\mathbf{R}-\mathbf{r}|-\omega t)}}{|\mathbf{R} - \mathbf{r}|} dV \qquad ; \kappa = \omega/c \\ &= \frac{e^{i(\kappa R - \omega t)}}{4\pi\epsilon_0 R} \left( \frac{R_\alpha \mu_\alpha^{(0)}}{R^2} + \frac{R_\alpha R_\beta \Theta_{\alpha\beta}^{(0)}}{R^4} - \frac{i\kappa R_\alpha \mu_\alpha^{(0)}}{R} \right. \\ &\quad \left. - \frac{i\kappa R_\alpha R_\beta \Theta_{\alpha\beta}^{(0)}}{R^3} - \frac{\kappa^2 R_\alpha R_\beta \sum_i e_i r_{i\alpha}^{(0)} r_{i\beta}^{(0)}}{2R^2} + \cdots \right) \end{aligned} \tag{A.2}$$

where we have Taylor expanded the $|\mathbf{R} - \mathbf{r}|^{-1}$ term, and expanded the charge density $\rho^{(0)}$ in terms of the charge $e$, dipole $\mu$, and quadrupole $\Theta$ contributions; the Einstein summation convention is assumed for repeated indices. Similarly, for the vector potential $\mathbf{A}$

$$\begin{aligned} \mathbf{A}(\mathbf{R}, t) &= \frac{\mu_0}{4\pi} \int \frac{\mathbf{J}^{(0)} e^{i(\kappa|\mathbf{R}-\mathbf{r}|-\omega t)}}{|\mathbf{R} - \mathbf{r}|} dV \\ &= -\frac{\mu_0}{4\pi R} e^{i(\kappa R - \omega t)} \left( \frac{\epsilon_{\alpha\beta\gamma} R_\beta m_\gamma^{(0)}}{R^2} + \frac{ic\kappa \mu_\alpha^{(0)}}{n} \right. \\ &\quad \left. - \frac{i\kappa \epsilon_{\alpha\beta\gamma} R_\beta m_\gamma^{(0)}}{R} + \frac{ic\kappa R_\beta \sum_i e_i r_{i\alpha}^{(0)} r_{i\beta}^{(0)}}{2nR^2} + \frac{c\kappa^2 R_\beta \sum_i e_i r_{i\alpha}^{(0)} r_{i\beta}^{(0)}}{2nR} + \cdots \right) \end{aligned} \tag{A.3}$$

The radiated electric field, $\mathbf{E}$, is then calculated from $\phi$ and $\mathbf{A}$ using

$$\mathbf{E} = -\frac{\delta \mathbf{A}}{\delta t} - \nabla \phi \tag{A.4}$$

For large distances compared to the wavelength ($R >> 1/\kappa$) and using $R_\alpha = R n_\alpha / n$, this radiated electric field becomes

$$\begin{aligned} E_\alpha(\mathbf{R}, t) \approx \frac{\omega^2 \mu_0}{4\pi R} e^{i(\kappa R - \omega t)} \Big[ \Big( \mu_\alpha^{(0)} - \frac{n_\alpha n_\beta}{n^2} \mu_\beta^{(0)} \Big) \\ - \frac{1}{c} \epsilon_{\alpha\beta\gamma} n_\beta m_\gamma^{(0)} - \frac{i\omega}{3c} \Big( n_\beta \Theta_{\alpha\beta}^{(0)} - \frac{n_\alpha n_\beta n_\gamma}{n^2} \Theta_{\beta\gamma}^{(0)} \Big) + \cdots \Big] \end{aligned} \tag{A.5}$$

In the case of light-induced scattering, such as in Rayleigh and Raman scattering, $\mu_\alpha^{(0)}$, $\Theta_{\alpha\beta}^{(0)}$, and $m_\alpha^{(0)}$ are the induced oscillating electric dipole, electric quadrupole and magnetic dipole, respectively. These may be expressed as functions of the molecule's polarizabilities as

$$\begin{aligned} \mu_\alpha^{(0)} &= \alpha_{\alpha\beta} (E_\beta)_0 + \frac{1}{3} A_{\alpha\beta\gamma} (E_{\beta\gamma})_0 + G_{\alpha\beta} (B_\beta)_0 + \cdots \\ &= \Big( \alpha_{\alpha\beta} + \frac{i\omega}{3c} n_\gamma^i A_{\alpha\gamma\beta} + \frac{1}{c} \epsilon_{\gamma\delta\beta} n_\delta^i G_{\alpha\gamma} + \cdots \Big) E_\beta^{(0)} \end{aligned} \tag{A.6}$$

$$\Theta_{\alpha\beta}^{(0)} = (A_{\gamma\alpha\beta}^* + \cdots) E_\gamma^{(0)} \tag{A.7}$$

$$m_\alpha^{(0)} = (G_{\alpha\beta}^* + \cdots) E_\beta^{(0)} \tag{A.8}$$

where $\mathbf{n}^i$ is the unit vector describing the direction of incident light and we will use $\mathbf{n}^d$ as the unit vector describing the direction of scattered light. In this equation, $\alpha_{\alpha\beta}$, $A_{\alpha\beta\gamma}$ and $G_{\alpha\beta}$ are the molecule's electric dipole-dipole, electric dipole-quadrupole, and electric dipole-magnetic dipole polarizabilities, respectively, and $\mathbf{E}^{(0)}$ is the electric field vector of the incident light. Using these descriptions of the induced multipole moments, the electric field of the scattered radiation may be expanded as

$$\begin{aligned} E_\alpha^d(\mathbf{R}, t) &= \frac{\omega^2 \mu_0}{4\pi R} e^{i(\kappa R - \omega t)} \Big[ \alpha_{\alpha\beta} + \frac{i\omega}{3c} (n_\gamma^i A_{\alpha\gamma\beta} - n_\gamma^d A_{\beta\gamma\alpha}^*) \\ &\quad + \frac{1}{c} (\epsilon_{\gamma\delta\beta} n_\delta^i G_{\alpha\gamma} + \epsilon_{\gamma\delta\alpha} n_\delta^d G_{\gamma\beta}^*) - n_\alpha^d n_\gamma^d \Big\{ \alpha_{\gamma\beta} \\ &\quad + \frac{i\omega}{3c} (n_\delta^i A_{\gamma\delta\beta} - n_\delta^d A_{\beta\delta\gamma}^*) + \frac{1}{c} \epsilon_{\epsilon\delta\beta} n_\delta^i G_{\gamma\epsilon}^* \Big\} + \cdots \Big] E_\beta^{(0)} \\ &= \frac{\omega^2 \mu_0}{4\pi R} e^{i(\kappa R - \omega t)} a_{\alpha\beta} E_\beta^{(0)} \end{aligned} \tag{A.9}$$

where

$$
\begin{aligned}
a_{\alpha\beta} = \alpha_{\alpha\beta} &+ \frac{i\omega}{3c}(n^i_\gamma A_{\alpha\gamma\beta} - n^d_\gamma A^*_{\beta\gamma\alpha}) \\
&+ \frac{1}{c}(\epsilon_{\gamma\delta\beta} n^i_\delta G_{\alpha\gamma} + \epsilon_{\gamma\delta\alpha} n^d_\delta G^*_{\gamma\beta}) - n^d_\alpha n^d_\gamma \left\{ \alpha_{\gamma\beta} \right. \\
&\left. + \frac{i\omega}{3c}(n^i_\delta A_{\gamma\delta\beta} - n^d_\delta A^*_{\beta\delta\gamma}) + \frac{1}{c}\epsilon_{\epsilon\delta\beta} n^i_\delta G^*_{\gamma\epsilon} \right\} + \cdots
\end{aligned}
\tag{A.10}
$$

## A.2 Stokes Parameters

The Stokes parameters may be used to completely describe any arbitrarily polarized light through the vectors of its electric field.[313] They are derived as follows: A plane monochromatic wave traveling in the $z$-direction can be written as the sum of two coherent waves linearly polarized in the $x$ and $y$ directions.

$$
\mathbf{E} = E_x \hat{\mathbf{i}} + E_y \hat{\mathbf{j}} \tag{A.11}
$$

A polarization state of such a wave can be represented by an ellipse. The ellipticity $\eta$ is determined by the ratio of the minor and major axes of the ellipse, $b$ and $a$, through

$$
\tan \eta = \frac{b}{a} \tag{A.12}
$$

The orientation of the ellipse is specified by the azimuth, $\theta$, which is the angle between $a$ and the $x$-axis. The Intensity, $I$, degree of polarization, $P$, ellipticity, $\eta$, and azimuth, $\theta$, are all expressed through the stokes parameters

$$
\begin{aligned}
S_0 &= E_x E_x^* + E_y E_y^* &&= E^{(0)^2} \\
S_1 &= E_x E_x^* - E_y E_y^* &&= P E^{(0)^2} \cos 2\eta \cos 2\theta \\
S_2 &= -(E_x E_y^* + E_y E_x^*) &&= P E^{(0)^2} \cos 2\eta \sin 2\theta \\
S_3 &= -i(E_x E_y^* - E_y E_x^*) &&= P E^{(0)^2} \sin 2\eta
\end{aligned}
\tag{A.13}
$$

where

$$
\begin{aligned}
I &= \frac{1}{2}\left(\frac{\epsilon_0}{\mu_0}\right)^{\frac{1}{2}} S_0 \\
P &= \frac{(S_1^2 + S_2^2 + S_3^2)^{\frac{1}{2}}}{S_0} \\
\theta &= \frac{1}{2}\tan\left(\frac{S_2}{S_1}\right) \\
\eta &= \frac{1}{2}\left(\frac{S_3}{(S_1^2 + S_2^2)^{\frac{1}{2}}}\right)
\end{aligned}
\tag{A.14}
$$

We now consider a molecule at the origin of a right-hand coordinate system ($x$, $y$, $z$) with unit vectors $\mathbf{i}$, $\mathbf{j}$, $\mathbf{k}$. An incident light, with $\mathbf{n}^i = \mathbf{k}$ hits the molecule and is scattered according to Equation A.9 some arbitrary angle $\xi$, where $\xi$ is the angle between the scattered ray (taken

to be in the $yz$-plane) and $\mathbf{k}$ (see Ref 313 Fig. 3.3). The scattered ray can be considered to be in it's own right-hand coordinate reference frame ($x^d$, $y^d$, $z^d$) with unit vectors $\mathbf{i}^d$, $\mathbf{j}^d$, $\mathbf{k}^d$. The transformation between these two reference frames are therefore

$$\begin{aligned}\mathbf{i}^d &= \mathbf{i} \\ \mathbf{j}^d &= \mathbf{j}\cos\xi - \mathbf{k}\sin\xi \\ \mathbf{k}^d &= \mathbf{k}\cos\xi + \mathbf{j}\sin\xi\end{aligned} \tag{A.15}$$

The Stokes parameters of the scattered electric field, $\mathbf{E}^d$ in the ($x^d$, $y^d$, $z^d$) system are

$$\begin{aligned}S_0^d &= E_{x^d}^d E_{x^d}^{d*} + E_{y^d}^d E_{y^d}^{d*} \\ S_1^d &= E_{x^d}^d E_{x^d}^{d*} - E_{y^d}^d E_{y^d}^{d*} \\ S_2^d &= -(E_{x^d}^d E_{y^d}^{d*} + E_{y^d}^d E_{x^d}^{d*}) \\ S_3^d &= -i(E_{x^d}^d E_{y^d}^{d*} - E_{y^d}^d E_{x^d}^{d*})\end{aligned} \tag{A.16}$$

For simplicity, here follows the derivation of the $S_0^d$ parameter. In the ($x$, $y$, $z$) system, this parameter is

$$\begin{aligned}S_0^d = {} & E_x^d E_x^{d*} + E_y^d E_y^{d*}\cos^2\xi + E_z^d E_z^{d*}\sin^2\xi \\ & - (E_y^d E_z^{d*} + E_z^d E_y^{d*})\sin\xi\cos\xi\end{aligned} \tag{A.17}$$

Also, from Equation A.9, we can write $E^d$ in terms of the incident field $E^{(0)}$ as

$$E_\alpha^d E_\beta^{d*} = \left(\frac{\omega^2\mu_0}{4\pi R}\right)^2 a_{\alpha\gamma}a_{\beta\delta}^* E_\gamma^{(0)} E_\delta^{(0)*} \tag{A.18}$$

Recalling that $E_z^{(0)} = 0$ and using the relationship $AB+CD = \frac{1}{2}[(A+C)(B+D)+(A-C)(B-D)]$, $S_0^d$ now becomes

$$\begin{aligned}S_0^d = {} & \left(\frac{\omega^2\mu_0}{4\pi R}\right)^2 [a_{x\gamma}a_{x\delta}^* E_\gamma E_\delta^* + a_{y\gamma}a_{y\delta}^* E_\gamma E_\delta^*\cos^2\xi + a_{z\gamma}a_{z\delta}^* E_\gamma E_\delta^*\sin^2\xi \\ & - (a_{y\gamma}a_{z\delta}^* E_\gamma E_\delta^* + a_{z\gamma}a_{y\delta}^* E_\gamma E_\delta^*)\sin\xi\cos\xi] \\ = {} & \left(\frac{\omega^2\mu_0}{4\pi R}\right)^2 [|a_{xx}|^2 E_x E_x^* + a_{xx}a_{xy}^* E_x E_y^* + a_{xy}a_{xx}^* E_y E_x^* + |a_{xy}|^2 E_y E_y^* \\ & + (|a_{yx}|^2 E_x E_x^* + a_{yx}a_{xy}^* E_x E_y^* + a_{yy}a_{xx}^* E_y E_x^* + |a_{yy}|^2 E_y E_y^*)\cos^2\xi \\ & + (|a_{zx}|^2 E_x E_x^* + a_{zx}a_{zy}^* E_x E_y^* + a_{zy}a_{zx}^* E_y E_x^* + |a_{zy}|^2 E_y E_y^*)\sin^2\xi \\ & + (a_{yx}a_{zx} E_x E_x^* + a_{yx}a_{zy}^* E_x E_y^* + a_{yy}a_{zx}^* E_y E_x^* + a_{yy}a_{zy} E_y E_y^* \\ & + a_{zx}a_{yx} E_x E_x^* + a_{zx}a_{yy}^* E_x E_y^* + a_{zy}a_{yx}^* E_y E_x^* + a_{zy}a_{yy} E_y E_y^*)\sin\xi\cos\xi]\end{aligned} \tag{A.19}$$

We shall consider each of the terms respect to $\xi$ in Equation A.19 separately, as they each reflect different scattering angles. Using the relationships $AB+CD = \frac{1}{2}[(A+C)(B+D)+(A-C)(B-D)]$, $AB^* + BA^* = 2\mathbf{Re}(AB^*)$, and $AB^* - BA^* = 2\mathbf{Im}(AB^*)$ we can write

$$
\begin{aligned}
&|a_{xx}|^2 E_x E_x^* + a_{xx} a_{xy}^* E_x E_y^* \\
&+ a_{xy} a_{xx}^* E_y E_x^* + |a_{xy}|^2 E_y E_y^* = \frac{1}{2}[(|a_{xx}|^2 + |a_{xy}|^2)(E_x E_x^* + E_y E_y^*) \\
&\qquad + (|a_{xx}|^2 - |a_{xy}|^2)(E_x E_x^* - E_y E_y^*) \\
&\qquad + (a_{xx} a_{xy}^* + a_{ay} a_{xx}^*)(E_x E_y^* + E_y E_x^*) \\
&\qquad + (a_{xx} a_{xy}^* - a_{ay} a_{xx}^*)(E_x E_y^* - E_y E_x^*)] \\
&\qquad = \frac{1}{2}[(|a_{xx}|^2 + |a_{xy}|^2) S_0 + (a_{xx} a_{xy}^* + a_{xy} a_{xx}^*) S_1 \\
&\qquad - 2\mathbf{Re}(a_{xx} a_{xy}^*) S_2 - 2\mathbf{Im}(a_{xx} a_{xy}^*) S_3]
\end{aligned}
\tag{A.20}
$$

for the $\xi$-independent terms. Similarly, we have

$$
\begin{aligned}
&|a_{yx}|^2 E_x E_x^* + a_{yx} a_{xy}^* E_x E_y^* \\
&+ a_{yy} a_{xx}^* E_y E_x^* + |a_{yy}|^2 E_y E_y^* = \frac{1}{2}[(|a_{yx}|^2 + |a_{yy}|^2) S_0 + (a_{yx} a_{yy}^* + a_{yy} a_{yx}^*) S_1 \\
&\qquad - 2\mathbf{Re}(a_{yx} a_{yy}^*) S_2 - 2\mathbf{Im}(a_{yx} a_{yy}^*) S_3]
\end{aligned}
\tag{A.21}
$$

for the $\cos^2 \xi$ terms,

$$
\begin{aligned}
&|a_{zx}|^2 E_x E_x^* + a_{zx} a_{zy}^* E_x E_y^* \\
&+ a_{zy} a_{zx}^* E_y E_x^* + |a_{zy}|^2 E_y E_y^* = \frac{1}{2}[(|a_{zx}|^2 + |a_{zy}|^2) S_0 + (a_{zx} a_{zy}^* + a_{zy} a_{zx}^*) S_1 \\
&\qquad - 2\mathbf{Re}(a_{zx} a_{zy}^*) S_2 - 2\mathbf{Im}(a_{zx} a_{zy}^*) S_3]
\end{aligned}
\tag{A.22}
$$

for the $\sin^2 \xi$ terms, and

$$
\begin{aligned}
&a_{yx} a_{zx} E_x E_x^* + a_{yx} a_{zy}^* E_x E_y^* \\
&+ a_{yy} a_{zx}^* E_y E_x^* + a_{yy} a_{zy} E_y E_y^* \\
&+ a_{zx} a_{yx} E_x E_x^* + a_{zx} a_{yy}^* E_x E_y^* \\
&+ a_{zy} a_{yx}^* E_y E_x^* + a_{zy} a_{yy} E_y E_y^* = \mathbf{Re}(a_{yx} a_{zx}^* + a_{yy} a_{zy}^*) S_0 \\
&\qquad + \mathbf{Re}(a_{yx} a_{zx}^* - a_{yy} a_{zy}^*) S_1 \\
&\qquad - \mathbf{Re}(a_{yx} a_{zy}^* + a_{zx} a_{yy}^*) S_2 \\
&\qquad - \mathbf{Im}(a_{yx} a_{zy}^* + a_{zx} a_{yy}^*) S_3
\end{aligned}
\tag{A.23}
$$

for the $\sin \xi \cos \xi$ terms.

From the results in Equations A.20, A.21, A.22, and A.23, Equation A.19 becomes:

$$
\begin{aligned}
S_0^d = \frac{1}{2}\left(\frac{\omega^2\mu_0}{4\pi R}\right)^2 \{&(|a_{xx}|^2 + |a_{xy}|^2)S_0 + (|a_{xx}|^2 - |a_{xy}|^2)S_1 \\
&- 2\mathbf{Re}(a_{xx}a_{xy}^*)S_2 - 2\mathbf{Im}(a_{xx}a_{xy}^*)S_3 \\
&+ [(|a_{yx}|^2 + |a_{yy}|^2)S_0 + (|a_{yx}|^2 - |a_{yy}|^2)S_1 \\
&- 2\mathbf{Re}(a_{yx}a_{yy}^*)S_2 - 2\mathbf{Im}(a_{yx}a_{yy}^*)S_3]\cos^2\xi \\
&+ [(|a_{zx}|^2 + |a_{zy}|^2)S_0 + (|a_{zx}|^2 - |a_{zy}|^2)S_1 \\
&- 2\mathbf{Re}(a_{zx}a_{zy}^*)S_2 - 2\mathbf{Im}(a_{zx}a_{zy}^*)S_3]\sin^2\xi \\
&- 2[\mathbf{Re}(a_{yx}a_{zx}^* + a_{yy}a_{zy}^*)S_0 + \mathbf{Re}(a_{yx}a_{zx}^* - a_{yy}a_{zy}^*)S_1 \\
&- \mathbf{Re}(a_{yx}a_{zy}^* + a_{zx}a_{yy}^*)S_2 - \mathbf{Im}(a_{yx}a_{zy}^* + a_{zx}a_{yy}^*)S_3]cos\xi\sin\xi\}
\end{aligned}
\tag{A.24}
$$

The other Stokes parameters are

$$
\begin{aligned}
S_1^d = \frac{1}{2}\left(\frac{\omega^2\mu_0}{4\pi R}\right)^2 \{&(|a_{xx}|^2 + |a_{xy}|^2)S_0 + (|a_{xx}|^2 - |a_{xy}|^2)S_1 \\
&- 2\mathbf{Re}(a_{xx}a_{xy}^*)S_2 - 2\mathbf{Im}(a_{xx}a_{xy}^*)S_3 \\
&- [(|a_{yx}|^2 + |a_{yy}|^2)S_0 + (|a_{yx}|^2 - |a_{yy}|^2)S_1 \\
&- 2\mathbf{Re}(a_{yx}a_{yy}^*)S_2 - 2\mathbf{Im}(a_{yx}a_{yy}^*)S_3]\cos^2\xi \\
&- [(|a_{zx}|^2 + |a_{zy}|^2)S_0 + (|a_{zx}|^2 - |a_{zy}|^2)S_1 \\
&- 2\mathbf{Re}(a_{zx}a_{zy}^*)S_2 - 2\mathbf{Im}(a_{zx}a_{zy}^*)S_3]\sin^2\xi \\
&+ 2[\mathbf{Re}(a_{yx}a_{zx}^* + a_{yy}a_{zy}^*)S_0 + \mathbf{Re}(a_{yx}a_{zx}^* - a_{yy}a_{zy}^*)S_1 \\
&- \mathbf{Re}(a_{yx}a_{zy}^* + a_{zx}a_{yy}^*)S_2 - \mathbf{Im}(a_{yx}a_{zy}^* + a_{zx}a_{yy}^*)S_3]cos\xi\sin\xi\}
\end{aligned}
\tag{A.25}
$$

$$
\begin{aligned}
S_2^d = \left(\frac{\omega^2\mu_0}{4\pi R}\right)^2 \{&[\mathbf{Re}(a_{xx}a_{yx}^* + a_{xy}a_{yy}^*)S_0 + \mathbf{Re}(a_{xx}a_{yx}^* - a_{xy}a_{yy}^*)S_1 \\
&- \mathbf{Re}(a_{xx}a_{yy}^* + a_{yx}a_{xy}^*)S_2 - \mathbf{Im}(a_{xx}a_{yy}^* + a_{yx}a_{xy}^*)S_3]\cos\xi \\
&- [\mathbf{Re}(a_{xx}a_{zx} + a_{xy}a_{zy}^*)S_0 + \mathbf{Re}(a_{xx}a_{zx}^* - a_{xy}a_{xy}^*)S_1 \\
&- \mathbf{Re}(a_{xx}a_{zy}^* + a_{zx}a_{xy}^*)S_2 - \mathbf{Im}(a_{xx}a_{zy} + a_{zx}a_{xy}^*)S_3]\sin\xi\}
\end{aligned}
\tag{A.26}
$$

$$
\begin{aligned}
S_3^d = \left(\frac{\omega^2\mu_0}{4\pi R}\right)^2 \{&[\mathbf{Im}(a_{xx}a_{yx}^* + a_{xy}a_{yy}^*)S_0 + \mathbf{Im}(a_{xx}a_{yx}^* - a_{xy}a_{yy}^*)S_1 \\
&- \mathbf{Im}(a_{xx}a_{yy}^* - a_{yx}a_{xy}^*)S_2 + \mathbf{Re}(a_{xx}a_{yy}^* - a_{yx}a_{xy}^*)S_3]\cos\xi \\
&- [\mathbf{Im}(a_{xx}a_{zx} + a_{xy}a_{zy}^*)S_0 + \mathbf{Im}(a_{xx}a_{zx}^* - a_{xy}a_{xy}^*)S_1 \\
&- \mathbf{Im}(a_{xx}a_{zy}^* - a_{zx}a_{xy}^*)S_2 + \mathbf{Re}(a_{xx}a_{zy} - a_{zx}a_{xy}^*)S_3]\sin\xi\}
\end{aligned}
\tag{A.27}
$$

In the simplest case, we could assume that our molecule is in a fixed-frame with no rotations, the incident light is un-polarized with $S_0 = (E^{(0)})^2$ and $S_1 = S_2 = S_3 = 0$, and we only consider either forward or back-scattered light ($\xi = 0, \pm\pi$). The $S_0^d$ parameter for the scattered radiation simplifies to

$$S_0^d = \frac{1}{2}\left(\frac{\omega^2\mu_0}{4\pi R}\right)^2 (|a_{xx}|^2 + |a_{xy}|^2 + |a_{yx}|^2 + |a_{yy}|^2)E^{(0)^2} \tag{A.28}$$

We could further simply this by assuming that our molecule is a dipolar scatterer and substituting $a_{\alpha\beta} = \alpha_{\alpha\beta}$. This additional simplification would give us the fixed-frame Raman scattering Stokes parameter for un-polarized incident light traveling in the $z$-direction.

## A.3 Beyond the $a_{\alpha\beta} \approx \alpha_{\alpha\beta}$ Approximation

Starting with the approximations made for Equation A.28, we may consider the expansion of $a_{\alpha\beta}$ given in Equation A.10. We do this so as to include other approximations of $a_{\alpha\beta}$, such as when the $A_{\alpha\beta\gamma}$ and/or the $G_{\alpha\beta}$ tensors contribute significantly to the scattering—these are particularly important when considering effects such as Raman optical activity. We then extend the approximation to the generalized scattering tensor $a_{\alpha\beta}$ as

$$a_{\alpha\beta} = \alpha_{\alpha\beta} + \frac{i\omega}{3c}(A_{\alpha z\beta} - A^*_{\beta z\alpha}) + \frac{1}{c}(\epsilon_{\gamma z\beta}G_{\alpha\gamma} + \epsilon_{\gamma z\alpha}G^*_{\gamma\beta}) + \cdots \tag{A.29}$$

which gives us

$$a_{xx} = \alpha_{xx} + \frac{i\omega}{3c}(A_{xzx} - A^*_{xzx}) + \frac{1}{c}(G_{xy} + G^*_{yx}) \tag{A.30}$$

$$a_{xy} = \alpha_{xy} + \frac{i\omega}{3c}(A_{xzy} - A^*_{yzx}) + \frac{1}{c}(-G_{xx} + G^*_{yy}) \tag{A.31}$$

$$a_{yx} = \alpha_{yx} + \frac{i\omega}{3c}(A_{yzx} - A^*_{xzy}) + \frac{1}{c}(-G_{yy} - G^*_{xx}) \tag{A.32}$$

$$a_{yy} = \alpha_{yy} + \frac{i\omega}{3c}(A_{yzy} - A^*_{yzy}) + \frac{1}{c}(-G_{yx} - G^*_{xy}) \tag{A.33}$$

Since, for un-polarized Raman scattering, we only need to solve for $|a_{xx}|^2$, $|a_{xy}|^2$, $|a_{yx}|^2$, and $|a_{yy}|^2$, we end up with

$$\begin{aligned}
|a_{xx}|^2 = \{&[\alpha_{xx} + \frac{i\omega}{3c}(A_{xzx} - A^*_{xzx}) + \frac{1}{c}(G_{xy} + G^*_{yx})] \\
&\cdot [\alpha^*_{xx} - \frac{i\omega}{3c}(A^*_{xzx} - A_{xzx}) + \frac{1}{c}(G^*_{xy} + G_{yx})]\} \\
&\approx |\alpha_{xx}|^2 + \frac{i\omega}{3c}(-\alpha_{xx}A^*_{xzx} + \alpha_{xx}A_{xzx} + \alpha^*_{xx}A_{xzx} - \alpha^*_{xx}A^*_{xzx}) \\
&+ \frac{1}{c}(\alpha_{xx}G^*_{xy} + \alpha_{xx}G_{yx} + \alpha^*_{xx}G_{xy} + \alpha^*_{xx}G^*_{yx}) \\
&= |\alpha_{xx}|^2 + \frac{2\omega}{3c}[\mathbf{Im}(\alpha_{xx}A^*_{xzx}) - \mathbf{Im}(\alpha_{xx}A_{xzx})] \\
&+ \frac{2}{c}[\mathbf{Re}(\alpha_{xx}G^*_{xy}) + \mathbf{Re}(\alpha_{xx}G_{yx})]
\end{aligned} \tag{A.34}$$

$$
\begin{aligned}
|a_{xy}|^2 = |\alpha_{xy}|^2 &+ \frac{2\omega}{3c}[\mathbf{Im}(\alpha_{xy}A^*_{xzy}) - \mathbf{Im}(\alpha_{xy}A_{yzx})] \\
&+ \frac{2}{c}[\mathbf{Re}(\alpha_{xy}G_{yy}) - \mathbf{Re}(\alpha_{xy}G^*_{xx})]
\end{aligned} \tag{A.35}
$$

$$
\begin{aligned}
|a_{yx}|^2 = |\alpha_{yx}|^2 &+ \frac{2\omega}{3c}[\mathbf{Im}(\alpha_{yx}A^*_{yzx}) - \mathbf{Im}(\alpha_{yx}A_{xzy})] \\
&+ \frac{2}{c}[\mathbf{Re}(\alpha_{yx}G^*_{yy}) - \mathbf{Re}(\alpha_{yx}G_{xx})]
\end{aligned} \tag{A.36}
$$

$$
\begin{aligned}
|a_{yy}|^2 = |\alpha_{yy}|^* &+ \frac{2\omega}{3c}[\mathbf{Im}(\alpha_{yy}A^*_{yzy}) - \mathbf{Im}(\alpha_{yy}A_{yzy})] \\
&- \frac{2}{c}[\mathbf{Re}(\alpha_{yy}G^*_{yx}) + \mathbf{Re}(\alpha_{yy}G_{xy})]
\end{aligned} \tag{A.37}
$$

However, we may wish to include other elements of $a_{\alpha\beta}$, which would be needed later when we consider orientational averaging. We will, therefore, consider each term in the expansion of $a_{\alpha\beta}$ separately. Consider the $A$ terms in the expansion of $a$

$$
a_{\alpha\beta} \approx \frac{i\omega}{3c}(n^i_\gamma A_{\alpha\gamma\beta} - n^d_\gamma A^*_{\beta\gamma\alpha}) \tag{A.38}
$$

Recall that we assumed that light is always traveling in the $z$-direction with respect to both the molecular frame for incident light, and to the scattered frame for scattered light. Therefore

$$
\begin{aligned}
n^i_x = n^i_y = n^d_x = n^d_y &= 0 \\
n^i_z = n^d_z &= 1
\end{aligned} \tag{A.39}
$$

Thus, Equation A.38 becomes

$$
a_{\alpha\beta} \approx \frac{i\omega}{3c}(A_{\alpha z\beta} - A_{\beta z\alpha}) \tag{A.40}
$$

We are only interested in the $a_{xx}$, $a_{xy}$, $a_{yx}$ and $a_{yy}$ components, but

$$
\begin{aligned}
a_{xx} &= \frac{i\omega}{3c}(A_{xzx} - A_{xzx}) \quad = 0 \\
a_{yy} &= \frac{i\omega}{3c}(A_{yzy} - A_{yzy}) \quad = 0
\end{aligned} \tag{A.41}
$$

and

$$
\begin{aligned}
a_{xy} &= \frac{i\omega}{3c}(A_{xzy} - A_{yzx}) \\
a_{yx} &= \frac{i\omega}{3c}(A_{yzx} - A_{xzy})
\end{aligned} \tag{A.42}
$$

For the $A$ terms, Equation A.28 now becomes

$$
\begin{aligned}
S_0^d &= \frac{1}{2}\left(\frac{\omega^2\mu_0}{4\pi R}\right)^2 (|a_{xy}|^2 + |a_{yx}|^2)E^{(0)^2} \\
&= \frac{1}{2}\left(\frac{\omega^2\mu_0}{4\pi R}\right)^2 \left(\frac{\omega^2}{9c^2}\right) (|A_{xzy} - A_{yzx}|^2 + |A_{yzx} - A_{xzy}|^2)E^{(0)^2} \\
&= \left(\frac{\omega^2\mu_0}{4\pi R}\right)^2 \left(\frac{\omega^2}{9c^2}\right) (|A_{xzy}|^2 - A_{xzy}A^*_{yzx} - A_{yzx}A^*_{yzx} + |A_{yzx}|^2)E^{(0)^2}
\end{aligned} \tag{A.43}
$$

For the $G$ terms in the expansion of $a$

$$
a_{\alpha\beta} \approx \frac{1}{c}(\epsilon_{\gamma\delta\beta} n^i_\delta G_{\alpha\gamma} + \epsilon_{\gamma\delta\alpha} n^d_\delta G_{\gamma\beta}) \tag{A.44}
$$

Using the result in Equation A.39, we expand this to get

$$
a_{\alpha\beta} = \frac{1}{c}(\epsilon_{\gamma z\beta} G_{\alpha\gamma} + \epsilon_{\gamma z\alpha} G_{\gamma\beta}) \tag{A.45}
$$

And for the $a_{xx}$ and $a_{xy}$ components, we get

$$
\begin{aligned}
a_{xx} &= \frac{1}{c}(\epsilon_{\gamma zx} G_{x\gamma} + \epsilon_{\gamma zx} G_{\gamma x}) \\
&= \frac{1}{c}(\epsilon_{yzx} G_{xy} + \epsilon_{yzx} G_{yx}) \\
&= \frac{1}{c}(G_{xy} + G_{yx}) \\
&= -a_{yy}
\end{aligned} \tag{A.46}
$$

$$
\begin{aligned}
a_{xy} &= \frac{1}{c}(\epsilon_{\gamma zy} G_{x\gamma} + \epsilon_{\gamma zx} G_{\gamma y}) \\
&= \frac{1}{c}(\epsilon_{xzy} G_{xx} + \epsilon_{yzx} G_{yy}) \\
&= \frac{1}{c}(G_{yy} - G_{xx}) \\
&= a_{yx}
\end{aligned} \tag{A.47}
$$

Therefore, the $G$ terms in Equation A.28 now becomes

$$
\begin{aligned}
S_0^d &= \frac{1}{2}\left(\frac{\omega^2\mu_0}{4\pi R}\right)^2 (|a_{xx}|^2 + |a_{xy}|^2 + |a_{yx}|^2|a_{yy}|^2)E^{(0)^2} \\
&= \left(\frac{\omega^2\mu_0}{4\pi R}\right)^2 \left(\frac{1}{c^2}\right) (|G_{xy} + G_{yx}|^2 + |G_{yy} - G_{xx}|^2)E^{(0)^2} \\
&= \left(\frac{\omega^2\mu_0}{4\pi R}\right)^2 \left(\frac{1}{c^2}\right) (|G_{xy}|^2 + |G_{yx}|^2 + G_{xy}G^*_{yx} + G_{yx}G^*_{xy} \\
&+ |G_{yy}|^2 + |G_{xx}|^2 - G_{yy}G^*_{xx} - G_{xx}G^*_{yy})E^{(0)^2}
\end{aligned} \tag{A.48}
$$

For the remaining term in the expansion of $a_{\alpha\beta}$ in Equation A.10

$$
a_{\alpha\beta} \approx -n^d_\alpha n^d_\gamma \left\{\alpha_{\gamma\beta} \ + \frac{i\omega}{3c}(n^i_\delta A_{\gamma\delta\beta} - n^d_\delta A_{\beta\delta\gamma}) + \frac{1}{c}\epsilon_{\epsilon\delta\beta} n^i_\delta G_{\gamma\epsilon}\right\} \tag{A.49}
$$

we only retain terms in $a_{z\beta}$ for $n_\alpha^d = n_z^d = 1$. However, these terms are not required for the solution of Equation A.28 and are therefore not considered. Thus, for the complete expression of $a_{\alpha\beta}$ from Equation A.10 into Equation A.28, we get

$$\begin{aligned}
S_0^d = &\left(\frac{\omega^2\mu_0}{4\pi R}\right)^2 \Bigg[\left(\frac{1}{2}\right)(|\alpha_{xx}|^2 + |\alpha_{xy}|^2 + |\alpha_{yx}|^2 + |\alpha_{yy}|^2) \\
&+ \left(\frac{\omega^2}{9c^2}\right)(|A_{xzy}|^2 - A_{xzy}A_{yzx}^* - A_{yzx}A_{yzx}^* + |A_{yzx}|^2) \\
&+ \left(\frac{1}{c^2}\right)(|G_{xy}|^2 + |G_{yx}|^2 + G_{xy}G_{yx}^* + G_{yx}G_{xy}^* \\
&+ |G_{yy}|^2 + |G_{xx}|^2 - G_{yy}G_{xx}^* - G_{xx}G_{yy}^*)\ \Bigg] E^{(0)^2} \\
= &\left(\frac{\omega^2\mu_0}{4\pi R}\right)^2 \Bigg\{\left(\frac{1}{2}\right)(|\alpha_{xx}|^2 + |\alpha_{xy}|^2 + |\alpha_{yx}|^2 + |\alpha_{yy}|^2) \\
&+ \left(\frac{\omega^2}{9c^2}\right)(|A_{xzy}|^2 - 2\mathbf{Re}(A_{xzy}A_{yzx}^*) + |A_{yzx}|^2) \\
&+ \left(\frac{1}{c^2}\right)[|G_{xy}|^2 + |G_{yx}|^2 + 2\mathbf{Re}(G_{xy}G_{yx}^*) \\
&+ |G_{yy}|^2 + |G_{xx}|^2 - 2\mathbf{Re}(G_{yy}G_{xx}^*)]\ \Bigg\} E^{(0)^2}
\end{aligned} \tag{A.50}$$

## A.4 Isotropically-Averaged Raman Scattering

For isotropically-averaged Raman, we shall start with Equation A.28. We will use the approximating $a_{\alpha\beta} \approx \alpha_{\alpha\beta}$ and consider isotropic averaging, where

$$\begin{aligned}
|\alpha_{xx}|^2 &= < \alpha_{xx}\alpha_{xx}^* > \\
&= \frac{1}{15}(\alpha_{\alpha\alpha}\alpha_{\beta\beta}^* + 2\alpha_{\alpha\beta}a_{\alpha\beta}^*) \\
&= |\alpha_{yy}|^2
\end{aligned} \tag{A.51}$$

$$\begin{aligned}
|\alpha_{xy}|^2 &= \frac{1}{30}(3\alpha_{\alpha\beta}\alpha_{\alpha\beta}^* - \alpha_{\alpha\alpha}\alpha_{\beta\beta}^*) \\
&= |\alpha_{yx}|^2
\end{aligned} \tag{A.52}$$

Substituting Equations A.51 and A.52 into Equation A.28 results in

$$S_0^d = \left(\frac{\omega^2\mu_0}{4\pi R}\right)^2 \left(\frac{7\alpha_{\alpha\beta}\alpha_{\alpha\beta}^* + \alpha_{\alpha\alpha}\alpha_{\beta\beta}^*}{30}\right) E^{(0)^2} \tag{A.53}$$

Using the approximation $a_{\alpha\beta} \approx \alpha_{\alpha\beta}$ and the anisotropic ($\alpha^2$) and anisotropic ($\beta(\alpha)^2$) invariants of the polarizability tensor

$$\begin{aligned}
\alpha^2 &= \frac{1}{9}\alpha_{\alpha\alpha}\alpha_{\beta\beta}^* \\
\beta(\alpha)^2 &= \frac{1}{2}(3\alpha_{\alpha\beta}\alpha_{\alpha\beta}^* - \alpha_{\alpha\alpha}\alpha_{\beta\beta}^*)
\end{aligned} \tag{A.54}$$

we get the following expression for $S_0^d$

$$S_0^d = \left(\frac{\omega^2\mu_0}{4\pi R}\right)^2 \left(\frac{45\alpha^2 + 7\beta(\alpha)^2}{45}\right) E^{(0)^2} \tag{A.55}$$

which is the isotropically averaged Raman scattering Stokes parameter.

## A.5 Isotropic Averaging About the $z$-Axis

Because Equation A.28 was derived for forward and back-scattering, it remains invariant to rotation about the $z$-axis. To show this, consider a rotation around the $z$-axis of $\phi$ degrees for the general scattering tensor $a_{\alpha\beta}$

$$\begin{aligned} a'_{\alpha\beta} &= R_{\alpha\gamma}R_{\beta\delta}a_{\gamma\delta} \\ &= R_{\alpha x}R_{\beta x}a_{xx} + R_{\alpha x}R_{\beta y}a_{xy} + R_{\alpha x}R_{\beta z}a_{xz} \\ &+ R_{\alpha y}R_{\beta x}a_{yx} + R_{\alpha y}R_{\beta y}a_{yy} + R_{\alpha y}R_{\beta z}a_{yz} \\ &+ R_{\alpha z}R_{\beta x}a_{zx} + R_{\alpha z}R_{\beta y}a_{zy} + R_{\alpha z}R_{\beta z}a_{zz} \end{aligned} \tag{A.56}$$

where

$$R = \begin{pmatrix} \cos\phi & -\sin\phi & 0 \\ \sin\phi & \cos\phi & 0 \\ 0 & 0 & 1 \end{pmatrix} \tag{A.57}$$

We shall now consider the $S_0^d$ Stokes parameter, where the relevant $|a_{\alpha\beta}|^2$ terms are

$$\begin{aligned} |a'_{xx}|^2 = {} & |a_{xx}|^2\cos^4\phi - a_{xx}a^*_{xy}\sin\phi\cos^3\phi - a_{xx}a^*_{yx}\sin\phi\cos^3\phi + a_{xx}a^*_{yy}\sin^2\phi\cos^2\phi \\ & - a_{xy}a^*_{xx}\sin\phi\cos^3\phi + |a_{xy}|^2\sin^2\phi\cos^2\phi + a_{xy}a^*_{yx}\sin^2\phi\cos^2\phi - a_{xy}a^*_{yy}\sin^3\phi\cos\phi \\ & - a_{yx}a^*_{xx}\sin\phi\cos^3\phi + a_{yx}a^*_{xy}\sin^2\phi\cos^2\phi + |a_{yx}|^2\sin^2\phi\cos^2\phi - a_{yx}a^*_{yy}\sin^3\phi\cos\phi \\ & + a_{yy}a^*_{xx}\sin^2\phi\cos^2\phi - a_{yy}a^*_{xy}\sin^3\phi\cos\phi - a_{yy}a^*_{yx}\sin^3\phi\cos\phi + |a_{yy}|^2\sin^3\phi\cos\phi \end{aligned} \tag{A.58}$$

$$\begin{aligned} |a'_{xy}|^2 = {} & |a_{xx}|^2\sin^2\phi\cos^2\phi + a_{xx}a^*_{xy}\sin\phi\cos^3\phi - a_{xx}a^*_{yx}\sin^3\phi\cos\phi - a_{xx}a^*_{yy}\sin^2\phi\cos^2\phi \\ & + a_{xy}a^*_{xx}\sin\phi\cos^3\phi + |a_{xy}|^2\cos^4\phi - a_{xy}a^*_{yx}\sin\phi\cos^3\phi - a_{xy}a^*_{yy}\sin\phi\cos^3\phi \\ & - a_{yx}a^*_{xx}\sin^3\phi\cos\phi - a_{yx}a^*_{xy}\sin^2\phi\cos^2\phi + |a_{yx}|^2\sin^4\phi + a_{yx}a^*_{yy}\sin^3\phi\cos\phi \\ & - a_{yy}a^*_{xx}\sin^2\phi\cos^2\phi - a_{yy}a^*_{xy}\sin\phi\cos^3\phi + a_{yy}a^*_{yx}\sin^3\phi\cos\phi + |a_{yy}|^2\sin^2\phi\cos^2\phi \end{aligned} \tag{A.59}$$

$$
\begin{aligned}
|a'_{yx}|^2 = {} & |a_{xx}|^2 \sin^2\phi\cos^2\phi - a_{xx}a^*_{xy}\sin^3\phi\cos\phi + a_{xx}a^*_{yx}\sin\phi\cos^3\phi - a_{xx}a^*_{yy}\sin^2\phi\cos^2\phi \\
& - a_{xy}a^*_{xx}\sin^3\phi\cos\phi + |a_{xy}|^2\sin^4\phi - a_{xy}a^*_{yx}\sin^2\phi\cos^2\phi + a_{xy}a^*_{yy}\sin^3\phi\cos\phi \\
& + a_{yx}a^*_{xx}\sin\phi\cos^3\phi - a_{yx}a^*_{xy}\sin^2\phi\cos^2\phi + |a_{yx}|^2\cos^4\phi - a_{yx}a^*_{yy}\sin\phi\cos^3\phi \\
& - a_{yy}a^*_{xx}\sin^2\phi\cos^2\phi + a_{yy}a^*_{xy}\sin^3\phi\cos\phi - a_{yy}a^*_{yx}\sin\phi\cos^3\phi + |a_{yy}|^2\sin^2\phi\cos^2\phi
\end{aligned}
\tag{A.60}
$$

$$
\begin{aligned}
|a'_{yy}|^2 = {} & |a_{xx}|^2 \sin^4\phi + a_{xx}a^*_{xy}\sin^3\phi\cos\phi + a_{xx}a^*_{yx}\sin^3\phi\cos\phi + a_{xx}a^*_{yy}\sin^2\phi\cos^2\phi \\
& + a_{xy}a^*_{xx}\sin^3\phi\cos\phi + |a_{xy}|^2\sin^2\phi\cos^2\phi + a_{xy}a^*_{yx}\sin^2\phi\cos^2\phi + a_{xy}a^*_{yy}\sin\phi\cos^3\phi \\
& + a_{yx}a^*_{xx}\sin^3\phi\cos\phi + a_{yx}a^*_{xy}\sin^2\phi\cos^2\phi + |a_{yx}|^2\sin^2\phi\cos^2\phi + a_{yx}a^*_{yy}\sin\phi\cos^3\phi \\
& + a_{yy}a^*_{xx}\sin^2\phi\cos^2\phi + a_{yy}a^*_{xy}\sin\phi\cos^3\phi + a_{yy}a^*_{yx}\sin\phi\cos^3\phi + |a_{yy}|^2\cos^4\phi
\end{aligned}
\tag{A.61}
$$

Adding Equations A.58, A.59, A.60, and A.61 and using the identity ($\sin^4\phi + 2\sin^2\phi\cos^2\phi + \cos^4\phi = 1$), we get

$$
|a'_{xx}|^2 + |a'_{xy}|^2 + |a'_{yx}|^2 + |a'_{yy}|^2 = |a_{xx}|^2 + |a_{xy}|^2 + |a_{yx}|^2 + |a_{yy}|^2 \tag{A.62}
$$

Thus showing that the fixed-frame Raman scattering described by Equation A.28 is also valid for Raman scattering rotationally averaged about the $z$-axis.

## A.6 Polarized Incident Light

In the case of polarized incident light $S_1$, $S_2$, and $S_3$ are non-zero. We shall consider the case of forward-scattered radiation ($\xi = 0$), where Equations A.24, A.25, A.26, and A.27 simplify to

$$
\begin{aligned}
S^d_0 = {} & \frac{1}{2}\left(\frac{\omega^2\mu_0}{4\pi R}\right)[(|a_{xx}|^2 + |a_{xy}|^2)S_0 + (|a_{xx}|^2 - |a_{xy}|^2)S_1 \\
& - 2\mathbf{Re}(a_{xx}a^*_{xy})S_2 - 2\mathbf{Im}(a_{xx}a^*_{xy})S_3 \\
& + (|a_{yx}|^2 + |a_{yy}|^2)S_0 + (|a_{yx}|^2 - |a_{yy}|^2)S_1 \\
& - \mathbf{Re}(a_{yx}a^*_{yy})S_2 - 2\mathbf{Im}(a_{yx}a^*_{yy})S_3]
\end{aligned}
\tag{A.63}
$$

$$
\begin{aligned}
S^d_1 = {} & \frac{1}{2}\left(\frac{\omega^2\mu_0}{4\pi R}\right)[(|a_{xx}|^2 + |a_{xy}|^2)S_0 + (|a_{xx}|^2 - |a_{xy}|^2)S_1 \\
& - 2\mathbf{Re}(a_{xx}a^*_{xy})S_2 - 2\mathbf{Im}(a_{xx}a^*_{xy})S_3 \\
& - (|a_{yx}|^2 + |a_{yy}|^2)S_0 + (|a_{yx}|^2 - |a_{yy}|^2)S_1 \\
& + \mathbf{Re}(a_{yx}a^*_{yy})S_2 + 2\mathbf{Im}(a_{yx}a^*_{yy})S_3]
\end{aligned}
\tag{A.64}
$$

$$
\begin{aligned}
S^d_2 = {} & -\left(\frac{\omega^2\mu_0}{4\pi R}\right)[\mathbf{Re}(a_{xx}a^*_{yx} + a_{xy}a^*_{yy})S_0 + \mathbf{Re}(a_{xx}a^*_{yx} - a_{xy}a^*_{yy})S_1 \\
& - \mathbf{Re}(a_{xx}a^*_{yy} + a_{yx}a^*_{xy})S_2 - \mathbf{Im}(a_{xx}a^*_{yy} + a_{yx}a^*_{xy})S_3]
\end{aligned}
\tag{A.65}
$$

$$
\begin{aligned}
S_3^d = + \left(\frac{\omega^2 \mu_0}{4\pi R}\right) [&\mathbf{Im}(a_{xx}a_{yx}^* + a_{xy}a_{yy}^*)S_0 + \mathbf{Im}(a_{xx}a_{yx}^* - a_{xy}a_{yy})S_1 \\
&- \mathbf{Im}(a_{xx}a_{yy}^* - a_{yx}a_{xy}^*)S_2 + \mathbf{Re}(a_{xx}a_{yy}^* - a_{yx}a_{xy}^*)S_3]
\end{aligned} \tag{A.66}
$$

And for back-scattered geometry ($\xi = \pm\pi$), we get

$$
\begin{aligned}
S_0^d(\pm\pi) &= S_0^d(0) \\
S_1^d(\pm\pi) &= S_1^d(0) \\
S_2^d(\pm\pi) &= -S_2^d(0) \\
S_3^d(\pm\pi) &= -S_3^d(0)
\end{aligned} \tag{A.67}
$$

For linearly polarized light ($P = 1$, $\eta = 0$), these simplify further to

$$
\begin{aligned}
S_0^d = \frac{1}{2} \left(\frac{\omega^2 \mu_0 {E^{(0)}}^2}{4\pi R}\right) [&(|a_{xx}|^2 + |a_{xy}|^2) + (|a_{xx}|^2 - |a_{xy}|^2)\cos 2\theta \\
&- 2\mathbf{Re}(a_{xx}a_{xy}^*)\sin 2\theta + (|a_{yx}|^2 + |a_{yy}|^2) \\
&+ (|a_{yx}|^2 - |a_{yy}|^2)\cos 2\theta - \mathbf{Re}(a_{yx}a_{yy}^*)\sin 2\theta]
\end{aligned} \tag{A.68}
$$

For polarization perpendicular to the scattering plane ($zy$-plane) $\theta = 0, \pi$, and for polarization parallel to the scattering plane $\theta = \pm\frac{\pi}{2}$. Therefore, the Raman intensity factor for linearly polarized light perpendicular to the scattering plane is

$$
S_0^d = \left(\frac{\omega^2 \mu_0 {E^{(0)}}^2}{4\pi R}\right) (|a_{xx}|^2 + |a_{yx}|^2) \tag{A.69}
$$

and for linearly polarized light parallel to the scattering plane, we get

$$
S_0^d = \left(\frac{\omega^2 \mu_0 {E^{(0)}}^2}{4\pi R}\right) (|a_{xy}|^2 + |a_{yy}|^2) \tag{A.70}
$$

# Appendix B
# Summary of the Dressed-tensors Formalism

Chulhai, D. V.; Hu, Z.; Moore, J.E.; Chen, X.; Jensen, L. "*Theory of Linear and Nonlinear Surface-enhanced Vibrational Spectroscopy*" *Annu. Rev. Phys. Chem.* **2016**, *67*, 541–564. (excerpts within)

## B.1 Derivation of the Formalism

The dressed-tensor formalism,[215,258] as presented and discussed in Part II of this dissertation, is similar to the Gersten-Nitzan formalism (without image field effects), except the interactions $\alpha^{\mathrm{NP}} \cdot \mathbf{T}^{(2)}$ and $\mathbf{T}^{(2)} \cdot \alpha^{\mathrm{NP}}$ have been replaced by the field enhancement matrix $\mathbf{F}$,

$$\frac{\alpha^{\mathrm{tot}}_{\alpha\beta}}{\partial Q_k} = \left[\delta_{\alpha\gamma} + F^{\alpha}_{\gamma}(\omega_S)\right] \frac{\partial \alpha^{\mathrm{M}}_{\gamma\delta}}{\partial Q_k} \left[\delta_{\delta\beta} + F^{\beta}_{\delta}(\omega_L)\right]. \tag{B.1}$$

The Einstein summation convention is assumed for repeated indices, where Greek indices represent Cartesian directions. $F^{\alpha}_{\beta}$ is the unitless local electric field matrix describing the fields induced in the $\beta$ Cartesian direction due to a unit incident perturbation in the $\alpha$ Cartesian direction, calculated at the incident laser ($\omega_L$) and Raman shifted ($\omega_S$) frequencies.

This equation removes the point-dipole approximation of the NP in Equation 2.22, and one can simulate the field enhancements from complex NP geometries using any classical ED method. It also makes it easier to increase the level of interaction between the molecule and NP. While this change may appear trivial, the dressed-tensor formalism implicitly includes other advantages, including: (a) a higher order multipole description of the NP, (b) multiple polarizable sources (such as the description from a DDA-type calculation or multiple point-polarizable NPs), and (c) inclusion of retardation effects. We will show how the field enhancement matrix accounts for each of these effects in turn.

To show that the field enhancement implicitly includes contributions from a NP with higher order multipoles, we shall consider a NP described by $\alpha^{\mathrm{NP}}$, dipole-quadrupole ($A^{\mathrm{NP}}$), quadrupole-dipole ($\mathscr{A}^{\mathrm{NP}}$), and quadrupole-quadrupole ($C^{\mathrm{NP}}$) polarizabilities. The QM definition of these tensors and how they relate to the induced multipoles are defined in Ref. 313, except that the $C$-tensor is not defined with the 1/3 factor to maintain consistency with the definition of the other polarizability tensors. All these response tensors will be frequency-dependent and complex, which we will ignore for simplicity.

The induced multipoles in the NP due to an external field are $\mu^{\mathrm{NP}}_{\alpha} = \alpha^{\mathrm{NP}}_{\alpha\beta} E^{0}_{\beta}$ and

$\theta^{\mathrm{NP}}_{\alpha\beta} = \mathscr{A}^{\mathrm{NP}}_{\alpha\beta,\gamma} E^0_\gamma$. The $A^{\mathrm{NP}}$ and $C^{\mathrm{NP}}$ do not contribute to the induced multipoles in the quasistatic limit since the field gradient of the incident field is effectively zero. The local field "felt" by the molecule due to these multipoles is

$$E^{\mathrm{loc}}_\alpha = T^{(2)}_{\alpha\beta}\mu^{NP}_\beta - \frac{1}{3}T^{(3)}_{\alpha\beta\gamma}\theta^{\mathrm{NP}}_{\beta\gamma} = \left(T^{(2)}_{\alpha\gamma}\alpha^{\mathrm{NP}}_{\gamma\beta} - \frac{1}{3}T^{(3)}_{\alpha\gamma\delta}\mathscr{A}^{\mathrm{NP}}_{\gamma\delta,\beta}\right)E^0_\beta = F^\beta_\alpha E^0_\beta. \tag{B.2}$$

And similarly, the dipole induced in the NP at the Raman shifted frequency due to the induced molecular dipole is

$$\mu^{\mathrm{NP,scat}}_\alpha = \left(\alpha^{\mathrm{NP}}_{\alpha\gamma}T^{(2)}_{\gamma\beta} + \frac{1}{3}A^{\mathrm{NP}}_{\alpha,\gamma\delta}T^{(3)}_{\gamma\delta\beta}(-\mathbf{R})\right)\mu^{\mathrm{M}}_\beta = F^\alpha_\beta\mu^{\mathrm{M}}_\beta. \tag{B.3}$$

The relationship above has been achieved using $-T^{(3)}(\mathbf{R}) = T^{(3)}(-\mathbf{R})$, $\mathscr{A}^{\mathrm{NP}}_{\alpha\beta,\gamma} = A^{\mathrm{NP}}_{\gamma,\alpha\beta}$, and the fact that the far-field radiation of the quadrupole induced in the NP does not contribute significantly to the scattering. Thus showing that the field enhancement matrix $\mathbf{F}$ implicitly accounts for higher order multipole descriptions of the NP.

We will show that the field enhancement matrix also accounts for a multiple-dipole approximation of the NP. In such cases, we assume that the NP consists of a series of $N$ point-polarizable objects with polarizability $\alpha^{\mathrm{NP},i}$ at position $\mathbf{r}^i$ ($i \in N$). The induced dipoles in such a system may be solved as $\mu^{\mathrm{NP},i}_\alpha = \sum_j^N \left(\mathbf{A}^{-1}\right)_{ij,\alpha\beta} \cdot E^{0,j}_\beta$, where $\mathbf{A}$ is the $3N \times 3N$ interaction matrix defined elsewhere[103,432]. The local field is then written as

$$E^{\mathrm{loc}}_\alpha(\mathbf{r}^{\mathrm{M}}) = \left[\sum_{i,j}^N T^{(2)}_{i,\alpha\beta}(\mathbf{r}^{\mathrm{M}} - \mathbf{r}^i)\left(\mathbf{A}^{-1}\right)_{ij,\beta\gamma}\right]E^0_\gamma = F^\beta_\alpha E^0_\beta, \tag{B.4}$$

where $\mathbf{r}^{\mathrm{M}}$ is the position of the molecular point-dipole, thereby defining the field enhancement matrix at this point.

For the total dipole induced in the NP at the scattered field due to the induced molecular dipole

$$\mu^{\mathrm{NP,scat}}_\alpha = \left[\sum_{i,j}^N \left(\mathbf{A}^{-1}\right)_{ij,\alpha\beta} T^{(2)}_{j,\beta\gamma}(\mathbf{r}^j - \mathbf{r}^{\mathrm{M}})\right]\mu^{\mathrm{M}}_\gamma = F^\alpha_\beta\mu^{\mathrm{M}}_\beta, \tag{B.5}$$

thereby showing that the field enhancement matrix in the dressed-tensor formalism may also describe multiple point-dipole NP systems.

Finally, to include retardation effects in the dressed-tensor formalism the $\mathbf{T}^{(2)}$ interaction matrix becomes the dipole relay tensor with retardation effects[2,120], which still retains the necessary symmetry ($T^{(2)}_{\alpha\beta} = T^{(2)}_{\beta\alpha}$ and $T^{(2)}(\mathbf{R}) = T^{(2)}(-\mathbf{R})$) to justify the above made claims for the dressed-tensor formalism.

## B.2 Local Field Gradients

More recent changes to the EM have come through exploration of the local field gradients[106,215–219,258]. In most cases, the local field varies greatly over the dimensions of the molecule[144,214]. This can often lead to the observation of Raman-inactive modes, as was observed and briefly discussed in the early 1980s[35–38].

The near-field gradients (in the quasi-static limit) are described by the $\mathbf{T}^{(3)}$ interaction tensor[123,124], which leads one to write the induced dipole in the molecule (using the Gersten-Nitzan model) as

$$\mu^{\mathrm{M}} = \left[\alpha^{\mathrm{M}} \cdot \left(\mathbf{I} + \mathbf{T}^{(2)} \cdot \alpha^{\mathrm{NP}}\right) + \frac{1}{3} A^{\mathrm{M}} \cdot \mathbf{T}^{(3)} \cdot \alpha^{\mathrm{NP}}\right] \cdot \mathbf{E}^{0}, \tag{B.6}$$

where $A^{\mathrm{M}}$ is the molecule's electric dipole-quadrupole polarizability tensor.

One consideration of the effects of the local field gradients was proposed by Jahncke and coworkers[216,217], who suggested that the induced molecular dipole may be expanded as

$$\frac{\partial \mu^{\mathrm{M}}}{\partial Q_k} = \left[\frac{\partial \alpha^{\mathrm{M}}}{\partial Q_k} \cdot \left(\mathbf{I} + \mathbf{T}^{(2)} \cdot \alpha^{\mathrm{NP}}\right) + \alpha^{\mathrm{M}} \cdot \frac{\partial \left(\mathbf{T}^{(2)} \cdot \alpha^{\mathrm{NP}}\right)}{\partial Q_k} + \frac{1}{3} \frac{\partial A}{\partial Q_k} \cdot \mathbf{T}^{(3)} \cdot \alpha^{\mathrm{NP}}\right] \cdot \mathbf{E}^{0}. \tag{B.7}$$

This is a modified form of Equation 3 from Ref. 216, rewritten in the style of the Gersten-Nitzan model and assuming a point-dipole NP. The first term is effectively the SERS term (without field gradients), the second term has been labelled as the "gradient-field Raman" term, while the third is the traditional field gradient SERS term. It is in fact this third term that results, as originally proposed[35–38], from the local electric field gradient.

We can easily account for this term in the dressed-tensor formalism, assuming that the molecule is described as a point-dipole with $\alpha^{\mathrm{NP}}$ and $A^{\mathrm{NP}}$ tensors. This leads to the dressed-tensor expression for the Raman polarizability as[13,36,258]

$$\frac{\partial \alpha^{\mathrm{tot}}_{\alpha\beta}}{\partial Q_k} = \left[\delta_{\alpha\gamma} + F^{\alpha}_{\gamma}(\omega_S)\right] \left\{\frac{\partial \alpha^{\mathrm{M}}_{\gamma\delta}}{\partial Q_k} \left[\delta_{\beta\delta} + F^{\beta}_{\delta}(\omega_L)\right] + \frac{1}{3} \frac{\partial A^{\mathrm{M}}_{\gamma,\delta\epsilon}}{\partial Q_k} F^{\beta}_{\delta\epsilon}(\omega_L)\right\}, \tag{B.8}$$

where we have introduced the field enhancement matrix $F^{\alpha}_{\beta\gamma}$ (in units of inverse length), describing the field gradient in the $\beta\gamma$ Cartesian direction due to an incident unit field in the $\alpha$ direction.

## B.3 Point-Dipole / Point-Quadrupole Molecule

With large field gradients, one may argue that a point-dipole description is often insufficient at describing the molecule. We will therefore describe the molecule as a point-dipole (described by $\alpha^{\mathrm{M}}$ and $A^{\mathrm{M}}$) and a point-quadrupole (described by the quadrupole-dipole ($\mathscr{A}^{\mathrm{M}}$) and the quadrupole-quadrupole ($C^{\mathrm{M}}$) polarizabilities). One may write the induced quadrupole in the molecule as

$$\theta^{\mathrm{M}} = \mathscr{A}^{\mathrm{M}} \cdot \left(\mathbf{E}^{0} + \mathbf{T}^{(2)} \cdot \mu^{NP}\right) + \frac{1}{3} C^{M} \cdot \mathbf{T}^{(3)} \cdot \mu^{NP}, \tag{B.9}$$

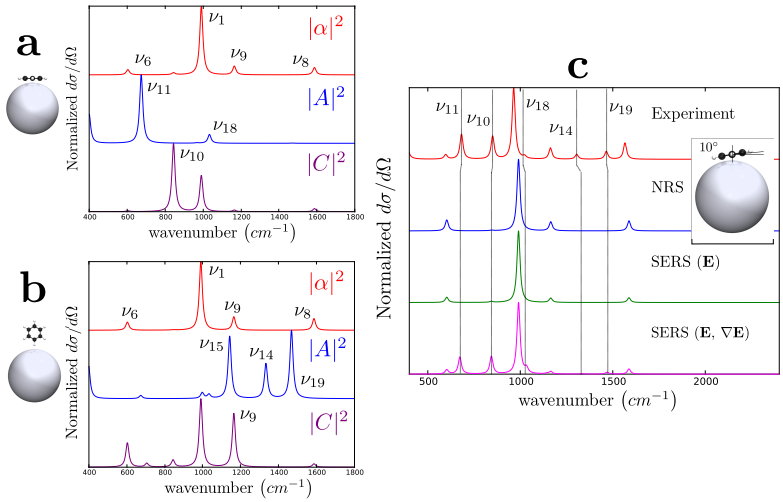


**Figure B.1.** The SERS surface selection rules from the $\alpha$, $A$ and $C$ tensors for benzene for (a) a flat and (b) vertical orientation. (c) Higher order tensors may assist in assigning binding orientations. Adapted from Ref. 258 with permission.

and the induced dipole of the NP as

$$\mu^{\mathrm{NP}} = \alpha^{\mathrm{NP}} \cdot \left( \mathbf{E}^0 + \mathbf{T}^{(2)}(-\mathbf{R}) \cdot \mu^{\mathrm{M}} - \frac{1}{3}\mathbf{T}^{(3)}(-\mathbf{R}) \cdot \theta^{\mathrm{M}} \right). \tag{B.10}$$

Solving these equations as in Ref. 119, ignoring the image field effects, substituting $\mathbf{T}^{(2)}(\mathbf{R}) = \mathbf{T}^{(2)}(-\mathbf{R})$ and $\mathbf{T}^{(3)}(\mathbf{R}) = -\mathbf{T}^{(3)}(-\mathbf{R})$, and replacing $\mathbf{T}^{(2)} \cdot \alpha^{\mathrm{NP}}$ and $\mathbf{T}^{(3)} \cdot \alpha^{\mathrm{NP}}$ with the appropriate local field or gradient enhancement matrix $\mathbf{F}$, we end up with the dressed-tensor formalism[258]

$$\begin{aligned}
\frac{\partial \alpha^{\mathrm{tot}}_{\alpha\beta}}{\partial Q_k} &= \left[\delta_{\alpha\gamma} + F^{\alpha}_{\gamma}(\omega_S)\right] \frac{\partial \alpha^{\mathrm{M}}_{\gamma\delta}}{\partial Q_k} \left[\delta_{\beta\delta} + F^{\beta}_{\delta}(\omega_L)\right] \\
&+ \frac{1}{3}\left[\delta_{\alpha\gamma} + F^{\alpha}_{\gamma}(\omega_S)\right] \frac{\partial A^{\mathrm{M}}_{\gamma,\delta\epsilon}}{\partial Q_k} F^{\beta}_{\delta\epsilon}(\omega_L) \\
&+ \frac{1}{3} F^{\alpha}_{\gamma\delta}(\omega_S) \frac{\partial \mathscr{A}^{\mathrm{M}}_{\gamma\delta,\epsilon}}{\partial Q_k} \left[\delta_{\beta\epsilon} + F^{\beta}_{\epsilon}(\omega_L)\right] \\
&+ \frac{1}{9} F^{\alpha}_{\gamma\delta}(\omega_S) \frac{\partial C^{\mathrm{M}}_{\gamma\delta,\epsilon\zeta}}{\partial Q_k} F^{\beta}_{\epsilon\zeta}(\omega_L).
\end{aligned} \tag{B.11}$$

In Ref. 258, it was noted that the induced point-quadrupole interaction with the NP's polarizability occurs through $\mathbf{T}^{(3)}$, which is the same level of interaction as the field gradients with a point-dipole molecule, and therefore should be considered simultaneously. The dressed-tensor, therefore allows one to easily account for higher order multipole description of the molecule as well as higher order gradients of the local electric field. We note that these four terms are effectively the same as those identified in the quadrupolar SERS theory of Polubotko[433].

This field gradient theory of SERS is not separate from the main $|\mathbf{E}|^4$ EM of SERS but rather a supplement to it. Importantly, the main SERS contribution is from the local fields and the dipole-dipole polarizability. The 1/3 prefactor for the dipole-quadrupole terms and the 1/9

**Table B.1.** EM enhancement factor contributions to the SERS intensity.

| Terms | Prefactor | Enhancement |
|---|---|---|
| $\lvert\alpha\rvert^2$ | 1 | $\lvert\mathbf{E}\rvert^4$ |
| $\mathbf{Re}(\alpha A^\dagger)$, $\mathbf{Re}(\alpha \mathscr{A}^\dagger)$ | $\frac{1}{3}$ | $\mathbf{E}^3 \cdot \nabla\mathbf{E}$ |
| $\lvert A\rvert^2$, $\lvert\mathscr{A}\rvert^2$, $\mathbf{Re}(A\mathscr{A}^\dagger)$, $\mathbf{Re}(\alpha C^\dagger)$ | $\frac{1}{9}$ | $\mathbf{E}^2 \cdot (\nabla\mathbf{E})^2$ |
| $\mathbf{Re}(AC^\dagger)$, $\mathbf{Re}(\mathscr{A}C^\dagger)$ | $\frac{1}{27}$ | $\mathbf{E} \cdot (\nabla\mathbf{E})^3$ |
| $\lvert C\rvert^2$ | $\frac{1}{81}$ | $\lvert\nabla\mathbf{E}\rvert^4$ |

prefactor for the quadrupole-quadrupole term indicate that they will be minor modifications to the SERS spectrum, and only significant for very large field gradient to field ratios or large quadrupolar polarizabilities. It allows for the observation of Raman inactive modes in molecules through an EM, rather than through symmetry lowering from adsorption to the surface—though both effects may be relevant. This is illustrated in Figure B.1, where the $A$ and $C$ surface selection rules are shown. The contributions to the EM enhancement (up to the $\mathbf{T}^{(3)}$ interaction level) is given in Table B.1, with their relevant prefactors. Each of the terms in Table B.1 may select for specific modes within a molecule. The $|\alpha|^2$ term select for the the Raman-active modes in the gas-phase molecules, and is the major contributing SERS term. The selection rules for the $|A|^2$ and $|\mathscr{A}|^2$ terms were also previously considered[35,36], and selects for modes that belong to representations that include cubic transformations.

## B.4 Other Dressed Polarizability Tensors

### B.4.1 Surface-enhanced Raman optical activity

The dressed-tensor SEROA formalism was first considered by Janesko & Scuseria[215], where the general theory was outlined, and later expanded in Chapter 6 of this dissertation to include the $\mathbf{T}^{(3)}$ level of interaction. Combining these two sets of dressed-tensor formalism gives the following generalized expressions for the relevant tensor derivatives (the dressed dipole-dipole polarizability remains the same as in SERS)

$$\frac{\partial A^{\text{tot}}_{\alpha,\beta\gamma}}{\partial Q_p} = 3F^\alpha_\delta \frac{\partial \alpha^{\text{M}}_{\delta\epsilon}}{\partial Q_p} (\nabla F)^{\beta\gamma}_\epsilon + F^\alpha_\delta \frac{\partial A^{\text{M}}_{\delta,\epsilon\zeta}}{\partial Q_p} (\nabla F)^{\beta\gamma}_{\epsilon\zeta} + F^\alpha_{\delta\epsilon} \frac{\partial \mathscr{A}^{\text{M}}_{\delta\epsilon,\zeta}}{\partial Q_p} (\nabla F)^{\beta\gamma}_\zeta + \frac{1}{3} F^\alpha_{\delta\epsilon} \frac{\partial C^{\text{M}}_{\delta\epsilon,\zeta\eta}}{\partial Q_p} (\nabla F)^{\beta\gamma}_{\zeta\eta}, \tag{B.12}$$

$$\frac{\partial \mathscr{A}^{\text{tot}}_{\alpha\beta,\gamma}}{\partial Q_p} = (\nabla F)^{\alpha\beta}_\delta \frac{\partial \alpha^{\text{M}}_{\delta\epsilon}}{\partial Q_p} F^\gamma_\epsilon + \frac{1}{3} (\nabla F)^{\alpha\beta}_\delta \frac{\partial A^{\text{M}}_{\delta,\epsilon\zeta}}{\partial Q_p} F^\gamma_{\epsilon\zeta} + (\nabla F)^{\alpha\beta}_{\delta\epsilon} \frac{\partial \mathscr{A}^{\text{M}}_{\delta\epsilon,\zeta}}{\partial Q_p} F^\gamma_\zeta + \frac{1}{3} (\nabla F)^{\alpha\beta}_{\delta\epsilon} \frac{\partial C^{\text{M}}_{\delta\epsilon,\zeta\eta}}{\partial Q_p} F^\gamma_{\zeta\eta}, \tag{B.13}$$

$$\frac{\partial G^{\text{tot}}_{\alpha\beta}}{\partial Q_p} = F^\alpha_\gamma \frac{\partial G^{\text{M}}_{\gamma\beta}}{\partial Q_p} + \frac{1}{3} F^\alpha_{\gamma\delta} \frac{\partial \mathscr{D}^{\text{M}}_{\gamma\delta,\beta}}{\partial Q_p}, \text{ and} \tag{B.14}$$

$$\frac{\partial \mathscr{G}^{\text{tot}}_{\alpha\beta}}{\partial Q_p} = \frac{\partial \mathscr{G}^{\text{M}}_{\alpha\gamma}}{\partial Q_p} F^{\beta}_{\gamma} + \frac{1}{3} \frac{\partial D^{\text{M}}_{\alpha,\gamma\delta}}{\partial Q_p} F^{\beta}_{\gamma\delta}. \tag{B.15}$$

We have introduced the gradient field enhancement matrix $\nabla\mathbf{F}$, where $(\nabla F)^{\alpha\beta}_{\gamma}$ describes the field in the $\gamma$ direction due to an incident field gradient in the $\alpha\beta$ directions (in units of length), and $(\nabla F)^{\alpha\beta}_{\gamma\delta}$ is the unitless matrix describing the field gradient enhancement in the $\gamma\delta$ directions due to the incident field gradient in the $\alpha\beta$ directions.

The equations in Ref. 215 contain placeholders for additional magnetic enhancement terms, which we neglect here since they contribute negligibly to the local field and gradients for non-magnetic NPs. Additionally, the $\nabla\mathbf{F}$ terms are only important for quadrupolar NPs. The $(\nabla F)^{\alpha\beta}_{\gamma}$ and $(\nabla F)^{\alpha\beta}_{\gamma\delta}$ enhancement terms are the $\mathbf{T}^{(2)}$ and $\mathbf{T}^{(3)}$ interactions from the multipoles in the NP induced by an incident electric field gradient. For dipolar NPs, we obtain $(\nabla F)^{\alpha\beta}_{\gamma} = 0$ and $(\nabla F)^{\alpha\beta}_{\gamma\delta} = \delta_{\alpha\gamma}\delta_{\beta\delta}$, which results in the equations presented in Ref. 124. These equations are also a generalized form of the equations by Johnson and coworkers[308,309], where the $\mathbf{T}^{(3)}$ interactions were not included.

### B.4.2 Nonlinear tensors

In spectroscopies such as hyper-Raman scattering and sum-frequency generation, we consider the second order response tensors—which we will term $\beta$ for simplicity. This tensor may be dressed as

$$\frac{\partial \beta^{\text{tot}}_{\alpha\beta\gamma}(\omega_1,\omega_2)}{\partial Q_k} = \left[\delta_{\alpha\delta} + F^{\alpha}_{\delta}(\omega_s)\right] \frac{\partial \beta^{\text{M}}_{\delta\epsilon\zeta}}{\partial Q_k} \left[\delta_{\beta\epsilon} + F^{\beta}_{\epsilon}(\omega_1)\right] \left[\delta_{\gamma\zeta} + F^{\gamma}_{\zeta}(\omega_2)\right], \tag{B.16}$$

where $\omega_1$ and $\omega_2$ are the relevant input frequencies, and $\omega_s$ is the output frequency, that describe the particular response tensor used.

Third order response tensors $\gamma$ may be dressed as

$$\frac{\partial \gamma^{\text{tot}}_{\alpha\beta\gamma\delta}(\omega_1,\omega_2,\omega_3)}{\partial Q_k} = \left[F^{\alpha}_{\epsilon}(\omega_s) + \delta_{\alpha\epsilon}\right] \frac{\partial \gamma^{\text{M}}_{\epsilon\zeta\eta\iota}}{\partial Q_k} \left[F^{\beta}_{\zeta}(\omega_1) + \delta_{\beta\zeta}\right] \left[F^{\gamma}_{\eta}(\omega_2) + \delta_{\gamma\eta}\right] \left[F^{\delta}_{\iota}(\omega_3) + \delta_{\delta\iota}\right] \tag{B.17}$$

We ignore contributions from the field gradient or a quadrupolar molecule for simplicity. The dressed tensors written in this way allows for quickly accounting for the local fields in these nonlinear spectroscopies and good estimations of expected enhancement factors.

# Appendix C
# Origin-dependence of Multipole Moments and Higher Order Polarizabilities

## C.1 Multipole Moments

### C.1.1 Electric dipole and quadrupole

The charge $q$ of a charge density $\rho$ is defined as

$$q = \int_V \rho dV \tag{C.1}$$

and the electric dipole $\mu$ is defined as

$$\mu_\alpha = \int_V r_\alpha \rho dV \tag{C.2}$$

where $r_\alpha$ is the position vector $\mathbf{r}$ in the $\alpha$ Cartesian direction. Similarly, the primitive quadrupole operator is defined as

$$q_{\alpha\beta} = \int_V r_\alpha r_\beta \rho dV \tag{C.3}$$

These moments depend on the choice of coordinate origin. Consider a translation of the coordinate origin $\mathbf{O}$ to some new origin $\mathbf{O} + \mathbf{R}$. This is equivalent to translating the position vector $\mathbf{r}$ to $\mathbf{r} - \mathbf{R}$. The electric dipole now becomes:

$$\begin{aligned} \mu_\alpha(\mathbf{O} + \mathbf{R}) &= \int_V (r_\alpha - R_\alpha)\rho dV \\ &= \mu_\alpha(\mathbf{O}) - R_\alpha q \end{aligned} \tag{C.4}$$

Similarly, for the primitive quadrupole moment

$$\begin{aligned} q_{\alpha\beta}(\mathbf{O} + \mathbf{R}) &= \int_V (r_\alpha - R_\alpha)(r_\beta - R_\beta)\rho dV \\ &= q_{\alpha\beta}(\mathbf{O}) - R_\alpha \mu_\beta(\mathbf{O}) - R_\beta \mu_\alpha(\mathbf{O}) + R_\alpha R_\beta q \end{aligned} \tag{C.5}$$

We now define the traceless quadrupole moment $\theta$ as

$$\theta_{\alpha\beta} = \frac{3}{2}q_{\alpha\beta} - \frac{1}{2}\delta_{\alpha\beta}q_{\gamma\gamma} \tag{C.6}$$

where $\delta$ is the Kronecker delta, and the Einstein summation convention is employed for repeated indices. The origin-dependence of $\theta$ is now

$$\begin{aligned}
\theta_{\alpha\beta}(\mathbf{O}+\mathbf{R}) &= \frac{3}{2}q_{\alpha\beta}(\mathbf{O}+\mathbf{R}) - \frac{1}{2}\delta_{\alpha\beta}q_{\gamma\gamma}(\mathbf{O}+\mathbf{R}) \\
&= \frac{3}{2}q_{\alpha\beta}(\mathbf{O}) - \frac{1}{2}\delta_{\alpha\beta}q_{\gamma\gamma}(\mathbf{O}) - \frac{3}{2}R_\beta\mu_\alpha(\mathbf{O}) - \frac{3}{2}R_\alpha\mu_\beta(\mathbf{O}) \\
&+ \delta_{\alpha\beta}R_\gamma\mu_\gamma(\mathbf{O}) + \frac{3}{2}R_\alpha R_\beta q - \frac{1}{2}\delta_{\alpha\beta}R_\gamma R_\gamma q \\
&= \theta_{\alpha\beta}(\mathbf{O}) - \frac{3}{2}R_\beta\mu_\alpha(\mathbf{O}) - \frac{3}{2}R_\alpha\mu_\beta(\mathbf{O}) + \delta_{\alpha\beta}R_\gamma\mu_\gamma(\mathbf{O}) \\
&+ \frac{3}{2}R_\alpha R_\beta q - \frac{1}{2}\delta_{\alpha\beta}R_\gamma R_\gamma q
\end{aligned} \tag{C.7}$$

### C.1.2 Magnetic dipole

The magnetic dipole $m$ of a material is defined as

$$m_\alpha = \frac{1}{2}\int_V \epsilon_{\alpha\beta\gamma} r_\beta \frac{\partial r_\gamma \rho}{\partial t} dV \tag{C.8}$$

We will consider the time dependence of $\rho$ to be $\rho(r,t) = \rho(r)e^{-i\omega t}$. This is true for molecules under the influence of an external electromagnetic field of angular freuquency $\omega$. In such cases, the magnetic dipole becomes

$$m_\alpha = \frac{1}{2}\int_V \epsilon_{\alpha\beta\gamma} r_\beta(-i\omega r_\gamma)\rho dV \tag{C.9}$$

The origin dependence of the magnetic dipole is therefore

$$m_\alpha(\mathbf{O}+\mathbf{R}) = \frac{1}{2}\int_V \epsilon_{\alpha\beta\gamma}(r_\beta - R_\beta)(-i\omega r_\gamma)\rho dv \tag{C.10}$$

$$= m_\alpha(\mathbf{O}) + \frac{i\omega}{2}\epsilon_{\alpha\beta\gamma}R_\beta\mu_\gamma \tag{C.11}$$

## C.2 Polarizabilities

In deriving the origin dependence of the polarizability tensors, we will assume that all species are electrically neutral and can therefore ignore the terms that depend on the specie charge $q$.

### C.2.1 Electric dipole-dipole polarizability

We will write the polarizability response using the notation:

$$\alpha_{\alpha\beta} = \langle\langle \mu_\alpha; \mu_\beta \rangle\rangle \tag{C.12}$$

However, if we ignore the dependence on the specie charge $q$, the electric dipole (and therefore the electric dipole-dipole polarizability) is independent of the choice of origin.

$$\alpha_{\alpha\beta}(\mathbf{O}+\mathbf{R}) = \alpha_{\alpha\beta}(\mathbf{O}) \tag{C.13}$$

### C.2.2 Electric dipole-quadrupole polarizability

The electric dipole-quadrupole polarizability, $A$, may be written as

$$A_{\alpha\beta\gamma} = \langle\langle \mu_\alpha; \theta_{\beta\gamma} \rangle\rangle \tag{C.14}$$

If we consider the origin-dependence of the quadrupole moment, we have

$$\begin{aligned}
A_{\alpha\beta\gamma}(\mathbf{O}+\mathbf{R}) &= \langle\langle \mu_\alpha; \theta_{\beta\gamma}(\mathbf{O}+\mathbf{R}) \rangle\rangle && \text{(C.15)}\\
&= \langle\langle \mu_\alpha; \theta_{\beta\gamma}(\mathbf{O}) - \frac{3}{2}R_\gamma\mu_\beta - \frac{3}{2}R_\beta\mu_\gamma + \delta_{\beta\gamma}R_\delta\mu_\delta \rangle\rangle && \text{(C.16)}\\
&= \langle\langle \mu_\alpha; \theta_{\beta\gamma} \rangle\rangle - \frac{3}{2}R_\gamma\langle\langle \mu_\alpha; \mu_\beta \rangle\rangle - \frac{3}{2}R_\beta\langle\langle \mu_\alpha; \mu_\gamma \rangle\rangle + \delta_{\beta\gamma}R_\delta\langle\langle \mu_\alpha; \mu_\delta \rangle\rangle && \text{(C.17)}\\
&= A_{\alpha\beta\gamma}(\mathbf{O}) - \frac{3}{2}R_\gamma\alpha_{\alpha\beta} - \frac{3}{2}R_\beta\alpha_{\alpha\gamma} + \delta_{\beta\gamma}R_\delta\alpha_{\alpha\delta} && \text{(C.18)}
\end{aligned}$$

Similar rules are obtained for the electric quadrupole-dipole polarizability, $\mathscr{A}$

$$\begin{aligned}
\mathscr{A}_{\alpha,\beta\gamma}(\mathbf{O}+\mathbf{R}) &= \langle\langle \theta_{\beta\gamma}(\mathbf{O}+\mathbf{R}); \mu_\alpha \rangle\rangle && \text{(C.19)}\\
&= \mathscr{A}_{\alpha,\beta\gamma}(\mathbf{O}) - \frac{3}{2}R_\gamma\alpha_{\beta\alpha} - \frac{3}{2}R_\beta\alpha_{\gamma\alpha} + \delta_{\beta\gamma}R_\delta\alpha_{\delta\alpha} && \text{(C.20)}
\end{aligned}$$

### C.2.3 Electric quadrupole-quadrupole polarizability

The electric quadrupole-quadrupole polarizability $C$ may be written as

$$C_{\alpha\beta,\gamma\delta} = \langle\langle \theta_{\alpha\beta}; \theta_{\gamma\delta} \rangle\rangle \tag{C.21}$$

Its origin-dependence may be found from

$$
\begin{aligned}
C_{\alpha\beta,\gamma\delta}(\mathbf{O}+\mathbf{R}) &= \langle\langle\theta_{\alpha\beta}(\mathbf{O}+\mathbf{R});\theta_{\gamma\delta}(\mathbf{O}+\mathbf{R})\rangle\rangle \\
&= \langle\langle\theta_{\alpha\beta}(\mathbf{O}) - \frac{3}{2}R_\beta\mu_\alpha - \frac{3}{2}R_\alpha\mu_\beta + \delta_{\alpha\beta}R_\epsilon\mu_\epsilon; \\
&\theta_{\gamma\delta}(\mathbf{O}) - \frac{3}{2}R_\delta\mu_\gamma - \frac{3}{2}R_\gamma\mu_\delta + \delta_{\gamma\delta}R_\zeta\mu_\zeta\rangle\rangle \\
&= \langle\langle\theta_{\alpha\beta}(\mathbf{O});\theta_{\gamma\delta}(\mathbf{O})\rangle\rangle - \frac{3}{2}R_\beta\langle\langle\mu_\alpha;\theta_{\gamma\delta}(\mathbf{O})\rangle\rangle - \frac{3}{2}R_\alpha\langle\langle\mu_\beta;\theta_{\gamma\delta}(\mathbf{O})\rangle\rangle \\
&+ \delta_{\alpha\beta}R_\epsilon\langle\langle\mu_\epsilon;\theta_{\gamma\delta}(\mathbf{O})\rangle\rangle - \frac{3}{2}R_\delta\langle\langle\theta_{\alpha\beta}(\mathbf{O});\mu_\gamma\rangle\rangle + \frac{9}{4}R_\delta R_\beta\langle\langle\mu_\alpha;\mu_\gamma\rangle\rangle \\
&+ \frac{9}{4}R_\delta R_\alpha\langle\langle\mu_\beta;\mu_\gamma\rangle\rangle - \frac{3}{2}\delta_{\alpha\beta}R_\delta R_\epsilon\langle\langle\mu_\epsilon;\mu_\gamma\rangle\rangle - \frac{3}{2}R_\gamma\langle\langle\theta_{\alpha\beta}(\mathbf{O});\mu_\delta\rangle\rangle \\
&+ \frac{9}{4}R_\gamma R_\beta\langle\langle\mu_\alpha;\mu_\delta\rangle\rangle + \frac{9}{4}R_\gamma R_\alpha\langle\langle\mu_\beta;\mu_\delta\rangle\rangle - \frac{3}{2}\delta_{\alpha\beta}R_\gamma R_\epsilon\langle\langle\mu_\epsilon;\mu_\delta\rangle\rangle \\
&+ \delta_{\gamma\delta}R_\zeta\langle\langle\theta_{\alpha\beta}(\mathbf{O});\mu_\zeta\rangle\rangle - \frac{3}{2}\delta_{\gamma\delta}R_\zeta R_\beta\langle\langle\mu_\alpha;\mu_\zeta\rangle\rangle - \frac{3}{2}\delta_{\gamma\delta}R_\zeta R_\alpha\langle\langle\mu_\beta;\mu_\zeta\rangle\rangle \\
&+ \delta_{\alpha\beta}\delta_{\gamma\delta}R_\zeta R_\epsilon\langle\langle\mu_\epsilon;\mu_\zeta\rangle\rangle
\end{aligned}
\tag{C.22}
$$

Therefore,

$$
\begin{aligned}
C_{\alpha\beta,\gamma\delta}(\mathbf{O}+\mathbf{R}) &= C_{\alpha\beta,\gamma\delta}(\mathbf{O}) - \frac{3}{2}R_\beta A_{\alpha\gamma\delta}(\mathbf{O}) - \frac{3}{2}R_\alpha A_{\beta\gamma\delta}(\mathbf{O}) \\
&+ \delta_{\alpha\beta}R_\epsilon A_{\epsilon\gamma\delta}(\mathbf{O}) - \frac{3}{2}R_\delta\mathscr{A}_{\gamma,\alpha\beta}(\mathbf{O}) - \frac{3}{2}R_\gamma\mathscr{A}_{\delta,\alpha\beta}(\mathbf{O}) \\
&+ \delta_{\gamma\delta}R_\zeta\mathscr{A}_{\zeta,\alpha\beta}(\mathbf{O}) + \frac{9}{4}R_\delta R_\beta\alpha_{\alpha\gamma} + \frac{9}{4}R_\delta R_\alpha\alpha_{\beta\gamma} \\
&- \frac{3}{2}\delta_{\alpha\beta}R_\delta R_\epsilon\alpha_{\epsilon\gamma} + \frac{9}{4}R_\gamma R_\beta\alpha_{\alpha\delta} + \frac{9}{4}R_\gamma R_\alpha\alpha_{\beta\delta} \\
&- \frac{3}{2}\delta_{\alpha\beta}R_\gamma R_\epsilon\alpha_{\epsilon\delta} - \frac{3}{2}\delta_{\gamma\delta}R_\zeta R_\beta\alpha_{\alpha\zeta} - \frac{3}{2}\delta_{\gamma\delta}R_\zeta R_\alpha\alpha_{\beta\zeta} \\
&+ \delta_{\alpha\beta}\delta_{\gamma\delta}R_\epsilon R_\zeta\alpha_{\epsilon\zeta}
\end{aligned}
\tag{C.23}
$$

### C.2.4 Electric dipole-magnetic dipole polarizability

The electric dipole-magnetic dipole, $G$, polarizability is found from

$$
G_{\alpha\beta} = \mathbf{Im}\left[\langle\langle\mu_\alpha;m_\beta\rangle\rangle\right] \tag{C.24}
$$

The origin-dependence of the frequency-dependent $G$-tensor is found from

$$
\begin{aligned}
G_{\alpha\beta}(\mathbf{O}+\mathbf{R}) &= \mathbf{Im}\left[\langle\langle\mu_\alpha;m_\beta(\mathbf{O}+\mathbf{R})\rangle\rangle\right] \\
&= \mathbf{Im}\left[\langle\langle\mu_\alpha;m_\alpha(\mathbf{O}) + \frac{i\omega}{2}\epsilon_{\beta\gamma\delta}R_\gamma\mu_\delta\rangle\rangle\right] \\
&= G_{\alpha\beta}(\mathbf{O}) + \frac{\omega}{2}\epsilon_{\beta\gamma\delta}R_\gamma\alpha_{\alpha\delta}
\end{aligned}
\tag{C.25}
$$

A similar expression may be derived for the magnetic dipole-electric dipole polarizability, $\mathscr{G}$, defined as

$$\mathscr{G}_{\alpha\beta} = \mathbf{Im}\left[\langle\langle m_\alpha; \mu_\beta\rangle\rangle\right] \tag{C.26}$$

The $\mathscr{G}$-tensor origin dependence is found from

$$\begin{aligned}
\mathscr{G}_{\alpha\beta}(\mathbf{O}+\mathbf{R}) &= \mathbf{Im}\left[\langle\langle m_\alpha(\mathbf{O}+\mathbf{R}); \mu_\beta\rangle\rangle\right] \\
&= \mathbf{Im}\left[\langle\langle m_\alpha(\mathbf{O}) + \frac{i\omega}{2}\epsilon_{\alpha\gamma\delta}R_\gamma\mu_\delta; \mu_\beta\rangle\rangle\right] \\
&= \mathscr{G}_{\alpha\beta}(\mathbf{O}) + \frac{\omega}{2}\epsilon_{\alpha\gamma\delta}R_\gamma\alpha_{\delta\beta}
\end{aligned} \tag{C.27}$$

### C.2.5 Electric quadrupole-magnetic dipole polarizability

The electric quadrupole-magnetic dipole polarizability, $D$, is defined as

$$D_{\alpha\beta,\gamma} = \mathbf{Im}\left[\langle\langle \theta_{\alpha\beta}; m_\gamma\rangle\rangle\right] \tag{C.28}$$

The $D$-tensor origin-dependence is derived as

$$\begin{aligned}
D_{\alpha\beta,\gamma}(\mathbf{O}+\mathbf{R}) &= \mathbf{Im}\left[\langle\langle \theta_{\alpha\beta}(\mathbf{O}+\mathbf{R}); m_\gamma(\mathbf{O}+\mathbf{R})\rangle\rangle\right] \\
&= \mathbf{Im}\left[\langle\langle \theta_{\alpha\beta}(\mathbf{O}) - \frac{3}{2}R_\beta\mu_\alpha - \frac{3}{2}R_\alpha\mu_\beta + \delta_{\alpha\beta}R_\delta\mu_\delta; m_\gamma(\mathbf{O}) + \frac{i\omega}{2}\epsilon_{\gamma\epsilon\zeta}R_\epsilon\mu_\zeta\rangle\rangle\right] \\
&= D_{\alpha\beta,\gamma}(\mathbf{O}) + \frac{\omega}{2}\epsilon_{\gamma\epsilon\delta}R_\epsilon\mathscr{A}_{\delta,\alpha\beta}(\mathbf{O}) \\
&- \frac{3}{2}R_\beta G_{\alpha\gamma}(\mathbf{O}) - \frac{3}{2}R_\alpha G_{\beta\gamma}(\mathbf{O}) + \delta_{\alpha\beta}R_\delta G_{\delta\gamma}(\mathbf{O}) \\
&- \frac{3\omega}{4}\epsilon_{\gamma\epsilon\delta}R_\beta R_\epsilon\alpha_{\alpha\delta} - \frac{3\omega}{4}\epsilon_{\gamma\epsilon\delta}R_\alpha R_\epsilon\alpha_{\beta\delta} + \frac{\omega}{2}\delta_{\alpha\beta}\epsilon_{\gamma\epsilon\zeta}R_\delta R_\epsilon\alpha_{\delta\zeta}
\end{aligned} \tag{C.29}$$

Similarly, we define the magnetic dipole-electric quadrupole, $\mathscr{D}$, tensor as

$$\mathscr{D}_{\alpha,\beta\gamma} = \mathbf{Im}\left[\langle\langle m_\alpha; \theta_{\beta\gamma}\rangle\rangle\right] \tag{C.30}$$

whose origin-dependence is found from

$$\begin{aligned}
\mathscr{D}_{\alpha,\beta\gamma}(\mathbf{O}+\mathbf{R}) &= \mathbf{Im}\left[\langle\langle m_\alpha(\mathbf{O}+\mathbf{R}); \theta_{\beta\gamma}(\mathbf{O}+\mathbf{R})\rangle\rangle\right] \\
&= \mathscr{D}_{\alpha,\beta\gamma}(\mathbf{O}) + \frac{\omega}{2}\epsilon_{\alpha\delta\epsilon}R_\delta A_{\epsilon\beta\gamma}(\mathbf{O}) \\
&- \frac{3}{2}R_\beta\mathscr{G}_{\alpha\gamma}(\mathbf{O}) - \frac{3}{2}R_\gamma\mathscr{G}_{\alpha\beta}(\mathbf{O}) + \delta_{\beta\gamma}R_\delta\mathscr{G}_{\alpha\delta}(\mathbf{O}) \\
&- \frac{3\omega}{4}\epsilon_{\alpha\delta\epsilon}R_\delta R_\gamma\alpha_{\epsilon\beta} - \frac{3\omega}{4}\epsilon_{\alpha\delta\epsilon}R_\delta R_\beta\alpha_{\epsilon\gamma} + \frac{\omega}{2}\delta_{\beta\gamma}\epsilon_{\alpha\delta\epsilon}R_\delta R_\zeta\alpha_{\epsilon\zeta}
\end{aligned} \tag{C.31}$$

# Appendix D
# Supporting Information for: Determining Molecular Orientation With Surface-Enhanced Raman Scattering Using Inhomogeneous Electric Fields

## D.1 Origin-Dependence of Terms

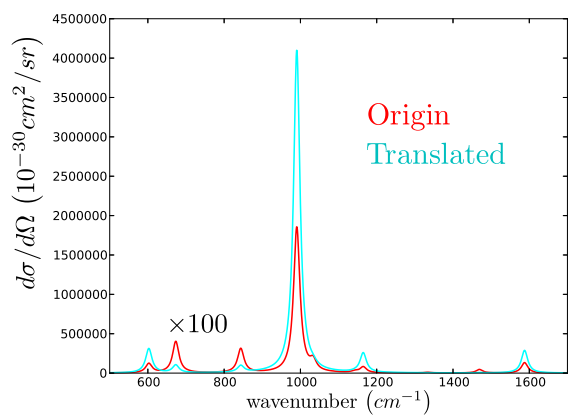


**Figure D.1.** The origin-dependence of the SERS spectrum for benzene translated 10Å along the z-axis as compared to the SERS of benzene centered at the origin.

The electric dipole-quadrupole ($A$) and electric quadrupole-quadrupole ($C$) tensors depend on the choice of origin. This leads to an effective polarizability, Eq. 5 of the main text, and therefore a SERS spectrum that also depends on choice of origin. An example of this is shown in Figure D.1, where we show the SERS of benzene titled 10° with respect to the surface of a 10 bohr sphere (similar to that of Figure 4 of the main text). In this Supporting Information, we will examine the origin-dependence of the terms contributing to the effective polarizability and propose and prove an origin-invariant solution.

### D.1.1 Origin-dependence of the induced dipole

Consider the dipole induced by incident and local electric field and gradient. This may be written as

$$\mu_\alpha^{\text{ind}} = \left[\alpha_{\alpha\gamma}\left(\delta_{\beta\gamma} + F_\gamma^\beta(\omega_L)\right) + \frac{1}{3}A_{\alpha\gamma\delta}F_{\gamma\delta}^\beta(\omega_L)\right]E_\beta^{(0)} \tag{D.1}$$

where $\alpha$ is the electric dipole-dipole polarizability, $A$ is the electric dipole-quadrupole polarizability, Greek subscripts refer to Cartesian directions and the Einstein summation convention is employed for repeated subscripts. $\delta$ is the Kronecker delta and $F_\gamma^\beta(\omega_L)$ is the local electric field enhancement in the $\gamma$ Cartesian direction due to an incident field in the $\beta$ direction at the incident frequency $\omega_L$. The bracketed terms may be collectively referred to as a modified polarizability $\alpha'$

$$\alpha'_{\alpha\beta} = \alpha_{\alpha\gamma}\left(\delta_{\beta\gamma} + F_\gamma^\beta\right) + \frac{1}{3}A_{\alpha\gamma\delta}F_{\gamma\delta}^\beta \tag{D.2}$$

This modified polarizability (and therefore induced dipole) depends on the choice of molecular origin since the $A$-tensor is origin-dependent according to

$$\begin{aligned} A_{\alpha\beta\gamma}(\mathbf{O}+\mathbf{d}) &= A_{\alpha\beta\gamma}(\mathbf{O}) + \frac{3}{2}d_\beta\alpha_{\alpha\gamma}(\mathbf{O}) + \frac{3}{2}d_\gamma\alpha_{\alpha\beta}(\mathbf{O}) - d_\delta\alpha_{\alpha\delta}(\mathbf{O})\delta_{\beta\gamma} \\ &= A_{\alpha\beta\gamma}(\mathbf{O}) + \frac{3}{2}d_\beta\alpha_{\alpha\gamma} + \frac{3}{2}d_\gamma\alpha_{\alpha\beta} - d_\delta\alpha_{\alpha\delta}\delta_{\beta\gamma} \end{aligned}$$

where $\mathbf{O}$ is the vector describing the origin in some general frame and $\mathbf{d}$ is a translation vector.

We may define the origin-dependence of the modified polarizability by considering the difference

$$\alpha'_{\alpha\beta}(\mathbf{O}+\mathbf{d}) - \alpha'_{\alpha\beta}(\mathbf{O}) = \frac{1}{2}\left(d_\gamma\alpha_{\alpha\delta}F_{\gamma\delta}^\beta + d_\delta\alpha_{\alpha\gamma}F_{\gamma\delta}^\beta\right) - \frac{1}{3}d_\epsilon\alpha_{\alpha\epsilon}\delta_{\gamma\delta}F_{\gamma\delta}^\beta \tag{D.3}$$

By recognizing that the field gradient tensor is symmetric ($F_{\gamma\delta}^\beta = F_{\delta\gamma}^\beta$) and that all subscripts are dummy variables, we can simplify this into

$$\alpha'_{\alpha\beta}(\mathbf{O}+\mathbf{d}) - \alpha'_{\alpha\beta}(\mathbf{O}) = \alpha_{\alpha\gamma}\left(d_\delta F_{\gamma\delta}^\beta - \frac{1}{3}d_\gamma F_{\delta\delta}^\beta\right) \tag{D.4}$$

The origin dependence of Eq. D.4 may be resolved by considering a common-origin expression of the local fields. In other words, for the expression to remain orgin-independent, the local field enhancements $F_\alpha^\beta$ also depends on the choice of origin according to

$$F_\alpha^\beta(\omega_L;\mathbf{O}+\mathbf{d}) = F_\alpha^\beta(\omega_L;\mathbf{O}) - \left(d_\gamma F_{\beta\gamma}^\beta(\omega_L;\mathbf{O}) - \frac{1}{3}d_\alpha F_{\gamma\gamma}^\beta(\omega_L;\mathbf{O})\right) \tag{D.5}$$

This is equivalent to a Taylor expansion of the fields about the vector $\mathbf{R}$ (the vector describing the separation of the molecule and substrate) accounting for the translation $\mathbf{d}$. Figure D.2 shows this common origin formalism, where the fields along $\mathbf{R}_{QQ}$ (Taylor expanded abour $\mathbf{R}$) is needed to maintain origin-independence using the molecular tensors calculated for a molecule translated some vector $\mathbf{d}$ from the origin of the molecular refrence frame $Q_M$. The third term in Eq. D.5 is present because the traceless polarizability tensors are used throughout. This term ensures that

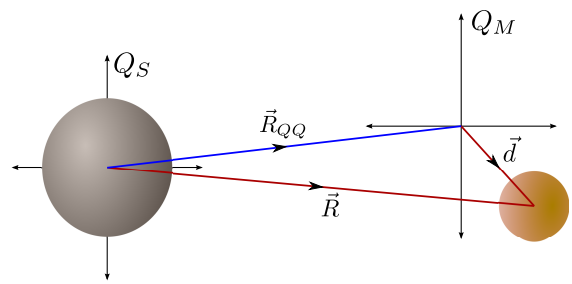


**Figure D.2.** Origin-independent SERS expression enhanced by a local field and gradient may be achieved by expressing the fields from the coordinate system of the substrate ($Q_S$) into the coordinate system of the molecule ($Q_M$) through vector $R_{QQ}$.

the field-gradient tensor is also traceless. The field gradient tensor is defined as traceless as per Eq. 12b of the main text, and therefore this final term may be dropped.

### D.1.2 Origin-dependence of the effective dipole

As explored in the main text, the effective dipoles contributing to SERS ($\mu^{\text{eff}}$) described by the effective scattering polarizability ($\alpha''$) originates from enhancement of the near fields of radiating dipoles and quadrupoles according to

$$\begin{aligned}\mu_\alpha^{\text{eff}} &= \alpha''_{\alpha\beta} E_\beta^{(0)} \\ &= \Bigg( \left[\delta_{\alpha\gamma} + F_\gamma^\alpha(\omega_S)\right] \left\{ \alpha_{\gamma\delta} \left[\delta_{\beta\delta} + F_\delta^\beta(\omega_L)\right] + \frac{1}{3} A_{\gamma\delta\epsilon} F_{\delta\epsilon}^\beta(\omega_L) \right\} \\ &+ \frac{1}{3} F_{\gamma\delta}^\alpha(\omega_S) \left\{ \mathscr{A}_{\epsilon,\gamma\delta} \left[\delta_{\beta\epsilon} + F_\epsilon^\beta(\omega_L)\right] + \frac{1}{3} C_{\gamma\delta,\epsilon\zeta} F_{\epsilon\zeta}^\beta(\omega_L) \right\} \Bigg) E_\beta^{(0)} \\ &= \left(\delta_{\alpha\beta} + F_\beta^\alpha(\omega_S)\right) \mu_\beta^{\text{ind}} + \frac{1}{3} F_{\beta\gamma}^\alpha(\omega_S) \theta_{\beta\gamma}^{\text{ind}}\end{aligned} \tag{D.6}$$

where $\omega_S$ is the Raman-shifted frequency, $\mu^{\text{ind}}$ is the induced dipole due to the incident and local fields as described by Eq. D.1, and $\theta^{\text{ind}}$ is the induced quadrupole due to the incident and local fields, defined as

$$\theta_{\alpha\beta}^{\text{ind}} = \left[ \mathscr{A}_{\gamma,\alpha\beta} \left(\delta_{\delta\gamma} + F_\gamma^\delta(\omega_L)\right) + \frac{1}{3} C_{\alpha\beta,\gamma\epsilon} F_{\gamma\epsilon}^\delta(\omega_L) \right] E_\delta^{(0)} \tag{D.7}$$

where $\mathscr{A}$ is the electric quadrupole-dipole polarizability tensor and $C$ is the electric quadrupole-quadrupole polarizability tensor.

The quadrupole moment $\theta$ is dependent on the choice of origin according to

$$\theta_{\alpha\beta}(\mathbf{O} + \mathbf{d}) = \theta_{\alpha\beta}(\mathbf{O}) + \frac{3}{2} d_\beta \mu_\alpha + \frac{3}{2} d_\alpha \mu_\beta - d_\gamma \mu_\gamma \delta_{\alpha\beta} \tag{D.8}$$

and therefore the origin-dependence of $\mu^{\text{eff}}$ is

$$\mu_\alpha^{\text{eff}}(\mathbf{O} + \mathbf{d}) - \mu_\alpha^{\text{eff}}(\mathbf{O}) = \frac{1}{2} d_\beta \mu_\gamma^{\text{ind}} F_{\gamma\beta}^\alpha(\omega_S) + \frac{1}{2} d_\gamma \mu_\beta^{\text{ind}} F_{\gamma\beta}^\alpha(\omega_S) - \frac{1}{3} d_\delta \mu_\delta^{\text{ind}} \delta_{\gamma\beta} F_{\gamma\beta}^\alpha(\omega_S) \tag{D.9}$$

$$= \mu_\beta^{\text{ind}} \left( d_\gamma F^\alpha_{\beta\gamma}(\omega_S) - \frac{1}{3} d_\beta F^\alpha_{\gamma\gamma}(\omega_S) \right) \tag{D.10}$$

This dependence is identical to that derived in Eq. D.4 and therefore the common origin expression of the local field enhancement derived in Eq. D.5 needs to be applied to the local fields at both the incident ($\omega_L$) and Raman-shifted ($\omega_S$) frequencies.

### D.1.3 Proof of origin-invariance

In order to show that the previously derived common-origin expression of the local fields leads to an origin-independent effective polarizability, we will consider the effective polarizability $\alpha''$ of a molecule translated from the origin $\mathbf{O}$ by some vector $\mathbf{d}$. This effective polarizability may be written as

$$\begin{aligned}
\alpha''_{\alpha\beta}(\mathbf{O}+\mathbf{d}) = \left[\delta_{\alpha\gamma} + F^\alpha_\gamma(\omega_S;\mathbf{O}+\mathbf{d})\right] \Big\{ & \alpha_{\gamma\delta}(\mathbf{O}+\mathbf{d}) \left[\delta_{\beta\delta} + F^\beta_\delta(\omega_L;\mathbf{O}+\mathbf{d})\right] \\
& + \frac{1}{3} A_{\gamma\delta\epsilon}(\mathbf{O}+\mathbf{d}) F^\beta_{\delta\epsilon}(\omega_L;\mathbf{O}+\mathbf{d}) \Big\} \\
& + \frac{1}{3} F^\alpha_{\gamma\delta}(\omega_S;\mathbf{O}+\mathbf{d}) \Big\{ \mathscr{A}_{\epsilon,\gamma\delta}(\mathbf{O}+\mathbf{d}) \left[\delta_{\beta\epsilon} + F^\beta_\epsilon(\omega_L;\mathbf{O}+\mathbf{d})\right] \\
& + \frac{1}{3} C_{\gamma\delta,\epsilon\zeta}(\mathbf{O}+\mathbf{d}) F^\beta_{\epsilon\zeta}(\omega_L;\mathbf{O}+\mathbf{d}) \Big\}
\end{aligned} \tag{D.11}$$

We now explicitly include the origin-dependent contributions to the local fields and polarizability tensors assuming that the field gradient tensor is traceless ($F^\alpha_{\beta\beta} = 0$).

$$\begin{aligned}
\alpha''_{\alpha\beta}(\mathbf{O}+\mathbf{d}) = \left[\delta_{\alpha\gamma} + F^\alpha_\gamma(\omega_S;\mathbf{O}) - d_\zeta F^\alpha_{\gamma\zeta}(\omega_S)\right] \Big\{ & \alpha_{\gamma\delta}(\mathbf{O}) \left[\delta_{\beta\delta} + F^\beta_\delta(\omega_L;\mathbf{O}) - d_\epsilon F^\beta_{\delta\epsilon}(\omega_L)\right] \\
& + \frac{1}{3} \left[ A_{\gamma\delta\epsilon}(\mathbf{O}) + \frac{3}{2} d_\delta \alpha_{\gamma\epsilon}(\mathbf{O}) + \frac{3}{2} d_\epsilon \alpha_{\gamma\delta}(\mathbf{O}) - d_\kappa \alpha_{\gamma\kappa}(\mathbf{O}) \delta_{\delta\epsilon} \right] F^\beta_{\delta\epsilon}(\omega_L) \Big\} \\
& + \frac{1}{3} F^\alpha_{\gamma\delta}(\omega_S) \Big\{ \left[ \mathscr{A}_{\epsilon,\gamma\delta}(\mathbf{O}) + \frac{3}{2} d_\gamma \alpha_{\epsilon\delta}(\mathbf{O}) + \frac{3}{2} d_\delta \alpha_{\epsilon\gamma}(\mathbf{O}) - d_\eta \alpha_{\epsilon\eta}(\mathbf{O}) \delta_{\gamma\delta} \right] \\
& \times \left[ \delta_{\beta\epsilon} + F^\beta_\epsilon(\omega_L;\mathbf{O}) - d_\zeta F^\beta_{\epsilon\zeta}(\omega_L) \right] \\
& + \frac{1}{3} \Big[ C_{\gamma\delta,\epsilon\zeta}(\mathbf{O}) + \frac{3}{2} d_\zeta \mathscr{A}_{\epsilon,\gamma\delta}(\mathbf{O}) + \frac{3}{2} d_\epsilon \mathscr{A}_{\zeta,\gamma\delta}(\mathbf{O}) - d_\kappa \mathscr{A}_{\kappa,\gamma\delta}(\mathbf{O}) \delta_{\epsilon\zeta} \\
& \frac{3}{2} d_\delta A_{\gamma\epsilon\zeta}(\mathbf{O}) + \frac{9}{4} d_\delta d_\zeta \alpha_{\gamma\epsilon}(\mathbf{O}) + \frac{9}{4} d_\delta d_\epsilon \alpha_{\gamma\zeta}(\mathbf{O}) - \frac{3}{2} d_\delta d_\kappa \alpha_{\gamma\kappa}(\mathbf{O}) \delta_{\epsilon\zeta} \\
& + \frac{3}{2} d_\gamma A_{\delta\epsilon\zeta}(\mathbf{O}) + \frac{9}{4} d_\gamma d_\zeta \alpha_{\delta\epsilon}(\mathbf{O}) + \frac{9}{4} d_\gamma d_\epsilon \alpha_{\delta\zeta}(\mathbf{O}) - \frac{3}{2} d_\gamma d_\kappa \alpha_{\delta\kappa}(\mathbf{O}) \delta_{\epsilon\zeta} \\
& - d_\kappa A_{\kappa\epsilon\zeta}(\mathbf{O}) \delta_{\gamma\delta} - \frac{3}{2} d_\kappa d_\zeta \alpha_{\kappa\epsilon}(\mathbf{O}) \delta_{\gamma\delta} - \frac{3}{2} d_\kappa d_\epsilon \alpha_{\kappa\zeta}(\mathbf{O}) \delta_{\gamma\delta} + d_\kappa d_\eta \alpha_{\kappa\eta}(\mathbf{O}) \delta_{\gamma\delta} \delta_{\epsilon\zeta} \Big] \\
& \times F^\beta_{\epsilon\zeta}(\omega_L;\mathbf{O}) \Big\}
\end{aligned} \tag{D.12}$$

The transformation used here for the $C$-tensor assumes a traceless tensor, where $C_{\alpha\alpha,\beta\gamma} = 0 =$

$C_{\alpha\beta,\gamma\gamma}$. All tensors now depend only on $\mathbf{O}$ and we will ignore explicitly writing this dependence. Also, the field gradient tensors are traceless and symmetric. This implies that all terms dependent on a Kronecker delta will vanish and we can group terms that differ with exchange of the field gradient indices. We are left with

$$\begin{aligned}
\alpha''_{\alpha\beta}(\mathbf{O}+\mathbf{d}) = &\left[\delta_{\alpha\gamma} + F^{\alpha}_{\gamma}(\omega_S) - d_\zeta F^{\alpha}_{\gamma\zeta}(\omega_S)\right]\Big\{\alpha_{\gamma\delta}\left[\delta_{\beta\delta} + F^{\beta}_{\delta}(\omega_L) - d_\epsilon F^{\beta}_{\delta\epsilon}(\omega_L)\right] \\
&+ \left[\frac{1}{3}A_{\gamma\delta\epsilon} + d_\delta \alpha_{\gamma\epsilon}\right] F^{\beta}_{\delta\epsilon}(\omega_L)\Big\} \\
&+ F^{\alpha}_{\gamma\delta}(\omega_S)\Big\{\left[\frac{1}{3}\mathscr{A}_{\epsilon,\gamma\delta} + d_\gamma \alpha_{\epsilon\delta}\right]\left[\delta_{\beta\epsilon} + F^{\beta}_{\epsilon}(\omega_L) - d_\zeta F^{\beta}_{\epsilon\zeta}(\omega_L)\right] \\
&+ \left[\frac{1}{9}C_{\gamma\delta,\epsilon\zeta} + \frac{1}{3}d_\zeta \mathscr{A}_{\epsilon,\gamma\delta} + \frac{1}{3}d_\delta A_{\gamma\epsilon\zeta} + d_\delta d_\zeta \alpha_{\gamma\epsilon}\right] F^{\beta}_{\epsilon\zeta}(\omega_L)\Big\}
\end{aligned} \tag{D.13}$$

We can now expand this expression and group terms that depend on the translation $\mathbf{d}$. This leaves us with

$$\begin{aligned}
\alpha''_{\alpha\beta}(\mathbf{O}+\mathbf{d}) = &[\delta_{\alpha\gamma} + F^{\alpha}_{\gamma}(\omega_S)]\alpha_{\gamma\delta}[\delta_{\beta\delta} + F^{\beta}_{\delta}(\omega_L)] - [\delta_{\alpha\gamma} + F^{\alpha}_{\gamma}(\omega_S)]\alpha_{\gamma\delta} d_\epsilon F^{\beta}_{\delta\epsilon}(\omega_L) \\
&- d_\zeta F^{\beta}_{\zeta\gamma}(\omega_S)\alpha_{\gamma\delta}[\delta_{\beta\delta} + F^{\beta}_{\delta}(\omega_L)] + d_\zeta F^{\beta}_{\zeta\gamma}(\omega_S)\alpha_{\gamma\delta} d_\epsilon F^{\beta}_{\delta\epsilon}(\omega_L) \\
&+ \frac{1}{3}[\delta_{\alpha\gamma} + F^{\alpha}_{\gamma}(\omega_S)]A_{\gamma\delta\epsilon}F^{\beta}_{\delta\epsilon}(\omega_L) + [\delta_{\alpha\gamma} + F^{\alpha}_{\gamma}(\omega_S)]d_\delta \alpha_{\gamma\epsilon}F^{\beta}_{\delta\epsilon}(\omega_L) \\
&- \frac{1}{3}d_\zeta F^{\alpha}_{\gamma\zeta}(\omega_S)A_{\gamma\delta\epsilon}F^{\beta}_{\delta\epsilon}(\omega_L) + d_\zeta F^{\alpha}_{\gamma\zeta}(\omega_S)d_\delta \alpha_{\gamma\epsilon}F^{\beta}_{\delta\epsilon}(\omega_L) \\
&+ \frac{1}{3}F^{\alpha}_{\gamma\delta}(\omega_S)\mathscr{A}_{\epsilon,\gamma\delta}[\delta_{\beta\epsilon} + F^{\beta}_{\epsilon}(\omega_L)] + F^{\alpha}_{\gamma\delta}(\omega_S)d_\gamma \alpha_{\epsilon\delta}[\delta_{\beta\epsilon} + F^{\beta}_{\epsilon}(\omega_L)] \\
&- \frac{1}{3}F^{\alpha}_{\gamma\delta}(\omega_S)\mathscr{A}_{\epsilon,\gamma\delta}d_\zeta F^{\beta}_{\epsilon\zeta}(\omega_L) - F^{\alpha}_{\gamma\delta}(\omega_S)d_\gamma \alpha_{\epsilon\delta}d_\zeta F^{\beta}_{\epsilon\zeta}(\omega_L) \\
&+ \frac{1}{9}F^{\alpha}_{\gamma\delta}(\omega_S)C_{\gamma\delta,\epsilon\zeta}F^{\beta}_{\epsilon\zeta}(\omega_L) + \frac{1}{3}F^{\alpha}_{\gamma\delta}(\omega_S)d_\zeta \mathscr{A}_{\epsilon,\gamma\delta}F^{\beta}_{\epsilon\zeta}(\omega_L) \\
&+ \frac{1}{3}F^{\alpha}_{\gamma\delta}(\omega_S)d_\delta A_{\gamma\epsilon\zeta}F^{\beta}_{\epsilon\zeta}(\omega_L) + F^{\alpha}_{\gamma\delta}(\omega_S)d_\delta d_\zeta \alpha_{\gamma\epsilon}F^{\beta}_{\epsilon\zeta}(\omega_L) \\
&= [\delta_{\alpha\gamma} + F^{\alpha}_{\gamma}(\omega_S)]\alpha_{\gamma\delta}[\delta_{\beta\delta} + F^{\beta}_{\delta}(\omega_L)] + \frac{1}{3}[\delta_{\alpha\gamma} + F^{\alpha}_{\gamma}(\omega_S)]A_{\gamma\delta\epsilon}F^{\beta}_{\delta\epsilon}(\omega_L) \\
&+ \frac{1}{3}F^{\alpha}_{\gamma\delta}(\omega_S)\mathscr{A}_{\epsilon,\gamma\delta}[\delta_{\beta\epsilon} + F^{\beta}_{\epsilon}(\omega_L)] + \frac{1}{9}F^{\alpha}_{\gamma\delta}(\omega_S)C_{\gamma\delta,\epsilon\zeta}F^{\beta}_{\epsilon\zeta}(\omega_L) \\
&= \alpha''_{\alpha\beta}(\mathbf{O})
\end{aligned} \tag{D.14}$$

which is the origin-independent effective polarizability. This shows that an expansion of the local field accounting for the translation of our molecular system, as derived in Eq. D.5, is sufficient to maintain origin-invariance of the effective polarizability.

With this common-origin solution, the SERS spectra including the field-gradient contributions becomes independent of the choice of origin as shown in Figure D.3. This Figure examines the same systems as Figure D.1 with the correct expansion of the local fields. As is clearly shown, the SERS spectra of the benzene translated 10Å along the z-axis is identical to that of benzene

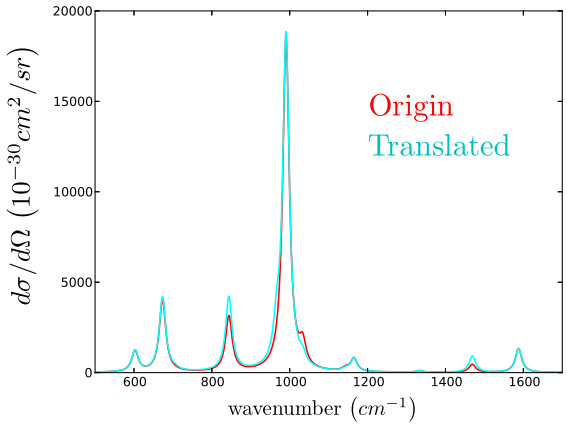


**Figure D.3.** The SERS spectrum for benzene translated 10Å along the z-axis (same as for Figure D.1) using the common-origin expression of the local fields.

centered at the origin.

# Appendix E
# Supporting Information for: Simulating Ensemble-Averaged Surface-Enhanced Raman Scattering

## E.1 Ag-Pyridine Force Field Details

The force field responsible for the Ag-pyr interactions were parameterized through the embedded-atom-method (EAM) potential modified by a Morse potential and DFT-D2[263–265]. In the EAM-like potential, the total electron density is written in terms of Ag-Ag electron density and Ag-N electron density.

$$\rho_\beta(r_{ij}) = \sum_{i\neq j}^{\mathrm{Ag}} \rho_{\mathrm{Ag-Ag}}(r_{ij}) + \sum_{i\neq j}^{\mathrm{N}} \rho_{\mathrm{N-Ag}}(r_{ij}). \tag{E.1}$$

It is assumed that $\rho_{\mathrm{N-Ag}}$ is proportional to $\rho_{\mathrm{Ag-Ag}}$. Accordingly, a scaling factor $f$ is applied to evaluate $\rho_{\mathrm{N-Ag}}$.

$$\sum_{i\neq j}^{\mathrm{N}} \rho_{\mathrm{N-Ag}}(r_{ij}) = f\rho_{\mathrm{Ag-Ag}}(r_{ij}). \tag{E.2}$$

The Morse potential is written as

$$\phi_{\mathrm{morse}}(r_{ij}) = D_{0,\mathrm{Ag-L}}\left[e^{-2\alpha_{\mathrm{Ag-L}}(r_{ij}-r_{0,\mathrm{Ag-L}})} - 2e^{-\alpha_{\mathrm{Ag-L}}(r_{ij}-r_{0,\mathrm{Ag-L}})}\right], \tag{E.3}$$

where $D_{0,\mathrm{Ag-L}}$, $\alpha_{\mathrm{Ag-L}}$ and $r_{0,\mathrm{Ag-L}}$ are the parameters describing the short-range interactions between Ag and pyridine molecules. The parameterization is carried out in the same way as reported in our previous work[267]. The parameters of morse potential and the scaling factor are collected in Table E.1.

**Table E.1.** Morse potential parameters and the scaling factor in electron-density function of EAM potential.

| | $D_{0,\mathrm{Ag-L}}$ (eV) | $\alpha_{\mathrm{Ag-L}}$ (Å$^{-1}$) | $r_0$(Å) | $f$ |
|---|---|---|---|---|
| Ag-C | 0.000497 | 1.099 | 5.286 | |
| Ag-N | 0.115876 | 1.954 | 2.607 | 2.443 |
| Ag-H | 0.000569 | 1.191 | 4.722 | |
| Ag-H[a] | 0.000324 | 1.261 | 4.646 | |

[a] H's nearest to N

The reference data used for the parametrization of the EAM-like potential were generated from the DFT calculations. The model system consists of pyridine and a $Ag_{56}$ cluster. Two configurations were considered: pyridine both perpendicular and parallel to the Ag(111) facet. The geometry optimizations were performed on the ADF program package[224], using the Becke-Perdew (BP86) XC-potential[153,154] and the triple-$\zeta$ with one polarization function (TZP) Slater type basis set from the ADF basis set library (keeping the 1s–3d core frozen for Ag). Scalar relativistic effects were taken into account by adopting the zeroth-order regular approximation (ZORA)[271–273] and dispersion effects were accounted for by the DFT-D3 approach[274].

The interaction energies as the function of the Ag-N distance obtained from DFT and the force field are compared in in Figure E.1. The binding energies predicted by force field well match with the DFT results, indicating the force field correctly describe the pyridine and Ag cluster interactions.

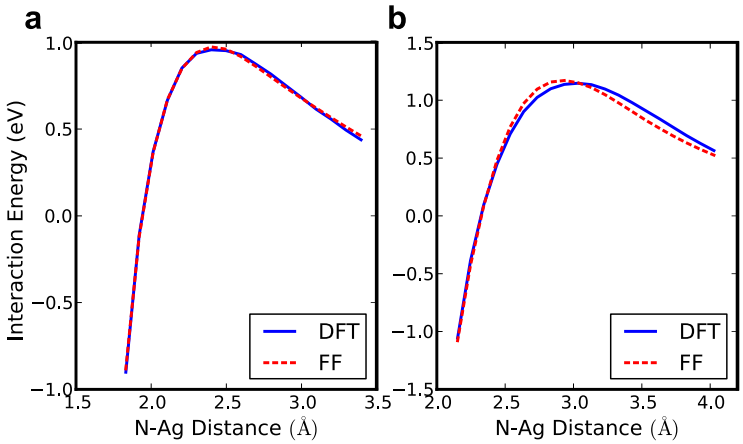


**Figure E.1.** The interaction energy as a function of the Ag–N distance as calculated by DFT (in blue) and the force field (in red) for pyr bound both *(a)* perpendicular and *(b)* parallel to the Ag(111) facet.

## E.2 Enhancement Distributions

| enhancement | sm. monomer | | lg. monomer | | dimer | |
|---|---|---|---|---|---|---|
| | % mol. | % sig. | % mol. | % sig. | % mol. | % sig. |
| $\leq 10^2$ | 67 | 7 | 57 | 1 | 52 | 0.1 |
| $10^2$–$10^3$ | 27 | 48 | 30 | 8 | 32 | 0.5 |
| $10^3$–$10^4$ | 6 | 44 | 11 | 25 | 11 | 2 |
| $10^4$–$10^5$ | | | 3 | 66 | 3 | 4 |
| $10^5$–$10^6$ | | | | | 0.7 | 7 |
| $10^6$–$10^7$ | | | | | 0.5 | 86 |

**Table E.2.** Signal contribution from the different nanoparticle systems

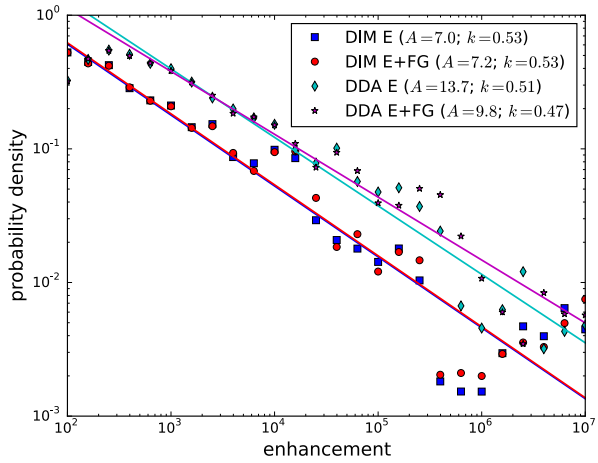


**Figure E.2.** TPD analysis for the DIM and DDA models with a homogeneous field (E) or both a field and gradient (E+FG).

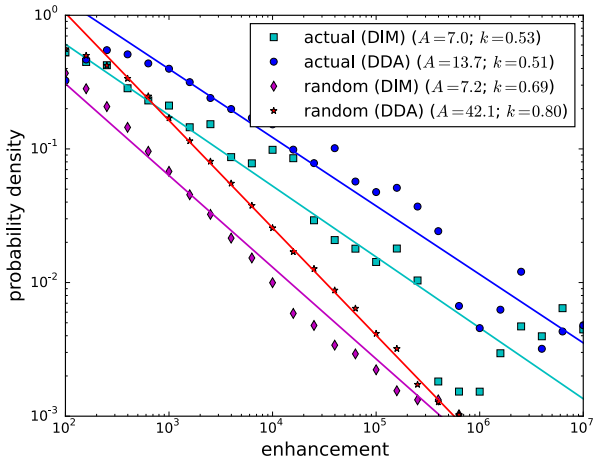


**Figure E.3.** TPD analysis for actual and random sampling using both the DIM and DDA models.

| enhancement | DIM | | DDA | | DIM - random | | DDA - random | |
|---|---|---|---|---|---|---|---|---|
| | % mol. | % sig. | % mol. | % sig. | % mol. | % sig. | % mol. | % sig. |
| $\leq 10^2$ | 52 | 0.1 | 20 | 0.03 | 81 | 2 | 59 | 2 |
| $10^2$–$10^3$ | 32 | 0.5 | 47 | 0.6 | 16 | 4 | 34 | 7 |
| $10^3$–$10^4$ | 11 | 2 | 22 | 2 | 2 | 6 | 6 | 12 |
| $10^4$–$10^5$ | 3 | 4 | 8 | 9 | 0.4 | 11 | 1 | 20 |
| $10^5$–$10^6$ | 0.7 | 7 | 2 | 19 | 0.1 | 35 | 0.2 | 29 |
| $10^6$–$10^7$ | 0.5 | 86 | 0.6 | 68 | 0.02 | 43 | 0.02 | 30 |
| $> 10^7$ | | | 0.002 | 0.7 | | | | |

**Table E.3.** Signal contribution from the different models

# Appendix F
# Supporting Information for: Simulating Surface-Enhanced Raman Optical Activity Using Atomistic Electrodynamics-Quantum Mechanical Models

## F.1 ROA of 2BrHH

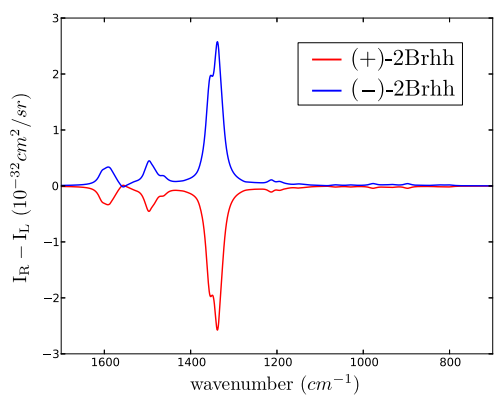


**Figure F.1.** ROA of the two enantiomers of 2Brhh calculated using the BP86-TZ2P level of theory.

## F.2 Origin-Dependence of *A*, *G'*, *C* and *D* Response Tensors

The dipole of a neutral molecule is independent of the choice of origin. However, higher order multipoles (and response tensors that depend on these multipole moment operators) all depend on the choice of origin. The translation rules for the electric dipole-quadrupole ($A$), electric dipole-magnetic dipole ($G'$), electric quadrupole-quadrupole ($C$), and electric quadrupole-magnetic dipole ($D$) response tensors are all stated below. In each case, we translate the coordinate origin $\mathbf{O}$ to some new origin $\mathbf{O}+\mathbf{R}$. This is equivalent to translating the position vector $\mathbf{r}$ to $\mathbf{r}-\mathbf{R}$.

$$A_{\alpha\beta\gamma}(\mathbf{O}+\mathbf{R}) = A_{\alpha\beta\gamma}(\mathbf{O}) - \frac{3}{2}R_\gamma\alpha_{\alpha\beta} - \frac{3}{2}R_\beta\alpha_{\alpha\gamma} + \delta_{\beta\gamma}R_\delta\alpha_{\alpha\delta} \tag{F.1}$$

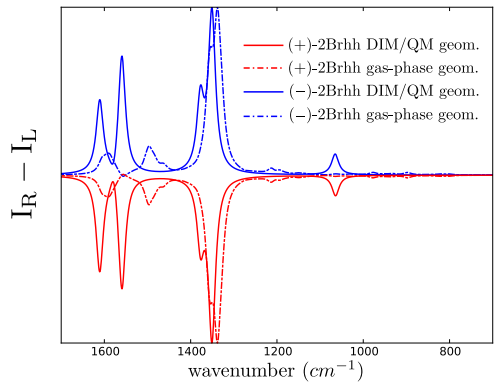


**Figure F.2.** ROA intensities of 2Brhh for the modes $\sim 1600$ and 1064 cm$^{-1}$ are increased relative to those $\sim 1350$ cm$^{-1}$ using the DIM/QM force field (the intensities in this spectrum are calculated in the absence of polarization and plasmon effects due to the nanoparticle) when compared to the gas-phase geometry.

$$G'_{\alpha\beta}(\mathbf{O}+\mathbf{R}) = G'_{\alpha\beta}(\mathbf{O}) + \frac{\omega}{2}\epsilon_{\beta\gamma\delta}R_\gamma\alpha_{\alpha\delta} \tag{F.2}$$

$$\begin{aligned} C_{\alpha\beta,\gamma\delta}(\mathbf{O}+\mathbf{R}) = {} & C_{\alpha\beta,\gamma\delta}(\mathbf{O}) - \frac{3}{2}R_\beta A_{\alpha\gamma\delta}(\mathbf{O}) - \frac{3}{2}R_\alpha A_{\beta\gamma\delta}(\mathbf{O}) \\ & + \delta_{\alpha\beta}R_\epsilon A_{\epsilon\gamma\delta}(\mathbf{O}) - \frac{3}{2}R_\delta \mathscr{A}_{\gamma,\alpha\beta}(\mathbf{O}) - \frac{3}{2}R_\gamma \mathscr{A}_{\delta,\alpha\beta}(\mathbf{O}) \\ & + \delta_{\gamma\delta}R_\zeta \mathscr{A}_{\zeta,\alpha\beta}(\mathbf{O}) + \frac{9}{4}R_\delta R_\beta \alpha_{\alpha\gamma} + \frac{9}{4}R_\delta R_\alpha \alpha_{\beta\gamma} \\ & - \frac{3}{2}\delta_{\alpha\beta}R_\delta R_\epsilon \alpha_{\epsilon\gamma} + \frac{9}{4}R_\gamma R_\beta \alpha_{\alpha\delta} + \frac{9}{4}R_\gamma R_\alpha \alpha_{\beta\delta} \\ & - \frac{3}{2}\delta_{\alpha\beta}R_\gamma R_\epsilon \alpha_{\epsilon\delta} - \frac{3}{2}\delta_{\gamma\delta}R_\zeta R_\beta \alpha_{\alpha\zeta} - \frac{3}{2}\delta_{\gamma\delta}R_\zeta R_\alpha \alpha_{\beta\zeta} \\ & + \delta_{\alpha\beta}\delta_{\gamma\delta}R_\epsilon R_\zeta \alpha_{\epsilon\zeta} \end{aligned} \tag{F.3}$$

$$\begin{aligned} D_{\alpha\beta,\gamma}(\mathbf{O}+\mathbf{R}) = {} & D_{\alpha\beta,\gamma}(\mathbf{O}) + \frac{\omega}{2}\epsilon_{\gamma\epsilon\delta}R_\epsilon \mathscr{A}_{\delta,\alpha\beta}(\mathbf{O}) \\ & - \frac{3}{2}R_\beta G'_{\alpha\gamma}(\mathbf{O}) - \frac{3}{2}R_\alpha G'_{\beta\gamma}(\mathbf{O}) + \delta_{\alpha\beta}R_\delta G'_{\delta\gamma}(\mathbf{O}) \\ & - \frac{3\omega}{4}\epsilon_{\gamma\epsilon\delta}R_\beta R_\epsilon \alpha_{\alpha\delta} - \frac{3\omega}{4}\epsilon_{\gamma\epsilon\delta}R_\alpha R_\epsilon \alpha_{\beta\delta} + \frac{\omega}{2}\delta_{\alpha\beta}\epsilon_{\gamma\epsilon\zeta}R_\delta R_\epsilon \alpha_{\delta\zeta} \end{aligned} \tag{F.4}$$

In the above equations, we assume that the electric dipole-dipole tensor ($\alpha$) is independent of the choice of origin and the Einstein summation convention is employed for repeated indices. Also, $\delta$ is the Kronecker dela, $\epsilon$ is the Levi-Civita tensor, $\omega$ is the angular frequency, and $\mathscr{A}$ is the electric quadrupole-dipole polarizability tensor.

## F.3 Damping in the Modified Velocity Gauge

### F.3.1 The modified velocity gauge

We start by considering the relationship $\langle n|[\hat{A},\hat{H}]|0\rangle$, where $n$ and 0 are eigenstates of $\hat{H}$, and $\hat{A}$ is some general operator. Because $\hat{H}$ is Hermitian, it can be shown that

$$\begin{aligned}\langle n|[\hat{A},\hat{H}]|0\rangle &= \langle n|\hat{A}\hat{H}|0\rangle - \langle n|\hat{H}\hat{A}|0\rangle \\ &= \epsilon_0\langle n|\hat{A}|0\rangle - \left(\hat{H}|n\rangle\right)^\dagger \hat{A}|0\rangle \\ &= \epsilon_0\langle n|\hat{A}|0\rangle - \epsilon_n\langle n|\hat{A}|0\rangle \\ &= -\omega_{n0}\langle n|\hat{A}|0\rangle\end{aligned} \tag{F.5}$$

where $\omega_{n0} = \epsilon_n - \epsilon_0$.

We can now use this relationship to transform between the length gauge (LG) and velocity gauge (VG) operators. Consider the LG dipole operator $\hat{r}$. Expressed in the VG, this becomes

$$\begin{aligned}\langle n|\hat{r}|0\rangle &= -\langle n|[\hat{r},\hat{H}]|0\rangle/\omega_{n0} \\ &= -\frac{i}{\omega_{n0}}\langle n|\hat{p}|0\rangle\end{aligned} \tag{F.6}$$

where $i\hat{p}$, the momentum operator, is the equivalent VG operator for the LG dipole.

We can now consider the polarizability response $\alpha_{\alpha\beta}(\omega)$ in the VG.[323,324]

$$\begin{aligned}\alpha_{\alpha\beta}(\omega) &= \langle\langle\hat{\mu}_\alpha;\hat{\mu}_\beta\rangle\rangle_\omega \\ &= \langle\langle\hat{r}_\alpha;\hat{r}_\beta\rangle\rangle_\omega \\ &= \sum_n\left[\frac{\langle 0|\hat{r}_\alpha|n\rangle\langle n|\hat{r}_\beta|0\rangle}{\omega_{n0}-\omega} + \frac{\langle 0|\hat{r}_\alpha|n\rangle\langle n|\hat{r}_\beta|0\rangle}{\omega_{n0}+\omega}\right] \\ &= 2\sum_n\frac{\omega_{n0}\langle 0|\hat{r}_\alpha|n\rangle\langle n|\hat{r}_\beta|0\rangle}{\omega_{n0}^2-\omega^2} \\ &= 2\sum_n\frac{\omega_{n0}\left(\frac{i}{\omega_{n0}}\langle 0|\hat{p}_\alpha|n\rangle\right)\left(\frac{-i}{\omega_{n0}}\langle n|\hat{p}_\beta|0\rangle\right)}{\omega_{n0}^2-\omega^2} \\ &= 2\sum_n\frac{\langle 0|\hat{p}_\alpha|n\rangle\langle n|\hat{p}_\beta|0\rangle}{\omega_{n0}(\omega_{n0}^2-\omega^2)}\end{aligned} \tag{F.7}$$

Using the dentity

$$\frac{1}{x(x^2-y^2)} = \frac{x}{y^2}\left(\frac{1}{x^2-y^2} - \frac{1}{x^2}\right) \tag{F.8}$$

we can re-write Eqn. F.7 as

$$
\begin{aligned}
\langle\langle \hat{\mu}_\alpha ; \hat{\mu}_\beta \rangle\rangle_\omega &= 2 \sum_n \frac{\langle 0|\hat{p}_\alpha|n\rangle\langle n|\hat{p}_\beta|0\rangle}{\omega_{n0}(\omega_{n0}^2 - \omega^2)} \\
&= \frac{2}{\omega^2} \sum_n \left[ \frac{\omega_{n0}\langle 0|\hat{p}_\alpha|n\rangle\langle n|\hat{p}_\beta|0\rangle}{\omega_{n0}^2 - \omega^2} - \frac{\omega_{n0}\langle 0|\hat{p}_\alpha|n\rangle\langle n|\hat{p}_\beta|0\rangle}{\omega_{n0}^2} \right] \\
&= \frac{1}{\omega^2} \left[ \langle\langle \hat{p}_\alpha ; \hat{p}_\beta \rangle\rangle_\omega - \langle\langle \hat{p}_\alpha ; \hat{p}_\beta \rangle\rangle_0 \right]
\end{aligned} \tag{F.9}
$$

Eqn. F.9 is commonly referred to as the modified velocity gauge (MVG), where the "static limit" is subtracted from the frequency-dependent response.[324,325]

We may also consider higher order response functions in the MVG by considering the following operator relations.[324]

$$
\begin{aligned}
\langle 0|\hat{r}|n\rangle &= \langle 0|[\hat{r}, \hat{H}]|n\rangle/\omega_{n0} \\
&= \langle 0|i\hat{p}|n\rangle/\omega_{n0}
\end{aligned} \tag{F.10}
$$

$$
\begin{aligned}
\langle 0|\hat{r}\hat{r}|n\rangle &= \langle 0|[\hat{r}\hat{r}, \hat{H}]|n\rangle/\omega_{n0} \\
&= \langle 0|i\hat{p}\hat{r} + i\hat{r}\hat{p}|n\rangle/\omega_{n0}
\end{aligned} \tag{F.11}
$$

$$
\begin{aligned}
\langle 0|\hat{r}\hat{r}\hat{r}|n\rangle &= \langle 0|[\hat{r}\hat{r}\hat{r}, \hat{H}]|n\rangle/\omega_{n0} \\
&= \langle 0|i\hat{p}\hat{r}\hat{r} + i\hat{r}\hat{p}\hat{r} + i\hat{r}\hat{r}\hat{p}|n\rangle/\omega_{n0}
\end{aligned} \tag{F.12}
$$

The magnetic dipole operator ($\hat{m}$) and magnetic quadrupole operator are identical in both gauges.[324]

### F.3.2 Finite lifetime effects in MVG

Earlier, we considered the response function (written below for two general operators $\hat{A}$ and $\hat{B}$) as

$$
\langle\langle \hat{A} ; \hat{B} \rangle\rangle_\omega = \sum_n \left[ \frac{\langle 0|\hat{A}|n\rangle\langle n|\hat{B}|0\rangle}{\omega_{n0} - \omega} + \frac{\langle 0|\hat{A}|n\rangle\langle n|\hat{B}|0\rangle}{\omega_{n0} + \omega} \right] \tag{F.13}
$$

This equation has no solution on resonance ($\omega = \omega_{n0}$), and leads to poles in the response function. We may overcome this by considering a finite lifetime ($1/\gamma_n$) of the excited state, which leads to

$$
\langle\langle \hat{A} ; \hat{B} \rangle\rangle_{\omega + i\gamma_n} = \sum_n \left[ \frac{\langle 0|\hat{A}|n\rangle\langle n|\hat{B}|0\rangle}{\omega_{n0} - \omega - i\gamma_n} + \frac{\langle 0|\hat{A}|n\rangle\langle n|\hat{B}|0\rangle}{\omega_{n0} + \omega + i\gamma_n} \right] \tag{F.14}
$$

A lifetime parameter for each excited state is unfeasible, and typically a single lifetime ($1/\Gamma$) is used. We can re-write this as a single term, similar to that in Eqn. F.7 as

$$
\begin{aligned}
\langle\langle \hat{A} ; \hat{B} \rangle\rangle_{\omega + i\Gamma} &= \sum_n \left[ \frac{\langle 0|\hat{A}|n\rangle\langle n|\hat{B}|0\rangle}{\omega_{n0} - \omega - i\Gamma} + \frac{\langle 0|\hat{A}|n\rangle\langle n|\hat{B}|0\rangle}{\omega_{n0} + \omega + i\Gamma} \right] \\
&= 2 \sum_n \frac{\omega_{n0}\langle 0|\hat{A}|n\rangle\langle n|\hat{B}|0\rangle}{\omega_{n0}^2 - (\omega + i\Gamma)^2}
\end{aligned} \tag{F.15}
$$

Using the gauge transformations ($\hat{A} \to \hat{A}^{VG}$ and $\hat{B} \to \hat{B}^{VG}$) and the identiy in Eqn. F.8, we can obtain the MVG form of the response as was done in Eqn. F.9

$$\begin{aligned}\langle\langle \hat{A}; \hat{B} \rangle\rangle_{\omega+i\Gamma} &= \frac{2}{(\omega+i\Gamma)^2} \sum_n \left[ \frac{\omega_{n0} \langle 0|\hat{A}^{VG}|n\rangle\langle n|\hat{B}^{VG}|0\rangle}{\omega_{n0} - (\omega+i\Gamma)^2} - \frac{\langle 0|\hat{A}^{VG}|n\rangle\langle n|\hat{B}^{VG}|0\rangle}{\omega_{n0}} \right] \\ &= \frac{1}{(\omega+i\Gamma)^2} \left[ \langle\langle \hat{A}^{VG}; \hat{B}^{VG} \rangle\rangle_{\omega+i\Gamma} - \langle\langle \hat{A}^{VG}; \hat{B}^{VG} \rangle\rangle_0 \right]\end{aligned} \tag{F.16}$$

# Appendix G
# Supporting Information for: Frozen Density Embedding with External Orthogonality

## G.1 System Geometries

**Table G.1.** Water dimer geometry (in Å).

| subsystem $I$ | | | | subsystem $II$ | | | |
|---|---|---|---|---|---|---|---|
| atom | $x$ | $y$ | $z$ | atom | $x$ | $y$ | $z$ |
| O | -1.4626 | 0.0000 | 0.0000 | O | 1.4626 | 0.0000 | 0.0000 |
| H | -1.7312 | 0.9302 | 0.0000 | H | 1.9309 | 0.3579 | 0.7697 |
| H | -0.4844 | 0.0275 | 0.0000 | H | 1.9309 | 0.3579 | -0.7697 |

**Table G.2.** $FHF^-$ geometry (in Å).

| FH subsystem | | | | $F^-$ subsystem | | | |
|---|---|---|---|---|---|---|---|
| atom | $x$ | $y$ | $z$ | atom | $x$ | $y$ | $z$ |
| F | 0.0000 | 0.0000 | 1.1587 | F | 0.0000 | 0.0000 | -1.1587 |
| H | 0.0000 | 0.0000 | 0.0000 | | | | |

**Table G.3.** $BH_3NH_3$ geometry (in Å).

| $BH_3$ subsystem | | | | $NH_3$ subsystem | | | |
|---|---|---|---|---|---|---|---|
| atom | $x$ | $y$ | $z$ | atom | $x$ | $y$ | $z$ |
| B | 0.0000 | 0.0000 | 0.8382 | N | 0.0000 | 0.0000 | -0.8158 |
| H | -0.5864 | -1.0157 | 1.1548 | H | 0.4765 | -0.8252 | -1.1862 |
| H | -0.5864 | 1.0157 | 1.1548 | H | 0.4765 | 0.8252 | -1.1862 |
| H | 1.1728 | 0.0000 | 1.1548 | H | -0.9529 | 0.0000 | -1.1862 |

**Table G.4.** $C_2H_6$ geometry (in Å).

| $CH_3^+$ subsystem | | | | $CH_3^-$ subsystem | | | |
|---|---|---|---|---|---|---|---|
| atom | $x$ | $y$ | $z$ | atom | $x$ | $y$ | $z$ |
| C | 0.0000 | 0.0000 | 0.7651 | C | 0.0000 | 0.0000 | -0.7651 |
| H | 0.0000 | -1.0222 | 1.1666 | H | 0.8853 | -0.5111 | -1.1666 |
| H | -0.8853 | 0.5111 | 1.1666 | H | 0.0000 | 1.0222 | -1.1666 |
| H | 0.8853 | 0.5111 | 1.1666 | H | -0.8853 | -0.5111 | -1.1666 |

**Table G.5.** $C_6H_{12}$ geometry (in Å).

| subsystem $I$ | | | | subsystem $II$ | | | |
|---|---|---|---|---|---|---|---|
| atom | $x$ | $y$ | $z$ | atom | $x$ | $y$ | $z$ |
| C | -3.1595 | -0.3535 | 0.0351 | C | 0.6165 | 0.2594 | -0.0400 |
| H | -3.1754 | -1.1510 | -0.7229 | H | 0.7222 | 1.3357 | -0.2323 |
| H | -4.0780 | 0.2386 | -0.0819 | C | 1.9083 | -0.5197 | 0.1097 |
| H | -3.1945 | -0.8346 | 1.0241 | H | 1.9381 | -1.3285 | -0.6388 |
| C | -1.9086 | 0.5199 | -0.1096 | H | 1.9250 | -1.0195 | 1.0921 |
| H | -1.9408 | 1.3297 | 0.6377 | C | 3.1600 | 0.3521 | -0.0367 |
| H | -1.9241 | 1.0183 | -1.0928 | H | 4.0779 | -0.2418 | 0.0744 |
| C | -0.6166 | -0.2579 | 0.0421 | H | 3.1807 | 1.1466 | 0.7245 |
| H | -0.7219 | -1.3344 | 0.2335 | H | 3.1915 | 0.8372 | -1.0239 |

**Table G.6.** $C_8H_{16}$ geometry (in Å).

| subsystem $I$ | | | | subsystem $II$ | | | |
|---|---|---|---|---|---|---|---|
| atom | $x$ | $y$ | $z$ | atom | $x$ | $y$ | $z$ |
| C | -0.5764 | -0.0196 | -4.2325 | C | 0.6473 | -0.3793 | 0.5416 |
| H | -1.4640 | 0.3376 | -4.7742 | H | 0.6756 | -1.4674 | 0.3942 |
| H | -0.5526 | -1.1169 | -4.3182 | C | 0.6194 | 0.0918 | 1.9688 |
| H | 0.3123 | 0.3729 | -4.7505 | H | 0.6127 | 1.1936 | 1.9948 |
| C | -0.6019 | 0.4206 | -2.7654 | H | 1.5461 | -0.2279 | 2.4798 |
| H | -1.5144 | 0.0423 | -2.2761 | C | -0.5819 | -0.4528 | 2.7648 |
| H | -0.6578 | 1.5208 | -2.7097 | H | -0.5780 | -1.5546 | 2.7114 |
| C | 0.6257 | -0.0595 | -1.9677 | H | -1.5127 | -0.1257 | 2.2730 |
| H | 1.5348 | 0.3101 | -2.4767 | C | -0.5836 | -0.0086 | 4.2309 |
| H | 0.6783 | -1.1600 | -1.9944 | H | -1.4521 | -0.4117 | 4.7713 |
| C | 0.6257 | 0.4116 | -0.5402 | H | -0.6190 | 1.0886 | 4.3135 |
| H | 0.5927 | 1.4996 | -0.3924 | H | 0.3236 | -0.3513 | 4.7521 |

**Table G.7.** $C_{10}H_{20}$ geometry (in Å).

| subsystem $I$ | | | | subsystem $II$ | | | |
|---|---|---|---|---|---|---|---|
| atom | $x$ | $y$ | $z$ | atom | $x$ | $y$ | $z$ |
| C | 0.0855 | 0.7963 | -5.0878 | C | 0.6551 | -0.3168 | 0.5133 |
| H | 1.1425 | 0.6724 | -4.8099 | H | 0.8182 | -1.3865 | 0.3246 |
| H | -0.1514 | 1.8703 | -5.0274 | C | 0.5973 | 0.0963 | 1.9579 |
| H | -0.0142 | 0.4921 | -6.1401 | H | 1.5590 | -0.1463 | 2.4425 |
| C | -0.8452 | -0.0226 | -4.1845 | H | 0.4764 | 1.1898 | 2.0253 |
| H | -1.8796 | 0.0812 | -4.5506 | C | -0.5445 | -0.5967 | 2.7292 |
| H | -0.5976 | -1.0945 | -4.2743 | H | -0.4254 | -1.6914 | 2.6431 |
| C | -0.8134 | 0.3794 | -2.7005 | H | -1.4963 | -0.3522 | 2.2300 |
| H | -1.6203 | -0.1476 | -2.1655 | C | -0.6397 | -0.2132 | 4.2150 |
| H | -1.0386 | 1.4570 | -2.6108 | H | -1.5758 | -0.6287 | 4.6225 |
| C | 0.5180 | 0.0813 | -1.9814 | H | -0.7327 | 0.8834 | 4.3007 |
| H | 1.3356 | 0.6078 | -2.5036 | C | 0.5342 | -0.6972 | 5.0755 |
| H | 0.7407 | -0.9960 | -2.0508 | H | 1.4888 | -0.2535 | 4.7565 |
| C | 0.5039 | 0.5014 | -0.5377 | H | 0.6399 | -1.7920 | 5.0177 |
| H | 0.3363 | 1.5704 | -0.3490 | H | 0.3870 | -0.4324 | 6.1328 |

**Table G.8.** $C_{12}H_{24}$ geometry (in Å).

| subsystem $I$ | | | | subsystem $II$ | | | |
|---|---|---|---|---|---|---|---|
| atom | $x$ | $y$ | $z$ | atom | $x$ | $y$ | $z$ |
| C | -0.0185 | 1.9689 | -5.3535 | C | 0.5329 | -0.3242 | 0.5389 |
| H | 0.7078 | 2.3769 | -6.0718 | H | 0.6786 | -1.4049 | 0.4054 |
| H | 0.0983 | 2.5311 | -4.4149 | C | 0.4734 | 0.1618 | 1.9608 |
| H | -1.0273 | 2.1795 | -5.7429 | H | 1.4386 | -0.0496 | 2.4538 |
| C | 0.1907 | 0.4628 | -5.1500 | H | 0.3485 | 1.2569 | 1.9725 |
| H | 0.1421 | -0.0403 | -6.1298 | C | -0.6596 | -0.4973 | 2.7728 |
| H | 1.2107 | 0.2810 | -4.7724 | H | -0.5347 | -1.5930 | 2.7429 |
| C | -0.8384 | -0.2018 | -4.2170 | H | -1.6162 | -0.2904 | 2.2656 |
| H | -0.6756 | -1.2933 | -4.2288 | C | -0.7606 | -0.0187 | 4.2321 |
| H | -1.8466 | -0.0407 | -4.6364 | H | -1.6753 | -0.4474 | 4.6771 |
| C | -0.8374 | 0.2806 | -2.7555 | H | -0.9053 | 1.0754 | 4.2356 |
| H | -1.6875 | -0.1833 | -2.2290 | C | 0.4333 | -0.3632 | 5.1415 |
| H | -1.0182 | 1.3683 | -2.7174 | H | 0.2707 | 0.1181 | 6.1200 |
| C | 0.4524 | -0.0438 | -1.9753 | H | 1.3544 | 0.0884 | 4.7370 |
| H | 1.3109 | 0.4211 | -2.4912 | C | 0.6527 | -1.8662 | 5.3570 |
| H | 0.6297 | -1.1316 | -1.9890 | H | 1.4814 | -2.0495 | 6.0565 |
| C | 0.4131 | 0.4437 | -0.5533 | H | 0.8961 | -2.3854 | 4.4179 |
| H | 0.2638 | 1.5238 | -0.4192 | H | -0.2486 | -2.3421 | 5.7752 |

**Table G.9.** $C_{14}H_{28}$ geometry (in Å).

| subsystem $I$ | | | | subsystem $II$ | | | |
|---|---|---|---|---|---|---|---|
| atom | $x$ | $y$ | $z$ | atom | $x$ | $y$ | $z$ |
| C | 0.6824 | 2.2735 | -6.4294 | C | 0.5178 | -0.3216 | 0.5731 |
| H | 1.7278 | 2.2052 | -6.0905 | H | 0.6394 | -1.4122 | 0.5234 |
| H | 0.4567 | 3.3362 | -6.5997 | C | 0.5068 | 0.2784 | 1.9520 |
| H | 0.6152 | 1.7576 | -7.3998 | H | 1.4752 | 0.0726 | 2.4408 |
| C | -0.2723 | 1.6525 | -5.4035 | H | 0.4193 | 1.3748 | 1.8779 |
| H | -0.2055 | 2.2196 | -4.4603 | C | -0.6291 | -0.2715 | 2.8375 |
| H | -1.3137 | 1.7638 | -5.7535 | H | -0.5512 | -1.3712 | 2.8820 |
| C | 0.0115 | 0.1666 | -5.1401 | H | -1.5903 | -0.0587 | 2.3413 |
| H | -0.0306 | -0.3753 | -6.1009 | C | -0.6676 | 0.3107 | 4.2617 |
| H | 1.0495 | 0.0540 | -4.7814 | H | -1.5858 | -0.0430 | 4.7586 |
| C | -0.9609 | -0.5106 | -4.1576 | H | -0.7703 | 1.4075 | 4.1934 |
| H | -0.7491 | -1.5934 | -4.1374 | C | 0.5484 | -0.0078 | 5.1537 |
| H | -1.9860 | -0.4102 | -4.5531 | H | 0.4107 | 0.5069 | 6.1207 |
| C | -0.9412 | 0.0234 | -2.7138 | H | 1.4550 | 0.4339 | 4.7081 |
| H | -1.7663 | -0.4416 | -2.1500 | C | 0.8087 | -1.5012 | 5.4252 |
| H | -1.1495 | 1.1065 | -2.7116 | H | 1.7426 | -1.5883 | 6.0048 |
| C | 0.3743 | -0.2385 | -1.9532 | H | 0.9986 | -2.0260 | 4.4738 |
| H | 1.2136 | 0.1865 | -2.5312 | C | -0.3173 | -2.2150 | 6.1845 |
| H | 0.5550 | -1.3239 | -1.8895 | H | -0.0503 | -3.2603 | 6.3992 |
| C | 0.3817 | 0.3591 | -0.5734 | H | -1.2560 | -2.2279 | 5.6108 |
| H | 0.2548 | 1.4490 | -0.5220 | H | -0.5229 | -1.7191 | 7.1466 |

**Table G.10.** $C_6H_8$ geometry (in Å).

| subsystem $I$ | | | | subsystem $II$ | | | |
|---|---|---|---|---|---|---|---|
| atom | $x$ | $y$ | $z$ | atom | $x$ | $y$ | $z$ |
| C | -3.0670 | -0.3214 | -0.0670 | C | 0.5943 | 0.3283 | 0.0291 |
| H | -4.0109 | 0.2224 | -0.0697 | H | 0.5913 | 1.4238 | 0.0304 |
| H | -3.1172 | -1.4114 | -0.1095 | C | 1.8844 | -0.3239 | 0.0331 |
| C | -1.8842 | 0.3233 | -0.0025 | H | 1.8786 | -1.4183 | 0.0662 |
| H | -1.8776 | 1.4175 | 0.0391 | C | 3.0673 | 0.3233 | -0.0025 |
| C | -0.5947 | -0.3299 | 0.0151 | H | 3.1159 | 1.4135 | -0.0379 |
| H | -0.5919 | -1.4255 | 0.0088 | H | 4.0122 | -0.2187 | 0.0088 |

**Table G.11.** $C_8H_{12}$ geometry (in Å).

| subsystem $I$ | | | | subsystem $II$ | | | |
|---|---|---|---|---|---|---|---|
| atom | $x$ | $y$ | $z$ | atom | $x$ | $y$ | $z$ |
| C | -4.4159 | 0.3378 | 0.0131 | C | 0.5969 | 0.3298 | -0.0130 |
| H | -4.3294 | 1.4325 | 0.0247 | H | 0.5956 | 1.4252 | -0.0124 |
| H | -4.9997 | 0.0306 | 0.8963 | C | 1.8847 | -0.3224 | -0.0036 |
| H | -5.0147 | 0.0496 | -0.8665 | H | 1.8804 | -1.4188 | -0.0018 |
| C | -3.0719 | -0.3224 | -0.0036 | C | 3.0739 | 0.3214 | 0.0049 |
| H | -3.0636 | -1.4184 | -0.0046 | H | 3.0711 | 1.4174 | 0.0004 |
| C | -1.8855 | 0.3265 | -0.0106 | C | 4.4144 | -0.3461 | 0.0209 |
| H | -1.8851 | 1.4230 | -0.0095 | H | 5.0130 | -0.0636 | -0.8607 |
| C | -0.5963 | -0.3228 | -0.0157 | H | 4.3219 | -1.4402 | 0.0358 |
| H | -0.5939 | -1.4182 | -0.0137 | H | 5.0016 | -0.0403 | 0.9023 |

**Table G.12.** $C_{10}H_{12}$ geometry (in Å).

| subsystem $I$ | | | | subsystem $II$ | | | |
|---|---|---|---|---|---|---|---|
| atom | $x$ | $y$ | $z$ | atom | $x$ | $y$ | $z$ |
| C | -5.5488 | -0.2968 | 0.0080 | C | 0.6003 | 0.3120 | -0.0192 |
| H | -6.4845 | 0.2609 | 0.0127 | H | 0.5937 | 1.4070 | -0.0160 |
| H | -5.6162 | -1.3867 | 0.0227 | C | 1.8776 | -0.3314 | -0.0154 |
| C | -4.3525 | 0.3311 | -0.0094 | H | 1.8868 | -1.4266 | -0.0116 |
| H | -4.3293 | 1.4260 | -0.0203 | C | 3.0716 | 0.3311 | -0.0094 |
| C | -3.0762 | -0.3389 | -0.0147 | H | 3.0632 | 1.4265 | -0.0123 |
| H | -3.0869 | -1.4340 | -0.0223 | C | 4.3597 | -0.3139 | 0.0196 |
| C | -1.8731 | 0.3068 | -0.0099 | H | 4.3592 | -1.4090 | 0.0154 |
| H | -1.8708 | 1.4021 | 0.0058 | C | 5.5419 | 0.3397 | 0.0609 |
| C | -0.5998 | -0.3448 | -0.0195 | H | 5.5851 | 1.4308 | 0.0706 |
| H | -0.5965 | -1.4394 | -0.0270 | H | 6.4892 | -0.1975 | 0.0876 |

**Table G.13.** $C_{12}H_{16}$ geometry (in Å).

| subsystem $I$ | | | | subsystem $II$ | | | |
|---|---|---|---|---|---|---|---|
| atom | $x$ | $y$ | $z$ | atom | $x$ | $y$ | $z$ |
| C | -6.8885 | 0.3419 | -0.0728 | C | 0.6022 | 0.3258 | 0.0897 |
| H | -6.7995 | 1.4363 | -0.0737 | H | 0.5997 | 1.4208 | 0.0908 |
| H | -7.5116 | 0.0473 | 0.7876 | C | 1.8769 | -0.3224 | 0.0686 |
| H | -7.4495 | 0.0431 | -0.9736 | H | 1.8794 | -1.4177 | 0.0714 |
| C | -5.5482 | -0.3224 | -0.0249 | C | 3.0765 | 0.3298 | 0.0271 |
| H | -5.5434 | -1.4184 | -0.0241 | H | 3.0752 | 1.4249 | 0.0216 |
| C | -4.3582 | 0.3232 | 0.0145 | C | 4.3585 | -0.3224 | -0.0249 |
| H | -4.3546 | 1.4197 | 0.0148 | H | 4.3552 | -1.4188 | -0.0166 |
| C | -3.0757 | -0.3291 | 0.0515 | C | 5.5475 | 0.3229 | -0.0922 |
| H | -3.0747 | -1.4242 | 0.0484 | H | 5.5427 | 1.4188 | -0.1023 |
| C | -1.8755 | 0.3225 | 0.0785 | C | 6.8860 | -0.3431 | -0.1607 |
| H | -1.8771 | 1.4178 | 0.0798 | H | 7.4280 | -0.0548 | -1.0765 |
| C | -0.6010 | -0.3263 | 0.0903 | H | 6.7961 | -1.4373 | -0.1479 |
| H | -0.5991 | -1.4213 | 0.0871 | H | 7.5274 | -0.0395 | 0.6831 |

**Table G.14.** $C_{14}H_{16}$ geometry (in Å).

| subsystem $I$ | | | | subsystem $II$ | | | |
|---|---|---|---|---|---|---|---|
| atom | $x$ | $y$ | $z$ | atom | $x$ | $y$ | $z$ |
| C | -8.0253 | -0.2506 | 0.0699 | C | 0.6022 | 0.2962 | -0.1200 |
| H | -8.1149 | -1.3381 | 0.0308 | H | 0.5907 | 1.3911 | -0.1146 |
| H | -8.9487 | 0.3255 | 0.1139 | C | 1.8755 | -0.3407 | -0.0986 |
| C | -6.8164 | 0.3542 | 0.0654 | H | 1.8897 | -1.4359 | -0.0947 |
| H | -6.7729 | 1.4477 | 0.1064 | C | 3.0732 | 0.3271 | -0.0592 |
| C | -5.5529 | -0.3348 | 0.0076 | H | 3.0583 | 1.4218 | -0.0605 |
| H | -5.5795 | -1.4291 | -0.0212 | C | 4.3496 | -0.3085 | 0.0046 |
| C | -4.3402 | 0.2958 | -0.0161 | H | 4.3615 | -1.4036 | 0.0148 |
| H | -4.3249 | 1.3907 | 0.0093 | C | 5.5439 | 0.3542 | 0.0654 |
| C | -3.0774 | -0.3675 | -0.0706 | H | 5.5395 | 1.4493 | 0.0547 |
| H | -3.0834 | -1.4621 | -0.0853 | C | 6.8256 | -0.2976 | 0.1464 |
| C | -1.8693 | 0.2818 | -0.0961 | H | 6.8159 | -1.3924 | 0.1682 |
| H | -1.8707 | 1.3767 | -0.0834 | C | 8.0135 | 0.3456 | 0.1949 |
| C | -0.6011 | -0.3651 | -0.1221 | H | 8.0685 | 1.4359 | 0.1754 |
| H | -0.5940 | -1.4597 | -0.1265 | H | 8.9542 | -0.2006 | 0.2523 |

**Table G.15.** $C_{16}H_{20}$ geometry (in Å).

| subsystem $I$ | | | | subsystem $II$ | | | |
|---|---|---|---|---|---|---|---|
| atom | $x$ | $y$ | $z$ | atom | $x$ | $y$ | $z$ |
| C | -9.2739 | -0.3141 | 0.5769 | C | 0.6156 | -0.3666 | -0.5073 |
| H | -9.6805 | -0.0164 | 1.5577 | H | 0.6172 | -1.4616 | -0.4963 |
| H | -9.1981 | -1.4092 | 0.5584 | C | 1.8778 | 0.2893 | -0.4390 |
| H | -10.0232 | -0.0062 | -0.1707 | H | 1.8726 | 1.3844 | -0.4526 |
| C | -7.9513 | 0.3380 | 0.3230 | C | 3.0836 | -0.3516 | -0.3041 |
| H | -7.9327 | 1.4336 | 0.3380 | H | 3.0905 | -1.4463 | -0.2790 |
| C | -6.7888 | -0.3194 | 0.0923 | C | 4.3356 | 0.3134 | -0.1383 |
| H | -6.7986 | -1.4155 | 0.0777 | H | 4.3254 | 1.4084 | -0.1649 |
| C | -5.5170 | 0.3208 | -0.1095 | C | 5.5261 | -0.3194 | 0.0923 |
| H | -5.5033 | 1.4158 | -0.0938 | H | 5.5380 | -1.4139 | 0.1247 |
| C | -4.3332 | -0.3422 | -0.2836 | C | 6.7726 | 0.3561 | 0.3342 |
| H | -4.3460 | -1.4373 | -0.2962 | H | 6.7551 | 1.4519 | 0.3010 |
| C | -3.0630 | 0.2963 | -0.4097 | C | 7.9421 | -0.2664 | 0.6191 |
| H | -3.0515 | 1.3912 | -0.3970 | H | 7.9520 | -1.3618 | 0.6511 |
| C | -1.8626 | -0.3629 | -0.4958 | C | 9.2368 | 0.4255 | 0.9096 |
| H | -1.8689 | -1.4581 | -0.4976 | H | 9.6140 | 0.1569 | 1.9103 |
| C | -0.5941 | 0.2833 | -0.5294 | H | 9.1327 | 1.5177 | 0.8674 |
| H | -0.5922 | 1.3785 | -0.5293 | H | 10.0216 | 0.1246 | 0.1963 |

**Table G.16.** $C_{18}H_{20}$ geometry (in Å).

| subsystem $I$ | | | | subsystem $II$ | | | |
|---|---|---|---|---|---|---|---|
| atom | $x$ | $y$ | $z$ | atom | $x$ | $y$ | $z$ |
| C | -10.4842 | 0.2977 | -0.2389 | C | 0.6032 | -0.3477 | 0.2105 |
| H | -11.4160 | -0.2626 | -0.3026 | H | 0.5890 | -1.4422 | 0.2122 |
| H | -10.5549 | 1.3873 | -0.2340 | C | 1.8718 | 0.2885 | 0.1794 |
| C | -9.2872 | -0.3277 | -0.1683 | H | 1.8836 | 1.3838 | 0.1770 |
| H | -9.2614 | -1.4226 | -0.1738 | C | 3.0765 | -0.3738 | 0.1330 |
| C | -8.0167 | 0.3437 | -0.0835 | H | 3.0690 | -1.4685 | 0.1325 |
| H | -8.0288 | 1.4389 | -0.0807 | C | 4.3406 | 0.2730 | 0.0721 |
| C | -6.8124 | -0.3001 | -0.0061 | H | 4.3407 | 1.3683 | 0.0738 |
| H | -6.8081 | -1.3954 | -0.0057 | C | 5.5498 | -0.3737 | -0.0013 |
| C | -5.5472 | 0.3537 | 0.0707 | H | 5.5582 | -1.4682 | -0.0055 |
| H | -5.5465 | 1.4484 | 0.0749 | C | 6.8067 | 0.2952 | -0.0845 |
| C | -4.3417 | -0.3011 | 0.1300 | H | 6.7859 | 1.3902 | -0.0878 |
| H | -4.3464 | -1.3960 | 0.1241 | C | 8.0216 | -0.3277 | -0.1683 |
| C | -3.0750 | 0.3426 | 0.1797 | H | 8.0561 | -1.4225 | -0.1685 |
| H | -3.0660 | 1.4371 | 0.1788 | C | 9.2761 | 0.3722 | -0.2625 |
| C | -1.8698 | -0.3194 | 0.2090 | H | 9.2227 | 1.4662 | -0.2724 |
| H | -1.8815 | -1.4144 | 0.2090 | C | 10.4887 | -0.2217 | -0.3354 |
| C | -0.6009 | 0.3183 | 0.2198 | H | 10.5880 | -1.3090 | -0.3312 |
| H | -0.5873 | 1.4134 | 0.2209 | H | 11.4048 | 0.3630 | -0.4028 |

**Table G.17.** $C_{20}H_{24}$ geometry (in Å).

| subsystem $I$ | | | | subsystem $II$ | | | |
|---|---|---|---|---|---|---|---|
| atom | $x$ | $y$ | $z$ | atom | $x$ | $y$ | $z$ |
| C | -10.2566 | -0.1748 | -3.1129 | C | 0.5891 | -0.2332 | 2.1222 |
| H | -10.0833 | 0.0411 | -4.1805 | H | 0.5318 | -1.3270 | 2.1221 |
| H | -11.2821 | 0.1660 | -2.8952 | C | 1.8798 | 0.3468 | 1.9709 |
| H | -10.2181 | -1.2635 | -2.9764 | H | 1.9426 | 1.4401 | 1.9681 |
| C | -9.2521 | 0.5277 | -2.2536 | C | 3.0186 | -0.3732 | 1.6858 |
| H | -9.2055 | 1.6187 | -2.3451 | H | 2.9429 | -1.4654 | 1.6617 |
| C | -8.3897 | -0.0834 | -1.4044 | C | 4.2567 | 0.1963 | 1.2729 |
| H | -8.4265 | -1.1758 | -1.3177 | H | 4.3384 | 1.2881 | 1.2883 |
| C | -7.3770 | 0.5939 | -0.6388 | C | 5.2966 | -0.5265 | 0.7373 |
| H | -7.3376 | 1.6852 | -0.7218 | H | 5.2009 | -1.6168 | 0.6987 |
| C | -6.4258 | -0.0404 | 0.1145 | C | 6.4415 | 0.0456 | 0.1047 |
| H | -6.4641 | -1.1332 | 0.1815 | H | 6.5363 | 1.1362 | 0.1345 |
| C | -5.3167 | 0.6091 | 0.7362 | C | 7.3603 | -0.6664 | -0.6190 |
| H | -5.2722 | 1.7008 | 0.6644 | H | 7.2586 | -1.7559 | -0.6638 |
| C | -4.2528 | -0.0525 | 1.3023 | C | 8.4120 | -0.0796 | -1.4057 |
| H | -4.2947 | -1.1459 | 1.3504 | H | 8.5123 | 1.0114 | -1.3646 |
| C | -3.0338 | 0.5680 | 1.6992 | C | 9.2367 | -0.7764 | -2.2259 |
| H | -2.9868 | 1.6608 | 1.6459 | H | 9.1253 | -1.8658 | -2.2696 |
| C | -1.8789 | -0.1206 | 1.9974 | C | 10.2815 | -0.1748 | -3.1129 |
| H | -1.9260 | -1.2144 | 2.0250 | H | 10.0903 | -0.4214 | -4.1708 |
| C | -0.5928 | 0.4753 | 2.1195 | H | 11.2834 | -0.5728 | -2.8833 |
| H | -0.5405 | 1.5690 | 2.0927 | H | 10.3141 | 0.9187 | -3.0199 |

## G.2 Energy, Density, and Dipole Differences

**Table G.18.** Energy difference ($\Delta E$, in $mE_h$) between the KS-DFT and FDE(EO,5ft) methods with different levels of basis set overlap.

| System $n$ | $d$ | m | e1 | e2 | e3 | e4 | e5 | e6 | e7 | e8 | e9 | e10 |
|---|---|---|---|---|---|---|---|---|---|---|---|---|
| 6 | 1 | -2784 | -517 | -12 | 2 | | | | | | | |
| | 3 | -1173 | -851 | -63 | 1 | | | | | | | |
| 8 | 1 | -2703 | -636 | -152 | -7 | 1 | | | | | | |
| | 3 | -2234 | -600 | -144 | -52 | 3 | | | | | | |
| 10 | 1 | -2827 | -757 | -313 | -65 | -3 | 2 | | | | | |
| | 5 | 5354$^\dagger$ | -623 | -220 | -84 | -45 | 1 | | | | | |
| 12 | 1 | -2882 | -749 | -376 | -112 | -5 | 2 | 2 | | | | |
| | 5 | 5409$^\dagger$ | -654 | -358 | -150 | -55 | -22 | 4 | | | | |
| 14 | 1 | -2951 | -782 | -405 | -201 | -1 | 2 | 2 | 2 | | | |
| | 7 | 121986$^\dagger$ | -723 | -332 | -165 | -83 | -40 | -10 | 2 | | | |
| 16 | 7 | 202558$^\dagger$ | -689 | -349 | -233 | -154 | -77 | -36 | -38 | -4 | | |
| 18 | 9 | 529592$^\dagger$ | -678 | -338 | -249 | -559 | -86 | -51 | -24 | -2 | 6 | |
| 20 | 9 | -2157.706 | -654 | -342 | -250 | -147 | -143 | -127 | -45 | -28 | -4 | 8 |

$n$ - number of carbon atoms; $d$ - number of conjugated double bonds.
$^\dagger$One or more SCF cycles failed to converge during the freeze-and-thaw iterations.

**Table G.19.** Integrated absolute density difference ($\Delta^{\text{abs}}$, in $e$) for the FDE(EO,5ft) method with different levels of basis set overlap.

| System $n$ | $d$ | m | e1 | e2 | e3 | e4 | e5 | e6 | e7 | e8 | e9 | e10 |
|---|---|---|---|---|---|---|---|---|---|---|---|---|
| 6 | 1 | 4.74 | 2.23 | 0.11 | 0.00 | | | | | | | |
| | 3 | 6.98 | 2.54 | 0.61 | 0.00 | | | | | | | |
| 8 | 1 | 5.65 | 2.29 | 0.93 | 0.08 | 0.00 | | | | | | |
| | 3 | 6.56 | 2.40 | 1.17 | 0.58 | 0.00 | | | | | | |
| 10 | 1 | 6.00 | 2.72 | 2.00 | 0.66 | 0.06 | 0.00 | | | | | |
| | 5 | 16.00$^\dagger$ | 2.54 | 1.66 | 0.95 | 0.44 | 0.00 | | | | | |
| 12 | 1 | 6.65 | 2.65 | 2.21 | 0.87 | 0.10 | 0.00 | 0.00 | | | | |
| | 5 | 18.26$^\dagger$ | 2.72 | 2.44 | 1.47 | 0.69 | 0.37 | 0.00 | | | | |
| 14 | 1 | 6.82 | 2.77 | 2.23 | 1.47 | 0.12 | 0.01 | 0.00 | 0.00 | | | |
| | 7 | 44.99$^\dagger$ | 2.76 | 2.47 | 1.66 | 1.05 | 0.64 | 0.26 | 0.00 | | | |
| 16 | 7 | 54.41$^\dagger$ | 2.86 | 2.54 | 2.45 | 1.76 | 1.04 | 0.46 | 0.55 | 0.01 | | |
| 18 | 9 | 67.99$^\dagger$ | 2.92 | 2.56 | 2.54 | 3.14 | 1.27 | 0.83 | 0.50 | 0.20 | 0.00 | |
| 20 | 9 | 6.37 | 2.98 | 2.61 | 2.59 | 1.91 | 1.88 | 1.59 | 0.80 | 0.40 | 0.20 | 0.00 |

$n$ - number of carbon atoms; $d$ - number of conjugated double bonds.
$^\dagger$One or more SCF cycles failed to converge during the freeze-and-thaw iterations.

**Table G.20.** Absolute dipole difference ($|\Delta\mu|$, in $D$) for the FDE(EO,5ft) method with different levels of basis set overlap.

| System $n$ | $d$ | m | e1 | e2 | e3 | e4 | e5 | e6 | e7 | e8 | e9 | e10 |
|---|---|---|---|---|---|---|---|---|---|---|---|---|
| 6 | 1 | 17.32 | 9.14 | 0.06 | 0.00 | | | | | | | |
| | 3 | 39.09 | 7.80 | 3.08 | 0.00 | | | | | | | |
| 8 | 1 | 26.34 | 9.27 | 2.16 | 0.20 | 0.00 | | | | | | |
| | 3 | 46.78 | 16.14 | 6.18 | 3.35 | 0.00 | | | | | | |
| 10 | 1 | 30.73 | 11.94 | 7.28 | 1.76 | 0.14 | 0.00 | | | | | |
| | 5 | 106.17$^{\dagger}$ | 22.49 | 12.19 | 7.23 | 0.08 | 0.01 | | | | | |
| 12 | 1 | 43.31 | 12.41 | 9.49 | 1.16 | 0.21 | 0.00 | 0.00 | | | | |
| | 5 | 121.73$^{\dagger}$ | 26.32 | 22.88 | 11.34 | 5.20 | 3.10 | 0.01 | | | | |
| 14 | 1 | 46.25 | 13.60 | 9.75 | 3.34 | 0.23 | 0.00 | 0.00 | 0.00 | | | |
| | 7 | 272.74$^{\dagger}$ | 33.11 | 29.84 | 16.62 | 10.39 | 6.54 | 2.70 | 0.00 | | | |
| 16 | 7 | 311.68$^{\dagger}$ | 35.45 | 31.80 | 30.20 | 18.65 | 10.21 | 4.06 | 5.88 | 0.05 | | |
| 18 | 9 | 407.66$^{\dagger}$ | 43.75 | 38.98 | 38.28 | 10.28 | 15.44 | 10.15 | 6.25 | 2.60 | 0.01 | |
| 20 | 9 | 64.86 | 41.79 | 37.43 | 36.98 | 23.31 | 23.19 | 18.78 | 8.87 | 3.72 | 2.54 | 0.04 |

$n$ - number of carbon atoms; $d$ - number of conjugated double bonds.

$^{\dagger}$One or more SCF cycles failed to converge during the freeze-and-thaw iterations.

## G.3 Extended Monomer Truncation

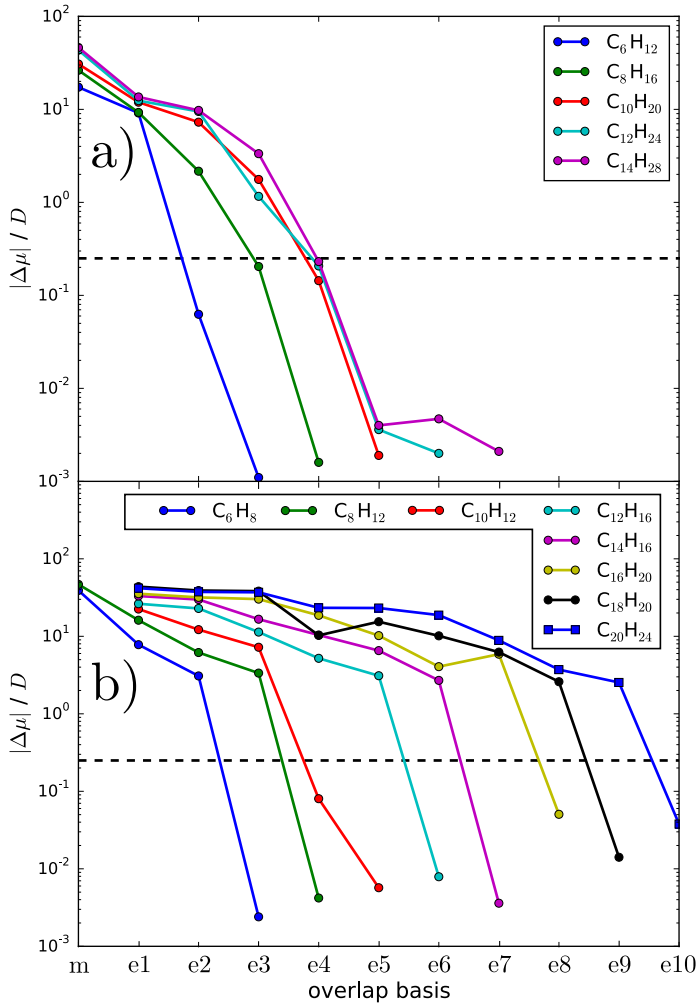


**Figure G.1.** $|\Delta\mu|$ for the FDE(EO,5ft) method with different levels of basis set overlap for (a) alkane-like systems, and (b) conjugated alkenes. The dashed line is the dipole difference threshold of 0.25 $D$.

## G.4 DZP-Truncated Basis Data

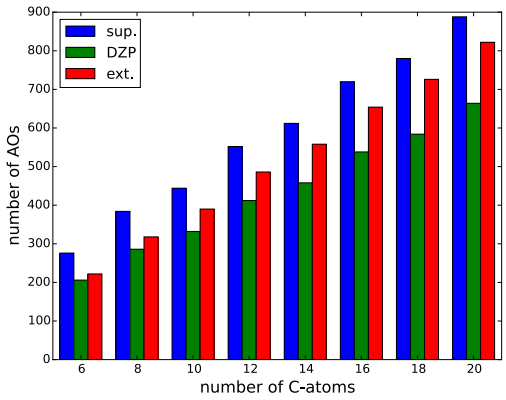


**Figure G.2.** Number of basis functions for the fragments of the conjugated alkenes in the supermolecular basis (sup.), the DZP truncated basis (DZP), and the largest extended monomer basis truncation (exp.).

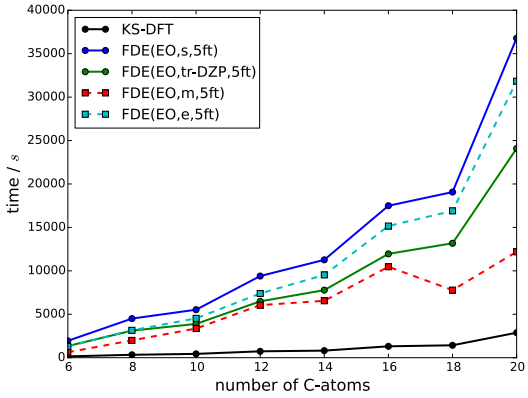


**Figure G.3.** Computation time (on 8 processors) for the KS-DFT method, and various levels of basis set truncations of the FDE(EO) method. FDE(EO,e) represents the largest extended monomer basis truncation.

# Appendix H
# Supporting Information for: External Orthogonality in Subsystem Time-dependent Density Functional Theory

## H.1 EO Operator in MO Basis

In the following derivation, $\chi$ are atomic orbitals (AOs), $\phi$ are molecular orbitals (MOs), superscripts indicate the subsystem the particular matrix is describing (for only two subsystems, A or B), and subscripts indicate particular elements of the respective matrix. Roman subscripts $i$, $j$, ... indicate occupied MOs; $a$, $b$, ... indicate virtual MOs; $p$, $q$, ... indicate general MOs; and Greek subscripts $\alpha$, $\beta$, ... describe AOs. Bold-face fonts (e.g. $\mathbf{A}$) indicate matrices in AO basis and blackboard-bold fonts (e.g. $\mathbb{A}$) indicate matrices in MO basis. The EO projection operator for subsystem A in the environment of B is[359]

$$\mathbf{V}^{\mathrm{EO,A(B)}} = \mathbf{S}^{\mathrm{A,B}}\mathbf{P}^{\mathrm{B}}\mathbf{S}^{\mathrm{B,A}} \tag{H.1}$$

where $\mathbf{S}^{\mathrm{A,B}}$ is the AO overlap matrix between subsystems A and B ($\mathbf{S}^{\mathrm{A,B}}_{\alpha\beta} = \langle\chi^{\mathrm{A}}_{\alpha}|\chi^{\mathrm{B}}_{\beta}\rangle$), and $\mathbf{P}^{\mathrm{B}}$ is the density matrix of subsystem B, defined as

$$\mathbf{P}^{\mathrm{B}}_{\alpha\beta} = \mathbf{C}^{\mathrm{B}}\mathbf{n}^{\mathrm{B}}(\mathbf{n}^{\mathrm{B}})^{T}(\mathbf{C}^{\mathrm{B}})^{T} \tag{H.2}$$

In this definition, $\mathbf{C}^{\mathrm{B}}$ is the MO coefficient matrix for all occupied and virtual orbitals of subsystem B and $\mathbf{n}^{\mathrm{B}}$ is a vector of the respective MO occupation numbers. We can therefore use this to write the MO density matrix as $\mathbb{P}^{\mathrm{B}} = \mathbf{n}^{\mathrm{B}}(\mathbf{n}^{\mathrm{B}})^{T}$. This allows us to write the EO operator in MO basis as

$$\begin{aligned}\mathbb{V}^{\mathrm{EO,A(B)}} &= (\mathbf{C}^{\mathrm{A}})^{T}\mathbf{S}^{\mathrm{A,B}}\mathbf{C}^{\mathrm{B}}\mathbb{P}^{\mathrm{B}}(\mathbf{C}^{\mathrm{B}})^{T}\mathbf{S}^{\mathrm{B,A}}\mathbf{C}^{\mathrm{A}} \\ &= \mathbb{S}^{\mathrm{A,B}}\mathbb{P}^{\mathrm{B}}\mathbb{S}^{\mathrm{B,A}}\end{aligned} \tag{H.3}$$

where $\mathbb{S}^{\mathrm{A,B}}$ is the MO overlap matrix

$$
\begin{aligned}
\mathbb{S}^{\mathrm{A,B}}_{pq} &= \left[(\mathbf{C}^{\mathrm{A}})^T \mathbf{S}^{\mathrm{A,B}} \mathbf{C}^{\mathrm{B}}\right]_{pq} \\
&= \left(\sum_{\alpha} \langle \chi^{\mathrm{A}}_{\alpha} | \mathbf{C}^{\mathrm{A}}_{\alpha p}\right) \left(\sum_{\beta} \mathbf{C}^{\mathrm{B}}_{\beta q} | \chi^{\mathrm{B}}_{\beta}\rangle\right) \\
&= \langle \phi^{\mathrm{A}}_{p} | \phi^{\mathrm{B}}_{q} \rangle
\end{aligned}
\tag{H.4}
$$

## H.2 Long-Range Correction to the NAKP

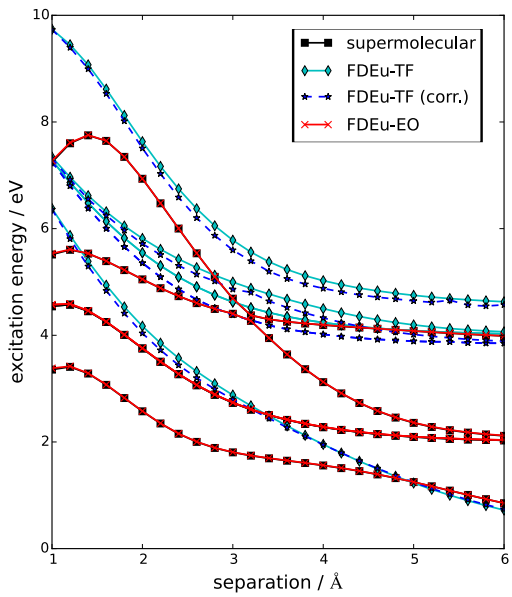


**Figure H.1.** Excitation energies of the five lowest transitions in the LiH system with respect to subsystem separation, showing the long-range correction to the NAKP (corr.).

## H.3 Significance of the EO Kernel

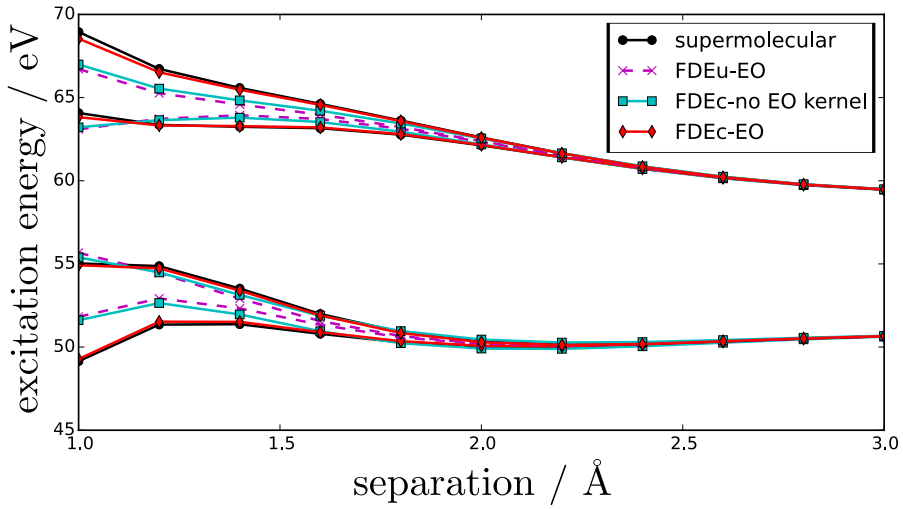


**Figure H.2.** Coupled excitation energies of the He-dimer showing the importance of the EO contribution to the coupled response kernel.

# Appendix I
# Potential Energy Distributions for all Normal Modes of Rhodamine-6G

| Mode ($cm^{-1}$) | Methyl (%) | Xanthene (%) | Ethyl (%) | Phenyl (%) | Ester (%) |
|---|---|---|---|---|---|
| 391 | 0.7 | 3.3 | 8.6 | 11.1 | 76.4 |
| 396 | 15.6 | 18.3 | 55.1 | 11.0 | 0.0 |
| 421 | 13.7 | 33.2 | 48.6 | 3.1 | 1.4 |
| 431 | 1.2 | 11.6 | 8.7 | 75.4 | 3.1 |
| 445 | 2.6 | 9.2 | 87.7 | 0.2 | 0.2 |
| 447 | 9.5 | 10.3 | 79.9 | 0.2 | 0.0 |
| 454 | 9.7 | 16.2 | 72.0 | 2.1 | 0.0 |
| 456 | 4.0 | 45.1 | 21.6 | 27.6 | 1.7 |
| 462 | 6.2 | 41.5 | 52.2 | 0.0 | 0.1 |
| 502 | 1.0 | 8.9 | 5.8 | 36.0 | 48.3 |
| 517 | 18.6 | 9.5 | 70.1 | 1.0 | 0.7 |
| 531 | 19.6 | 26.1 | 11.7 | 42.4 | 0.1 |
| 549 | 21.6 | 27.7 | 24.4 | 26.2 | 0.0 |
| 559 | 32.4 | 27.3 | 39.6 | 0.6 | 0.1 |
| 610 | 7.4 | 42.6 | 34.1 | 15.9 | 0.0 |
| 616 | 3.5 | 39.2 | 6.0 | 51.1 | 0.1 |
| 632 | 0.4 | 66.8 | 3.7 | 25.7 | 3.4 |
| 666 | 0.7 | 19.3 | 1.3 | 72.2 | 6.5 |
| 669 | 22.5 | 71.7 | 5.8 | 0.1 | 0.0 |
| 694 | 27.3 | 69.7 | 1.9 | 1.0 | 0.2 |
| 700 | 3.5 | 9.8 | 2.1 | 72.2 | 12.3 |
| 703 | 2.6 | 45.2 | 1.0 | 44.0 | 7.2 |
| 707 | 9.4 | 89.7 | 0.7 | 0.1 | 0.0 |
| 724 | 3.8 | 20.4 | 59.5 | 15.4 | 0.9 |
| 736 | 7.8 | 13.9 | 12.4 | 63.9 | 1.9 |
| 748 | 0.4 | 94.3 | 1.8 | 3.2 | 0.3 |
| 759 | 1.2 | 12.3 | 84.7 | 1.6 | 0.2 |

| Mode ($cm^{-1}$) | Methyl (%) | Xanthene (%) | Ethyl (%) | Phenyl (%) | Ester (%) |
|---|---|---|---|---|---|
| 772 | 16.8 | 42.3 | 39.7 | 1.1 | 0.2 |
| 775 | 4.5 | 9.4 | 19.5 | 66.6 | 0.0 |
| 794 | 0.0 | 0.5 | 4.8 | 26.7 | 68.0 |
| 803 | 0.2 | 1.8 | 37.6 | 8.1 | 52.3 |
| 806 | 0.5 | 4.1 | 54.2 | 12.2 | 29.0 |
| 821 | 6.9 | 15.6 | 73.6 | 2.8 | 1.1 |
| 826 | 0.2 | 98.2 | 1.6 | 0.0 | 0.0 |
| 831 | 0.2 | 97.8 | 1.8 | 0.1 | 0.1 |
| 855 | 0.3 | 6.3 | 7.4 | 18.3 | 67.6 |
| 870 | 0.1 | 4.2 | 4.6 | 3.6 | 87.4 |
| 885 | 2.3 | 33.2 | 0.6 | 63.8 | 0.2 |
| 886 | 6.2 | 93.2 | 0.2 | 0.2 | 0.2 |
| 888 | 4.3 | 63.2 | 0.1 | 32.3 | 0.1 |
| 891 | 2.1 | 2.9 | 92.8 | 1.0 | 1.1 |
| 895 | 1.4 | 2.6 | 95.7 | 0.3 | 0.0 |
| 925 | 1.0 | 40.8 | 32.0 | 22.8 | 3.4 |
| 951 | 11.9 | 17.2 | 3.1 | 67.8 | 0.1 |
| 959 | 16.8 | 18.2 | 3.0 | 62.0 | 0.0 |
| 989 | 0.0 | 0.0 | 0.0 | 99.9 | 0.0 |
| 1009 | 92.8 | 6.8 | 0.2 | 0.1 | 0.0 |
| 1012 | 0.2 | 0.0 | 0.0 | 3.1 | 96.7 |
| 1019 | 77.9 | 14.7 | 7.1 | 0.3 | 0.0 |
| 1039 | 5.8 | 8.2 | 72.0 | 14.0 | 0.0 |
| 1048 | 33.9 | 3.2 | 4.0 | 58.2 | 0.7 |
| 1049 | 92.8 | 7.1 | 0.1 | 0.0 | 0.0 |
| 1052 | 4.6 | 14.8 | 80.4 | 0.1 | 0.0 |
| 1082 | 2.6 | 5.4 | 48.5 | 38.2 | 5.4 |
| 1089 | 1.2 | 3.0 | 73.1 | 19.8 | 2.9 |
| 1091 | 0.6 | 2.4 | 97.1 | 0.0 | 0.0 |
| 1118 | 0.2 | 0.8 | 0.9 | 7.2 | 90.9 |
| 1129 | 13.5 | 27.5 | 40.5 | 16.1 | 2.4 |
| 1138 | 3.8 | 22.4 | 73.7 | 0.0 | 0.0 |
| 1144 | 0.1 | 15.4 | 79.2 | 5.1 | 0.2 |
| 1150 | 0.0 | 0.3 | 0.1 | 92.4 | 7.2 |
| 1162 | 0.0 | 0.0 | 0.0 | 0.0 | 100.0 |
| 1164 | 24.0 | 42.6 | 33.4 | 0.0 | 0.0 |
| 1174 | 0.0 | 0.0 | 0.0 | 100.0 | 0.0 |
| 1182 | 4.0 | 81.2 | 14.7 | 0.1 | 0.0 |
| 1195 | 0.4 | 61.2 | 38.3 | 0.1 | 0.0 |

| Mode ($cm^{-1}$) | Methyl (%) | Xanthene (%) | Ethyl (%) | Phenyl (%) | Ester (%) |
|---|---|---|---|---|---|
| 1195 | 6.7 | 28.0 | 15.0 | 50.0 | 0.3 |
| 1247 | 0.8 | 88.8 | 10.4 | 0.0 | 0.0 |
| 1265 | 0.4 | 34.5 | 4.4 | 26.3 | 34.4 |
| 1271 | 0.7 | 70.0 | 17.5 | 9.3 | 2.5 |
| 1273 | 2.2 | 62.8 | 35.0 | 0.0 | 0.0 |
| 1274 | 0.1 | 10.1 | 0.4 | 89.3 | 0.2 |
| 1285 | 0.0 | 0.0 | 0.0 | 0.0 | 100.0 |
| 1298 | 1.0 | 34.9 | 60.9 | 2.4 | 0.8 |
| 1305 | 0.7 | 6.8 | 26.5 | 61.6 | 4.5 |
| 1310 | 0.1 | 15.2 | 84.7 | 0.0 | 0.0 |
| 1314 | 0.4 | 9.1 | 87.5 | 3.0 | 0.1 |
| 1321 | 3.8 | 11.7 | 84.4 | 0.0 | 0.0 |
| 1356 | 10.8 | 49.8 | 28.4 | 11.1 | 0.0 |
| 1367 | 0.2 | 4.7 | 93.9 | 1.2 | 0.0 |
| 1371 | 8.2 | 28.5 | 63.3 | 0.0 | 0.0 |
| 1380 | 3.3 | 22.8 | 73.9 | 0.0 | 0.0 |
| 1384 | 0.0 | 0.0 | 0.0 | 0.9 | 99.1 |
| 1399 | 0.4 | 0.1 | 99.6 | 0.0 | 0.0 |
| 1400 | 2.1 | 0.1 | 97.8 | 0.0 | 0.0 |
| 1403 | 92.2 | 1.3 | 6.2 | 0.2 | 0.0 |
| 1405 | 98.1 | 1.0 | 0.9 | 0.0 | 0.0 |
| 1412 | 0.0 | 0.0 | 0.0 | 0.5 | 99.5 |
| 1424 | 37.9 | 30.3 | 17.1 | 14.5 | 0.2 |
| 1441 | 37.8 | 11.6 | 47.9 | 2.7 | 0.0 |
| 1450 | 0.3 | 2.1 | 1.3 | 95.9 | 0.4 |
| 1471 | 39.0 | 5.8 | 55.2 | 0.0 | 0.0 |
| 1475 | 0.0 | 0.0 | 0.0 | 0.0 | 100.0 |
| 1477 | 57.7 | 0.3 | 42.0 | 0.0 | 0.0 |
| 1477 | 96.7 | 0.1 | 3.2 | 0.0 | 0.0 |
| 1479 | 29.4 | 0.7 | 69.9 | 0.0 | 0.0 |
| 1481 | 0.8 | 0.3 | 98.9 | 0.0 | 0.0 |
| 1482 | 0.7 | 0.3 | 98.8 | 0.0 | 0.1 |
| 1484 | 0.1 | 0.0 | 0.1 | 0.0 | 99.8 |
| 1490 | 35.9 | 26.3 | 37.8 | 0.0 | 0.0 |
| 1491 | 17.8 | 7.2 | 4.2 | 68.0 | 2.8 |
| 1497 | 33.6 | 1.6 | 63.2 | 1.5 | 0.1 |
| 1497 | 1.7 | 4.0 | 94.3 | 0.0 | 0.0 |
| 1497 | 47.1 | 6.8 | 41.9 | 3.9 | 0.3 |
| 1503 | 0.0 | 0.0 | 0.1 | 0.4 | 99.5 |

| Mode ($cm^{-1}$) | Methyl (%) | Xanthene (%) | Ethyl (%) | Phenyl (%) | Ester (%) |
|---|---|---|---|---|---|
| 1507 | 58.0 | 20.7 | 21.3 | 0.0 | 0.0 |
| 1515 | 11.8 | 28.2 | 58.1 | 1.8 | 0.1 |
| 1535 | 6.8 | 38.6 | 54.5 | 0.0 | 0.0 |
| 1561 | 1.3 | 73.0 | 24.2 | 1.5 | 0.0 |
| 1574 | 0.6 | 11.6 | 87.9 | 0.0 | 0.0 |
| 1579 | 1.8 | 11.5 | 86.1 | 0.5 | 0.0 |
| 1582 | 0.1 | 6.9 | 1.9 | 90.8 | 0.4 |
| 1607 | 0.0 | 3.6 | 0.0 | 96.2 | 0.2 |
| 1621 | 16.8 | 78.2 | 5.0 | 0.0 | 0.0 |
| 1658 | 8.9 | 89.6 | 1.3 | 0.0 | 0.2 |
| 1730 | 0.0 | 0.8 | 0.0 | 2.7 | 96.4 |

Table I.1: Theoretical potential energy distributions (PEDs) for the vibrational modes of R6G molecule: R6G molecule is divided into five regions, the xanthene ring, the phenyl ring, the methyl groups attached to the xanthene ring ("Methyl"), the ethylamine groups attached to the xanthene ring ("Ethyl"), and the ester group attached to the phenyl ring ("Ester"). Depending on the normal mode vectors, the contributions (in percentage) of each of these five groups to the normal modes were calculated.

# Bibliography


[1] Raman, C. V.; Krishnan, K. S. *Nature* **1928**, *121*, 501–502.

[2] Long, D. A. *The Raman Effect: A Unified Treatment of the Theory of Raman Scattering by Molecules*; John Wiley & Sons, Ltd.: West Sussex, England, 2002.

[3] Fleischmann, M.; Hendra, P.; McQuillan, A. *Chem. Phys. Lett.* **1974**, *26*, 163 – 166.

[4] Jeanmaire, D. L.; Van Duyne, R. P. *J. Electroanal. Chem.* **1977**, *84*, 1–20.

[5] Albrecht, M. G.; Creighton, J. A. *J. Am. Chem. Soc.* **1977**, *99*, 5215–5217.

[6] Moskovits, M.; Tay, L.-L.; Yang, J.; Haslett, T. In *Optical Properties of Nanostructured Random Media*; Shalaev, V. M., Ed.; Top. Appl. Phys.; Springer Berlin / Heidelberg: Heidelburg, Germany, 2002; Vol. 82; Chapter 13, pp 215–227.

[7] Schatz, G. C.; Young, M. A.; Van Duyne, R. P. In *Surface-Enhanced Raman Scattering - Physics and Applications*; Kneipp, K., Moskovits, M., Kneipp, H., Eds.; Top. Appl. Phys.; Springer-Verlag Berlin: Heidelberg, Germany, 2006; Vol. 103; Chapter 2, pp 19–45.

[8] Lombardi, J. R.; Birke, R. L. *J. Chem. Phys.* **2012**, *136*, 144704.

[9] Le Ru, E. C.; Etchegoin, P. G. *Ann. Rev. Phys. Chem.* **2012**, *63*, 65–87.

[10] Kelly, K. L.; Coronado, E.; Zhao, L. L.; Schatz, G. C. *J. Phys. Chem. B* **2003**, *107*, 668–677.

[11] Eustis, S.; El-Sayed, M. A. *Chem. Soc. Rev.* **2005**, *35*, 209.

[12] Morton, S. M.; Silverstein, D. W.; Jensen, L. *Chem. Rev.* **2011**, *111*, 3962–3994.

[13] Moskovits, M. *Rev. Mod. Phys.* **1985**, *57*, 783–826.

[14] Sharma, B.; Frontiera, R. R.; Henry, A.-I.; Ringe, E.; Van Duyne, R. P. *Mater. Today* **2012**, *15*, 16–25.

[15] Gates, B. D.; Xu, Q.; Stewart, M.; Ryan, D.; Willson, C. G.; Whitesides, G. M. *Chem. Rev.* **2005**, *105*, 1171–1196.

[16] Zhang, X.; Whitney, A. V.; Zhao, J.; Hicks, E. M.; Van Duyne, R. P. *J. Nanosci. Nanotechnol.* **2006**, *6*, 1920–1934.

[17] Henzie, J.; Barton, J. E.; Stender, C. L.; Odom, T. W. *Acc. Chem. Res.* **2006**, *39*, 249–257.

[18] Le Ru, E. C.; Meyer, M.; Etchegoin, P. G. *J. Phys. Chem. B* **2006**, *110*, 1944–1948.

[19] Dieringer, J. A.; Lettan, R. B.; Scheidt, K. A.; Van Duyne, R. P. *J. Am. Chem. Soc.* **2007**, *129*, 16249–16256.

[20] Shafer-Peltier, K. E.; Haynes, C. L.; Glucksberg, M. R.; Van Duyne, R. P. *J. Am. Chem. Soc.* **2003**, *125*, 588–593.

[21] Lyandres, O.; Yuen, J. M.; Shah, N. C.; VanDuyne, R. P.; Walsh, J. T.; Glucksberg, M. R. *Diabetes Technol. Ther.* **2008**, *10*, 257–265.

[22] Zhang, X.; Young, M. A.; Lyandres, O.; Van Duyne, R. P. *J. Am. Chem. Soc.* **2005**, *127*, 4484–4489.

[23] Ko, H.; Chang, S.; Tsukruk, V. V. *ACS Nano* **2008**, *3*, 181–188.

[24] Kneipp, K.; Kneipp, H.; Itzkan, I.; Dasari, R. R.; Feld, M. S. *Chem. Rev.* **1999**, *99*, 2957–2976.

[25] Mirkin, C. A.; Letsinger, R. L.; Mucic, R. C.; Storhoff, J. J. *Nature* **1996**, *382*, 607–609.

[26] Cao, Y. C.; Jin, R.; Mirkin, C. A. *Science* **2002**, *297*, 1536–1540.

[27] Brosseau, C. L.; Rayner, K. S.; Casadio, F.; Grzywacz, C. M.; Van Duyne, R. P. *Anal. Chem.* **2009**, *81*, 7443–7447.

[28] Wustholz, K. L.; Brosseau, C. L.; Casadio, F.; Van Duyne, R. P. *Phys. Chem. Chem. Phys.* **2009**, *11*, 7350–7359.

[29] Casadio, F.; Leona, M.; Lombardi, J. R.; Van Duyne, R. *Acc. Chem. Res.* **2010**, *43*, 782–791.

[30] Sonntag, M. D.; Klingsporn, J. M.; Garibay, L. K.; Roberts, J. M.; Dieringer, J. A.; Seideman, T.; Scheidt, K. A.; Jensen, L.; Schatz, G. C.; Van Duyne, R. P. *J. Phys. Chem. C* **2012**, *116*, 478–483.

[31] Stöckle, R. M.; Suh, Y. D.; Deckert, V.; Zenobi, R. *Chem. Phys. Lett.* **2000**, *318*, 131–136.

[32] Pozzi, E. A.; Sonntag, M. D.; Jiang, N.; Chiang, N.; Seideman, T.; Hersam, M. C.; Van Duyne, R. P. *J. Phys. Chem. Lett.* **2014**, *5*, 2657–2661.

[33] Pozzi, E. A.; Sonntag, M. D.; Jiang, N.; Klingsporn, J. M.; Hersam, M. C.; Van Duyne, R. P. *ACS Nano* **2013**, *7*, 885–888.

[34] Zhang, R.; Zhang, Y.; Dong, Z. C.; Jiang, S.; Zhang, C.; Chen, L. G.; Zhang, L.; Liao, Y.; Aizpurua, J.; Luo, Y.; Yang, J. L.; Hou, J. G. *Nature* **2013**, *498*, 82–86.

[35] Moskovits, M.; DiLella, D. P.; Maynard, K. J. *Langmuir* **1988**, *4*, 67–76.

[36] Sass, J. K.; Neff, H.; Moskovits, M.; Holloway, S. *J. Phys. Chem.* **1981**, *85*, 621–623.

[37] Moskovits, M.; DiLella, D. P. *J. Chem. Phys.* **1980**, *73*, 6068–6075.

[38] Wolkow, R. A.; Moskovits, M. *J. Chem. Phys.* **1986**, *84*, 5196–5199.

[39] Metiu, H.; Das, P. *Ann. Rev. Phys. Chem.* **1984**, *35*, 507–536.

[40] Schatz, G. C. *Acc. Chem. Res.* **1984**, *17*, 370–376.

[41] Jensen, L.; Aikens, C. M.; Schatz, G. C. *Chem. Soc. Rev.* **2008**, *37*, 1061–1073.

[42] Moskovits, M. *Phys. Chem. Chem. Phys.* **2013**, *15*, 5301–5311.

[43] Chiang, N.; Jiang, N.; Chulhai, D. V.; Pozzi, E. A.; Hersam, M. C.; Jensen, L.; Seideman, T.; Van Duyne, R. P. *Nano Lett.* **2015**, *15*, 4114–4120.

[44] Sonntag, M. D.; Chulhai, D.; Seideman, T.; Jensen, L.; Van Duyne, R. P. *J. Am. Chem. Soc.* **2013**, *135*, 17187–17192.

[45] Klingsporn, J. M.; Jiang, N.; Pozzi, E. A.; Sonntag, M. D.; Chulhai, D.; Seideman, T.; Jensen, L.; Hersam, M. C.; Duyne, R. P. V. *J. Am. Chem. Soc.* **2014**, *136*, 3881–3887.

[46] Strutt, H. J. *Philos. Mag.* **1871**, *41*, 274–279.

[47] Kramers, H. A.; Heisenberg, W. *Z. Phys.* **1925**, *31*, 681.

[48] Dirac, P. A. M. *Proc. R. Soc. Lond. A* **1927**, *114*, 710.

[49] Placzek, G. In *Handbuch der Radiologie*; Marx, E., Ed.; Akademishce, Leipzig, 1934; p 205.

[50] Jensen, L.; Zhao, L. L.; Autschbach, J.; Schatz, G. C. *J. Chem. Phys.* **2005**, *123*, 174110.

[51] Kane, K. A.; Jensen, L. *J. Phys. Chem. C* **2010**, *114*, 5540–5546.

[52] Albrecht, A. C. *J. Chem. Phys.* **1961**, *34*, 1476–1484.

[53] Tang, J.; Albrecht, A. C. *J. Chem. Phys.* **1968**, *49*, 1144.

[54] Albrecht, A. C.; Hutley, M. C. *J. Chem. Phys.* **1971**, *55*, 4438.

[55] Heller, E. J.; Sundberg, R.; Tannor, D. *J. Phys. Chem.* **1982**, *86*, 1822.

[56] Lee, S.-Y.; Heller, E. J. *J. Chem. Phys.* **1979**, *71*, 4777.

[57] Heller, E. J. *Acc. Chem. Res.* **1981**, *14*, 368–375.

[58] Asher, S. A. *Ann. Rev. Phys. Chem.* **1988**, *39*, 537–588.

[59] Champion, P. M.; Albrecht, A. C. *Ann. Rev. Phys. Chem.* **1982**, *33*, 353–376.

[60] Myers, A. B. *Chem. Rev.* **1996**, *96*, 911.

[61] Myers, A. B. *Acc. Chem. Res.* **1997**, *30*, 519–527.

[62] Aroca, R. *Surface-Enhanced Vibrational Spectroscopy*; John Wiley and Sons Ltd., 2006.

[63] Jensen, L.; Schatz, G. C. *J. Phys. Chem. A* **2006**, *110*, 5973–5977.

[64] Tang, J.; Albrecht, A. C. In *Raman Spectroscopy: Theory and Practice*; Szymanski, H. A., Ed.; Springer US: Boston, MA, 1970; Chapter Developments in the Theories of Vibrational Raman Intensities, pp 33–68.

[65] Neese, F.; Petrenko, T.; Ganyushin, D.; Olbrich, G. *Coord. Chem. Rev.* **2007**, *251*, 288.

[66] Corni, S.; Tomasi, J. *Chem. Phys. Lett.* **2001**, *342*, 135–140.

[67] Corni, S.; Tomasi, J. *Chem. Phys. Lett.* **2002**, *365*, 552–553.

[68] Neugebauer, J.; Reiher, M.; Kind, C.; Hess, B. A. *J. Comput. Chem.* **2002**, *23*, 895–910.

[69] Willets, K. A.; Van Duyne, R. P. *Ann. Rev. Phys. Chem.* **2007**, *58*, 267–297.

[70] Myers Kelley, A. *Ann. Rev. Phys. Chem.* **2010**, *61*, 41–61.

[71] Sonntag, M. D.; Pozzi, E. A.; Jiang, N.; Hersam, M. C.; Duyne, R. P. V. *J. Phys. Chem. Lett.* **2014**, *5*, 3125–3130.

[72] Keller, E. L.; Brandt, N. C.; Cassabaum, A. A.; Frontiera, R. R. *Analyst* **2015**, *140*, 4922–4931.

[73] Milojevich, C. B.; Mandrell, B. K.; Turley, H. K.; Iberi, V.; Best, M. D.; Camden, J. P. *J. Phys. Chem. Lett.* **2013**, *4*, 3420–3423.

[74] Zhang, Y.; Zhen, Y.-R.; Neumann, O.; Day, J. K.; Nordlander, P.; Halas, N. J. *Nature Comm.* **2014**, *5*, 4424.

[75] Campion, A.; Kambhampati, P. *Chem. Soc. Rev.* **1998**, *27*, 241–250.

[76] Link, S.; El-Sayed, M. A. *Ann. Rev. Phys. Chem.* **2003**, *54*, 331–366.

[77] Otto, A. *J. Raman Spectrosc.* **1991**, *22*, 743–752.

[78] Kneipp, K.; Kneipp, H.; Itzkan, I.; Dasari, R. R.; Feld, M. S. *J. Phys.: Condens. Matter* **2002**, *14*, R597.

[79] Moskovits, M. *J. Raman Spectrosc.* **2005**, *36*, 485–496.

[80] Stiles, P. L.; Dieringer, J. A.; Shah, N. C.; Van Duyne, R. P. *Annu. Rev. Anal. Chem.* **2008**, *1*, 601–626.

[81] Kneipp, K.; Wang, Y.; Kneipp, H.; Perelman, L. T.; Itzkan, I.; Dasari, R. R.; Feld, M. S. *Phys. Rev. Lett.* **1997**, *78*, 1667–1670.

[82] Nie, S. M.; Emory, S. R. *Science* **1997**, *275*, 1102–1106.

[83] Xu, H.; Bjerneld, E. J.; Käll, M.; Börjesson, L. *Phys. Rev. Lett.* **1999**, *83*, 4357–4360.

[84] Michaels, A. M.; Nirmal, M.; Brus, L. E. *J. Am. Chem. Soc.* **1999**, *121*, 9932–9939.

[85] Haes, A. J.; Hall, W. P.; Chang, L.; Klein, W. L.; ; Van Duyne, R. P. *Nano Lett.* **2004**, *4*, 1029.

[86] Yonzon, C. R.; Haynes, C. L.; Zhang, X.; Walsh, J. T.; Van Duyne, R. P. *Anal. Chem.* **2004**, *76*, 78–85.

[87] Schultz, D. A. *Curr. Opin. Biotech.* **2003**, *14*, 13–22.

[88] Penn, S. G.; He, L.; Natan, M. J. *Curr. Opin. Chem. Biol.* **2003**, *7*, 609–615.

[89] Kneipp, K.; Kneipp, H.; Kartha, V. B.; Manoharan, R.; Deinum, G.; Itzkan, I.; Dasari, R. R.; Feld, M. S. *Phys. Rev. E* **1998**, *57*, R6281–R6284.

[90] Bell, S. E. J.; Sirimuthu, N. M. S. *J. Am. Chem. Soc.* **2006**, *128*, 15580–15581.

[91] Barhoumi, A.; Zhang, D.; Tam, F.; Halas, N. J. *J. Am. Chem. Soc.* **2008**, *130*, 5523–5529.

[92] Kneipp, K.; Haka, A. S.; Kneipp, H.; Badizadegan, K.; Yoshizawa, N.; Boone, C.; Shafer-Peltier, K. E.; Motz, J. T.; Dasari, R. R.; Feld, M. S. *Appl. Spectrosc.* **2002**, *56*, 150–154.

[93] Sylvia, J. M.; Janni, J. A.; Klein, J. D.; Spencer, K. M. *Anal. Chem.* **2000**, *72*, 5834–5840.

[94] Zhang, X.; Zhao, J.; Whitney, A. V.; Elam, J. W.; Van Duyne, R. P. *J. Am. Chem. Soc.* **2006**, *128*, 10304–10309.

[95] Stuart, D. A.; Biggs, K. B.; Van Duyne, R. P. *Analyst* **2006**, *131*, 568–572.

[96] Yan, F.; Vo-Dinh, T. *Sens. Actuators B* **2007**, *121*, 61–66.

[97] Pearman, W. F.; Fountain, A. W. *Appl. Spectrosc.* **2006**, *60*, 356–365.

[98] Xia, Y.; Halas, N. J. *MRS Bulletin* **2005**, *30*, 338–348.

[99] Murphy, C. J.; Sau, T. K.; Gole, A. M.; Orendorff, C. J.; Gao, J.; Gou, L.; Hunyadi, S. E.; Li, T. *J. Phys. Chem. B* **2005**, *109*, 13857–13870.

[100] Jadzinsky, P. D.; Calero, G.; Ackerson, C. J.; Bushnell, D. A.; Kornberg, R. D. *Science* **2007**, *318*, 430–433.

[101] Wang, H.; Brandl, D. W.; Nordlander, P.; Halas, N. J. *Acc. Chem. Res.* **2007**, *40*, 53–62.

[102] Prodan, E.; Radloff, C.; Halas, N. J.; Nordlander, P. *Science* **2003**, *302*, 419–422.

[103] Yang, W.-H.; Schatz, G. C.; Duyne, R. P. V. *J. Chem. Phys.* **1995**, *103*, 869–875.

[104] Tallarida, N.; Rios, L.; Apkarian, V. A.; Lee, J. *Nano Lett.* **2015**, *15*, 6386–6394.

[105] Yampolsky, S.; Fishman, D. A.; Dey, S.; Hulkko, E.; Banik, M.; Potma, E. O.; Apkarian, V. A. *Nat. Photonics* **2014**, *8*, 650–656.

[106] Banik, M.; El-Khoury, P. Z.; Nag, A.; Rodriguez-Perez, A.; Guarrottxena, N.; Bazan, G. C.; Apkarian, V. A. *ACS Nano* **2012**, *6*, 10343–10354.

[107] Payton, J. L.; Morton, S. M.; Moore, J. E.; Jensen, L. *Acc. Chem. Res.* **2014**, *47*, 88–99.

[108] Osawa, M.; Matsuda, N.; Yoshii, K.; Uchida, I. *J. Phys. Chem.* **1994**, *98*, 12702–12707.

[109] Wu, D.-Y.; Liu, X.-M.; Huang, Y.-F.; Ren, B.; Xu, X.; Tian, Z.-Q. *J. Phys. Chem. C* **2009**, *113*, 18212–18222.

[110] Huang, Y.-F.; Zhu, H.-P.; Liu, G.-K.; Wu, D.-Y.; Ren, B.; Tian, Z.-Q. *J. Am. Chem. Soc.* **2010**, *132*, 9244–9246.

[111] Zhao, L. L.; Jensen, L.; Schatz, G. C. *Nano Lett.* **2006**, *6*, 1229–1234.

[112] Jensen, L.; Zhao, L. L.; Schatz, G. C. *J. Phys. Chem. C* **2007**, *111*, 4756–4764.

[113] King, F. W.; Duyne, R. P. V.; Schatz, G. C. *J. Chem. Phys.* **1978**, *69*, 4472–4481.

[114] Moskovits, M. *J. Chem. Phys.* **1978**, *69*, 4159–4161.

[115] Moskovits, M. *Solid State Commun.* **1979**, *32*, 59–62.

[116] Kerker, M.; Wang, D.-S.; Chew, H. *Appl. Opt.* **1980**, *19*, 4159–4174.

[117] Gersten, J. I. *J. Chem. Phys.* **1980**, *72*, 5779–5780.

[118] Gersten, J. I. *J. Chem. Phys.* **1980**, *72*, 5780–5781.

[119] Gersten, J.; Nitzan, A. *J. Chem. Phys.* **1980**, *73*, 3023–3037.

[120] Le Ru, E. C.; Etchegoin, P. G. *Principles of Surface-Enhanced Raman Spectroscopy*; Elsevier, 2009.

[121] Silberstein, L. *Philos. Mag.* **1917**, *33*, 521–533.

[122] Jensen, L.; Astrand, P.; Osted, A.; Kongsted, J.; Mikkelsen, K. *J. Chem. Phys.* **2002**, *116*, 4001–4010.

[123] Morton, S. M.; Jensen, L. *J. Chem. Phys.* **2010**, *133*, 074103.

[124] Chulhai, D. V.; Jensen, L. *J. Phys. Chem. A* **2014**, *118*, 9069–9079.

[125] Efrima, S.; Metiu, H. *J. Chem. Phys.* **1979**, *70*, 1602–1613.

[126] Efrima, S.; Metiu, H. *J. Chem. Phys.* **1979**, *70*, 1939–1947.

[127] Efrima, S.; Metiu, H. *J. Chem. Phys.* **1979**, *70*, 2297–2309.

[128] Litz, J. P.; Brewster, R. P.; Lee, A. B.; Masiello, D. J. *J. Phys. Chem. C* **2013**, *117*, 12249–12257.

[129] Masiello, D. J. *Int. J. Quantum Chem.* **2014**, *114*, 1413–1420.

[130] Corni, S.; Tomasi, J. *J. Chem. Phys.* **2001**, *114*, 3739–3751.

[131] Corni, S.; Tomasi, J. *J. Chem. Phys.* **2002**, *117*, 7266–7278.

[132] Corni, S.; Tomasi, J. *J. Chem. Phys.* **2002**, *116*, 1156–1164.

[133] Jørgensen, S.; Ratner, M. A.; Mikkelsen, K. V. *J. Chem. Phys.* **2001**, *115*, 3792–3803.

[134] Neuhauser, D.; Lopata, K. *J. Chem. Phys.* **2007**, *127*, 154715.

[135] Lopata, K.; Neuhauser, D. *J. Chem. Phys.* **2009**, *130*, 104707.

[136] Arcisauskaite, V.; Kongsted, J.; Hansen, T.; Mikkelsen, K. V. *Chem. Phys. Lett.* **2009**, *470*, 285–288.

[137] Masiello, D. J.; Schatz, G. C. *Phys. Rev. A* **2008**, *78*, 042505.

[138] Masiello, D. J.; Schatz, G. C. *J. Chem. Phys.* **2010**, *132*, 064102.

[139] Chen, H.; McMahon, J. M.; Ratner, M. A.; Schatz, G. C. *J. Phys. Chem. C* **2010**, *114*, 14384–14392.

[140] Watson, M. A.; Rappoport, D.; Lee, E. M. Y.; Olivares-Amaya, R.; Aspuru-Guzik, A. *J. Chem. Phys.* **2012**, *136*, 024101–14.

[141] Jensen, L. L.; Jensen, L. *J. Phys. Chem. C* **2008**, *112*, 15697–15703.

[142] Jensen, L. L.; Jensen, L. *J. Phys. Chem. C* **2009**, *113*, 15182–15190.

[143] Morton, S. M.; Jensen, L. *J. Chem. Phys.* **2011**, *135*, 134103.

[144] Payton, J. L.; Morton, S. M.; Moore, J. E.; Jensen, L. *J. Chem. Phys.* **2012**, *136*, 214103.

[145] Thomas, L. H. *Math. Proc. Cambridge Philos. Soc.* **1927**, *23*, 542–548.

[146] Fermi, E. *Z. Phys.* **1928**, *48*, 9.

[147] Hohenberg, P.; Kohn, W. *Phys. Rev.* **1964**, *136*, B864–B871.

[148] Kohn, W.; Sham, L. J. *Phys. Rev.* **1965**, *140*, A1133–A1138.

[149] Parr, R. G.; Yang, W. In *Density-Functional Theory of Atoms and Molecules*; Breslow, R., Goodenough, J. B., Halpern, J., Rowlinson, J. S., Eds.; International Series of Monographs on Chemistry; Oxford Science Publications: New York, NY, 1989; Vol. 16.

[150] Perdew, J. P.; Zunger, A. *Phys. Rev. B* **1981**, *23*, 5048.

[151] Vosko, S. H.; Wilk, L.; Nusair, M. *Can. J. Phys.* **1980**, *58*, 1200–1211.

[152] Perdew, J. P.; Wang, Y. *Phys. Rev. B* **1992**, *45*, 13244–13249.

[153] Becke, A. D. *Phys. Rev. A* **1988**, *38*, 3098–3100.

[154] Perdew, J. P. *Phys. Rev. B* **1986**, *33*, 8822–8824.

[155] Lee, C.; Yang, W.; Parr, R. G. *Phys. Rev. B* **1988**, *37*, 785–789.

[156] Miehlich, B.; Savin, A.; Stoll, H.; Preuss, H. *Chem. Phys. Lett.* **1989**, *157*, 200 – 206.

[157] Perdew, J. P.; Burke, K.; Ernzerhof, M. *Phys. Rev. Lett.* **1996**, *77*, 3865–3868.

[158] Scuseria, G. E.; Staroverov, V. N. In *Theory and Application of Computational Chemistry: The First 40 Years*; Dykstra, C., Frenking, G., Kim, K., Scuseria, G., Eds.; Elsevier: Amsterdam, 2005; Chapter Progress in the development of exchange-correlation functionals, p 669.

[159] Perdew, J. P.; Schmidt, K. *AIP Conf. Proc.* **2001**, *577*, 1–20.

[160] Casida, M. E. *ACS Symposium Series*; American Chemical Society, 2002; Vol. 828; pp 199–220.

[161] Casida, M.; Huix-Rotllant, M. *Ann. Rev. Phys. Chem.* **2012**, *63*, 287–323.

[162] Johnson, B. G.; Gill, P. M. W.; Pople, J. A. *J. Chem. Phys.* **1993**, *98*, 5612–5626, journal article.

[163] Jang, Y. H.; Hwang, S.; Kim, Y.-H.; Jang, S. S.; Goddard, W. A. *J. Am. Chem. Soc.* **2004**, *126*, 12636.

[164] Jacquemin, D.; Planchat, A.; Adamo, C.; Mennucci, B. *J. Chem. Theor. Comput.* **2012**, *8*, 2359–2372.

[165] te Velde, G.; Bickelhaupt, F. M.; Baerends, E. J.; Fonseca Guerra, C.; van Gisbergen, S. J. A.; Snijders, J. G.; Ziegler, T. *J. Comput. Chem.* **2001**, *22*, 931–967.

[166] Stratmann, R. E.; Scuseria, G. E.; Frisch, M. J. *J. Chem. Phys.* **1998**, *109*, 8218–8224.

[167] Lange, A. W.; Herbert, J. M. *J. Am. Chem. Soc.* **2009**, *131*, 3913.

[168] Barngrover, B. M.; Aikens, C. M. *J. Am. Chem. Soc.* **2012**, *134*, 12590–12595.

[169] Johnson, H. E.; Aikens, C. M. *J. Phys. Chem. A* **2009**, *113*, 4445.

[170] Rohrdanz, M. A.; Martins, K. M.; Herbert, J. M. *J. Chem. Phys.* **2009**, *130*, 054112.

[171] Johnson, E. R.; Keinan, S.; Mori-Sánchez, P.; Contreras-Garciá, J.; Cohen, A. J.; Yang, W. *J. Am. Chem. Soc.* **2010**, *132*, 6498–6506.

[172] Senn, H. M.; Thiel, W. *Angew. Chem., Int. Edit.* **2009**, *48*, 1198–1229.

[173] Chung, L. W.; Hirao, H.; Li, X.; Morokuma, K. *Wiley Interdiscip. Rev.: Comput. Mol. Sci.* **2012**, *2*, 327–350.

[174] Mennucci B, C. R., Ed. *Continuum Solvation Models in Chemical Physics: From Theory to Application*; John Wiley and Sons Ltd.: New York, 2007.

[175] Senatore, G.; Subbaswamy, K. R. *Phys. Rev. B* **1986**, *34*, 5754–5757.

[176] Johnson, M. D.; Subbaswamy, K. R.; Senatore, G. *Phys. Rev. B* **1987**, *36*, 9202–9211.

[177] Cortona, P. *Phys. Rev. B* **1991**, *44*, 8454–8458.

[178] Jacob, C. R.; Neugebauer, J. *Wiley Interdiscip. Rev.: Comput. Mol. Sci.* **2014**, *4*, 325–362.

[179] Wesolowski, T. A.; Warshel, A. *J. Phys. Chem.* **1993**, *97*, 8050–8053.

[180] Gritsenko, O. V.; Visscher, L. *Phys. Rev. A* **2010**, *82*, 032519.

[181] Gritsenko, O. V. *Recent Advances in Computational Chemistry*; World Scientific, 2012; Vol. Volume 6; pp 355–365.

[182] Wesolowski, T. A. *Phys. Rev. A* **2008**, *77*, 012504.

[183] Wesolowski, T. A.; Savin, A. *Recent Advances in Computational Chemistry*; World Scientific, 2012; Vol. Volume 6; pp 275–295.

[184] Götz, A. W.; Beyhan, S. M.; Visscher, L. *J. Chem. Theor. Comput.* **2009**, *5*, 3161–3174.

[185] Lembarki, A.; Chermette, H. *Phys. Rev. A* **1994**, *50*, 5328–5331.

[186] Wesolowski, T. A.; Chermette, H.; Weber, J. *J. Chem. Phys.* **1996**, *105*, 9182–9190.

[187] Fux, S.; Kiewisch, K.; Jacob, C. R.; Neugebauer, J.; Reiher, M. *Chem. Phys. Lett.* **2008**, *461*, 353–359.

[188] Fux, S.; Jacob, C. R.; Neugebauer, J.; Visscher, L.; Reiher, M. *J. Chem. Phys.* **2010**, *132*, 164101.

[189] Artiukhin, D. G.; Jacob, C. R.; Neugebauer, J. *J. Chem. Phys.* **2015**, *142*, 234101.

[190] Khait, Y. G.; Hoffmann, M. R. In *Annu. Rep. Comput. Chem.*; Wheeler, R. A., Ed.; Elsevier, 2012; Vol. 8; Chapter 3, pp 53–70.

[191] Tamukong, P. K.; Khait, Y. G.; Hoffmann, M. R. *J. Phys. Chem. A* **2014**, *118*, 9182–9200.

[192] Lykos, P. G.; Parr, R. G. *J. Chem. Phys.* **1956**, *24*, 1166–1173.

[193] Barandiarán, Z.; Seijo, L. *J. Chem. Phys.* **1988**, *89*, 5739–5746.

[194] Phillips, J. C.; Kleinman, L. *Phys. Rev.* **1959**, *116*, 287–294.

[195] Stoll, H.; Paulus, B.; Fulde, P. *J. Chem. Phys.* **2005**, *123*, 144108.

[196] Mata, R. A.; Werner, H.-J.; Schütz, M. *J. Chem. Phys.* **2008**, *128*, 144106.

[197] Henderson, T. M. *J. Chem. Phys.* **2006**, *125*, 014105.

[198] Manby, F. R.; Stella, M.; Goodpaster, J. D.; Miller, T. F. *J. Chem. Theor. Comput.* **2012**, *8*, 2564–2568.

[199] Barnes, T. A.; Goodpaster, J. D.; Manby, F. R.; Miller, T. F. *J. Chem. Phys.* **2013**, *139*, 024103.

[200] Goodpaster, J. D.; Barnes, T. A.; Manby, F. R.; Miller, T. F. *J. Chem. Phys.* **2014**, *140*, 18A507.

[201] Runge, E.; Gross, E. K. U. *Phys. Rev. Lett.* **1984**, *52*, 997–1000.

[202] Rosa, A.; Ricciardi, G.; Gritsenko, O.; Baerends, E. J. *Principles and Applications of Density Functional Theory in Inorganic Chemistry I*; Springer Berlin Heidelberg: Berlin, Heidelberg, 2004; Chapter Excitation Energies of Metal Complexes with Time-dependent Density Functional Theory, pp 49–116.

[203] Autschbach, J.; Ziegler, T. *Coord. Chem. Rev.* **2003**, *238/239*, 83 – 126, Theoretical and Computational Chemistry.

[204] Casida, M. E.; Wesolowski, T. A. *Int. J. Quantum Chem.* **2004**, *96*, 577–588.

[205] Wesolowski, T. A. *J. Am. Chem. Soc.* **2004**, *126*, 11444–11445.

[206] Neugebauer, J. *J. Chem. Phys.* **2007**, *126*, 134116.

[207] Neugebauer, J.; Louwerse, M. J.; Baerends, E. J.; Wesolowski, T. A. *J. Chem. Phys.* **2005**, *122*, 094115.

[208] Neugebauer, J.; Jacob, C. R.; Wesolowski, T. A.; Baerends, E. J. *J. Phys. Chem. A* **2005**, *109*, 7805–7814.

[209] Jacob, C. R.; Neugebauer, J.; Jensen, L.; Visscher, L. *Phys. Chem. Chem. Phys.* **2006**, *8*, 2349–2359.

[210] Neugebauer, J.; Baerends, E. J. *J. Phys. Chem. A* **2006**, *110*, 8786–8796.

[211] Iozzi, M. F.; Mennucci, B.; Tomasi, J.; Cammi, R. *J. Chem. Phys.* **2004**, *120*, 7029–7040.

[212] Hsu, C.-P.; Fleming, G. R.; Head-Gordon, M.; Head-Gordon, T. *J. Chem. Phys.* **2001**, *114*, 3065–3072.

[213] Le Ru, E. C.; Etchegoin, P. G. *Chem. Phys. Lett.* **2006**, *423*, 63–66.

[214] Feibelman, P. J. *Phys. Rev. B* **1975**, *12*, 1319–1336.

[215] Janesko, B. G.; Scuseria, G. E. *J. Chem. Phys.* **2006**, *125*, 124704.

[216] Ayars, E. J.; Hallen, H. D.; Jahncke, C. L. *Phys. Rev. Lett.* **2000**, *85*, 4180–4183.

[217] Hallen, H. D.; Jahncke, C. L. *J. Raman Spectrosc.* **2003**, *34*, 655–662.

[218] Aikens, C. M.; Madison, L. R.; Schatz, G. C. *Nat. Photonics* **2013**, *7*, 508–510.

[219] Takase, M.; Ajiki, H.; Mizumoto, Y.; Komeda, K.; Nara, M.; Nabika, H.; Yasuda, S.; Ishihara, H.; Murakoshi, K. *Nat. Photonics* **2013**, *7*, 550–554.

[220] Gao, X.; Davies, J. P.; Weaver, M. J. *J. Phys. Chem.* **1990**, *94*, 6858–6864.

[221] García de Abajo, F. J. *J. Phys. Chem. C* **2008**, *112*, 17983.

[222] Halas, N. J.; Lal, S.; Chang, W.-S.; Link, S.; Nordlander, P. *Chem. Rev.* **2011**, *111*, 3913–3961.

[223] Toscano, G.; Raza, S.; Xiao, S.; Wubs, M.; Jauho, A.-P.; Bozhevolnyi, S. I.; Mortensen, N. A. *Opt. Lett.* **2012**, *37*, 2538–2540.

[224] Baerends, E. et al. Amsterdam Density Functional. 2008; `http://www.scm.com`.

[225] Zhao, L.; Jensen, L.; Schatz, G. C. *J. Am. Chem. Soc.* **2006**, *128*, 2911–2919.

[226] Jensen, L.; Autschbach, J.; Schatz, G. C. *J. Chem. Phys.* **2005**, *122*, 224115.

[227] Johnson, P. B.; Christy, R. W. *Phys. Rev. B* **1972**, *6*, 4370–4379.

[228] Lund, P.; Smardzewski, R.; Tevault, D. *Chem. Phys. Lett.* **1982**, *89*, 508 – 510.

[229] Krasser, W.; Ervens, H.; Fadini, A.; Renouprez, A. J. *J. Raman Spectrosc.* **1980**, *9*, 80–84.

[230] Lund, P. A.; Tevault, D. E.; Smardzewski, R. R. *J. Phys. Chem.* **1984**, *88*, 1731–1735.

[231] Demuth, J. E.; Christmann, K.; Sanda, P. N. *Chem. Phys. Lett.* **1980**, *76*, 201–206.

[232] Bader, M.; Haase, J.; Frank, K.-H.; Puschmann, A.; Otto, A. *Phys. Rev. Lett.* **1986**, *56*, 1921–1924.

[233] Lee, J.-G.; Ahner, J.; Yates, Jr, J. T. *J. Chem. Phys.* **2001**, *114*, 1414–1419.

[234] Dougherty, D. B.; Lee, J.; Yates, J. T. *J. Phys. Chem. B* **2006**, *110*, 11991–11996.

[235] Hahn, J. R.; Ho, W. *J. Chem. Phys.* **2006**, *124*, 204708.

[236] Hou, J. Q.; Kang, H. S.; Kim, K. W.; Hahn, J. R. *J. Chem. Phys.* **2008**, *128*, 134707.

[237] Creighton, J. A.; Albrecht, M. G.; Hester, R. E.; Matthew, J. A. D. *Chem. Phys. Lett.* **1978**, *55*, 55–58.

[238] Krasser, W.; Kettler, U.; Bechthold, P. S. *Chem. Phys. Lett.* **1982**, *86*, 223–227.

[239] Clark, R. J. H.; Williams, C. S. *Inorg. Chem.* **1965**, *4*, 350–357.

[240] Creighton, J. *Surf. Sci.* **1983**, *124*, 209 – 219.

[241] Arenas, J. F.; Lopez Tocon, I.; Otero, J. C.; Marcos, J. I. *J. Phys. Chem.* **1996**, *100*, 9254–9261.

[242] Creighton, J. *Surf. Sci.* **1986**, *173*, 665 – 672.

[243] Moore, J. E.; Morton, S. M.; Jensen, L. *J. Phys. Chem. Lett.* **2012**, *3*, 2470–2475.

[244] Mullin, J. M.; Autschbach, J.; Schatz, G. C. *Comput. Theor. Chem.* **2012**, *987*, 32–41.

[245] Kedziora, G. S.; Schatz, G. C. *Spectrochim. Acta A* **1999**, *55*, 625–638.

[246] Otto, A. In *Light Scattering in Solids IV: Electronics Scattering, Spin Effects, SERS, and Morphic Effects*; Cardona, M., Güntherodt, G., Eds.; Top. Appl. Phys.; Springer, Berlin/Heidelberg, 1984; Vol. 54; pp 289–418.

[247] Schatz, G. C.; Van Duyne, R. P. In *Handbook of Vibrational Spectroscopy*; Chalmers, J. M., Griffiths, P. R., Eds.; John Wiley and Sons, Ltd: New York, 2002; Vol. 1; pp 759–774.

[248] Chulhai, D. V.; Hu, Z.; Moore, J. E.; Chen, X.; Jensen, L. *Ann. Rev. Phys. Chem.* **2016**, *67*, 541–564.

[249] Xu, H.; Wang, X.-H.; Persson, M. P.; Xu, H. Q.; Käll, M.; Johansson, P. *Phys. Rev. Lett.* **2004**, *93*, 243002.

[250] Jiang,; Bosnick, K.; Maillard, M.; Brus, L. *J. Phys. Chem. B* **2003**, *107*, 9964–9972.

[251] Morton, S. M.; Jensen, L. *J. Am. Chem. Soc.* **2009**, *131*, 4090–4098.

[252] Saikin, S. K.; Chu, Y.; Rappoport, D.; Crozier, K. B.; Aspuru-Guzik, A. *J. Phys. Chem. Lett.* **2010**, *1*, 2740–2746.

[253] Vukovic, S.; Corni, S.; Mennucci, B. *J. Phys. Chem. C* **2009**, *113*, 121–133.

[254] Weiss, A.; Haran, G. *J. Phys. Chem. B* **2001**, *105*, 12348–12354.

[255] Futamata, M.; Maruyama, Y.; ; Ishikawa, M. *J. Phys. Chem. B* **2004**, *108*, 13119–13127.

[256] Haran, G. *Acc. Chem. Res.* **2010**, *43*, 1135–1143.

[257] Maher, R. C.; Dalley, M.; Le Ru, E. C.; Cohen, L. F.; Etchegoin, P. G.; Hartigan, H.; Brown, R. J. C.; Milton, M. J. T. *J. Chem. Phys.* **2004**, *121*, 8901–8910.

[258] Chulhai, D. V.; Jensen, L. *J. Phys. Chem. C* **2013**, *117*, 19622–19631.

[259] Plimpton, S. *J. Comput. Phys.* **1995**, *117*, 1–19.

[260] http://lammps.sandia.gov.

[261] Wang, J.; Wolf, R. M.; Caldwell, J. W.; Kollman, P. A.; Case, D. A. *J. Comput. Chem.* **2004**, *25*, 1157–1174.

[262] Wang, J.; Wang, W.; Kollman, P. A.; Case, D. A. *J. Mol. Graph. Mod.* **2006**, *25*, 247–260.

[263] Grochola, G.; Snook, I. K.; Russo, S. P. *J. Chem. Phys.* **2007**, *127*, 194707.

[264] Zhou, Y.; Saidi, W. A.; Fichthorn, K. A. *J. Phys. Chem. C* **2014**, *118*, 3366–3374.

[265] Grimme, S. *J. Comput. Chem.* **2006**, *27*, 1787.

[266] Hinterwirth, H.; Kappel, S.; Waitz, T.; Prohaska, T.; Lindner, W.; Lämmerhofer, M. *ACS Nano* **2013**, *7*, 1129–1136.

[267] Chen, X.; Moore, J.; Zekarias, M.; Jensen, L. *Nature Comm.* **2015**, 8921.

[268] Purcell, E. M.; Pennypacker, C. R. *Astrophys. J.* **1973**, *186*, 705–714.

[269] Draine, B. T.; Flatau, P. J. *J. Opt. Soc. Am. A* **1994**, *11*, 1491–1499.

[270] Mayer, A. *Phys. Rev. B* **2007**, *75*, 045407.

[271] van Lenthe, E.; Baerends, E. J.; Snijders, J. G. *J. Chem. Phys.* **1993**, *99*, 4597–4610.

[272] van Lenthe, E.; Baerends, E. J.; Snijders, J. G. *J. Chem. Phys.* **1994**, *101*, 9783–9792.

[273] van Lenthe, E.; Ehlers, A.; Baerends, E.-J. *J. Chem. Phys.* **1999**, *110*, 8943–8953.

[274] Grimme, S.; Antony, J.; Ehrlich, S.; Krieg, H. *J. Chem. Phys.* **2010**, *132*, 154104.

[275] Birke, R. L.; Znamenskiy, V.; Lombardi, J. R. *J. Chem. Phys.* **2010**, *132*, 214707.

[276] El-Khoury, P. Z.; Hu, D.; Hess, W. P. *J. Phys. Chem. Lett.* **2013**, *4*, 3435–3439.

[277] Le Ru, E. C.; Etchegoin, P. G.; Meyer, M. *J. Chem. Phys.* **2006**, *125*, 204701.

[278] Fang, Y.; Seong, N.-H.; Dlott, D. D. *Science* **2008**, *321*, 388–392.

[279] Scholl, J. A.; Koh, A. L.; Dionne, J. A. *Nature* **2012**, *483*, 421–427.

[280] Zhu, W.; Crozier, K. B. *Nature Comm.* **2014**, *5*, 5228.

[281] Savage, K. J.; Hawkeye, M. M.; Esteban, R.; Borisov, A. G.; Aizpurua, J.; Baumberg, J. J. *Nature* **2012**, *491*, 574–577.

[282] Esteban, R.; Borisov, A. G.; Nordlander, P.; Aizpurua, J. *Nature Comm.* **2012**, *3*, 825.

[283] Tiggesbäumker, J.; Köller, L.; Meiwes-Broer, K.-H.; Liebsch, A. *Phys. Rev. A* **1993**, *48*, 1749.

[284] Liebsch, A. *Phys. Rev. B* **1993**, *48*, 11317–11328.

[285] Mortensen, N. A.; Raza, S.; Wubs, M.; Søndergaard, T.; Bozhevolnyi, S. I. *Nature Comm.* **2014**, *5*, 3809.

[286] Barron, L. D.; Buckingham, A. D. *Chem. Phys. Lett.* **2010**, *492*, 199–213.

[287] Barron, L. D.; Hecht, L.; McColl, I. H.; Blanch, E. W. *Mol. Phys.* **2004**, *102*, 731–744.

[288] Pecul, M. *Chirality* **2009**, *21*, E98–E104.

[289] Atkins, P.; Barron, L. *Mol. Phys.* **1969**, *16*, 453–466.

[290] Buckingham, A. D.; Dunn, M. B. *J. Chem. Soc. A* **1971**, 1988–1991.

[291] Barron, L.; Buckingham, A. *Mol. Phys.* **1971**, *20*, 1111–1119.

[292] Barron, L. D.; Bogaard, M. P.; Buckingham, A. D. *J. Am. Chem. Soc.* **1973**, *95*, 603–605.

[293] Hug, W.; Kint, S.; Bailey, G. F.; Scherer, J. R. *J. Am. Chem. Soc.* **1975**, *97*, 5589–5590.

[294] Polavarapu, P. L. *Chirality* **2008**, *20*, 664–672.

[295] Chruszcz-Lipska, K.; Blanch, E. W. In *Optical Spectroscopy and Computational Methods in Biology and Medicine*; Baranska, M., Ed.; Challenges and Advances in Computational Chemistry and Physics; Springer Netherlands, 2014; Vol. 14; Chapter 4, pp 61–81.

[296] Abdali, S. *J. Raman Spectrosc.* **2006**, *37*, 1341–1345.

[297] Abdali, S.; Johannessen, C.; Nygaard, J.; Nørbygaard, T. *J. Phys.: Condens. Matter* **2007**, *19*, 285205.

[298] Johannessen, C.; White, P. C.; Abdali, S. *J. Phys. Chem. A* **2007**, *111*, 7771–7776.

[299] Abdali, S.; Blanch, E. W. *Chem. Soc. Rev.* **2008**, *37*, 980–992.

[300] Osinska, K.; Pecul, M.; Kudelski, A. *Chem. Phys. Lett.* **2010**, *496*, 86–90.

[301] Sun, M.; Zhang, Z.; Wang, P.; Li, Q.; Ma, F.; Xu, H. *Light: Sci. & Appl.* **2013**, *2*, e112.

[302] Efrima, S. *Chem. Phys. Lett.* **1983**, *102*, 79–82.

[303] Efrima, S. *J. Chem. Phys.* **1985**, *83*, 1356–1362.

[304] Hecht, L.; Barron, L. D. *Chem. Phys. Lett.* **1994**, *225*, 519–524.

[305] Hecht, L.; Barron, L. *J. Mol. Struct.: THEOCHEM* **1995**, *348*, 217–220, Molecular Spectroscopy and Molecular Structure 1994.

[306] Bouř, P. *J. Chem. Phys.* **2007**, *126*, 136101.

[307] Novák, V.; Šebestík, J.; Bouř, P. *J. Chem. Theor. Comput.* **2012**, *8*, 1714–1720.

[308] Acevedo, R.; Lombardini, R.; Halas, N. J.; Johnson, B. R. *J. Phys. Chem. A* **2009**, *113*, 13173–13183.

[309] Lombardini, R.; Acevedo, R.; Halas, N. J.; Johnson, B. R. *J. Phys. Chem. C* **2010**, *114*, 7390–7400.

[310] Jensen, L. *J. Phys. Chem. A* **2009**, *113*, 4437–4444.

[311] Janesko, B. G.; Scuseria, G. E. *J. Phys. Chem. C* **2009**, *113*, 9445–9449.

[312] Rinaldi, J. M.; Morton, S. M.; Jensen, L. *Mol. Phys.* **2013**, *111*, 1322–1331.

[313] Barron, L. D. In *Molecular Light Scattering and Optical Activity*, 2nd ed.; Barron, L. D., Ed.; Cambridge University Press, 2004.

[314] Nafie, L. A. *Vibrational Optical Activity: Principles and Applications*; John Wiley & Sons, Ltd, 2011; Chapter 5, pp 131–167.

[315] Schulman, J. M.; Detrano, R.; Musher, J. I. *Phys. Rev. A* **1972**, *5*, 1125–1131.

[316] Schulman, J. M.; Detrano, R. *Phys. Rev. A* **1974**, *10*, 1192–1197.

[317] Schulman, J. M.; Lee, W. S. *J. Chem. Phys.* **1981**, *74*, 4930–4935.

[318] Lee, S. *J. Chem. Phys.* **1982**, *76*, 3064–3074.

[319] Lee, S.-Y. *J. Chem. Phys.* **1983**, *78*, 723–734.

[320] London, F. *J. Phys. Radium* **1937**, *8*, 397–409.

[321] Helgaker, T.; Jørgensen, P. *J. Chem. Phys.* **1991**, *95*, 2595–2601.

[322] Bak, K. L.; Hansen, A. E.; Ruud, K.; Helgaker, T.; Olsen, J.; Jørgensen, P. *Theor. Chim. Acta* **1995**, *90*, 441–458.

[323] Olsen, J.; Jørgensen, P. *J. Chem. Phys.* **1985**, *82*, 3235–3264.

[324] Krykunov, M.; Autschbach, J. *J. Chem. Phys.* **2007**, *126*, 24101.

[325] Pedersen, T. B.; Koch, H.; Boman, L.; Sanchez de Meras, A. M. *Chem. Phys. Lett.* **2004**, *393*, 319–326.

[326] Fonseca Guerra, C.; Snijders, J. G.; te Velde, G.; Baerends, E. J. *Theor. Chem. Acc.* **1998**, *99*, 391–403.

[327] Johannessen, C.; Blanch, E. W.; Villani, C.; Abbate, S.; Longhi, G.; Agarwal, N. R.; Tommasini, M.; Lightner, D. A. *J. Phys. Chem. B* **2013**, *117*, 2221–2230.

[328] Greenfield, N. J. *Nat. Protoc.* **2007**, *1*, 2876–2890.

[329] Manning, M. C.; Woody, R. W. *Biopolymers* **1991**, *31*, 569–586.

[330] Formaggio, F.; Peggion, C.; Crisma, M.; Kaptein, B.; Broxterman, Q. B.; Mazaleyrat, J.-P.; Wakselman, M.; Toniolo, C. *Chirality* **2004**, *16*, 388–397.

[331] Oh, H. S.; Liu, S.; Jee, H.; Baev, A.; Swihart, M. T.; Prasad, P. N. *J. Am. Chem. Soc.* **2010**, *132*, 17346–17348.

[332] Gansel, J. K.; Thiel, M.; Rill, M. S.; Decker, M.; Bade, K.; Saile, V.; von Freymann, G.; Linden, S.; Wegener, M. *Science* **2009**, *325*, 1513–1515.

[333] Pendry, J. B. *Science* **2004**, *306*, 1353–1355.

[334] Ben-Moshe, A.; Maoz, B. M.; Govorov, A. O.; Markovich, G. *Chem. Soc. Rev.* **2013**, *42*, 7028–7041.

[335] Wang, Y.; Xu, J.; Wang, Y.; Chen, H. *Chem. Soc. Rev.* **2013**, *42*, 2930–2962.

[336] Kuzyk, A.; Schreiber, R.; Fan, Z.; Pardatscher, G.; Roller, E.-M.; Hogele, A.; Simmel, F. C.; Govorov, A. O.; Liedl, T. *Nature* **2012**, *483*, 311–314.

[337] Slocik, J. M.; Govorov, A. O.; Naik, R. R. *Nano Lett.* **2011**, *11*, 701–705.

[338] Maoz, B. M.; Chaikin, Y.; Tesler, A. B.; Bar Elli, O.; Fan, Z.; Govorov, A. O.; Markovich, G. *Nano Lett.* **2013**, *13*, 1203–1209.

[339] Govorov, A. O.; Fan, Z.; Hernandez, P.; Slocik, J. M.; Naik, R. R. *Nano Lett.* **2010**, *10*, 1374–1382.

[340] Govorov, A. O. *J. Phys. Chem. C* **2011**, *115*, 7914–7923.

[341] Li, X.; Rinkevicius, Z.; Ågren, H. *J. Phys. Chem. C* **2014**, *118*, 5833–5840.

[342] Krykunov, M.; Kundrat, M. D.; Autschbach, J. *J. Chem. Phys.* **2006**, *125*, 194110.

[343] Baerends, E. et al. Amsterdam Density Functional. 2013; `http://www.scm.com`.

[344] Jacob, C. R.; Luber, S.; Reiher, M. *J. Phys. Chem. B* **2009**, *113*, 6558–6573.

[345] Holzwarth, G.; Doty, P. *J. Am. Chem. Soc.* **1965**, *87*, 218–228.

[346] Dreuw, A.; Head-Gordon, M. *J. Am. Chem. Soc.* **2003**, *126*, 4007–4016.

[347] Kaminský, J.; Kubelka, J.; Bouř, P. *J. Phys. Chem. A* **2011**, *115*, 1734–1742.

[348] Toniolo, C.; Polese, A.; Formaggio, F.; Crisma, M.; Kamphuis, J. *J. Am. Chem. Soc.* **1996**, *118*, 2744–2745.

[349] Gordon, M. S.; Fedorov, D. G.; Pruitt, S. R.; Slipchenko, L. V. *Chem. Rev.* **2012**, *112*, 632–672.

[350] Warshel, A.; Levitt, M. *J. Mol. Biol.* **1976**, *103*, 227–249.

[351] Lin, H.; Truhlar, D. *Theor. Chem. Acc.* **2007**, *117*, 185–199.

[352] Bernard, Y. A.; Dulak, M.; Kaminski, J. W.; Wesolowski, T. A. *J. Phys. A: Math. Gen.* **2008**, *41*, 055302.

[353] Jacob, C. R.; Neugebauer, J.; Visscher, L. *J. Comput. Chem.* **2008**, *29*, 1011–1018.

[354] Jacob, C. R.; Beyhan, S. M.; Bulo, R. E.; Gomes, A. S. P.; Götz, A. W.; Kiewisch, K.; Sikkema, J.; Visscher, L. *J. Comput. Chem.* **2011**, *32*, 2328–2338.

[355] Jacob, C. R.; Visscher, L. *J. Chem. Phys.* **2008**, *128*, 155102.

[356] Beyhan, S. M.; Götz, A. W.; Jacob, C. R.; Visscher, L. *J. Chem. Phys.* **2010**, *132*, 044114.

[357] Kiewisch, K.; Eickerling, G.; Reiher, M.; Neugebauer, J. *J. Chem. Phys.* **2008**, *128*, 044114.

[358] Olsen, J. M. H.; Steinmann, C.; Ruud, K.; Kongsted, J. *J. Phys. Chem. A* **2015**, *119*, 5344–5355.

[359] Chulhai, D. V.; Jensen, L. *J. Chem. Theor. Comput.* **2015**, *11*, 3080–3088.

[360] Baerends, E. et al. Amsterdam Density Functional. 2014.

[361] Van Lenthe, E.; Baerends, E. J. *J. Comput. Chem.* **2003**, *24*, 1142–1156.

[362] Jacob, C. R.; Beyhan, S. M.; Visscher, L. *J. Chem. Phys.* **2007**, *126*, 234116.

[363] Hager, J.; Wallace, S. C. *J. Phys. Chem.* **1985**, *89*, 3833–3841.

[364] Auwarter, W.; Ecija, D.; Klappenberger, F.; Barth, J. V. *Nat. Chem.* **2015**, *7*, 105–120.

[365] Barlow, D. E.; Scudiero, L.; Hipps, K. W. *Langmuir* **2004**, *20*, 4413–4421.

[366] Buchner, F.; Schwald, V.; Comanici, K.; Steinrück, H.-P.; Marbach, H. *Comput. Phys. Commun.* **2007**, *8*, 241–243.

[367] Qiu, X.; Wang, C.; Zeng, Q.; Xu, B.; Yin, S.; Wang, H.; Xu, S.; Bai, C. *J. Am. Chem. Soc.* **2000**, *122*, 5550–5556.

[368] Scudiero, L.; Barlow, D. E.; Mazur, U.; Hipps, K. W. *J. Am. Chem. Soc.* **2001**, *123*, 4073–4080.

[369] Suto, K.; Yoshimoto, S.; Itaya, K. *J. Am. Chem. Soc.* **2003**, *125*, 14976–14977.

[370] Yokoyama, T.; Yokoyama, S.; Kamikado, T.; Okuno, Y.; Mashiko, S. *Nature* **2001**, *413*, 619–621.

[371] Joshi, S.; Bischoff, F.; Koitz, R.; Ecija, D.; Seufert, K.; Seitsonen, A. P.; Hutter, J.; Diller, K.; Urgel, J. I.; Sachdev, H.; Barth, J. V.; AuwÃďrter, W. *ACS Nano* **2014**, *8*, 430–442.

[372] Phan, T. H.; Wandelt, K. *Surf. Sci.* **2013**, *607*, 82–91.

[373] Heim, D.; Écija, D.; Seufert, K.; Auwärter, W.; Aurisicchio, C.; Fabbro, C.; Bonifazi, D.; Barth, J. V. *J. Am. Chem. Soc.* **2010**, *132*, 6783–6790.

[374] Yang, Y.; Wang, C. *Chem. Soc. Rev.* **2009**, *38*, 2576–2589.

[375] Kudernac, T.; Lei, S.; Elemans, J. A. A. W.; De Feyter, S. *Chem. Soc. Rev.* **2009**, *38*, 402–421.

[376] Sedona, F.; Di Marino, M.; Basagni, A.; Colazzo, L.; Sambi, M. *J. Phys. Chem. C* **2014**, *118*, 1587–1593.

[377] Hao, E.; Schatz, G. C. *J. Chem. Phys.* **2004**, *120*, 357–366, journal article.

[378] Jiang, N.; Foley, E. T.; Klingsporn, J. M.; Sonntag, M. D.; Valley, N. A.; Dieringer, J. A.; Seideman, T.; Schatz, G. C.; Hersam, M. C.; Van Duyne, R. P. *Nano Lett.* **2012**, *12*, 5061–5067.

[379] Steidtner, J.; Pettinger, B. *Phys. Rev. Lett.* **2008**, *100*, 236101.

[380] Chen, C.; Hayazawa, N.; Kawata, S. *Nature Comm.* **2014**, *5*, 3312.

[381] Deckert-Gaudig, T.; Kämmer, E.; Deckert, V. *J. Biophotonics* **2012**, *5*, 215–219.

[382] Bylaska, E. J. et al. NWChem, A Computational Chemistry Package for Parallel Computers, Version 5.1. Pacific Northwest National Laboratory: Richland, Washington 99352-0999, USA, 2007; A modified version.

[383] Valiev, M.; Bylaska, E.; Govind, N.; Kowalski, K.; Straatsma, T.; Van Dam, H.; Wang, D.; Nieplocha, J.; Apra, E.; Windus, T.; de Jong, W. *Comput. Phys. Commun.* **2010**, *181*, 1477–1489.

[384] Silverstein, D. W.; Jensen, L. *J. Chem. Phys.* **2012**, *136*, 064110.

[385] Li, B.; Johnson, A. E.; Mukamel, S.; Myers, A. B. *J. Am. Chem. Soc.* **1994**, *116*, 11039–11047.

[386] Myers, A. B. *Ann. Rev. Phys. Chem.* **1998**, *49*, 267–295.

[387] Yang, P.; Qi, D.; You, G.; Shen, W.; Li, M.; He, R. *J. Chem. Phys.* **2014**, *141*, 124304.

[388] Yang, L.; Zhu, C.; Yu, J.; Lin, S. H. *Chem. Phys.* **2012**, *400*, 126–136.

[389] Neacsu, C. C.; Dreyer, J.; Behr, N.; Raschke, M. B. *Phys. Rev. B* **2006**, *73*, 193406.

[390] Zhang, W.; Yeo, B. S.; Schmid, T.; Zenobi, R. *J. Phys. Chem. C* **2007**, *111*, 1733–1738.

[391] Emory, S. R.; Jensen, R. A.; Wenda, T.; Han, M.; Nie, S. *Faraday Discuss.* **2006**, *132*, 249–259.

[392] Futamata, M.; Maruyama, Y.; Ishikawa, M. *Vib. Spectrosc.* **2004**, *35*, 121–129.

[393] Michaels, A. M.; Jiang,; Brus, L. *J. Phys. Chem. B* **2000**, *104*, 11965–11971.

[394] Etchegoin, P. G.; Meyer, M.; Blackie, E.; Le Ru, E. C. *Anal. Chem.* **2007**, *79*, 8411–8415.

[395] Etchegoin, P. G.; Meyer, M.; Le Ru, E. C. *Phys. Chem. Chem. Phys.* **2007**, *9*, 3006–3010.

[396] Domke, K. F.; Zhang, D.; Pettinger, B. *J. Phys. Chem. C* **2007**, *111*, 8611–8616.

[397] Pettinger, B.; Ren, B.; Picardi, G.; Schuster, R.; Ertl, G. *J. Raman Spectrosc.* **2005**, *36*, 541–550.

[398] Silverstein, D. W.; Jensen, L. *J. Chem. Phys.* **2012**, *136*, 064111.

[399] Nelder, J. A.; Mead, R. *Computer Journal* **1965**, *7*, 308–313.

[400] Le Ru, E. C.; Etchegoin, P. G. *Principles of Surface-Enhanced Raman Spectroscopy*; Elsevier: Amsterdam, 2009; Chapter 4, pp 185 – 264.

[401] Banik, M.; Apkarian, V. A.; Park, T. H.; Galperin, M. *J. Phys. Chem. Lett.* **2013**, *4*, 88–92.

[402] Hennessy, M. H.; Kelley, A. M. *Phys. Chem. Chem. Phys.* **2004**, *6*, 1085–1095.

[403] Shorr, E.; Myers Kelley, A. *Phys. Chem. Chem. Phys.* **2007**, *9*, 4785–4792.

[404] Hildebrandt, P.; Stockburger, M. *J. Phys. Chem.* **1984**, *88*, 5935–5944.

[405] Liu, Z.; Ding, S.-Y.; Chen, Z.-B.; Wang, X.; Tian, J.-H.; Anema, J. R.; Zhou, X.-S.; Wu, D.-Y.; Mao, B.-W.; Xu, X.; Ren, B.; Tian, Z.-Q. *Nature Comm.* **2011**, *2*, 305–.

[406] Opilik, L.; Bauer, T.; Schmid, T.; Stadler, J.; Zenobi, R. *Phys. Chem. Chem. Phys.* **2011**, *13*, 9978–9981.

[407] Stadler, J.; Schmid, T.; Zenobi, R. *ACS Nano* **2011**, *5*, 8442–8448.

[408] van Schrojenstein Lantman, E. M.; Deckert-Gaudig, T.; Mank, A. J. G.; Deckert, V.; Weckhuysen, B. M. *Nat. Nanotechnol.* **2012**, *7*, 583–586.

[409] Hayazawa, N.; Yano, T.; Watanabe, H.; Inouye, Y.; Kawata, S. *Chem. Phys. Lett.* **2003**, *376*, 174–180.

[410] Domke, K. F.; Zhang, D.; Pettinger, B. *J. Am. Chem. Soc.* **2007**, *129*, 6708–6709.

[411] Artur, C.; Le Ru, E. C.; Etchegoin, P. G. *J. Phys. Chem. Lett.* **2011**, *2*, 3002–3005.

[412] Temple, P. A.; Hathaway, C. E. *Phys. Rev. B* **1973**, *7*, 3685–3697.

[413] Tsai, C.-S.; Lin, C.-E.; Lin, J.-C.; Wang, J.-K. *Chem. Phys. Lett.* **1998**, *295*, 509–515.

[414] Anger, P.; Feltz, A.; Berghaus, T.; Meixner, A. J. *J. Microsc.* **2003**, *209*, 162–166.

[415] Wustholz, K. L.; Henry, A.-I.; McMahon, J. M.; Freeman, R. G.; Valley, N.; Piotti, M. E.; Natan, M. J.; Schatz, G. C.; Duyne, R. P. V. *J. Am. Chem. Soc.* **2010**, *132*, 10903–10910.

[416] McCreery, R. L. *Raman spectroscopy for chemical analysis*; Chemical Analysis Monograph Series; John Wiley & Sons, 2005; Vol. 225.

[417] Zheng, R.-h.; Wei, W.-m.; Zhu, L.-l.; Shi, Q. *Spectrochim. Acta A* **2014**, *133*, 707 – 713.

[418] Duan, S.; Tian, G.; Luo, Y. *Angew. Chem.* **2016**, *128*, 1053–1057.

[419] Meng, L.; Yang, Z.; Chen, J.; Sun, M. *Sci. Rep.* **2015**, *5*, 9240.

[420] Duan, S.; Tian, G.; Ji, Y.; Shao, J.; Dong, Z.; Luo, Y. *J. Am. Chem. Soc.* **2015**, *137*, 9515–9518.

[421] Kometani, N.; Tsubonishi, M.; Fujita, T.; Asami, K.; Yonezawa, Y. *Langmuir* **2001**, *17*, 578–580.

[422] Wiederrecht, G. P.; Wurtz, G. A.; Hranisavljevic, J. *Nano Lett.* **2004**, *4*, 2121–2125.

[423] Ambjörnsson, T.; Mukhopadhyay, G.; Apell, S. P.; Käll, M. *Phys. Rev. B* **2006**, *73*, 085412.

[424] Sugawara, Y.; Kelf, T. A.; Baumberg, J. J.; Abdelsalam, M. E.; Bartlett, P. N. *Phys. Rev. Lett.* **2006**, *97*, 266808.

[425] Uwada, T.; Toyota, R.; Masuhara, H.; Asahi, T. *J. Phys. Chem. C* **2007**, *111*, 1549–1552.

[426] Kelley, A. M. *Nano Lett.* **2007**, *7*, 3235–3240.

[427] Juluri, B. K.; Lu, M.; Zheng, Y. B.; Huang, T. J.; Jensen, L. *J. Phys. Chem. C* **2009**, *113*, 18499–18503.

[428] Zheng, Y. B.; Juluri, B. K.; Lin Jensen, L.; Ahmed, D.; Lu, M.; Jensen, L.; Huang, T. J. *Adv. Mater.* **2010**, *22*, 3603–3607.

[429] Chulhai, D. V.; Jensen, L. *Phys. Chem. Chem. Phys.* **2016**, DOI:10.1039/C6CP00310A.

[430] Neugebauer, J. *J. Phys. Chem. B* **2008**, *112*, 2207–2217.

[431] Neugebauer, J. *J. Chem. Phys.* **2009**, *131*, 084104.

[432] Jensen, L.; Åstrand, P.-O.; Mikkelsen, K. V. *Int. J. Quantum Chem.* **2001**, *84*, 513–522.

[433] Polubotko, A. *Phys. Lett. A* **1990**, *146*, 81–84.

# Vita

**Dhabih V. Chulhai**

## Education

| | |
|---|---|
| 2011 to 2016 | Ph.D., Chemistry<br>The Pennsylvania State University<br>University Park, PA |
| 2009 to 2011 | B.S., Chemistry<br>City University of New York \| York College<br>New York, NY |
| 2006 to 2007 | University of Guyana \| Turkeyen Campus<br>Georgetown, Guyana |

## Awards and Honors

| | |
|---|---|
| 2015 | Eugene and Jane Apple Science Graduate Fellowship |
| 2011 | Incoming Class New Graduate Student Award |

## Publications

**D.V. Chulhai**, X. Chen and L. Jensen; "Simulating Ensemble-Averaged Surface-Enhanced Raman Scattering" *J. Phys. Chem. C* **2016**, DOI:10.1021/acs.jpcc.6b02159

**D.V. Chulhai** and L. Jensen; "External Orthogonality in Subsystem Time-dependent Density Functional Theory" *Phys. Chem. Chem. Phys.* **2016**, DOI:10.1039/c6cp00310a

**D.V. Chulhai**, Z. Hu, J.E. Moore, X. Chen and L. Jensen; "Theory of Linear and Nonlinear Surface-Enhanced Vibrational Spectroscopy" *Annu. Rev. Phys. Chem.* **2016**, *67*, 541–564.

**D.V. Chulhai** and L. Jensen; "Frozen Density Embedding with External Orthogonality in Delocalized Covalent Systems" *J. Chem. Theory Comput.* **2015**, *11*, 3080–3088.

N. Chiang, N. Jiang, **D.V. Chulhai**, E.A. Pozzi, M.C. Hersam, L. Jensen, T. Seideman, R.P. Van Duyne; "Molecular-Resolution Interrogation of a Porphyrin Monolayer by Ultrahigh Vacuum Tip-Enhanced Raman and Fluorescence Spectroscopy" *Nano Lett.* **2015**, *15*, 4114–4120.

**D.V. Chulhai** and L. Jensen; "Plasmonic Circular Dichroism of 310- and $\alpha$-Helix using a Discrete Interaction Model/Quantum Mechanics Method" *J. Phys. Chem. A* **2015**, *119* 5218–5223.

**D.V. Chulhai** and L. Jensen; "Simulating Surface-Enhanced Raman Optical Activity Using Atomistic Electrodynamics-Quantum Mechanical Models" *J. Phys. Chem. A* **2014**, *118*, 9069–9079.

J.M. Klingsporn, N. Jiang, E.A. Pozzi, M.D. Sonntag, **D. Chulhai**, T. Seideman, L. Jensen, M.C. Hersam and R.P. Van Duyne; "Intramolecular Insight into Adsorbate–Substrate Interactions via Low-Temperature, Ultrahigh-Vacuum Tip-Enhanced Raman Spectroscopy" *J. Am. Chem. Soc.* **2014**, *136*, 3881–3887.

**D.V. Chulhai** and L. Jensen; "Determining Molecular Orientation with Surface-Enhanced Raman Scattering Using Inhomogenous Electric Fields" *J. Phys. Chem. C* **2013**, *117*, 19622–19631.

M.D. Sonntag, **D. Chulhai**, T. Seideman, L. Jensen and R.P. Van Duyne; "The Origin of Relative Intensity Fluctuations in Single-Molecule Tip-Enhanced Raman Spectroscopy" *J. Am. Chem. Soc.* **2013**, *135*, 17187–17192.